

On the effects of fluid pressure variations on rock-mass and fault mechanical behaviour

Présentée le 5 mars 2021

Faculté de l'environnement naturel, architectural et construit
Laboratoire expérimental de mécanique des roches
Programme doctoral en mécanique

pour l'obtention du grade de Docteur ès Sciences

par

Corentin Jean-Marie Rémi NOËL

Acceptée sur proposition du jury

Prof. J.-F. Molinari, président du jury
Prof. M. E. S. Violay, directrice de thèse
Prof. T.-F. Wong, rapporteur
Prof. A. Schubnel, rapporteur
Prof. A. Ferrari, rapporteur

Acknowledgements

This manuscript summarizes the research I have carried out in the Laboratory of Experimental Rock Mechanics (LEMR) at École Polytechnique Fédérale de Lausanne (EPFL). This work was funded by Gaznat SA, grant FRICTION: Fault Reactivation during CO₂ sequestraTION.

I would like to thank my thesis supervisor, professor Marie Violay, for her patient (and sometimes impatient) guidance, enthusiasm for strange results and encouragement. You are a great person, I could not have expected a better supervisor and I am grateful that you welcomed me to the LEMR as a PhD student. It has been a great opportunity to work with you, thank you!

I would like to thank all the members of the jury, professor Teng-fong Wong, professor Alexandre Schubnel, professor Alessio Ferrari, and the president of the jury Jean-François Molinari for having taking the time and consideration to evaluate my research. Thank you for all the constructive discussion, criticism and comments.

I am also thankful to Prof. Lucas Pimienta, Dr. Carolina Giorgetti, Dr. François Passelègue and Prof. Patrick Baud for the discussion, support and revision process of our research. I am honoured that you are my co-authors.

During these years, I have been lucky to be surrounded by fantastic colleagues and friends. I would like to thank Laurent, Federica, Benjamin and Aurélien for the discussions, technical support in sample preparation process and for helping me solve laboratory issues. Laurent, thank you also for the winter snow reports and advising me on beautiful splitboard routes! I am also thankful to the mechanical workshop team of EPFL (especially Laurent and Michel) who helped me for the design and realization of the mechanical parts I required for the experiments. I also would like to thank Rosa Ana for her assistance and for having taking care of all the administrative work I needed.

I am very happy to have been part of the LEMR family (that is becoming quite big!), and I wish to thank all of you: Felipe, Mateo, Chiara, Federica P., Francesco, Lucas, François, Carolina, Barnaby, Henri, Gabriel, Mathias, Federica S., Rosa Ana, Laurent, Aurélien, and of course Marie. I will never forget the nice moments we spent together, the (sometimes very long) coffee breaks and discussions we had.

There is also a life outside the office (thankfully!). Merci à vous les copains de la maison Vallaire, Nathan, Kat, Lucas, Pierre, Antho, Pipi et Erick, pour tous ces bons moments à la maison, au lac, à la montagne et ailleurs. Merci aux copains de la montagne avec qui j'ai passé plein de super moments. Sylwia et Matchieu pour les grimpes chill, le snow dans la grosse popow et les raclettes. Pipi et Théo pour les grimpes beaucoup moins chill, promis un jour j'aurais plus peur ! Mateo, un jour on arrivera à faire une course d'alpi sans se perdre... Barnaby, un jour tu vas arrêter

d'être blessé ? Jacques pour les découvertes de la Chartreuse et du Vercors, mais aussi pour toutes les bières qui m'ont tué plusieurs fois. Merci aux grimpeurs de tartine, de sarriette, de falaise et de paluarde pour les trips Verdoneque, les nouvel an dans la joie et tout ça tout ça : Rémy (on oubliera plus de vérifier les grigris dans l'Escalès et les frontales en grande voie), Adam (bois ta pinte de vin !), Canty (paie à la main morte dans la mainmorte), Memel (grand maitre du jeu de mots et de la grande voie sous tempête), Senicourt (il s'agirait de déménager !), Reneu (beuneuneuuu reuneuuu), Paps (Tom souilleuur), et tous ceux qui nous rejoindront.

Merci à tous !!!

Lausanne, 05 February 2021

Corentin

Abstract

In the past 20 years, the growing interest in deep geo-reservoirs for purposes such as carbon storage, waste water disposal, or geothermal energy exploitation have led to large-volume fluid injections into the upper continental crust. These fluid injections have caused a massive increase in the seismicity rate in some normally “quiet” regions. Recent observations suggested that different injection strategies could produce different mechanical responses in these reservoirs. In this vein, cyclic fluid injections have been proposed as an alternative to conventional monotonic injections to mitigate induced earthquakes. Additionally, recent studies have suggested that injection into deeper geo-reservoirs, at the brittle-ductile transition, could reduce (or suppress) induced earthquakes.

In this context, this research has aimed at bettering our understanding of reservoir deformation during different fluid injection strategies. Laboratory experiments were performed on porous reservoir rock under different reservoir conditions and fluid injection strategies.

In the first section, it is demonstrated that water-saturated conditions, compared to dry conditions, cause a reduction in uniaxial compression strength in five sandstones. Additional experiments suggest that this water weakening of sandstones is due to the reduction of the fracture toughness and of the static friction of the materials.

In the second section, it is shown that under drained conditions, pore fluid pressure oscillations affect the long-term mechanical behaviour of intact porous rocks. More than the amplitude of the oscillations, the period controls the time-to-failure, failure strength and dilatancy rate of the sample. Additionally, the pore fluid pressure oscillations control the AE events (a proxy for the seismicity): the AE events rate oscillates in-phase with the pore fluid pressure variations. Increasing the differential stress, the amplitude and the period of the oscillations accentuates this behaviour.

In the third section, it is demonstrated that under drained conditions, pore fluid pressure oscillations strongly affect the mechanical behaviour of faults. The pore fluid pressure signal directly controls the instabilities’ (i.e., stick-slip and AE events) distribution, with an increase of events at elevated pore fluid pressure. For initially stable sliding faults, the pore fluid pressure oscillation signal controls the onset of unstable slip: the higher the pore fluid pressure oscillation’s amplitude, the lower the stress and displacement at the onset of a seismic event.

In the fourth section, it is shown that under quasi-drained conditions, a pore fluid pressure increase within a rock undergoing ductile deformation causes instantaneous dilation of the system. Further increasing the pore fluid pressure leads to the development of localized deformations and the shear fracturing of the rock. The macroscopic shear fracturing is not instantaneous when the ductile to brittle transition is passed. Prior to this, a creeping phase is necessary. The time and strain length of this creeping phase are controlled by the rate of pore fluid pressure increase: the faster the injection, the longer the creeping phase.

This work provides new insight into the mechanical behaviour of rock masses and faults under various crustal conditions during pore fluid pressure variations. It helps to constrain the mechanisms involved in deep geo-reservoirs submitted to different injection strategies.

Keywords: fluid-rock interactions, fluid-fault interactions, fluid injections, fluid pressure oscillation, induced seismicity, triaxial experiment

Résumé

Ces 20 dernières années, l'utilisation croissante des réservoirs géologiques profonds pour le stockage de carbone, le traitement des eaux usées, ou l'exploitation géothermique a conduit à l'injection massive de fluides dans la croûte continentale supérieure. Ces injections ont provoqué une augmentation drastique de la sismicité dans des régions asismiques. De récentes observations suggèrent que différentes stratégies d'injection produisent différentes réponses mécaniques des réservoirs. Dans cet esprit, il a été suggéré que des injections cycliques plutôt que monotoniques réduisent les séismes induits. De plus, il a été récemment proposé que des injections plus profondes, à la transition fragile-ductile, pourraient réduire (ou supprimer) les séismes induits.

Dans ce contexte, ce travail a pour but une meilleure compréhension de la déformation des réservoirs lors de différentes stratégies d'injection. Des expériences en laboratoire sur des roches poreuses soumises à différentes conditions crustales et stratégies d'injection ont été effectuées.

Dans une première partie, il est montré que des conditions saturées en eau, par rapport à sèches, induisent une réduction de la résistance en compression uniaxiale dans cinq grès. Des expériences additionnelles suggèrent que cet affaiblissement par l'eau est dû à la réduction de la ténacité et de la friction statique des matériaux.

Dans une deuxième partie, il est montré que dans des conditions drainées, des oscillations de pression de pore affectent le comportement long terme des roches. Plus que l'amplitude des oscillations, la période contrôle le temps à la rupture, la résistance et le taux de dilataance des échantillons. De plus, les oscillations de pression de pore contrôlent les événements acoustiques : le taux d'évènement oscille en phase avec la pression de pore. Augmenter la contrainte différentielle, l'amplitude et la période des oscillations accentue ce comportement.

Dans une troisième section, il est montré que dans des conditions drainées, des oscillations de pression de pore affectent grandement le comportement mécanique des failles. Le signal de pression de pore contrôle la distribution des instabilités (séismes et événement acoustiques), avec une augmentation d'évènements lorsque la pression de pore est élevée. Pour une faille initialement stable, une pression de pore oscillante contrôle l'initiation de glissement instable : l'augmentation de l'amplitude des oscillations favorise l'apparition d'évènements sismiques à plus basse contrainte et pour de plus petits déplacements.

Dans une quatrième section, il est montré que, dans des conditions quasi-drainées, une augmentation de la pression de pore au sein d'une roche ductile provoque la dilataance instantanée du système. Augmenter davantage la pression de pore conduit au développement de déformations localisées et à la fracturation de la roche. La fracturation macroscopique n'est pas instantanée lorsque la transition ductile-fragile est passée, et requiert une phase de fluage. La durée du fluage est contrôlée par le taux d'injection de pression de pore : plus l'injection est rapide, plus la phase est longue.

Ce travail apporte une meilleure connaissance du comportement mécanique des masses rocheuses et des failles soumises à différentes conditions crustales pendant des variations de pression de pore. Il aide à contraindre les mécanismes impliqués dans la déformation des réservoirs géologiques soumis à différentes stratégies d'injection.

Mots-clés : interactions fluide-roche, interactions fluide-faille, injections de fluide, pression de pore oscillante, sismicité induite, expériences triaxiales

Contents

Acknowledgements	iii
Abstract.....	vi
Résumé	viii
Chapter 1 CO₂ geological sequestration	1
1.1 Generalities	1
1.2 Main issues.....	2
1.3 Injection rate strategies	3
Chapter 2 Reservoir rock deformation.....	5
2.1 Intact reservoir rock mechanics: the brittle domain	6
2.1.1 Brittle deformations	6
2.1.2 Micro-mechanism of brittle failure.....	6
2.1.3 Short-term macroscopic failure criterion.....	9
2.1.4 Effect of pore fluid	10
2.1.5 Long-term strength	11
2.1.6 Fatigue behaviour	14
2.2 Fault mechanics.....	15
2.2.1 Fault reactivation	15
2.2.2 Fault stability	16
2.3 Deep reservoir rock mechanics: the ductile domain	18
2.3.1 Ductile deformation	19
2.3.2 Microscopic analysis of the deformations	20
2.3.3 The brittle-ductile transition	22
2.4 Objectives of the thesis	24
2.5 Organisation of the thesis.....	25
Chapter 3 Effect of water on sandstone's fracture toughness and frictional parameters: brittle strength constraints	27
3.1 Abstract	28
3.2 Introduction	28
3.3 Experimental methodology	30
3.3.1 Starting materials	30

3.3.2	Experimental methods	33
3.3.2.1	Uniaxial compression.....	33
3.3.2.2	Fracture toughness	34
3.3.2.3	Friction.....	35
3.4	Results.....	38
3.4.1	Uniaxial compression	38
3.4.2	Fracture toughness	40
3.4.3	Friction.....	42
3.5	Discussion	44
3.5.1	Water weakening of sandstone	44
3.5.2	Micro-mechanical interpretation of water weakening under uniaxial compression	52
3.5.2.1	Description of micro-mechanical models	53
3.5.2.2	Water weakening: experimental data and models prediction	54
3.5.2.3	Extrapolation to water weakening under triaxial conditions	56
3.6	Conclusions	58
Chapter 4	Time-dependent deformations of sandstone during pore fluid pressure oscillations: Implications for natural and induced seismicity	60
4.1	Abstract	61
4.2	Introduction.....	61
4.3	Experimental methodology	63
4.3.1	Starting sample	63
4.3.2	Triaxial deformation	65
4.3.2.1	Apparatus	65
4.3.2.2	Constant displacement rate experiments.....	66
4.3.2.3	Constant stress experiments	67
4.3.3	Data treatment and analysis	70
4.4	Results	71
4.4.1	Constant displacement rate experiments	71
4.4.2	Creep experiments at constant pore fluid pressure	73
4.4.3	Creep experiments under oscillating pore fluid pressure	74
4.4.3.1	Amplitude effects.....	74

4.4.3.2	Period effects	77
4.4.3.3	Dilatancy	81
4.5	Interpretation and discussion.....	81
4.5.1	Pore fluid pressure level	82
4.5.2	Dilatancy and soft stimulations	82
4.5.3	Pore fluid pressure controlling the deformation and AE event rates.....	83
4.5.4	Implication for the upper crust deformation.....	87
4.6	Conclusions	88
	Acknowledgments	88
Chapter 5	Fault reactivation during fluid pressure oscillations: transition from stable to unstable slip.....	89
5.1	Abstract	90
5.2	Introduction	90
5.3	Experimental methodology	91
5.3.1	Starting sample	91
5.3.2	Apparatus.....	91
5.3.3	Experimental procedure.....	92
5.3.4	Data analysis.....	93
5.4	Results	93
5.5	Interpretation and discussion.....	98
5.5.1	Theoretical framework for fault reactivation and frictional stability	98
5.5.2	Fluid pressure oscillation influences the events distribution.....	99
5.5.3	Fluid pressure oscillations promote early instability	99
5.5.4	Implications for natural and induced seismicity.....	103
5.6	Conclusions	104
	Acknowledgments	104
Chapter 6	Brittle faulting of ductile rock induced by pore fluid pressure build-up	105
6.1	Abstract	106
6.2	Introduction.....	106
6.3	Experimental methodology	108
6.3.1	Starting sample	108
6.3.2	Triaxial deformations	110

6.3.2.1	Apparatus	110
6.3.2.2	Constant pore fluid pressure experiments.....	112
6.3.3	Injection experiments	113
6.3.4	Data treatment and analysis	114
6.4	Results	115
6.4.1	Constant pore fluid pressure experiments	115
6.4.2	Injection experiments	118
6.5	Interpretation and discussion.....	125
6.5.1	Brittle-ductile transition with increasing effective confining pressure.....	125
6.5.2	Ductile to brittle deformation induced by pore pressure increase	126
6.5.3	Implication for deep deformations and earthquakes.....	128
6.6	Conclusions	129
	Acknowledgments	130
Chapter 7	General conclusion and perspectives	131
7.1	Main findings	131
7.1.1	Short-term water weakening.....	131
7.1.2	Pore fluid pressure oscillations on intact rock.....	132
7.1.3	Pore fluid oscillations on faulted rock.....	132
7.1.4	Pore fluid pressure increase in ductile rock.....	132
7.2	Implications for reservoir deformations.....	133
7.3	Future work	134
	Bibliography	136
	Appendix A	157
	Appendix B	159
	Curriculum Vitae	162

Chapter 1 CO₂ geological sequestration

1.1 Generalities

Global warming due to the increase of atmospheric greenhouse gases content has become a worldwide concern. In order to reduce the amount of carbon dioxide released into the atmosphere, the capture of the emitted CO₂ generated by coal or gas-fired power plants and its storage into geological reservoirs is seen as a promising option. This technique is known as carbon capture and storage (CCS). Geological storage (i.e. sequestration) of CO₂ involves the high-pressure injection of CO₂ into deep underground reservoirs. The reservoir rock must be at a depth below 800 m so that the pressure and temperature met result in CO₂ being in a supercritical state (this phase imply minimal temperature and pressure of 31.1°C and 7.4 MPa, respectively). Indeed, the phase change from gaseous to supercritical state provides a dramatic increase in the CO₂ density, in turn providing two main advantages: a higher storable CO₂ mass and a decrease of the CO₂ buoyancy compared to *in situ* fluid (e.g. Benson & Cole, 2008).

A suitable reservoir for CO₂ sequestration is composed of a reservoir rock and a caprock (Figure 1. 1). The reservoir rock must be a porous and permeable rock (e.g. sandstone, molasses or oolitic limestone) to allow for a high storage capacity and a fast injection rate, respectively. It must be overlain by an impermeable caprock (e.g. clay, evaporite or gypsum) to prevent the upward migration of CO₂. After injection of the CO₂ into the reservoir rock, the sequestration occurs via four combined physical and chemical mechanisms (here sorted from lower to higher storage security, e.g. Benson & Cole, 2008; Metz et al., 2005):

- (1) Structural trapping: The impermeable caprock serves as a barrier to the upward migration of CO₂. This kind of trapping requires structural features, such as anticline folds or faulted formations, to provide efficient sequestration.
- (2) Residual or capillary trapping: When the CO₂ migrates through a formation, small amounts are retained in the pore space by capillary forces and remain immobile, trapping a significant amount of CO₂.
- (3) Solubility trapping: Injected CO₂ can dissolve into the *in situ* brine which eliminates the buoyancy forces preventing its upward migration. The solubility of the CO₂ into brine increases with pressure but decreases with temperature and salinity.
- (4) Mineral trapping: A fraction of the CO₂ injected can be converted into stable carbonate mineral (CaCO₃). The reaction involves bicarbonate ions provided by the reaction of CO₂ with water ($\text{CO}_2 + \text{H}_2\text{O} \leftrightarrow \text{H}_2\text{CO}_3 \leftrightarrow \text{H}^+ + \text{HCO}_3^- \leftrightarrow 2\text{H}^+ + \text{CO}_3^{2-}$) and calcium ions (Ca²⁺).

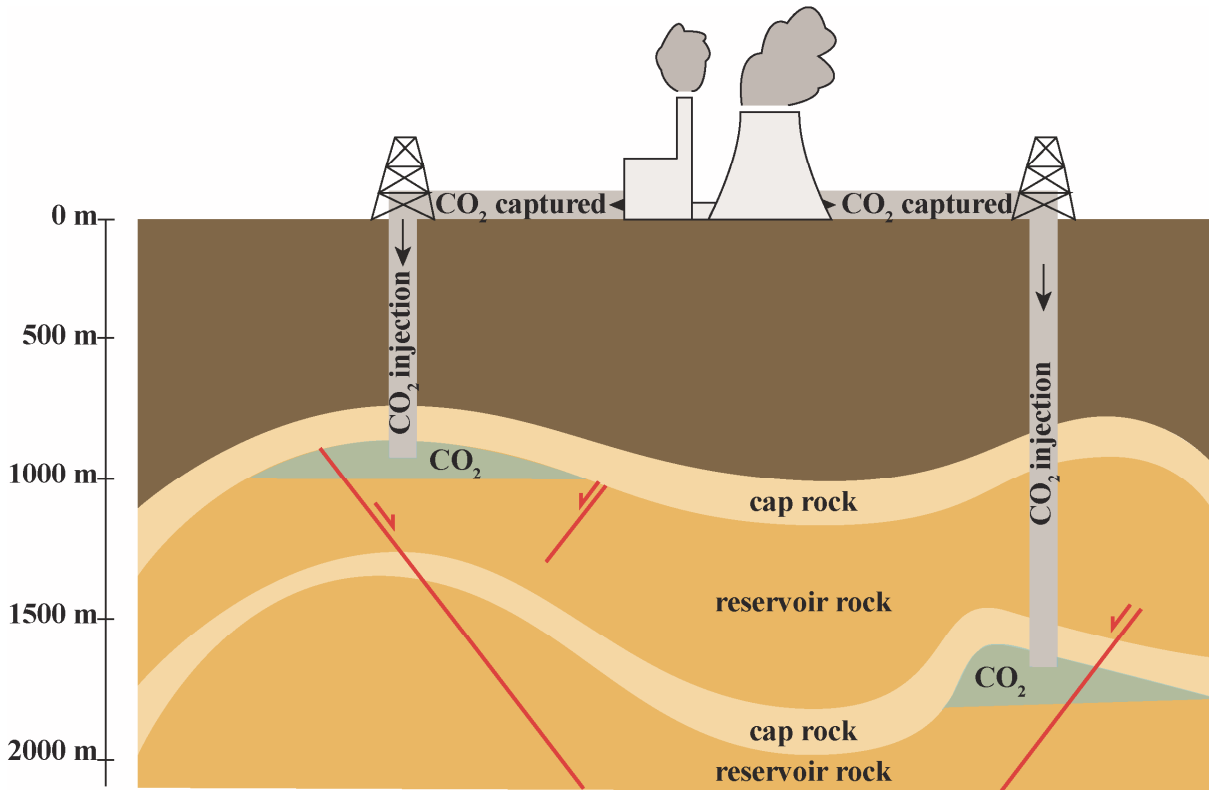


Figure 1. 1: Schematic illustration of the concept of CO₂ sequestration into a deep geo-reservoir. After its capture, CO₂ is injected at depth > 800 m. Here, the CO₂ is trapped physically by the caprock preventing its upward migration.

The formation water must be distant from its ultimate discharge area for a longer storage time (Chevalier et al., 2010). Obviously, active fault zones should be avoided to prevent induced seismicity and leakage.

In Switzerland, potential deep geological formations were determined by Chevalier et al. (2010) by taking into account the depth, the potential seismicity, the geothermal gradient, the fault density and the groundwater residence time. Only the Swiss Molasse Basin and the Jura were considered in their study. Indeed, the Alps domain is mainly comprised of highly fractured metamorphic rocks with low porosity and permeability, leading CO₂ sequestration to be unlikely. The best targets in Switzerland are reservoirs located in the crescent Fribourg-Bienne-Baden-St. Gallen. Four regional reservoir rock-caprock candidates have been found in the Swiss Molasse Basin: (i) top basement and basal Mesozoic sandstone sealed by a Lower Triassic Anhydrite group, (ii) Upper Muschelkalk dolomite sealed by Keuper gypsum, (iii) Hauptrogenstein oolitic limestone sealed by mudstone from the Effinger Member, (iv) Upper Malm and Lower Cretaceous limestone sealed by an Oligocene Lower Freshwater Molasse.

1.2 Main issues

If at first glance geological sequestration of CO₂ seems to be a promising method to reduce carbon dioxide emission into the atmosphere, it also involved issues.

First, the injected CO₂ must remain trapped in the reservoir for an extensive period of time (minimal of around 1000 years to be effective, see Metz et al. (2005) and reference therein) involving

careful attention to CO₂ leakage from the reservoir. Indeed, CO₂ leakage can occur both through the injection path (i.e. the borehole) or natural (i.e. discontinuities) paths. At the borehole, many pathways are possible for a CO₂ leakage (Celia et al., 2004): between cement and casing, through cement, through the casing, or between cement and surrounding rock. Moreover, reservoir rocks commonly contain natural discontinuities such as lateral variation, anisotropy, faults, etc. The permeability of those discontinuities is generally different from that of the main rock, leading to possible CO₂ leakage through these paths and migration upward to possible other aquifers (e.g. groundwater table) or the surface.

Furthermore, injecting pressurized fluids into deep reservoirs affects the mechanical behaviour of the rock mass through thermal, chemical and mechanical interactions (e.g. Handin et al., 1963; Robinson, 1959). Pore fluid pressure decreases the *in situ* effective stresses, lowering the rock strength and bringing the rock mass and faults closer to failure conditions. During and after injection into deep geo-reservoirs, deformations are expected to take place. These deformations occur at different time and space scales. Figure 1. 2 shows the example of the In Salah pilot project in Algeria. On the one hand, the deformations are occurring slowly with uplift measured at the surface of about 5 mm.year⁻¹, on a large area around the injection boreholes (i.e. about 5 km) (Figure 1. 2a). On the other hand, much faster and localised deformations are also occurring during injection. Indeed, seismicity is recorded within the reservoir (Figure 1. 2b). These events are occurring on localized fault structures and the slip rate during such events is of the order of m.s⁻¹.

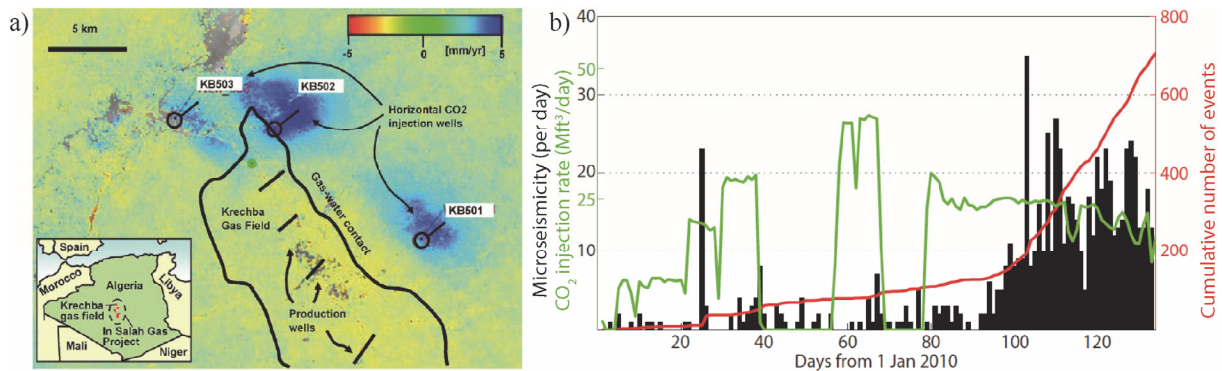


Figure 1. 2: Example of deformation at In Salah (Algeria) CO₂ injection project site where injection started in 2004. a) InSAR data showing the average rate of vertical displacement (i.e. surface uplift or subsidence) 3 years after the start of CO₂ injection. Injection is performed at point KB501, KB502 and KB503. From Rutqvist et al., (2010). b) Microseismicity (dark), CO₂ injection rate (green) and cumulative number of events (red) for the 4 first months of 2010. From Verdon et al., (2013).

In summary, three main geological issues can occur during CO₂ geological sequestration: leaks of CO₂ toward upper aquifers or the surface, slow and distributed surface deformations (i.e. uplift) and fast and localised deformations (i.e. induced seismicity).

1.3 Injection rate strategies

Recent studies on the mechanical behaviour of reservoirs have shown that, for a given *in situ* pore fluid pressure, different injection strategies result in different seismic responses of the reservoir. In order to inhibit induced seismicity, cyclic fluid injections were proposed as an alternative to conventional monotonic fluid injections for geo-reservoir stimulations. The method is often referred to as *soft stimulation* and aims to increase the reservoir performance (i.e., increasing the porosity

and permeability of the reservoir via micro-fracturation and dilatancy) while reducing the induced seismicity compared to conventional stimulations.

Numerical studies showed that cyclic fluid injection seems to trigger less seismicity compared to a monotonic injection strategy (Yoon et al., 2014; Zang et al., 2013). Particularly, laboratory and *in situ* studies have shown that not only the number of seismic events but also the maximum recorded event magnitude are reduced (Zang et al., 2018). With the growing interest in the use of geo-reservoirs, such cyclic stimulation might be of great interest for future injections, both for CO₂ injection context but also for other geo-energy involving fluid injection strategies. However, only a small number of experimental studies have been performed with the aim of increasing the understanding of such phenomena (Chanard et al., 2019; Farquharson et al., 2016; Zhuang et al., 2016). Note that during the time-lapse of this Ph.D. thesis, the first large scale cyclic fluid injections in the field have been operated in Pohang (Korea) (Hofmann et al., 2019). If during the injections the largest earthquake recorded was of small magnitude (M_w 1.9), later that year, a magnitude 5.5 (largest actual human induced earthquake) event occurred nearby the injection site, suspended all the injection operations.

Chapter 2 Reservoir rock deformation

This PhD thesis focuses on the rock deformations (slow and fast, localised and distributed) that occur within the reservoir rock during CO₂ geological sequestration, or other types of injections. This chapter aims to provide a brief overview of the current state of knowledge on reservoir rock deformation.

In the context of CO₂ sequestration, the reservoir rock must be porous and permeable enough to allow for high storage capacity and high injection rate, respectively. Typical reservoir rocks having these two characteristics are sedimentary rocks such as sandstones or porous limestone. Because of their importance as a building material or as oil/gas bearing reservoirs, they are the subject of many experimental studies. Their mechanical behaviour very depends on the applied confining pressure (P_c). Under low confining pressures ($P_c < 80$ MPa), and depending on their initial porosity, they deform in a brittle manner, i.e. the final deformation is localised through shear fractures. Under higher confining pressures ($P_c > 80$ MPa), the deformation is macroscopically ductile, i.e. distributed along the sample, and accommodated through cataclastic flow, compaction bands and crystal plasticity (Wong & Baud, 2012). The transition from brittle to ductile deformation is gradual because the onset of cataclastic flow and plasticity in polycrystalline rock is gradual, and also depends on the far-field strain rate.

For efficient CO₂ sequestration, interval depths of 800-2500 m are desired so that the lithostatic pressure is in the range of 20-60 MPa and the fluid injected can be in a supercritical state. Therefore, most of the deformations that are occurring are within the brittle field. However, some ductile deformation might occur for deeper reservoirs, especially in carbonate rich rock where the brittle-ductile transition occurs at low pressure and temperature (e.g. Wong and Baud, 2012). Therefore, this chapter focuses on three aspects. First, the mechanical behaviour of intact rock in the brittle domain is reviewed. Particularly, the short- and long-term typical behaviour and strength dependence, as well as fatigue behaviour are explored. Then, fault mechanical behaviour and stability of the sliding are detailed. Finally, ductile deformations that can occur in deep reservoirs are described and microstructural/micromechanical deformations and the brittle-ductile transition are presented. As a convention, compressions and compactive strains (shortening and porosity reduction) are positive. Additionally, even if stress and strain are tensor parameters, this experimental works have been performed under isotropic conditions, therefore, for simplicity they are noted σ and ε , respectively.

2.1 Intact reservoir rock mechanics: the brittle domain

2.1.1 Brittle deformations

In this thesis, the term brittle deformation refers to localized deformation at a sample size scale (≈ 8 cm). During triaxial compression deformation, shear fracturing is the dominant mode of failure in the brittle field. It is formed by the nucleation, propagation and coalescence of micro-cracks. Figure 2. 1 shows typical mechanical data obtained during the brittle deformation of a rock sample subjected to a differential stress (i.e., the difference between the axial stress and the confining pressure: $\sigma_1 - P_c$). First, the sample elastically deforms (i.e. reversible) and is subjected to compaction. On the stress – strain curve, elastic deformation is characterised by a linear increase of strain with stress (Figure 2. 1). From its slope, the Young's modulus (E) can be obtained. Beyond a certain stress level, the sample starts to dilate, and an inflexion of the stress – strain curve is observed. From this point, called the onset of dilatancy (C'), the deformation is plastic (i.e. irreversible) and micro-cracks are nucleated and propagated within the sample. At a higher stress level, dilatancy becomes predominant compared to compacting behaviours, this point is denoted D' . When stress increases further, it reaches a peak (σ_{peak} , i.e. sample strength) and the sample breaks by means of shear fractures. The macroscopic fracture originates from the coalescence of cracks which start to grow from the C' stress level. Finally, the stress decreases to a residual stress (σ_{residual}) that corresponds to the stress needed to slide on the formed fractures. Analysis of a post-mortem sample often shows that the obtained macroscopic failure has an angle of about 30° from the maximal principal stress (σ_1), with a tendency of this angle to increase when approaching the ductile field (e.g. Paterson, 1958; Paterson & Wong, 2005).

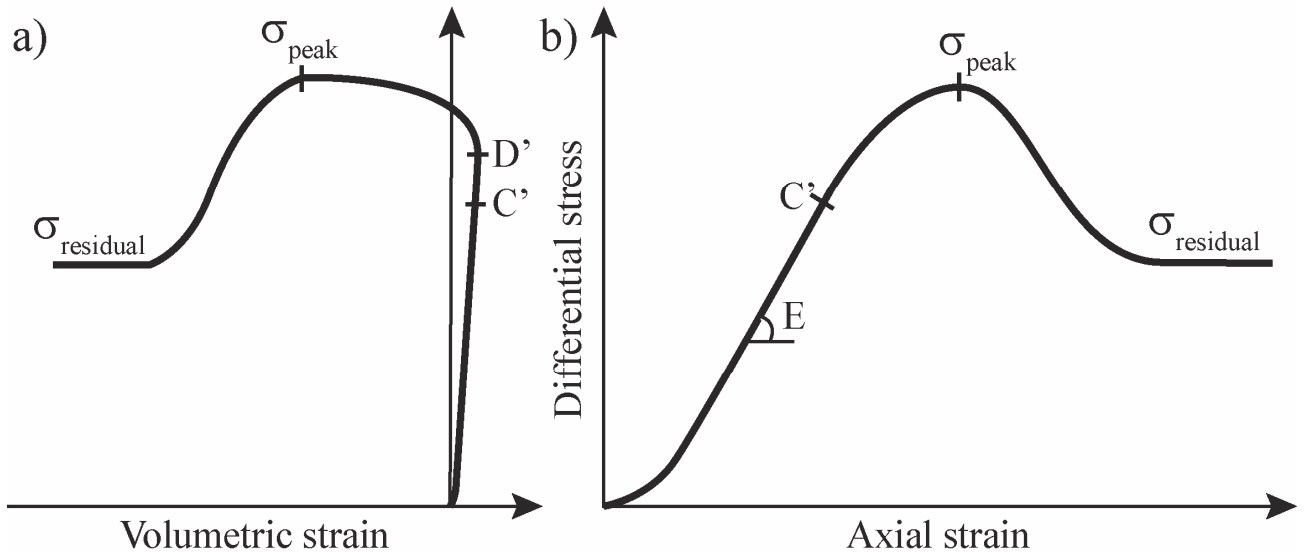


Figure 2. 1: Mechanical curves typical of the brittle field. a) Differential stress as function of the volumetric strain. b) differential stress as function of the axial strain. The Young modulus (E), onset of dilatancy (C'), passage from compactant to dilatant (D'), strength (σ_{peak}), and residual strength (σ_{residual}) are shown.

2.1.2 Micro-mechanism of brittle failure

In rocks and other materials, the strength measured experimentally is much lower than the theoretical one. This strength difference originates from stress concentrations that occur at real material

imperfections. Indeed, under far field tensile stresses (σ_T), an elliptical hole contained in a homogeneous elastic material causes stress concentrations at the ellipse vertex, that is proportional to the semi-major axis (c) of elliptical hole and approximately equal to $2\sigma_T\sqrt{c/r}$, where r is the radius of curvature at the ellipse vertex (Griffith, 1920; Inglis, 1913). Therefore, for a material containing long and narrow cracks, the strength of the material at the crack tips can be attained at stresses much lower than the material theoretical strength. Griffith (1920) posed this problem of material strength in term of energy balance for a crack to propagate. He considered a system, made of an elastic body that contains a crack of half-length c , submitted to extensional forces at its extremity. The crack propagates only if it minimises the system total energy (U), that is, the sum of the work done by the external forces (W), the internal elastic strain energy (U_e) and the surfaces energy (U_s): $U = (-W + U_e) + U_s$. In the case of a rod under uniform tensional stress, this energy criterion gives a failure of the material at $\sigma_f = \sqrt{(2E\gamma/\pi c)}$, where E is the Young's modulus and γ is the specific surface energy.

The macroscopic failure of a rock sample under compression originates from the nucleation, propagation and coalescence of many micro-scale cracks. Three basic modes of crack propagation are possible (Figure 2. 2a): tensile/opening propagation mode (Mode I), in-plane shear propagation mode (Mode II), and out-of-plane shear propagation mode (Mode III). Combined modes are also possible and are referred to as mix mode of propagation. Under compressive loading, cracks nucleate and propagate from natural inhomogeneities of the rock, i.e. pores, pre-existing micro-cracks, inclusions, small strength particles, etc., that give rise to stress concentrations (e.g. Inglis, 1913). From the variety of possible defects where cracks nucleate, two extreme cases can be considered (Ashby & Sammis, 1990): a spherical pore (Figure 2. 2b) and a sharp inclined crack (Figure 2. 2c). For the case of a spherical pore, the crack nucleates in a direction parallel to σ_1 due to a stress concentration (Figure 2. 2 b, Sammis and Ashby, 1986). The case of a sharp inclined crack has been the most studied (e.g. Ashby and Sammis, 1990; Brace et al., 1966; Brace and Bombolakis, 1963) and is often referred to as the *sliding crack* or the *wing crack* model (Figure 2. 2c). In this model, the remote stresses are inducing shear stress on the inclined crack. If the shear stress overcomes the frictional strength of the crack, the opposite faces start to slide, inducing tensile stress at the tips of the crack. In turn, the tensile stress induced may cause wing crack to nucleate. The driving force for crack nucleation is the mode I stress intensity factor (K_I). The wing crack can nucleate only if K_I overcomes a critical value K_{Ic} (i.e. the fracture toughness of the material where the crack propagates). In the case of a rock containing randomly oriented micro-cracks, the wing cracks should nucleate first on a sliding crack oriented at $\gamma = \frac{1}{2}\tan^{-1}\left(\frac{1}{\mu}\right)$, and at a stress of (Ashby & Hallam, 1986; Ashby & Sammis, 1990; Nemat-Nasser & Horii, 1982):

$$\sigma_1 = \frac{\sqrt{1+\mu^2}+\mu}{\sqrt{1+\mu^2}-\mu}\sigma_3 + \frac{\sqrt{3}}{\sqrt{1+\mu^2}-\mu}\frac{K_{Ic}}{\sqrt{\pi a}} \quad \text{Equation (2. 1)}$$

Where σ_1 and σ_3 are the maximum and minimum principal stress, μ is the friction coefficient and a is the half micro-crack length. The stress state described by equation (2. 1) corresponds to the onset of dilatancy C' in Figure 2. 1. Under compressional stresses and for a single wing crack propagating in an infinite medium, the mode I stress intensity factor at the tip of the wing crack is decreasing with increasing length l . This implies that crack growth is stable and that each increment of crack

length requires an increment of load (Ashby & Sammis, 1990; Horii & Nemat-Nasser, 1985). Then, in a medium containing randomly oriented sharp cracks (e.g. in rocks), an increment of stress has two major consequences: First, the already nucleated wing cracks that originates from the favourably oriented sliding crack will grow in length. Second, the less favourably oriented sliding cracks can be activated, in turn nucleating new wing cracks. Therefore, with the progressive increase of stress, the wing cracks are increasing both in length and number (i.e. increasing the damage state of the rock sample). Finally, the wing cracks stress fields start to overlap, leading to crack interaction. The interaction between the wing cracks depends then on the crack spacing and crack density of the rock. Ultimately, after the coalescence of numerous micro-cracks, a localised branching of the micro-deformations arises, leading to macroscopic shear failure.

Some specific cases have been theoretically studied. For example, Ashby and Sammis (1990) analysed the crack nucleation, propagation and interaction of an idealised medium under compressive stress, where cracks of radius a and oriented at an angle φ from the principal stress σ_1 , are uniformly spaced and oriented. They showed that the wing crack length l and the stress intensity factor K_I are linked by:

$$K_I = [(A_1\sigma_1 - A_3\sigma_3)(c_1 + c_2) - \sigma_3c_3] \times \sqrt{\pi a} \quad \text{Equation (2. 2)}$$

$$\text{with } c_1 = \pi^{-2} \left(\frac{l}{a} + \beta \right)^{-\frac{3}{2}} \quad \text{Equation (2. 3)}$$

$$c_2 = \frac{2(\pi\alpha)^{-2} \sqrt{\frac{l}{a}}}{\rho_0^{-\frac{2}{3}} - \left(1 + \frac{l}{aa}\right)^2} \quad \text{Equation (2. 4)}$$

$$c_3 = \frac{2}{\pi} \sqrt{\frac{l}{a}} \quad \text{Equation (2. 5)}$$

A_1 and A_3 are constants given by Ashby & Sammis (1990), $\alpha = \cos(\varphi)$ is the projection of the crack in the vertical plane, and $\rho_0 = \frac{4}{3}\pi N_V(\alpha a)^3$ represents the initial damage of the sample, with N_V being the number of cracks per unit of volume. β is an empirical parameter to restrict K_I to finite values when l is small. As K_I increases with the remote applied stress, it ultimately reaches the value of K_{Ic} and cracks propagate in order to maintain $K_I = K_{Ic}$. Rewriting equation (2.2) under this condition provides a relationship between the wing crack length and the applied stress (Ashby & Sammis, 1990; Brantut et al., 2012):

$$\sigma'_1(l) = \frac{\left(\frac{K_{Ic}}{\sqrt{\pi a}} + \sigma_3(c_3 + A_3(c_1 + c_2)) \right)}{A_1(c_1 + c_2)} \quad \text{Equation (2. 6)}$$

Equation (2.6) has a maximum value of $\sigma_1(l)$, corresponding to the short-term strength of the rock sample.

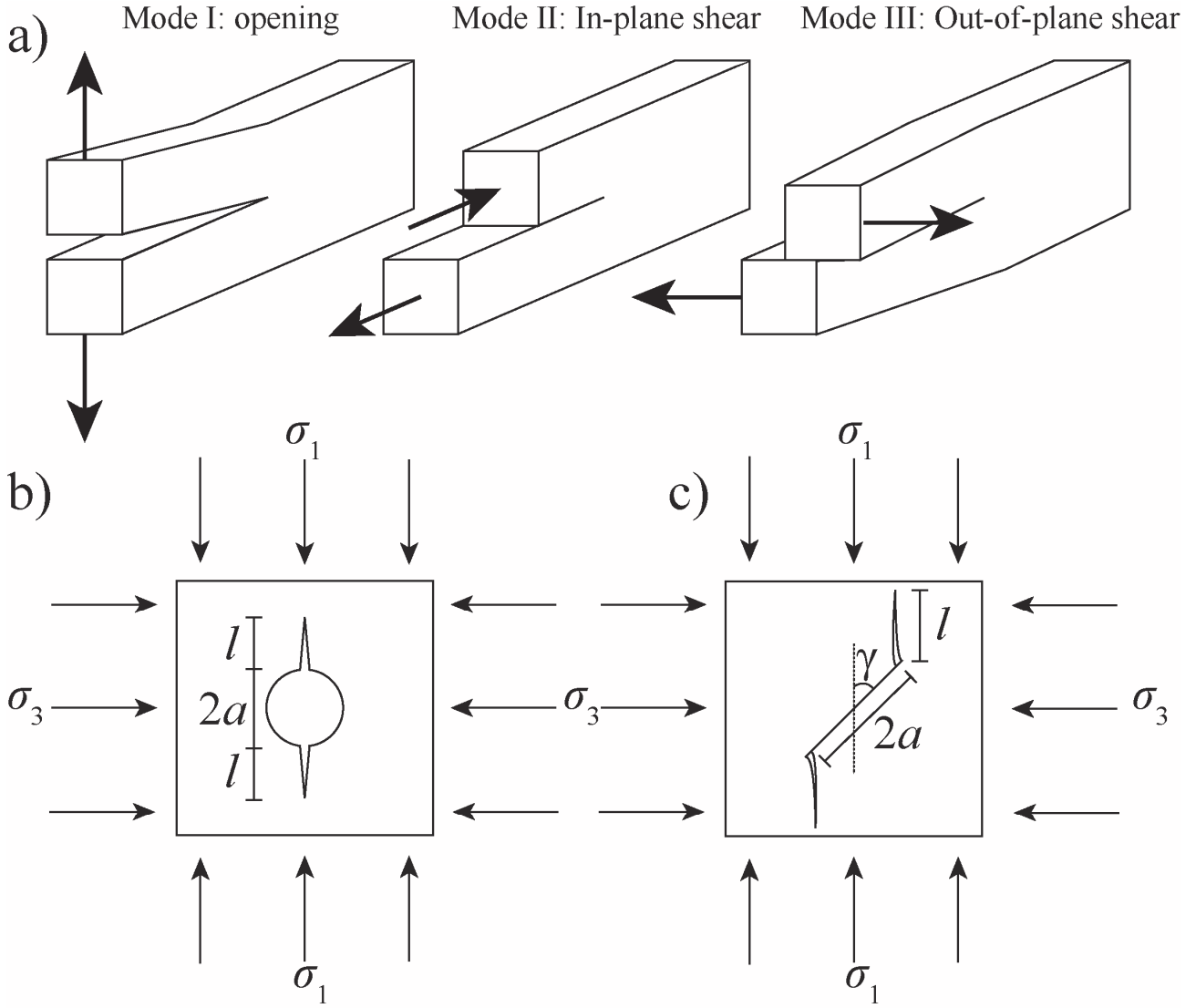


Figure 2. a) Crack propagation modes. Combined modes are possible and are referred to as mixed mode. b) Crack initiation from stress concentration around a spherical pore. c) Wing crack initiation from wedge opening at the tip of a sharp inclined crack.

2.1.3 Short-term macroscopic failure criterion

The strength of rock is usually expressed as a function of the principal stresses ($\sigma_1, \sigma_2, \sigma_3$). Under triaxial conditions and in the brittle field, failure occurs by shear fracturing. Experimental studies show that the maximum differential stress ($\sigma_1 - \sigma_3 = \sigma_1 - P_c$) before shear failure greatly depends on the confining pressure (P_c) applied to the rock sample. Over a moderate range of confining pressures, the strength of the rock can be represented by:

$$\sigma_1 - P_c = \sigma_{UCS} + P_c \tan(\psi) \quad \text{Equation (2. 7)}$$

Where σ_{UCS} is the uniaxial compressive strength of the rock sample and $\tan(\psi)$ is a constant value generally between 1 and 10 (Paterson & Wong, 2005). This relation can be expressed in terms of normal stress (σ_n) and shear stress (τ) (e.g. Jaeger, 1969) leading to the Coulomb failure criterion:

$$\tau = C + \sigma_n \tan(\phi) \quad \text{Equation (2. 8)}$$

Where C is the cohesion and φ the friction angle. $\tan(\varphi)$ can be expressed by the coefficient of internal friction μ with values usually ranging from 0.5 to 1.5 (Paterson & Wong, 2005). However, for many experimental data, the strength dependence to the confining pressure is not linear and curved relationship is often preferred to the linear Coulomb relation. Many curved relationships have been proposed to fit the experimental strength data such as the often used Hoek and Brown criterion (Hoek & Brown, 1980):

$$\sigma_1 - P_c = (m \sigma_{UCS} P_c + s \sigma_{UCS}^2)^{1/2} \quad \text{Equation (2. 9)}$$

Where m and s are rock parameters, with s being ≈ 1 for rock matrix.

For porous reservoir rock, the short-term strength is strongly affected by the rock porosity (e.g. Chang et al., 2006; Dunn et al., 1973; Palchik, 1999). The lower the porosity, the stronger the rock is. This effect can be illustrated by performing triaxial experiments on Fontainebleau sandstone (Figure 2. 3). Indeed, depending on the degree of cementation, Fontainebleau sandstone's porosity spans from 4 to 30%, for the same initial mineral composition (almost 100% quartz). At 20 MPa confining pressure, a 16% porosity Fontainebleau sandstone is almost three times less resistant than a 6% porosity one (Figure 2. 3).

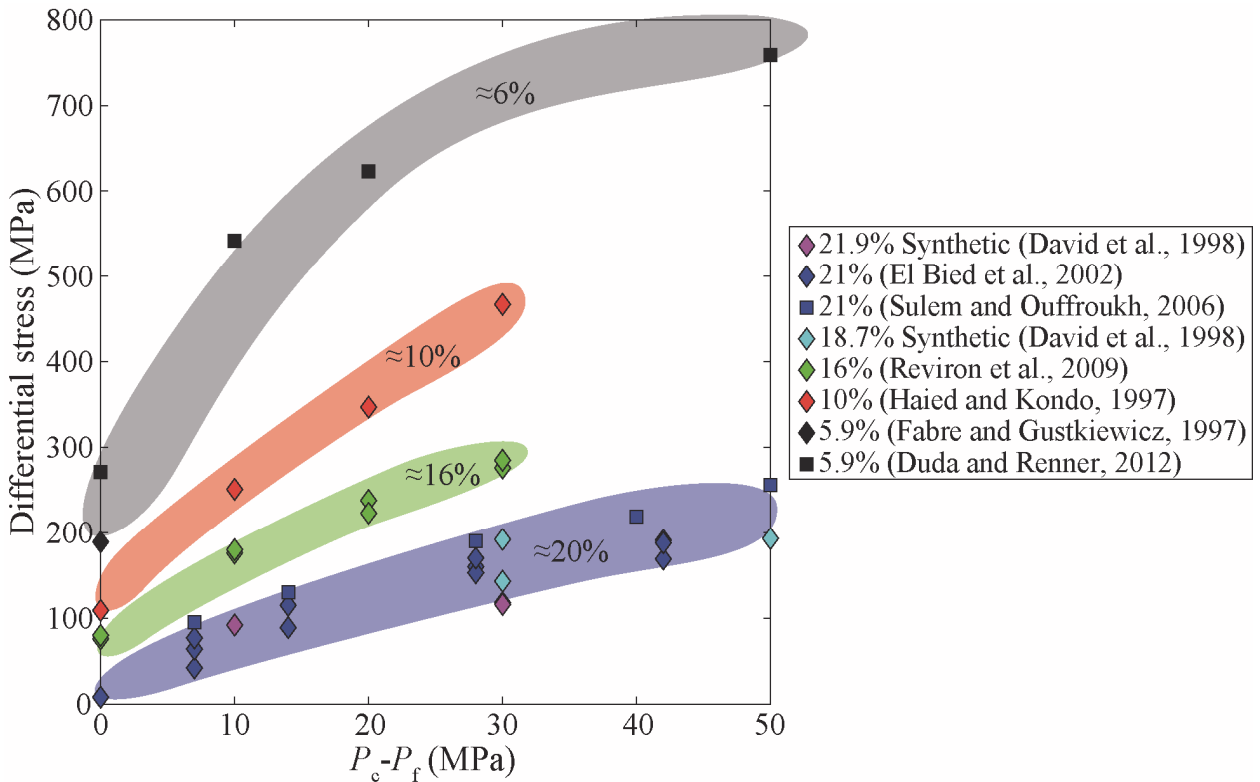


Figure 2. 3: Data compilation of differential stress ($\sigma_1 - P_c$) as function of the effective confining pressure ($P_c - P_f$) for different porosities of Fontainebleau sandstone and synthetic Fontainebleau sandstone. Data from Bied et al., 2002; David et al., 1998; Duda and Renner, 2013; Fabre and Gustkiewicz, 1997; Haied and Kondo, 1997; Revirion et al., 2009; Sulem and Ouffroukh, 2006.

2.1.4 Effect of pore fluid

Rock masses are porous media with internal pore networks and multiscale discontinuities often filled by pressurized fluids. The presence of fluid affects the mechanical behaviour of the rock mass

through chemical and mechanical interactions (e.g. Handin et al., 1963; Robinson, 1959). Even if chemical interactions such as precipitation, dissolution or phase changes are of importance, here, we mainly focus on the mechanical effects of pore fluid. Because of the internal pore structure present within the rocks, the total effective stresses that apply to the rock mass also includes the stresses given by the fluid phase present in the pore network. As a consequence, the strength of the rock mass is controlled by the effective principal stresses (σ_i') acting on it:

$$\sigma_i' = \sigma_i - nP_f \quad \text{Equation (2. 10)}$$

Where σ_i are the macroscopic principal stresses (σ_1, σ_2 and σ_3), P_f is the pore fluid pressure and n is the effective pressure coefficient which is often assumed to be 1 for rock at failure. As a consequence, pore fluid pressure decreases the *in situ* effective stresses, lowering the rock strength and bringing the rock mass closer to failure conditions.

If it has been experimentally shown that for rock failure, in the great majority of the case, the effective pressure coefficient is unity (e.g., Handin et al., 1963; Robinson, 1959), it is not always the case for other measured properties. For example, effective stress coefficient for permeability was measured both lower (e.g., Meng et al., 2019) and higher (e.g., Zoback & Byerlee, 1975) than 1. In the poroelastic community, to describe the mechanical behaviour of a rock with internal pores filled with a fluid and subjected to elastic deformations, two main parameters are used, the Biot-Willis (Biot & Willis, 1957) and the Skempton (Skempton, 1961) coefficients: $\alpha = 1 - \frac{K}{K_s}$ and $B = \frac{\frac{1}{K} - \frac{1}{K_s}}{\frac{1}{K} - \frac{1}{K_s} + \phi(\frac{1}{K_f} - \frac{1}{K_s})}$, respectively. Where K , K_s and K_f are the bulk modulus of the rock sample, the rock matrix and the fluid, respectively, and ϕ is the porosity.

2.1.5 Long-term strength

In brittle rock materials, over large time scales, irreversible deformation and failure may occur even though stresses are lower than the short-term strength of the material. Indeed, the nucleation, growth, and coalescence of cracks can occur at stresses below the short-term peak strength, a phenomenon known as subcritical crack growth (Atkinson, 1984; Olsson, 1974). Under low stress conditions, stress corrosion is the principal mechanism contributing to crack propagation. Stress corrosion is a stress-assisted chemical reaction that occurs between a chemically active pore fluid (liquid or gas) and the mineral/rock specimen at the atomic bonds close to the crack tip (Anderson & Grew, 1977; Atkinson, 1984; Brantut et al., 2013). Such reaction is important in silica-water system, where oxygen bonds are replaced by weaker hydrogen bonds, facilitating crack growth (Freiman, 1984; Michalske & Freiman, 1983). Figure 2. 4a shows the theoretical crack velocity (v) – mode I stress intensity factor (K_I) relationship typical for a single crystal. The v – K_I curve is bounded by two limits: K_0 , the stress intensity factor threshold below which no crack growth can occur, and K_{Ic} , the critical stress intensity factor (also called fracture toughness) at which crack propagation is spontaneous (no stress corrosion). From K_0 to K_{Ic} , three region can be observed: region 1 where the crack velocity is controlled by the stress corrosion reaction rate at the crack tip, region 2 where the crack velocity is controlled by the transport rate of the reactive species toward the crack tip, region 3

where the crack velocity is not controlled by stress corrosion but by a combination of purely mechanical and thermally activated processes (Freiman, 1984; Meredith, 1983).

For polycrystalline materials (i.e. rocks), crack velocity as a function of the mode I stress intensity factor (Figure 2. 4b) can be obtained by means of tensile tests performed on single macro-cracked (i.e. machined cracked) specimens. Under low stress conditions (region 1 in Figure 2. 4a), the main factors influencing the subcritical crack growth rate are: (1) the stress intensity factor at the crack tip, (2) the activity of the corrosive environment, (3) the confining pressure, (4) the temperature, (5) microstructural parameters such as the mineralogy, the grain size, the porosity, the heterogeneity, etc. (see Atkinson (1984) for a review).

- (1) The stress intensity factor at the crack tip is a major parameter affecting subcritical crack growth. Indeed, the crack growth velocity (v) and the mode I stress intensity factor (K_I) can be linked by (e.g. Atkinson and Meredith, 1981):

$$\log_{10}(v) = \alpha \log_{10}(K_I)^n \quad \text{Equation (2. 11)}$$

Where α and n are empirical constants, n is known as the stress corrosion index.

- (2) The activity of a chemical agent is crucial to activate the stress corrosion mechanism. Under geological conditions, the most predominant corrosive agent is water. Interestingly, water is a very active chemical agent on the quartz mineral (Freiman, 1984). Indeed, increasing the water content increases the subcritical crack growth rate (e.g. Meredith and Atkinson, 1985, 1983). However, it is not clear whether it is the ionized water (H^+ , OH^-) activity or the molecular water (H_2O) activity that is the key agent of the reaction (Atkinson, 1984). Atkinson and Meredith (1981) showed using HCl and NaOH as chemical agents that decreasing the pH of the environment (i.e. increasing the OH^- content) increases the crack growth rate of quartz. In the context of carbon geological sequestration, the injected CO_2 might acidify the *in situ* brine and change the activity of the pore fluid.
- (3) Very little is known about the effect of confining pressure on the subcritical crack growth rate. Three effects of the confining pressure can be determined: the stress tensor in the solid, the mechanical properties of the fluid in the crack, and the chemical reaction taking place between the solid and liquid phases (Anderson and Grew, 1977).
- (4) Increasing the temperature has two effects: First, it enhances the activity of the reactive species accelerating stress corrosion at the crack tip. Second, it changes the micro-crack state of the rock material (i.e. increasing the temperature increases the micro-crack density). From temperatures between 20 and 100°C, the two effects are opposed. It is believed that, as the number of thermal micro-cracks created is small, when the macro-crack tip advances and meets an unfavourably isolated micro-crack, the micro-crack has the effect of blunting the macro-crack and a larger stress intensity is needed to continue its advanced. At higher temperatures, the number of created thermal micro-cracks is higher, and the two effects favour higher crack velocity growth (e.g. Meredith and Atkinson, 1985).
- (5) The microstructural parameter mainly influenced the stress corrosion cracking by affecting the process zone size and its configuration (see Atkinson (1984) p.4102-4103 for a description of some influencing microstructural parameters).

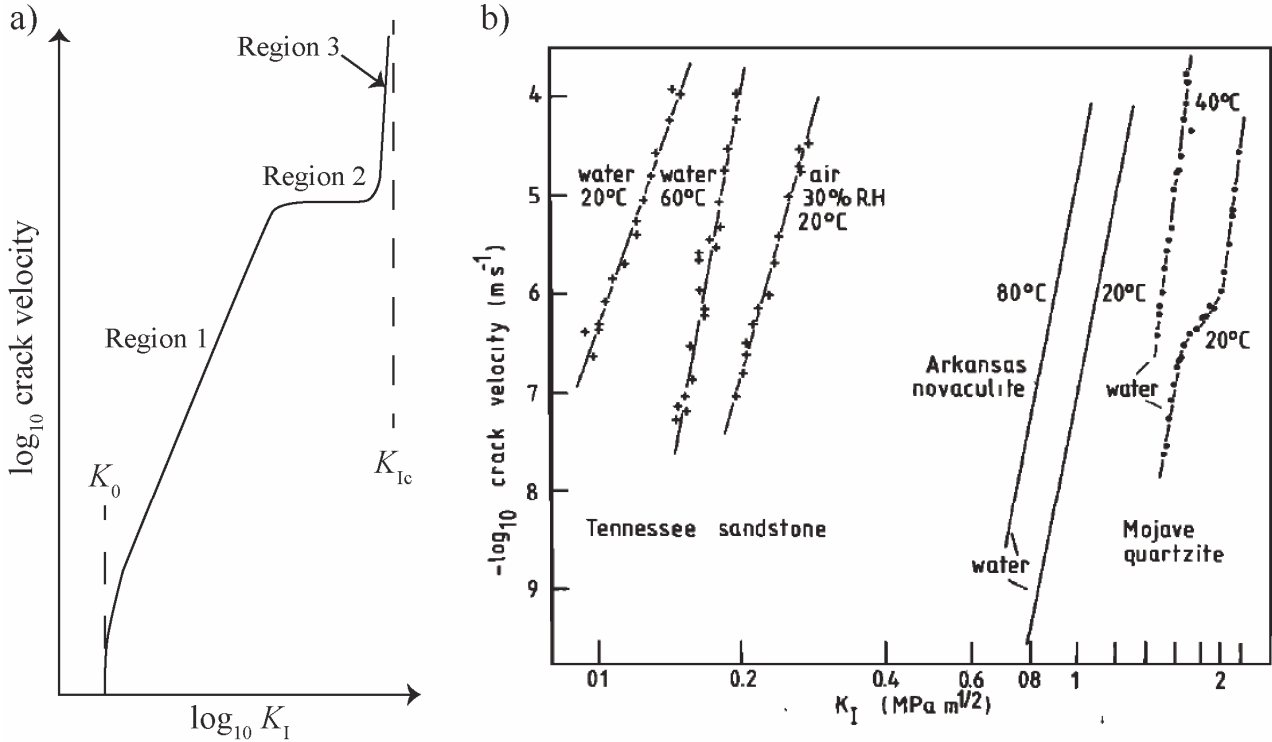


Figure 2. 4: a) Schematic crack velocity- K_I diagram showing the different regions of crack growth. b) Data of crack velocity as a function of K_I for different rock specimens. Data of the Tennessee sandstone and Mojave quartzite are from Atkinson (1984), data of the Arkansas novaculite are from Atkinson (1980).

Under natural conditions, rocks are subjected to compressional forces and the micro-cracks' nucleation, propagation and coalescence within the material are more complex than the propagation of a single machined macroscopic crack, described above. However, over the past decade, brittle time-dependent deformation of rock under compressional forces has been the subject of a number of experimental and theoretical studies (e.g. Baud and Meredith, 1997; Brantut et al., 2014; Carter and Kirby, 1978; Heap et al., 2009a, 2009b; Lockner, 1993; Mallet et al., 2015; Scholz, 1968a; see Brantut et al., 2013 for a review). The most used method to study this phenomenon is to perform uniaxial or triaxial experiments where a constant stress (below the rock strength) is applied to a rock sample until failure. Such experiments are called *static fatigue* tests or also commonly referred as *brittle creep* tests. While stresses are maintained constant, the sample strain rate first decreases with time down to a minimum and then increases until macroscopic failure (Figure 2. 5). The minimum strain rate experienced by the rock increases, that is, the time-to-failure decreases, when the (1) axial stress ($\sigma_{ax}=\sigma_1$) increases (Baud & Meredith, 1997), (2) temperature increases (Heap et al., 2009a), and (3) effective confining pressure decreases (Lockner, 1998; Ngwenya et al., 2001). Varying pore fluid pressure level, while keeping the effective pressure constant, seems to not influence the deformation rates (Heap et al., 2009b).

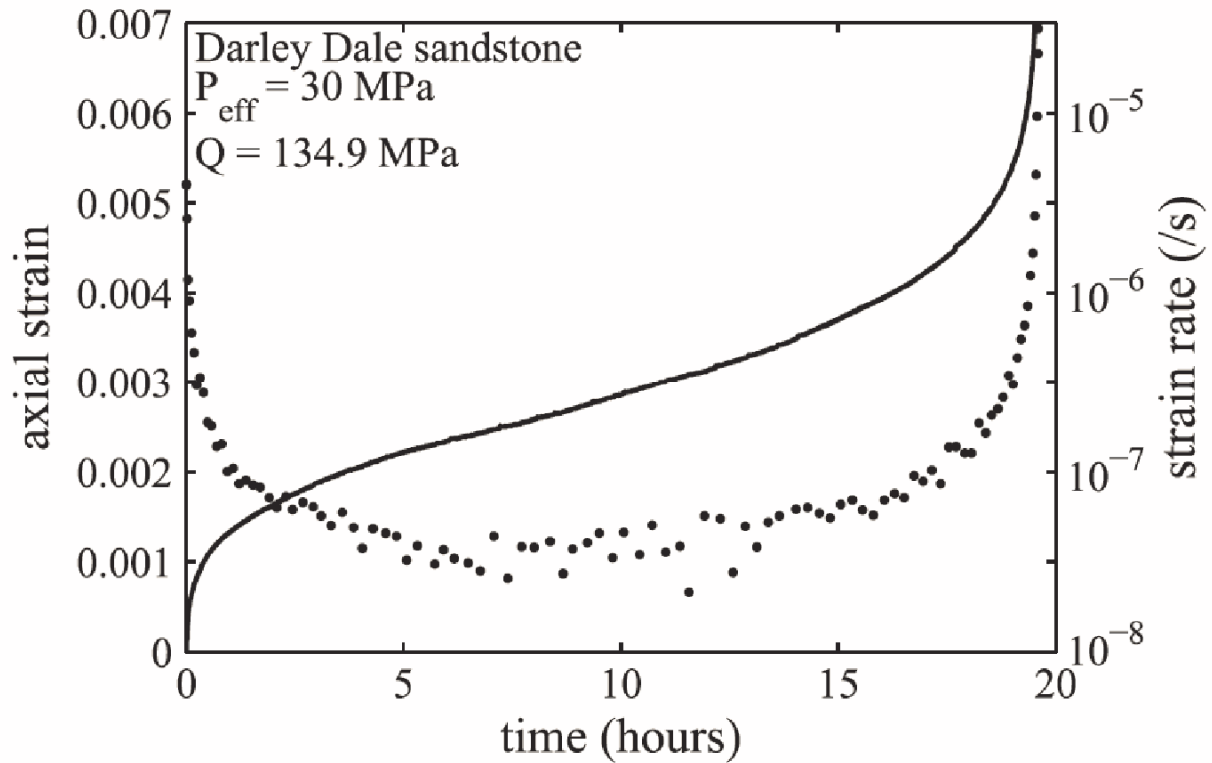


Figure 2. 5: From Brantut et al. (2014): Typical strain (solid curve) and strain rate (dots) as functions of time during a constant stress phase of a brittle creep experiment. Here the experiment was performed on Darley Dale sandstone at an effective confining pressure (here noted P_{eff}) of 30 MPa and a constant differential stress (Q) of 134.9 MPa.

2.1.6 Fatigue behaviour

Rock mass subjected to repeated cyclic loading (with a maximum value lower than the short-term strength) may fail due to *fatigue* behaviour. Due to frequent environmental or man-induced cyclic loading, the fatigue behaviour of rock has been the subject of many experimental studies. Most fatigue studies investigate the mechanical response of a dry rock sample submitted to cyclic axial loading of constant amplitude and mean stress value (see Cerfontaine and Collin (2017) for a review). The principal characteristics of such fatigue tests performed under dry conditions are (1) strength reduction of the rock samples (e.g. Royer-Carfagni and Salvatore, 2000) as compared to short-term strength; (2) residual and permanent deformations accumulated cycle after cycle; and (3) variation of the residual strain accumulated after cycles during experiment, with the first and last cycles before rupture having the highest strain accumulation (e.g. Liu and He, 2012).

In the context of reservoir injections, the rock mass can be subjected to repeated pore fluid pressure variation, especially in the context of soft stimulation, and thus suffers from fatigue induced by pore fluid pressure variation. This phenomenon is often referred to as *hydraulic fatigue*. Very few experimental studies have aimed to understand the mechanical behaviour of a rock subjected to cyclic pore fluid pressure oscillations (Chanard et al., 2019; Farquharson et al., 2016; Patel et al., 2017; Zhuang et al., 2016; Zhuang et al., 2019). Even if some data show conflicting results, overall cyclic pore fluid pressure experiments have shown that rock samples fail at lower stress than the short-term stress with more complex fractures (i.e. more branched and generally wider).

2.2 Fault mechanics

Often, if not always, geological reservoirs include major discontinuities such as faults. Faults are geological fractures where a frictional relative displacement occurs between two opposite blocks of rock. These systems can be either stable or unstable. In the stable case, the deformation will be accommodated through creeping, i.e. displacements accommodated by continuous movement on the fault plane without a brutal release of elastic energy. Fault creep can occur at strain rates ranging between nm.s^{-1} to mm.s^{-1} . In the unstable case, following a period of energy build up, slip occurs almost instantaneously as the rupture propagates dynamically. In turn, this movement creates seismic waves that propagate to the surface during an earthquake.

Rock friction, fault geometry and rupture dynamics are key elements to understand fault and earthquake mechanics. In the past 20 years, the growing interest in and the use of deep georeservoirs for purposes such as carbon storage, waste water disposal, or geothermal energy exploitation have induced massive increases in seismicity in some normally “quiet” regions (e.g. Ellsworth, 2013). In order to better understand induced seismicity, new knowledge of the frictional behaviour of faults and fluid – fault interaction is required.

In the following, fault reactivation and fault stability are described using two distinct criteria. On the one hand, the Coulomb failure criterion is often used to describe the onset of fault sliding (i.e. fault reactivation). On the other hand, the velocity dependence of friction and the competition between the fault stiffness and the surrounding medium stiffness are used to describe fault stability.

2.2.1 Fault reactivation

The resistance to sliding between two rock blocks separated by a fault is controlled by the coefficient of friction (μ). It is defined by the ratio between the shear forces and the normal forces necessary to have a relative movement between two blocks of rock on a fault. Even though μ is often seen as a material constant, the ratio between the shear and the normal forces might be different to initiate sliding (static friction) and to maintain sliding (dynamic friction). Here, we are interested at the reactivation of the fault, thus the static friction is of interest. A common criterion used to describe the relationship between the shear stress and the normal stress of a fault at reactivation (i.e. fault strength) is:

$$\tau = S_0 + \mu'(\sigma_n - P_f) \quad \text{Equation (2. 12)}$$

where S_0 and μ' are empirical constants. By analogy with the Coulomb failure criterion for intact rock, S_0 and μ' are often called cohesion and coefficient of friction.

Based on laboratory data, Byerlee (1978) demonstrated that the friction of rocks (except for clay rich rocks) can be described by two linear relationships (Figure 2. 6):

- For $\sigma_n < 200$ MPa: $\tau = 0.85\sigma_n$
- For $200 < \sigma_n < 1700$ MPa: $\tau = 50 + 0.6\sigma_n$ (in MPa)

This rule is often evoked in the literature as *Byerlee's rule* or *Byerlee's law*.

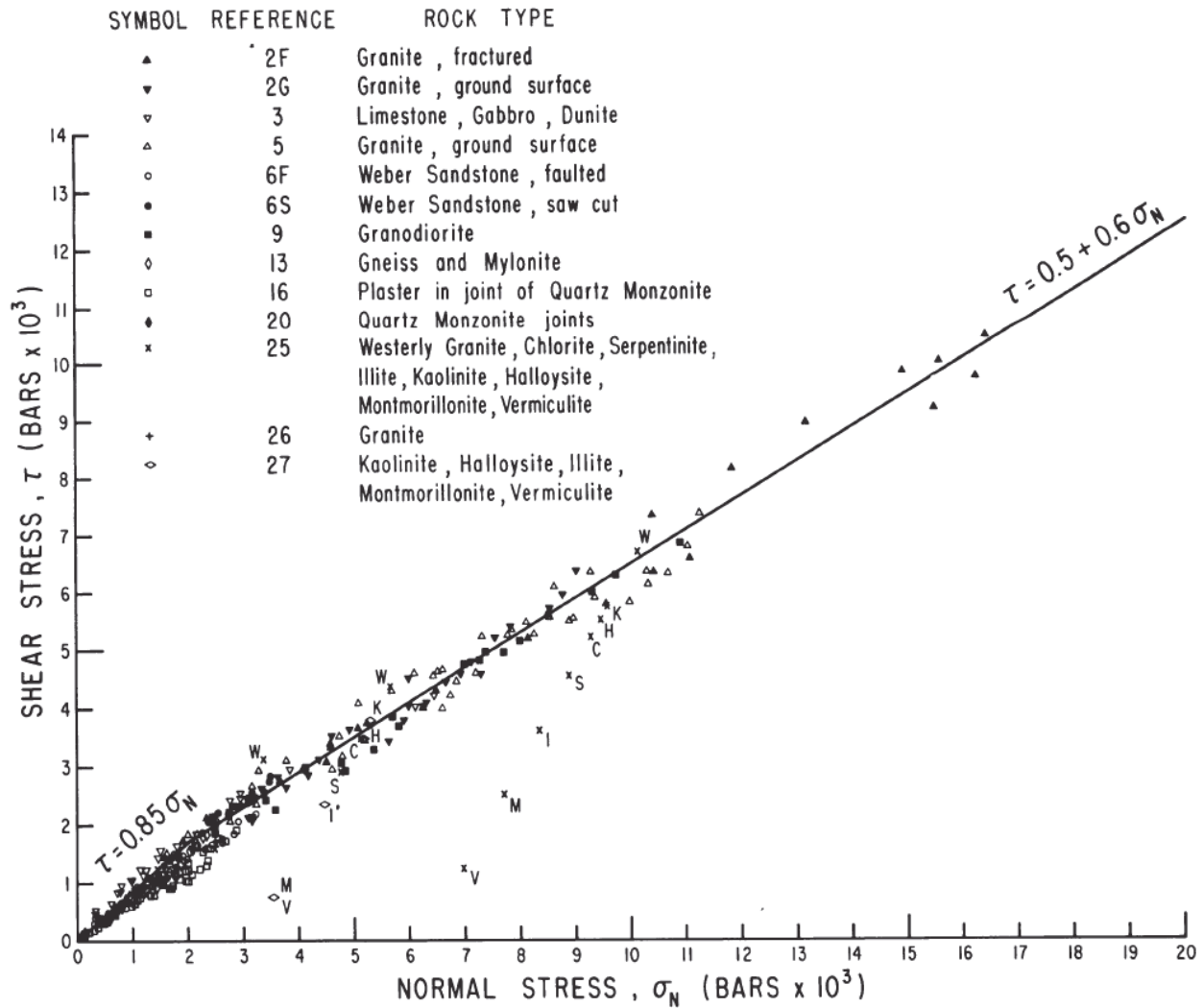


Figure 2. 6: From Byerlee (1978). Shear stress as a function of normal stress for a large variety of rocks.

2.2.2 Fault stability

Although the Coulomb criterion allows for the investigation of fault reactivation, it cannot be used to analyse the stability of a sliding. Indeed, when shear failure occurs on a fault, the fault can accommodate slip either by stable (gentle creep) or unstable sliding (earthquake). To differentiate between stable and unstable motion, two parameters are of interest: 1) the velocity dependence of friction (i.e. how friction is evolving when the fault is subjected to a velocity jump) and 2) the capacity of the surrounding medium to store energy compared to the one released on the fault, which is often associated with the difference between the fault stiffness and the surrounding medium stiffness (e.g. Dieterich and Linker, 1992; Gu et al., 1984; Rice and Ruina, 1983; Ruina, 1983). Here, a short description of the rate-and-state and spring – slider models are given and used to discriminate the sliding behaviour of a fault.

The rate-and-state friction model considers that the friction varies with the loading history and depends on both the instantaneous slip rate and a state variable that describes the gradual evolution of the sliding interfaces (Dieterich, 1978; Ruina, 1983). At constant normal stress, the evolution of the frictional coefficient during slip can be estimated as follows:

$$\mu \equiv \mu(V, \theta) = \mu_0 + a \ln\left(\frac{V}{V_0}\right) + b \ln\left(\frac{V_0 \theta}{D_c}\right), \quad \text{Equation (2. 13)}$$

where, considering the ageing law (also called the Dieterich law), the state variable's (θ) evolution is:

$$\frac{d\theta}{dt} = 1 - \frac{V\theta}{D_c} \quad \text{Equation (2. 14)}$$

and considering the slip law (also called the Ruina law) its evolution is:

$$\frac{d\theta}{dt} = -\frac{V\theta}{D_c} \ln\left(\frac{V\theta}{D_c}\right) \quad \text{Equation (2. 15)}$$

With μ_0 being the reference friction at the velocity V_0 , where V is the slip velocity. The parameters a , b and D_c are the rate-and-state parameters (Figure 2. 7). When the sliding velocity is increased, the rate-and-state model first predicts a jump in friction proportional to the parameter a , called the direct effect. Then, a friction decay follows up to a new steady-state value (higher or lower than the one at V_0). The decay is proportional to b and occurs over a sliding distance D_c . The parameter D_c is called the *critical* or *characteristic slip distance* and correspond to the slip necessary to renew all the frictional contacts. In this model, the difference between the parameters a and b is of major importance for fault stability. Indeed, if $(a - b) > 0$, the fault exhibits a *velocity strengthening* behaviour and is intrinsically stable as all slip acceleration will be arrested. However, $(a - b) < 0$, the fault exhibits a *velocity weakening* behaviour and might experience dynamic instability. For a velocity weakening frictional interface, the stability of the sliding is then controlled by the competition between the fault and the surrounding medium stiffnesses.

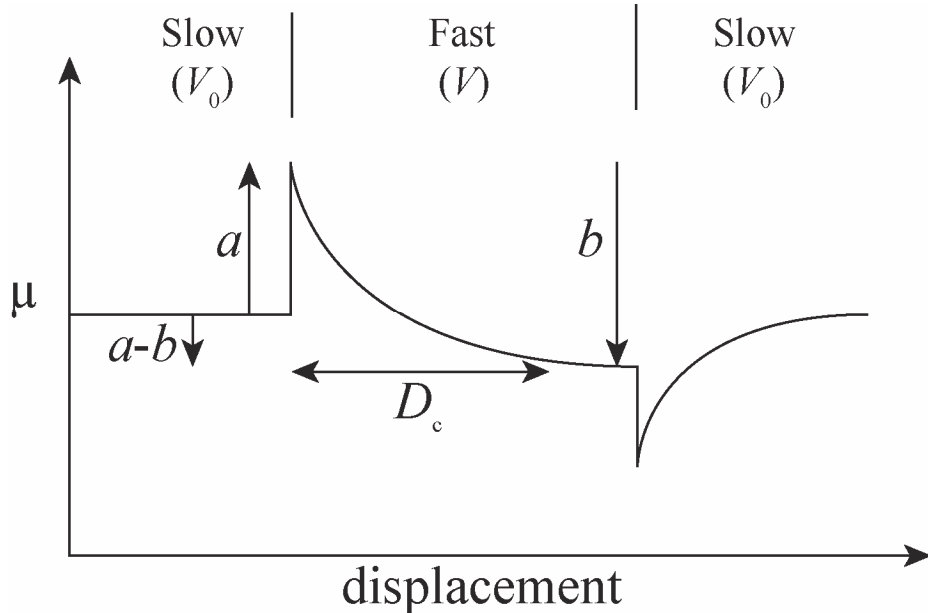


Figure 2. 7: Friction evolution of a frictional interface as function of displacement when it is subjected to a velocity increase and decrease according to the rate-and-state model.

Considering a spring – slider model where a frictional velocity weakening surface (representing a fault) is subjected to a normal stress and a shear stress, the shear stress is applied by pulling a spring of stiffness K (representing surrounding medium of the fault) at a constant displacement rate

(Figure 2. 8). Then, the competition between the stiffness of the fault (K_{fault}) and the stiffness of the surrounding medium (K) controls the fault slip behaviour. If $K_{\text{fault}} > K$, following the elastic loading of the fault, and if the peak strength of the fault is reached, the force will decrease faster with fault slip (d) than K creating a force imbalance leading to slider acceleration and unstable slip behaviour. On the other hand, if $K_{\text{fault}} < K$, the fault slip remains stable and creep behaviour is observed. Unstable slip is often followed by a period of no motion of the fault allowing the system to reload up to the next unstable motion. This behaviour where the fault slip is accommodated through regular unstable motion is called *stick-slip*.

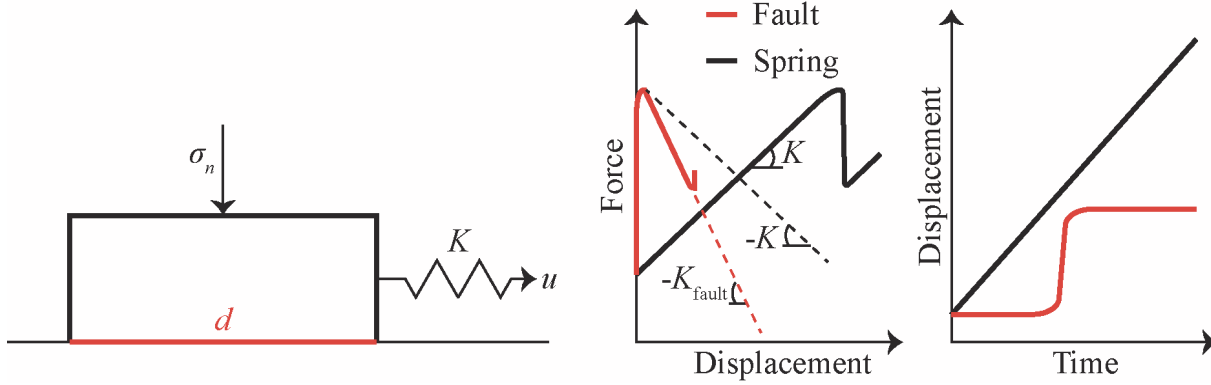


Figure 2. 8: Schematic diagram of the spring – slider model and typical mechanical curves of unstable slip behaviour. Both force – displacement and displacement – time curves are shown. The red curves represent the fault slip and the black curve the spring displacement.

Coupling the rate-and-state friction approach with a one-dimensional spring – slider model, the transition from stable to unstable slip can be found at the critical stiffness (Dieterich, 1979; Gu et al., 1984; Rice, 1993; Ruina, 1983):

$$K_c = \frac{(b-a)(\sigma_n - P_f)}{D_c} \quad \text{Equation (2. 16)}$$

In summary, after fault reactivation (i.e., fault strength is overcome), the fault frictional behaviour can be divided into three stability domains: (1) if $(a - b) > 0$, the system is stable; (2) if $(a - b) < 0$ and $K > K_c$, the system is conditionally stable (i.e., stable under quasistatic loading); or (3) if $(a - b) < 0$ and $K < K_c$, the system is unstable.

2.3 Deep reservoir rock mechanics: the ductile domain

As mentioned above, at the geo-reservoir depths suitable for CO₂ sequestration, most of the deformations are occurring within the brittle field. However, for deeper reservoirs, or depending on the targeted reservoir rock, some ductile deformations might also occur. For example, for carbonate rich rocks such as limestone (often targeted as a reservoir rock for CO₂ sequestration), the brittle – ductile transition occurs at low pressure and temperature (i.e. shallow depth). Such reservoirs can be of interest because the brittle – ductile transition may be the maximum depth at which seismicity occurs (Sibson, 1977; 1982).

2.3.1 Ductile deformation

In this thesis, the term ductile deformation refers to distributed deformation at the sample scale. In other words, the rock sample has the capacity to deform by changing its initial shape without macroscopic localised shear fracture. In the ductile regime, different microscopic deformation mechanisms can occur (e.g. crystal plasticity, granular flow, cataclastic flow, etc.), which has led to the use of different terminology to distinguish between the nature of the mechanisms involved: semi-brittle deformations and plastic deformation (Carter & Kirby, 1978; Evans et al., 1990; Paterson & Wong, 2005; Rutter, 1986). For high porosity rocks, semi-brittle deformation characterises a macroscopically distributed deformation which is microscopically accommodated through brittle process (i.e. micro-fracture and pore collapse). For low porosity rocks, the term semi-brittle is used to describe rock that undergo both plastic and brittle micro-deformation (i.e. some minerals behave plastically whereas other remain brittle). On the other hand, plastic deformation characterises a macroscopically distributed deformation which is microscopically accommodated through crystal plasticity and diffusion processes (e.g. dislocation flow, grain boundary sliding, twinning, diffusion creep, etc.).

During triaxial deformation of a rock sample in the ductile regime, after an initial elastic deformation, the sample can behave differently depending upon 1) its micromechanical deformation (i.e. semi-brittle or plastic) and 2) its initial porosity. For low-porosity rocks, the permanent deformation can be accompanied by dilatancy if the semi-brittle regime (i.e. distributed micro-cracking) is dominant, or compacting if the deformation is fully plastic (Evans et al., 1990; Fischer & Paterson, 1989). For higher porosity rocks, the compaction or dilatancy behaviour depends upon the difference between pore collapse and micro-fracturing, which have opposite effects (Wong & Baud, 2012). Figure 2. 9 gives a summary of the mechanical curves that can be obtained in the ductile regime for initially low-porosity rocks (Figure 2. 9a and b) and initially high-porosity rocks (Figure 2. 9c and d). On such curves, the onset of inelastic compaction, denoted C^* , is marked by the deviation of the mean stress ($[\sigma_1 + \sigma_2 + \sigma_3]/3$) as function of volumetric strain from the hydrostatic curve (Figure 2. 9a and c). For porous rocks, the onset of pore collapse under hydrostatic compression can also be reached experimentally. This is denoted P^* .

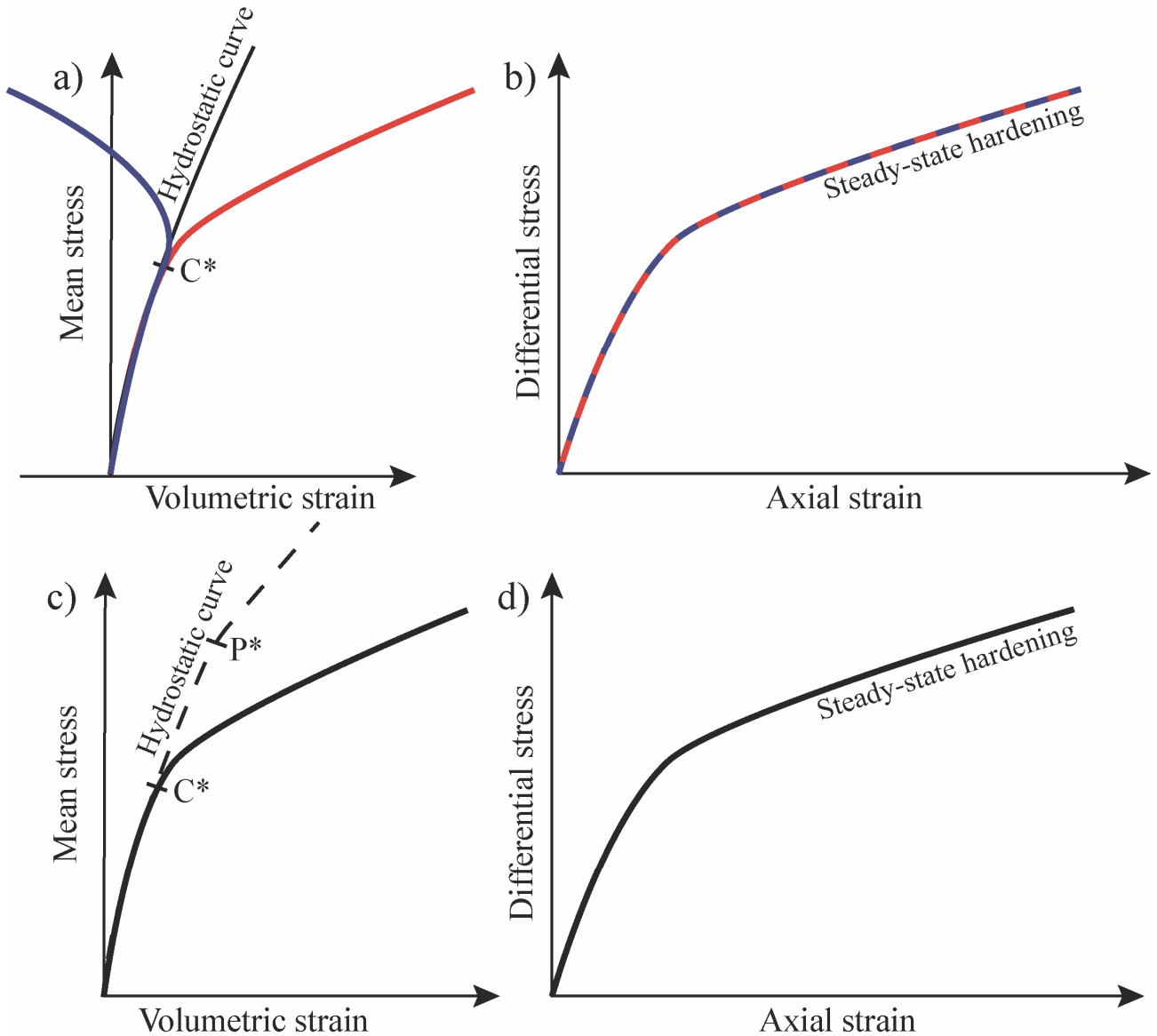


Figure 2. 9: Mechanical curves typical of the ductile field. Both the mean stress as function of the volumetric strain and the differential stress as function of the axial strain are presented. a and b) For initially low-porosity rock deformed in the semi-brittle regime (bleu curve) and plastic regime (red curve). c and d) For initially high-porosity rocks. The deviation of the triaxial data from the hydrostatic curve (dotted line) gives the onset of inelastic compaction (C^*). The pore collapse under a hydrostatic regime is denoted by P^* .

2.3.2 Microscopic analysis of the deformations

Two classes of deformations can be observed in microscopic analysis of post-mortem samples that have undergone ductile deformation (Paterson & Wong, 2005):

- 1) The deformation of the individual grains is similar to the deformation of the macroscopic sample, i.e. homogeneous deformation down to grain scale and no relative movements between grains are observed. In this class, two types of deformation are observed:
 - Crystal plasticity: This involves intra-granular plastic deformations that occur mainly by intra-crystalline slip (dislocation motion) and twinning (Figure 2. 10a-c). Intra-crystalline slip is characterised by blocks that slide one over an-

other such that the orientations of the slipped parts remain coincident (Poirier, 1985) (Figure 2. 10a and b). This can often be distinguished under microscope image as fine lines and steps visible at the grain boundary. Twinning occurs by translating some layers of atoms in the crystal, all by the same amount one with respect to the other (Figure 2. 10a and c). The result is homogeneous shear in which two parts of the crystal have mirrored orientations (Lyll, 1965). Crystal plasticity is a relatively low pressure dependence phenomenon (Paterson, 1967) and is initiated on defects in the crystal lattice such as vacancies or dislocations (Paterson, 2013; Poirier, 1985).

- Diffusion flow: It involves grain shape changes by diffusion of material from one part to another. Diffusion paths can be through the grain or around the grain boundary (e.g. Herring, 1950). In porous rocks the diffusion path may be also through a fluid phase in the porosity network as, for example, in pressure solution mechanisms (e.g. Durney, 1972).
- 2) The deformation of an individual or a group of grains is different from the macroscopic deformation, i.e. the macroscopic deformation results from grain position rearrangement. In this class again, two types of deformation are observed:
- Cataclastic flow: The strain is achieved first by a distributed fracturing of the grain (i.e. the cataclastic part) and then by relative movements of the fragments (i.e. the granular flow part) (Figure 2. 10d). Two properties are of importance during cataclastic flow: friction between grains and porosity change due to grains reorganisation. Because the confining pressure contributes to the normal stress acting on the frictional sliding part, cataclastic flow is highly pressure sensitive. Depending on the initial porosity of the rock, compaction or dilation can occur during cataclastic flow. For low porosity rocks (e.g. crystalline rocks) dilation of the pore space is usually observed (Fredrich et al., 1989; De Paola et al., 2009; Zhang et al., 1994; Siddiqi et al., 1997), whereas for high initial porosity rock, compaction (i.e. reduction of porosity) occurs (Brace, 1978b; Carroll, 1980; Edmond & Paterson, 1972; Fischer & Paterson, 1989; Wong et al., 1997).
 - Microplastic granular flow: The strain is achieved by relative movement of grains without fracture and without disruption of grain boundaries. It thus involves diffusion along the grain boundary or dislocation flow within the grains (e.g. Ashby and Verrall, 1973). It is favoured at high temperatures, low strain rates and for rocks having fine grain size (Paterson & Wong, 2005).

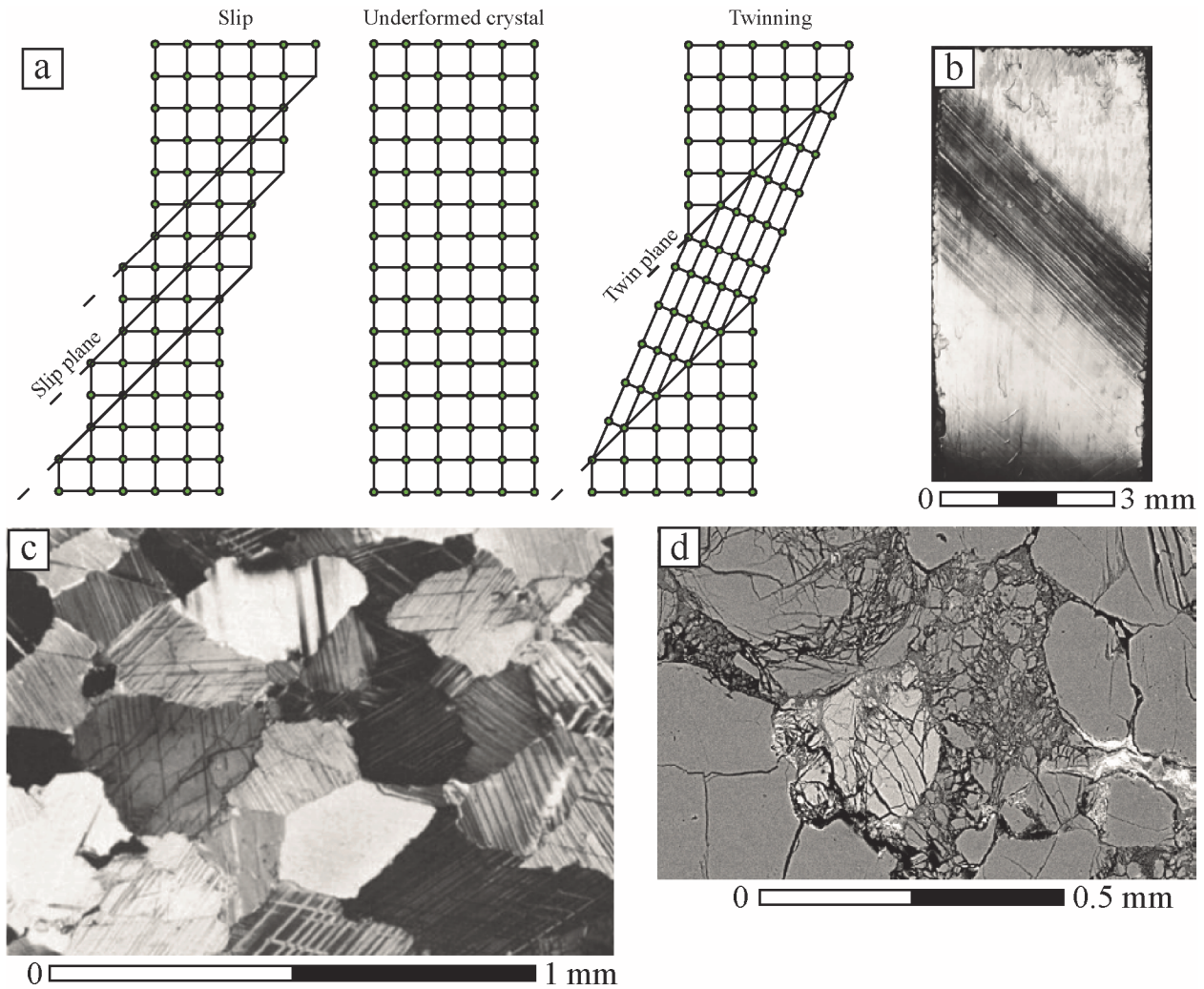


Figure 2. 10: Deformations typical of the ductile regime. a) Schematic diagram showing crystal deformation during slip (left) and twinning (right). b) Micrograph of a galena crystal after 10% shear strain showing slip bands. Image from Lyall (1965). c) Micrograph image of Carrara marble deformed at 120 MPa confining pressure after 2.99% of axial strain showing twinning of the calcite minerals. Image from Fredrich et al. (1989). d) Secondary electron microscopy (SEM) image of a Darley Dale sandstone failed by cataclastic flow. Image from Wong and Baud (2012).

2.3.3 The brittle-ductile transition

The transition from brittle to ductile deformation depends mainly upon (1) the confining pressure and (2) temperature (i.e. depth of the reservoir rock), (3) the pore fluid pressure and (4) the rate of deformation of the rock. Here, the effect of these parameters is briefly described.

- (1) Confining pressure (P_c): The effects of the confining pressure on the brittle-ductile transition have been shown using calcite rocks such as marble (e.g. Fredrich et al., 1989; Paterson, 1958; von Kármán, 1911). Experimental deformation has shown that (Figure 2. 11): 1) The strain at failure increases with the confining pressure. Rocks that undergo brittle deformation usually fail at less than few percent of deformation whereas rocks that undergo ductile deformation support more deformation before failure. A value of 3% at failure is often taken as a transition value (Evans et al., 1990). 2) The global level of the stress – strain curve is increased with P_c . 3) The hardening rate during ductile deformation increases with P_c . For high

initial porosity rock the confining pressure of the brittle – ductile transition decreases greatly as the initial porosity of the rock is increased (Wong & Baud, 2012).

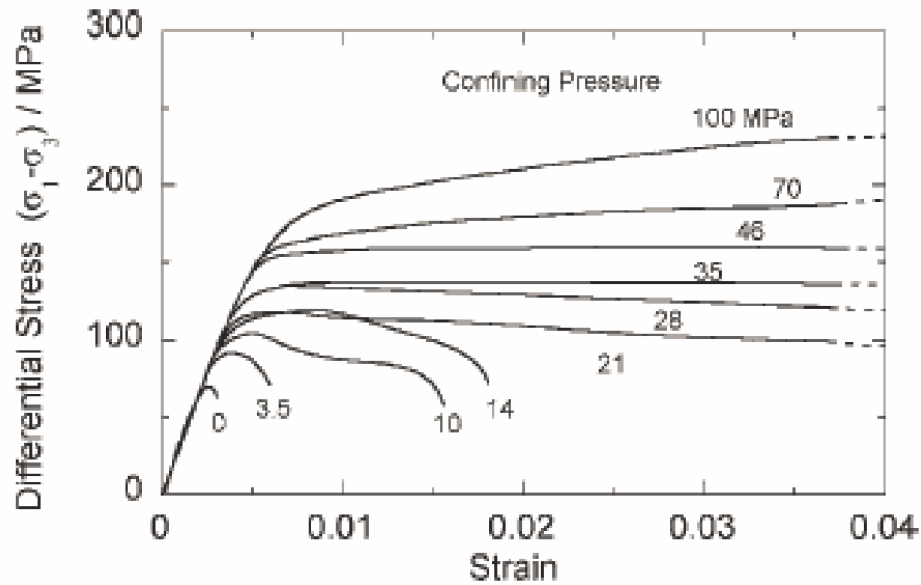


Figure 2. 11: Differential stress as a function of axial strain for Wombeyan marble deformed at confining pressures ranging from 0 to 100 MPa. From Paterson, (1958).

- (2) Pore fluid pressure (P_f): In presence of a pore fluid phase in the porous network of the rock, the transition from brittle to ductile deformation depends mainly on the mechanical effect of the fluid phase and thus on the effective confining pressure $P_c - P_f$ (Bernabe & Brace, 1990; Handin et al., 1963; Robinson, 1959; Rutter, 1972).
- (3) Temperature: Increasing the temperature has, in general, the effect of increasing the ductility of the rock. For example, high temperature experiments performed at $P_c - P_f = 100$ MPa, have shown that for basalt, the transition from brittle to ductile deformation occurs around 850°C (Violay et al., 2012; 2015), whereas for granite it occurs around 1000°C (Violay et al., 2017). The temperature effect can be seen on a pressure – temperature diagram that maps the brittle – ductile transition. For example, on the more porous Solnhofen limestone (Figure 2. 12), the confining pressure at which the brittle – ductile transition occurs falls with increasing temperature (Heard, 1960).
- (4) Strain rate: In general, decreasing the strain rate favours a lower brittle – ductile transition. For example, Tullis and Yund (1980) found that for wet albite deformed at 1500 MPa confining pressure and 800°C , the transition from brittle to ductile deformation can be passed by decreasing the strain rate from 10^{-4} to 10^{-6} s^{-1} .

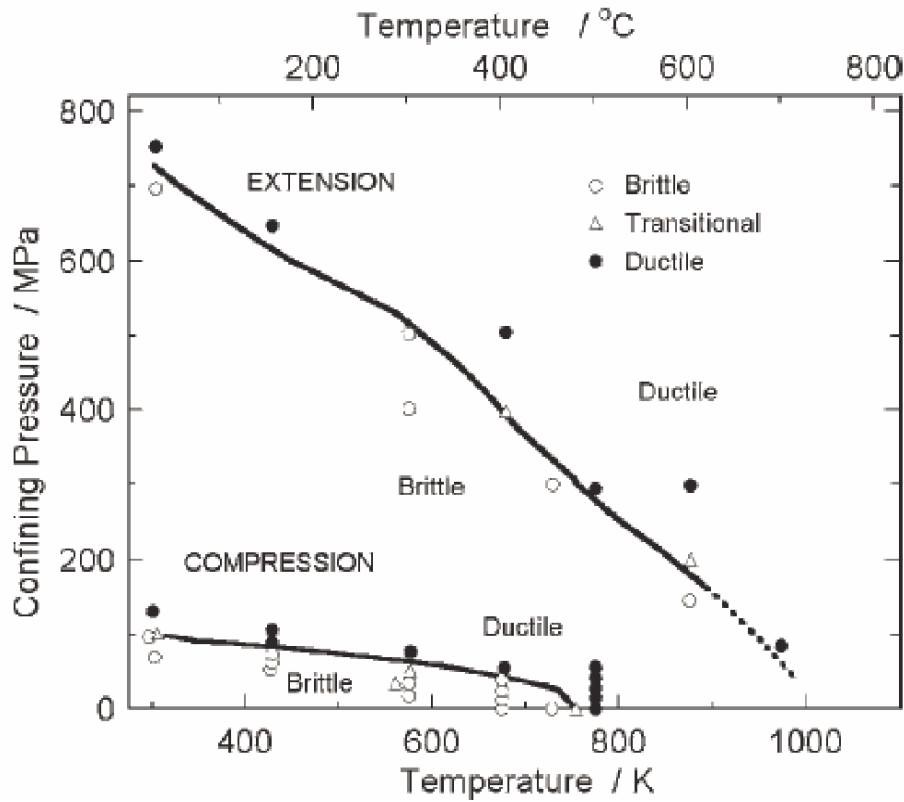


Figure 2. 12: Pressure-temperature diagram showing the brittle ductile transition of the Solnhofen limestone. After Heard, (1960).

Note that the transition is not abrupt but occurs across a more diffused zone, where brittle and ductile deformations coexist (e.g. Fredrich et al., 1989). In porous sandstones, *compaction bands* can develop during sample deformation under a transient regime. Compaction bands are localized deformation bands that are distributed across the sample length. These bands are planar cataclastic structures, sub-perpendicular to the maximum principal stress, that have undergone compaction (Wong & Baud, 2012).

The transition from brittle to ductile deformation is of major importance as it marks the limit depth of seismicity (e.g. Sibson, 1977, 1982) and the limit of hydrothermal circuits in the crust (Violay et al., 2012, 2015, 2017). These two characteristics have led this domain to become of interest for deep reservoirs (e.g. Asanuma et al., 2012; Bignall & Carey, 2011; Frioleifsson et al., 2014; Tsuchiya et al., 2015).

2.4 Objectives of the thesis

As mentioned earlier, CO₂ capture and storage is seen as a promising technique to reduce greenhouse gas emissions into the atmosphere. This method involves CO₂ injection into deep reservoir rocks which in turn involves three main geological issues: leaks of CO₂ toward upper aquifers or the surface, slow and distributed surface deformations and induced seismicity. This thesis is centred around reservoir rock deformations, and particularly the potential of induced seismicity, that occur during such fluid injections. Both reservoir rock and fault deformation are studied. The cyclic fluid injection technique, recently suggested to trigger less seismicity, is tested as well as different injection strategies into deeper ductile reservoirs.

Laboratory rock deformation is used to characterise and perform fluid stimulation on rock samples. Indeed, laboratory scale experiments allow for the deformation of rock samples under a variety of controllable, repeatable environmental conditions. Moreover, most of the processes that occur during earthquakes are scale invariant. Indeed, many similarities between laboratory and natural earthquakes can be found, for example: 1) the stress drops in laboratory experiments generate acoustic emissions similar to high- and low-frequency earthquakes (e.g. Burlini et al., 2009); 2) scaling laws, such as the Gutenberg-Richter law, can be observed in both laboratory and natural earthquakes (e.g. Scholz, 1968b); 3) the fracture energy of both natural and laboratory earthquake scales with magnitude and slip (e.g. Nielsen et al., 2016); and 4) the rupture during earthquakes in the laboratory and in natural systems are similar (Passetlègue et al., 2013).

In this Ph.D. thesis, the chemical aspect that can occur during CO₂ sequestration is not covered, and only the mechanical aspect is of interest. Sandstone and limestone are used during the experiments as they are typical target reservoir rocks for CO₂ sequestration, i.e. porous and permeable. During sample deformation, geophysical methods are used to investigate the physics underlying deformation processes. Particularly, in addition to usual mechanical properties, high-frequency acoustic emission signals and ultrasonic wave velocity measurements are monitored. These data provide new constraints on reservoir rock and fault deformation during geo-reservoir stimulation.

In this thesis, four main questions are addressed:

- 1) How does the presence of fluid affect the short-term rock strength? What are the involved mechanisms?
- 2) How does cyclic stimulation affect the mechanics of intact reservoir rock over time? Does it reduce induced seismicity compared to traditional monotonic injections?
- 3) How does cyclic stimulation affect fault mechanics? Does it favour stable or unstable sliding?
- 4) How does a ductile reservoir react to fluid injection? Can localised deformation and potential seismicity nucleate?

2.5 Organisation of the thesis

With the aim of answering the above questions, the following thesis is divided into four main chapters, each dedicated to one question. The chapters are based on a compilation of articles published or submitted to peer-review journals and following EPFL regulations. In the manuscript reader can find:

- Chapter 3: The objective of this chapter is to address the effect of fluid on the short-term strength, fracture toughness and frictional properties of sandstones. It includes uniaxial compression, fracture toughness and friction experiments performed on five sandstones under dry and water-saturated conditions.
- Chapter 4: The objective of this chapter is to address the effect of cyclic pore fluid pressure oscillations on a porous reservoir rock. The chapter has been published in the peer-reviewed *Journal of Geophysical Research: Solid Earth* in 2019. It includes long-term triaxial experiments on the Fontainebleau sandstone subjected to various pore pressure

conditions. The pore fluid level as well as cyclic sinusoidal stimulation with various amplitudes and periods are tested.

Reference: Noël, C., Pimienta, L., & Violay, M. (2019). Time-dependent deformations of sandstone during pore fluid pressure oscillations: Implications for natural and induced seismicity. *Journal of Geophysical Research: Solid Earth*, 124(1), 801-821. <https://doi.org/10.1029/2018JB016546>

- Chapter 5: The objective of this chapter is to address the effect of cyclic pore fluid pressure oscillations on a reservoir fault. The chapter has been published in the peer-reviewed *Journal of Geophysical Research: Solid Earth* in 2019. It includes triaxial experiments on faulted Fontainebleau sandstone samples subjected to various pore fluid pressure conditions. Extra velocity step experiments have been performed to compute the rate-and-state parameters of the sample under different conditions.
Reference: Noël, C., Passelègue, F. X., Giorgetti, C., & Violay, M. (2019). Fault reactivation during fluid pressure oscillations: transition from stable to unstable slip. *Journal of Geophysical Research: Solid Earth*, 124(11), 10940-10953. <https://doi.org/10.1029/2019JB018517>
- Chapter 6: The objective of this chapter is to address the effect of pore fluid pressure increases in a reservoir that is under ductile deformation conditions. The chapter is under review in the *Journal of Geophysical Research: Solid Earth*. It includes triaxial deformation experiments on Tavel limestone under ductile deformation conditions. The impact of the injection rate on the deformations is investigated.
- Chapter 7: This chapter summarizes the general conclusion of the manuscript. It also highlights some future work and development linked to this thesis.

Chapter 3 Effect of water on sandstone's fracture toughness and frictional parameters: brittle strength constraints

Highlights:

- Fracture toughness and friction coefficient are reduced in presence of water.
- Fracture toughness reduction with water can explain water weakening in sandstone's compressive strength.
- Micro-mechanical models predict the water weakening well, with a general slight overestimation

3.1 Abstract

Water presence causes a dramatic reduction of sandstone strength. Under compressive stress conditions, the strength of a rock sample is controlled by frictional parameters and the fracture toughness of the material. Here, we report fracture toughness and frictional and uniaxial compression tests performed on five sandstones under dry and water-saturated conditions, that provide new insight into the mechanical influence of water on sandstone strength. The mechanical data show that water saturation causes a reduction of i) the fracture toughness and fracture energy ranging from 6 to 35 % and 21 to 52 %, respectively; and ii) the static friction ranging from 0 to 19 %, suggesting that the water weakening in sandstones (with a reduction of the uniaxial compression strength ranging from 0 to 30 %); is due to the reduction of the fracture toughness and of the static friction of the materials. The measured fracture toughness and frictional parameters are then introduced into two micro-mechanical models (a pore-emanating cracks model and a wing crack model) to predict the water weakening. It is shown that the models predict the water weakening relatively well with a general slight overestimation (10 to 20%). Finally, a parametric analysis on the wing crack model revealed that a sandstone's absolute strength can be estimated by means of combined physical and mechanical parameter measurements.

3.2 Introduction

Among the environmental parameters affecting rock mechanical behaviour and strength, the presence of fluid, particularly water, has been shown to be primordial. Because it is meaningful for many applications including earthquake nucleation, landslide triggering, reservoir stimulation, mining, geotechnics, etc., rock-fluid interactions have been widely studied. Water weakening has been reported in most types of rocks such as sandstones (e.g., Baud et al., 2000; Duda & Renner, 2013; Hawkins & McConnell, 1992), carbonates (e.g., Lisabeth & Zhu, 2015; Nicolas et al., 2016), tuff (e.g., Zhu et al., 2011) or basalts (e.g., Zhu et al., 2016). The primary mechanical effect of fluid is to reduce the effective stress acting on the rock mass (Terzaghi et al., 1996). Under isotropic mechanical behaviour, the effective stresses are defined by $\sigma^{\text{eff}} = \sigma - AP_f$, where σ is the macroscopic stress P_f if the pore fluid pressure and A is the effective stress coefficient, which depends on the rock and measured properties. Following the work of Terzaghi for soils, it has been shown that for rock strength and under drained pore fluid conditions, A is close to (or equal to) unity (e.g., Handin et al., 1963; Heard, 1960; Robinson, 1959). For porous sandstones, the effective pressure coefficient for brittle strength and shear-enhanced compaction were also observed to be very close to unity (Baud et al., 2015). Additionally, water favours rock-fluid interactions, weakening the rock mass by activating mechanisms such as: stress corrosion cracking (Anderson & Grew, 1977; Barry Kean Atkinson, 1984; Freiman, 1984; Michalske & Freiman, 1983; Simmons & Freiman, 1981) or mineral dissolution/alteration (e.g. Rutter, 1983).

Among the studies on rock water weakening, the largest published sets of experimental data are on sandstones. These data sets have shown that water-saturated sandstones can present a lower uniaxial and triaxial strength than dry samples. For example, Berea, Darley Dale, Flechtingen, Pennant sandstones or different Buntsandstein unit sandstones from Soultz-sous-Forêt (France) present a water weakening of 8, 14, 40, 43 and 20 to 40%, respectively (Baud et al., 2000; Hadizadeh & Law, 1991; Heap et al., 2019; Zang et al., 1996). However, other sandstones like Fontainebleau show no

strength weakening in the presence of water (Duda & Renner, 2013; Reviron et al., 2009). Hawkins & McConnell (1992) studied the effect of moisture content on 35 British sandstones, and found that the strength sensitivity to water is dependent on the quartz and clay mineral content: the higher the quartz and the lower the clay contents, the less sensitive the sandstone strength is to water saturation.

Under compressive stress, rock failure originates from the nucleation, propagation and coalescence of micro-cracks. In turn, micro-crack growth is primarily controlled by 1) the frictional parameters of the pre-existing cracks, and 2) the fracture toughness of the non-damaged material (e.g., Ashby & Sammis, 1990; Brace et al., 1966; Brace & Bombolakis, 1963). Based on classical micro-mechanical models, Baud et al. (2000) indeed interpreted water weakening in four sandstones, both in the brittle and cataclastic flow regimes, due to a reduction of both of these parameters in the presence of water. However, the respective contribution of these parameters to the water weakening of rocks is poorly constrained by systematic measurements.

Experimental studies on the effect of water on frictional parameters of rock surfaces have shown that static friction is reduced in the presence of water for granite (e.g., Byerlee, 1967), quartzite (e.g., Dieterich & Conrad, 1984), limestone (e.g., Rutter, 1972), and granitic gneiss (e.g., Jaeger, 1959). For example, Jaeger (1959) found a reduction of the static friction of about 10% in the presence of water compared to dry conditions for Hawkesbury sandstone. Two main possibilities can explain such a reduction: 1) water decreases the adhesion forces at contact points, and 2) water reduces the strength of the asperities supporting the shear stress. Additionally, a reduction of the fracture toughness of rocks in the presence of water has been interpreted as due to: stress corrosion (e.g., Kataoka et al., 2015), mineral dissolution (e.g., Maruvanchery & Kim, 2019), capillary forces at the crack tip (e.g., Nara et al., 2012), clay weakening (e.g., Wang et al., 2007), grain contact lubrication (e.g., Guha Roy et al., 2017), or a reduction of surface energy via adsorption mechanisms (e.g., Baud et al., 2000). For instance, for sandstones, the presence of water causes a reduction of the mode I fracture toughness typically ranging from 30 to 50 % compared to dry conditions (e.g., Guha Roy et al., 2017; Maruvanchery & Kim, 2019; Nara et al., 2012).

In summary, under drained conditions and at an equivalent effective stress, the presence of water can reduce the macroscopic rock strength via the reduction of fracture toughness and the static friction. The weakening mechanisms are mechanical and chemical processes that occur at the microscopic (i.e., grain) scale. A plethora of mechanisms can explain such water weakening, and depend on a defined set of conditions (i.e., pressure, temperature, strain rate, etc.) and/or rock type. However, for simple experimental conditions and a defined rock type, it is not clear if one (or more) mechanisms prevail over the others.

Here, we address the following questions: 1) do systematic measurements of the fracture toughness and static friction reveal a significant reduction under water-saturated conditions compared to dry conditions? 2) Since water weakening in sandstones may depend on the quartz and clay mineral content, are the measured fracture toughnesses and static friction coefficients in direct agreement with this? 3) How do new data improve the micro-mechanical interpretation of water weakening in sandstones? To answer these questions, we measured the effect of water on the uniaxial compressive strength (UCS) of five sandstones to quantify their water weakening. Then, the mode I fracture

toughness and static friction were measured under dry and water-saturated conditions in order to constrain the relative influence of the involved parameters. These measured mechanical parameters are used in micro-mechanical models aiming to better constrain the physico-chemical mechanisms involved in the water weakening of sandstones.

3.3 Experimental methodology

3.3.1 Starting materials

Five sandstones were used in this study: Fontainebleau sandstone (FS) (south of Paris, France), Bentheim sandstone (BS) (Bentheim, Germany), Adamswiller sandstone (AS) (Bas-Rhin, France), Rothbach sandstone (RS) (Bas-Rhin, France), Darley Dale sandstone (DS) (Derbyshire, England). These sandstones were chosen because they span a wide range of initial porosities and different mineral compositions (Table 3. 1), and because their mechanical properties are well documented in the literature (e.g., Baud & Meredith, 1997; Baud et al., 2004, 2006; Bésuelle et al., 2003; Bourbié & Zinszner, 1985; Duda & Renner, 2013; Louis et al., 2009; Noël et al., 2019; Reviron et al., 2009; Wong et al., 1997).

In order to characterize the tested sandstones, X-ray crystallography and optical microscopic surveys were first performed (Table 3. 1 and Figure 3. 1). These surveys revealed that FS and BS are almost pure quartz sandstones (97 and 89 %, respectively). In addition to quartz grains, AS and RS are also composed of a high quantity of K-feldspar (73 and 57 % of quartz, and 17 and 35% of K-feldspar, respectively). DS is mainly composed of quartz (69 %), plagioclase (10 %) and K-feldspar (10 %). The tested sandstones have a phyllosilicate (i.e., including clay mineral) content ranging from 3 to 9 %. The optical microscopic survey revealed that the average grain sizes of FS, BS, AS, RS and DS are 200, 200, 135, 250 and 220 μm , respectively. The porosity of the five sandstones can be divided into equant pores (i.e., more or less spherical pores) and grain contacts that form elongated cracks (Figure 3. 1). FS, BS, AS, RS and DS have equant pores of diameter ranging from 10 to 100, 20 to 100, 6 to 60, 15 to 200 and 20 to 100 μm , respectively; their cracks linearly extend from 200 to 400, 200 to 600, 135 to 400, 250 to 900 and 220 to 650 μm , respectively.

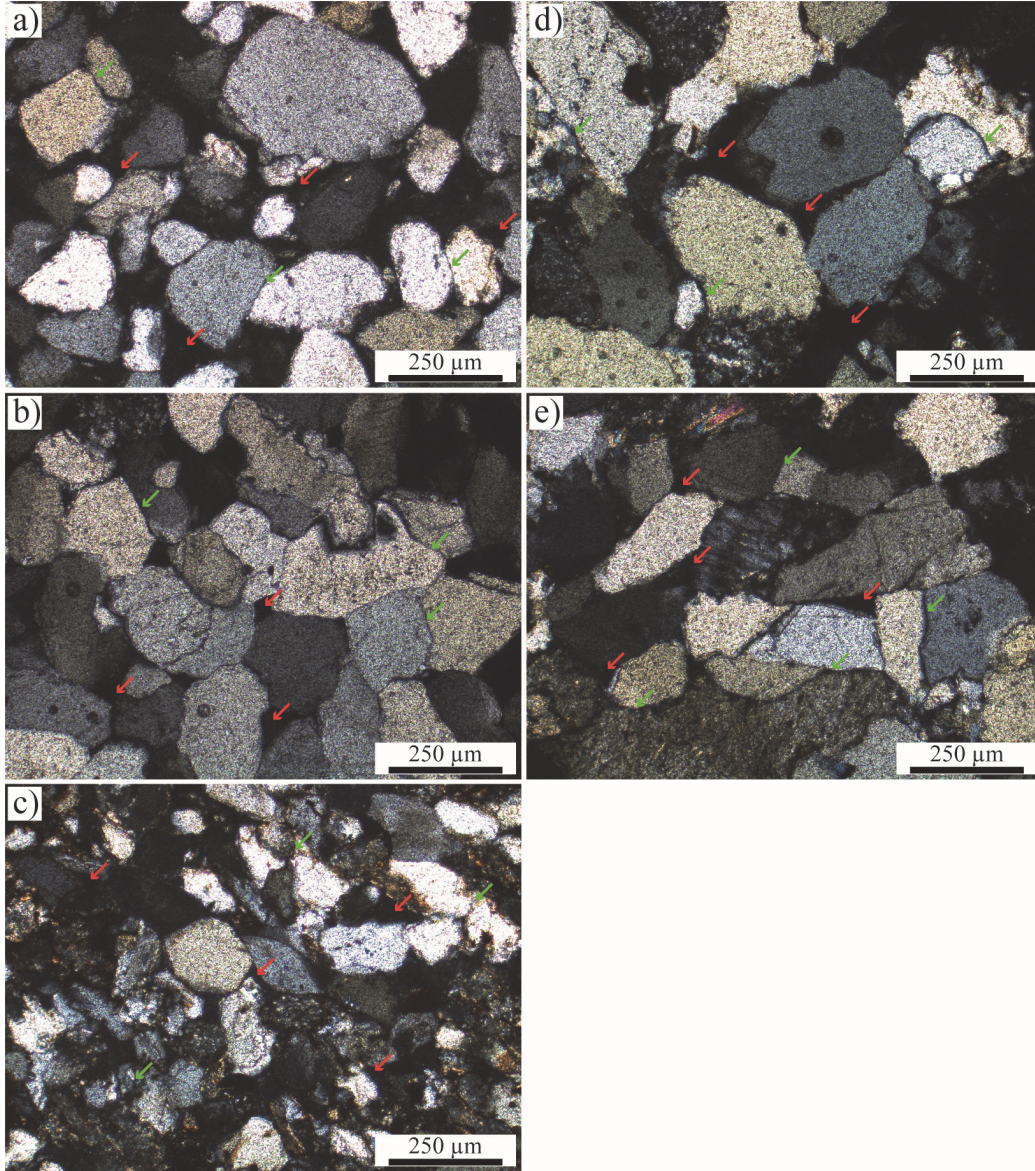


Figure 3. 1: Optical micrographs under a cross-polarized microscope of a) Fontainebleau sandstone, b) Bentheim sandstone, c) Ad-amswiller sandstone, d) Rothbach sandstone and e) Darley Dale sandstone. The red and green arrows show equant pores and cracks at the grain junctions, respectively.

Then, prior deformation, porosity and ultrasonic P- and S-wave propagation velocities were measured at room pressure and temperature to ensure experiment reproducibility. From these measurements, the dynamic elastic moduli were inferred.

Porosities and bulk densities of the sandstones were measured using the triple weight method (i.e., weighing the sample dry, saturated, and saturated and immersed) assuming Archimedes' principle (see Guéguen & Palciauskas, 1994). The five tested sandstones have initial porosities ranging from 5 to 25% and bulk densities ranging from 2000 to 2500 g/cm³ (Table 3. 1).

Ultrasonic P- and S-wave velocities were measured at room pressure and temperature using two P- and S-wave piezoelectric transducers (*Olympus V103-RB* and *Olympus V153-RB*, respectively). The electrical signal was delivered by a generator at 1-MHz frequency and recorded with a numerical oscilloscope. The time of the P- and S-wave arrivals were handpicked and used to compute the

P- and S-wave velocities across the samples (V_p and V_s , respectively). The measurements were performed both under dry and water-saturated conditions. The obtained values for V_p and V_s are directly linked to the sample porosity, with decreasing velocity values for higher sample porosities (Table 3. 1).

Table 3. 1: Mineral composition and physical properties of the five studied sandstones. Sat = water-saturated sample.

Sample	Mineral composition	Average grain size (μm)	Porosity (%)	Bulk dry density (g/cm^3)	V_p (m/s)		V_s (m/s)	
					Dry	Sat	Dry	Sat
Fontainebleau	97% quartz, 3% phyllosilicates	200	4.99 ± 0.7	2526 ± 52	3643 ± 566	4562 ± 324	2210 ± 431	2631 ± 198
Bentheim	89% quartz, 8% phyllosilicates, 2% K-feldspar, 0.6% Na-plagioclase, 0.8% dolomite	200	24.0 ± 0.2	2010 ± 9	2965 ± 76	3198 ± 206	1850 ± 48	1840 ± 94
Adamswiller	73% quartz, 9% phyllosilicates, 17% K-feldspar, 0.7% hematite	135	24.3 ± 0.4	2011 ± 16	2516 ± 113	2921 ± 122	1621 ± 40	1513 ± 63
Rothbach	57% quartz, 6% phyllosilicates, 35% K-feldspar	240	19.9 ± 0.4	2117 ± 15	3022 ± 113	3413 ± 201	2002 ± 48	1955 ± 79
Darley Dale	69% quartz, 9% phyllosilicates, 10% K-feldspar, 10% Na-plagioclase	220	15.3 ± 0.6	2243 ± 21	2985 ± 58	3454 ± 176	1994 ± 60	1924 ± 111

Assuming that the samples are isotropic (note that BS, AS and RS present a slight transverse anisotropy), their dynamic elastic moduli have been computed from the measured porosity (ϕ), density (ρ), V_p and V_s , as:

$$E = \frac{[\rho V_s^2(3V_p^2 - 4V_s^2)]}{(V_p^2 - V_s^2)} \quad \text{Equation (3.1.1)}$$

$$G = \rho V_s^2 \quad \text{Equation (3.1.2)}$$

$$K = \lambda + \frac{2G}{3} \quad \text{Equation (3.1.3)}$$

$$\lambda = \rho V_p^2 - 2G \quad \text{Equation (3.1.4)}$$

$$\nu = \frac{(V_p^2 - 2V_s^2)}{2(V_p^2 - V_s^2)} \quad \text{Equation (3.1.5)}$$

where E , G , K , λ , and ν are the Young, shear, and bulk moduli, Lamé's first parameter and Poisson's ratio, respectively (Table 3. 2).

Table 3. 2: Dynamic elastic parameters obtained from the dry P- and S-wave velocity survey (i.e., equations 3.1) for the five tested sandstones.

Sample	E (GPa)	G (GPa)	K (GPa)	λ (GPa)	ν
Fontainebleau	30.3 ± 10.7	12.7 ± 4.9	17.2 ± 4.8	34.2 ± 10.5	0.20 ± 0.07
Bentheim	16.2 ± 0.8	6.9 ± 0.4	8.5 ± 0.7	17.7 ± 0.9	0.18 ± 0.02
Adamswiller	12.1 ± 0.7	5.3 ± 0.3	5.7 ± 0.7	12.7 ± 0.9	0.14 ± 0.03
Rothbach	18.8 ± 1.2	8.5 ± 0.4	8.0 ± 1.2	19.4 ± 1.5	0.11 ± 0.04
Darley Dale	19.4 ± 0.5	8.9 ± 0.6	8.1 ± 1.3	20.0 ± 0.7	0.09 ± 0.06

3.3.2 Experimental methods

Three different types of experiments were performed in this study: uniaxial compression, fracture toughness and friction experiments. They required different specific initial sample geometries, deformation apparatuses, experimental procedures and data analyses. The following is divided into three methodology sections, one for each type of experiment.

In order to understand how water influences the mechanical behaviour of sandstones, the experiments were performed under both dry and water-saturated conditions. In the following, “dry experiment” refers to experiments performed with samples that have been placed in an oven for at least 12 hours and then placed in a desiccator at room temperature for at least 5 hours prior to deformation at room temperature. For all setups (uniaxial compression, fracture toughness and friction experiments), “saturated experiment” refers to experiments performed with samples that have been first placed in an oven for at least 12 hours, then saturated under vacuum with de-aired distilled water at ambient pressure and temperature. Additionally, the saturated experiments were all performed under immersed (i.e., samples immersed into distilled water during their deformation) and drained conditions.

Note that the following sample preparation processes were done with tap water as cooling fluid and that samples were prepared from unique blocks to reduce inhomogeneity.

3.3.2.1 Uniaxial compression

For the uniaxial compression experiments, samples were first diamond drilled to a diameter of 36- or 28-mm, depending on available materials. Cylinders were then sawed and the opposite faces ground flat in order to prevent any parallelism defects ($\pm 50\text{-}\mu\text{m}$ precision) for a final length of 72 or 56 mm (i.e., twice the sample diameter). For BS, AS and RS, bedding planes were clearly visible, and samples were cored with the planes perpendicular to the sample axis (Figure 3. 2a).

The uniaxial compression experiments were performed with a hydraulic press from Walter and Bai company. Samples were inserted between two pistons placed under the press (Figure 3. 2a). The top piston is equipped with a ball joint to prevent any misalignment (Figure 3. 2aA). The equipment allows for an axial stress up to 1 GPa (± 50 -kPa resolution) on 36 mm diameter samples. During the sample deformation, axial displacements were measured using two linear optoelectronic transducers mounted close to the sample, with a precision of 1 μ m. Radial displacements were measured with an extensometer mounted on a chain at the centre of the sample with a 1- μ m precision (Figure 3. 2aF). In addition, wideband (200–950 kHz) piezoelectric sensors were placed in each piston (Figure 3. 2aB) to monitor the high-frequency Acoustic Emission (AE) events which radiated from the samples during their deformations. The emitted signal was amplified to 40 dB through preamplifiers, and the trigger was set to only record events with an amplitude higher than 0.056 V, that is, ≈ 1.75 times higher than the background noise of the experimental setup (measured at 0.032 V), preventing noise recording. Each event that fulfilled this condition was recorded at a 1-MHz sampling rate, in a 400 μ s window.

After placing the sample between the two pistons, the axial stress was increased by applying a constant displacement rate of 7.2×10^{-4} mm.s $^{-1}$ or 5.6×10^{-4} mm.s $^{-1}$ for the 72 or 56 mm long samples, respectively, which corresponds to a strain rate of $\dot{\epsilon}_{ax} \approx 10^{-5}$ s $^{-1}$. The experiments were stopped after the sample's macroscopic failure. During sample deformation, the recording rate was set to 0.5 Hz. Note that each uniaxial compression experiment was performed twice to verify the experimental reproducibility.

The axial displacements were corrected for the elastic distortion of the apparatus (i.e., press column and pistons), calibrated using a metal plug of known stiffness. The axial strain was then inferred from the ratio between the corrected axial displacement and the initial sample length. The radial strain was computed as the ratio between the extension of the chain placed around the sample and its initial perimeter. The volumetric strain was computed by summing the axial strain and twice the radial strain ($\epsilon_{vol} = \epsilon_{ax} + 2\epsilon_{rad}$).

3.3.2.2 Fracture toughness

The Cracked Chevron-notched Brazilian Disk (CCNBD) geometry was used for fracture toughness measurements. This geometry was chosen because it allows for a stable crack propagation using a relatively simple machined specimen and standard rock testing apparatus. Cores were first diamond drilled to a diameter of 80 mm. Disks were then sawed and opposite faces ground flat (± 100 μ m) for a final height of 30 mm. Then, a notch was made by inserting 16 mm of a diamond saw (50.95-mm diameter) on both sides of the sample at its centre following the ISRM norms (Fowell et al., 1995). If bedding planes were observed, the sample was cored parallel and the notched perpendicular to the planes. Fracture toughness was therefore measured perpendicular to the bedding planes (i.e., arrester orientation, Figure 3. 2b).

For the fracture toughness experiments, the CCNBD samples were placed under the hydraulic press described above (Figure 3. 2b). Large pistons were attached to the press to facilitate sample positioning (Figure 3. 2bH). The system allows for an axial force up to 2 MN with a resolution of 0.5 kN. During the sample deformation, axial displacements were measured with two linear optoelectronic transducers mounted close to the sample with a precision of 1 μ m. The crack mouth open-

ing (i.e., the horizontal opening of the machined notch) was monitored with an extensometer ($\pm 1\text{-}\mu\text{m}$ precision) placed between two “L-shape” metal plates glued on the sample (Figure 3. 2bK).

After placing the sample under the press with the machined notch aligned parallel to the direction of the applied force, a constant displacement rate of $2.5 \times 10^{-2} \text{ mm.s}^{-1}$ was applied up to crack propagation. This fast displacement rate was chosen so that the experiments would last less than 10 seconds, as recommended by the ISRM (Fowell et al., 1995). During the sample deformation, the recording rate was 0.01 Hz.

The mode I stress intensity factor at the machined crack tips was computed by (Fowell et al., 1995, 2006; Fowell & Xu, 1993, 1994; Xu & Fowell, 1994):

$$K_I = \frac{F_{ax}}{B\sqrt{R}} Y^* \quad \text{Equation (3.2.1)}$$

where F_{ax} is the axial force applied on the CCNBD sample, B and R are the sample thickness and radius, respectively. For the geometry used,

$$Y^* = u \exp(v\alpha_1) \quad \text{Equation (3.2.2)}$$

where u and v are constants listed in the ISRM norms and α_1 is the long half machined crack length normalised by the sample radius. The mode I fracture toughness (i.e., critical stress intensity factor), K_{Ic} , of the sample was computed using equation 3.2 and for the maximum axial force recorded during the experiment. From the measured K_{Ic} and the computed Young's modulus and Poisson's ratio (inferred from V_p and V_s) the fracture energy, G_c , could be computed assuming plane strain conditions by:

$$G_c = \frac{K_{Ic}^2(1-\nu^2)}{E} = 2\gamma \quad \text{Equation (3.3)}$$

To compute G_c , even if static moduli can be derived from uniaxial compression experiments, to take sample variability into account, we chose to use the dynamic moduli as they can be measured just before the fracture toughness experiment of each sample. Indeed, they are non-destructive measurements, as opposed to uniaxial compression experiments. Note that the values of the static and dynamic moduli are quite similar (Table 3. 3).

3.3.2.3 Friction

To find the frictional parameters of the tested sample, direct shear experiments were performed in a single shear configuration. Two rectangular cuboids of $70 \times 35 \times 13 \text{ mm}$ and $20 \times 35 \times 13 \text{ mm}$ ($\pm 10 \mu\text{m}$) were prepared for each experiment (Figure 3. 2c). The sliding surfaces were polished with a rough abrasive disc (Struers® MDpiano 80, comparable to no. 80 SiC abrasive paper), however, the surface roughness was mostly controlled by the samples grain size and porosity.

The biaxial deformation apparatus was composed of three forcing blocks of stainless steel (Figure 3. 2c). For simplicity, only one side was used for rock friction (Figure 3. 2cN and P). On the other side, a frictionless surface (i.e., GLYCODUR®, PTFE-based 3-layers material, with friction < 0.02) was used (Figure 3. 2cL). The apparatus is equipped with a horizontal hydraulic piston providing a normal force to the samples up to 180 kN ($\pm 0.04\text{-kN}$ precision), and a vertical piston

connected to four high velocity linear motors that apply the shear force up to 193 kN with an accuracy of 0.04 kN. The system allows for the shearing of the sample at velocities ranging from $1 \mu\text{m.s}^{-1}$ to 0.25 m.s^{-1} . The horizontal (i.e., normal) and vertical (i.e., shear) displacements are measured with optical encoders having a resolution of 5 nm.

After placing the samples in the sample holders (Figure 3. 2cM and O) and positioning them in the biaxial apparatus, the normal stress was raised slowly at 1 MPa/min up to 5 MPa. Then, the shear stress was increased by applying a constant displacement rate on the vertical piston at $1 \mu\text{m/s}$. After 2 mm of displacement, the axial piston was stopped and the shear stress released. The normal stress was raised again to 10 MPa prior to shearing the sample another 2 mm. This procedure was performed 5 times to obtain the frictional behaviour of the sandstones at different normal stress (5, 10, 15, 20 and 25 MPa). During sample deformation, the recording rate was 0.1 Hz.

The normal and shear displacements were corrected from the elastic distortion of the horizontal and vertical pistons, respectively, calibrated using a metal plug of known stiffness. The normal and shear stresses applied on the fault were computed as the ratio of the normal force and the shear force, respectively, with the sample contact area ($\sigma_n = F_n/A$ and $\tau = F_s/A$). The shear stress was corrected for the machine's friction contribution. For each normal stress the static shear stress, τ_s (i.e., the shear stress at the onset of sliding), was picked. The linear regression between the static shear stress and the normal stress applied was computed to obtain the static coefficient of friction, μ_s , of the tested rock samples, with a cohesion (C) that is assumed to be 0 (i.e., $\tau_s = \mu_s \sigma_n + C$).

3.4 Results

3.4.1 Uniaxial compression

For all the tested sandstones and under both dry and saturated conditions, the mechanical results of the uniaxial compression experiments (Figure 3. 3 and Figure 3. 4) follow the classical five stages of deformation. Initially, the axial stress – axial strain curves (Figure 3. 3a and Figure 3. 4b) are non-linear due to the closure of the micro-cracks oriented sub-perpendicular to the direction of compression. During this phase, almost no radial strain is observed and no AE events are emitted. Then, the samples show a linear increase in axial stress with the axial and volumetric strain. Again, no AE events are recorded. This phase ends at the onset of dilatancy, a point denoted C' (Figure 3. 3 and Figure 3. 4a and b), which is marked by a deviation from linearity of the axial stress – axial strain and axial stress – volumetric strain curves, as well as an onset of AE events. After C' is reached, the axial stress versus strain curves follows a non-linear increase until the peak axial stress is reached (Figure 3. 3 and Figure 3. 4a and b), and AE events follow an exponential increase. Ultimately, the sample enters a strain softening phase (i.e., stress drop) and the sample macroscopically fails.

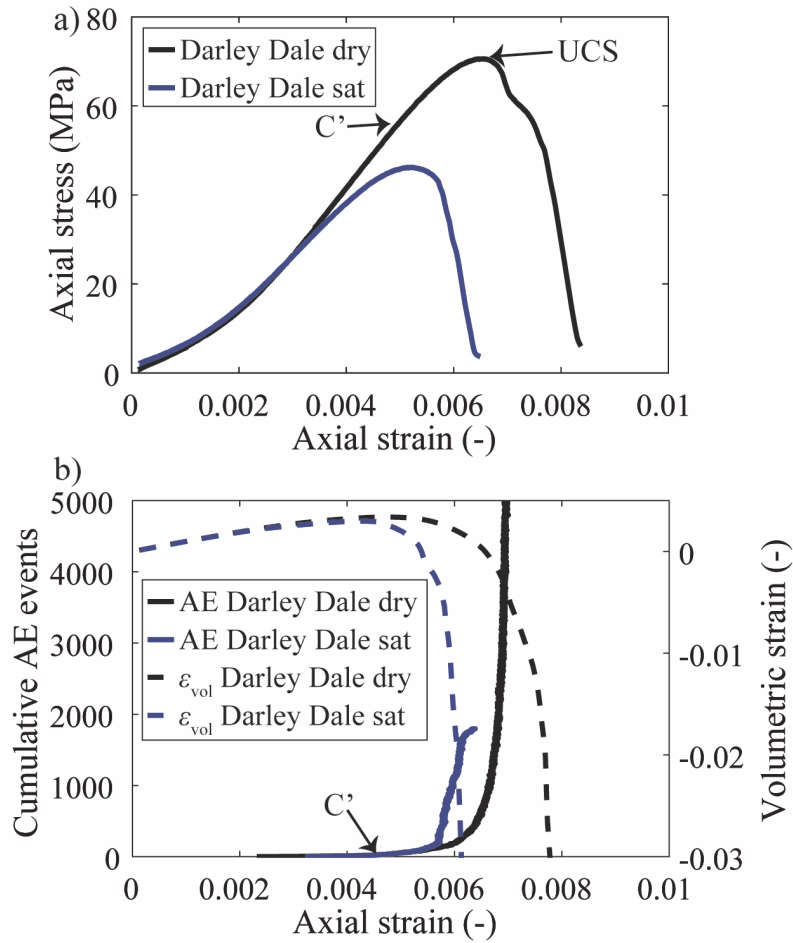


Figure 3. 3: Mechanical and AE data obtained for the uniaxial compression tests of Darley Dale sandstones deformed under dry and saturated conditions. a) Axial stress as a function of the axial strain, b) cumulative AE events and volumetric strain as a function of the axial strain. An example of C' and the UCS is shown for a dry sample.

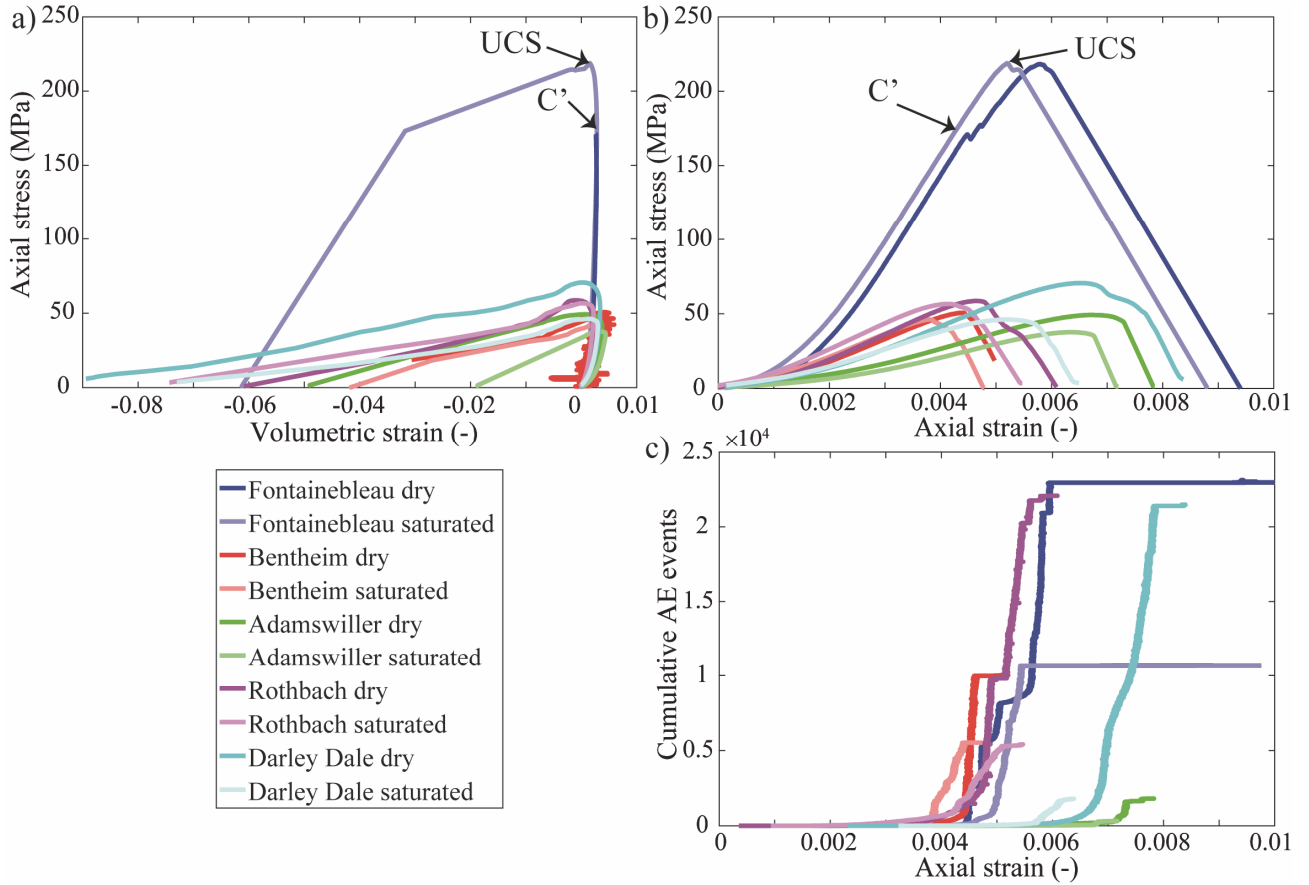


Figure 3. 4: Mechanical and AE data obtained for the uniaxial compression tests of the five sandstones deformed under dry and water-saturated conditions. a) Axial stress as a function of the volumetric strain, b) axial stress as a function of the axial strain and c) cumulative AE events as a function of the axial strain. An example of C' and the UCS is shown for a Fontainebleau sandstone experiment performed under water-saturated conditions. Note that the AE data are very well correlated with the mechanical data, presenting an increase in events before and at each stress drop.

The sample's UCS (peak axial stress) and C' decay with increasing the sample porosity (Figure 3. 5). The five tested sandstones present lower C' and UCS under water-saturated conditions as opposed to dry conditions, i.e., water weakening (Figure 3. 4, Figure 3. 5 and Table 3. 3). Under water-saturated conditions, the axial stress at C' is 97, 92, 83, 96 and 70 % of that observed in the dry experiments and the UCS is 90, 92, 77, 95 and 70 % of that observed in the dry experiments for FS, BS, AS, RS and DS, respectively. Moreover, water-saturated samples reach C' and their UCS at lower axial strain values than dry samples (Figure 3. 4b). AEs are also strongly reduced under water-saturated conditions (Figure 3. 4c).

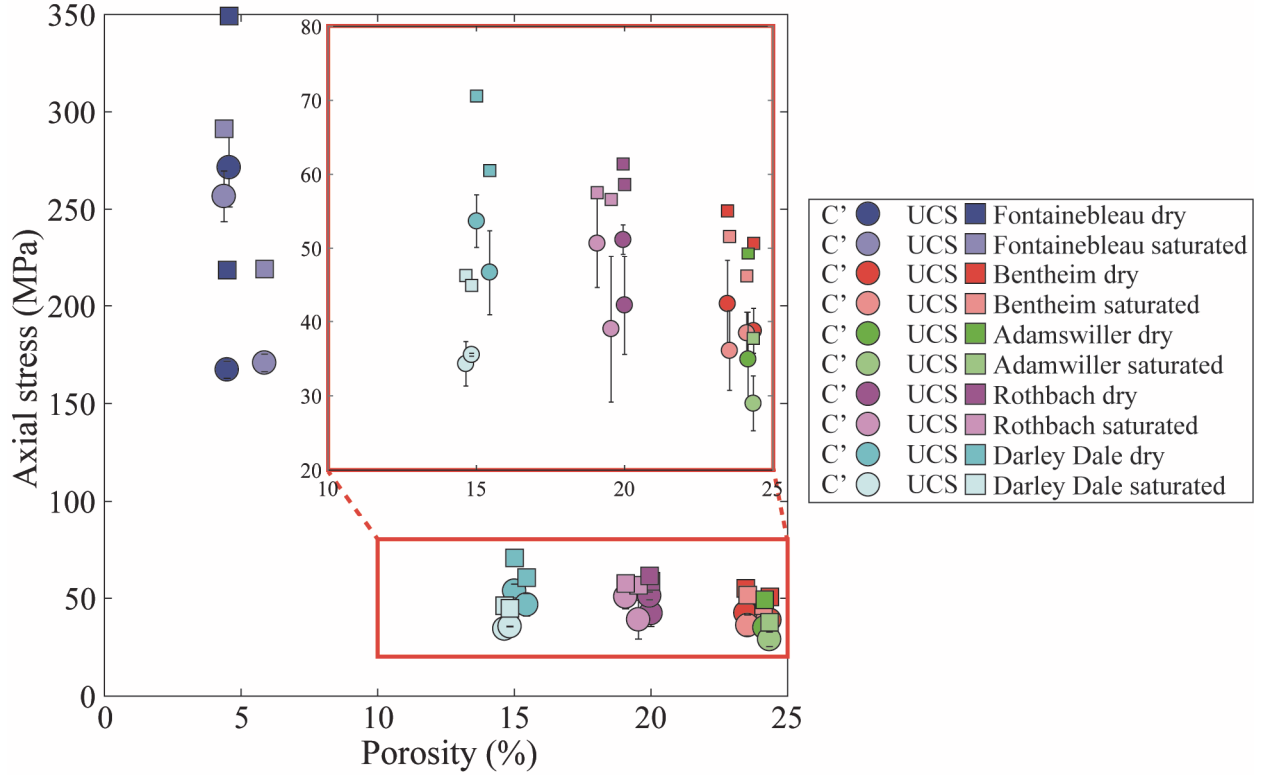


Figure 3. 5: Axial stress at C' and the uniaxial compressive strength (UCS) of the five tested sandstones under dry and water-saturated conditions as a function of the initial measured porosity. The red rectangle presents a zoom on BS, AS, RS and DS. For C' data, the error bars correspond to the difference between the deviation of linearity of the axial stress – axial strain curves and the onset of AE events.

3.4.2 Fracture toughness

For the tested sandstones and both under dry and water-saturated conditions, the mechanical data of the fracture toughness experiments all show similar trends (Figure 3. 6). First, the data show a quasi-linear increase of K_I as a function of both the axial displacement and the crack mouth opening, followed by a deviation from linearity prior to reaching a peak (K_{Ic}). After the peak value, a drop in K_I and a large crack mouth opening occur as the sample fractures. Note that all the experiments are considered valid as the sample failed with the formation of a crack aligned with the machined notch (i.e., mode I fracturing), as recommended by the ISRM. A visual inspection of the fractured surface at the end of the experiments revealed that the fractures mainly propagate at the grain junctions and not within the grains.

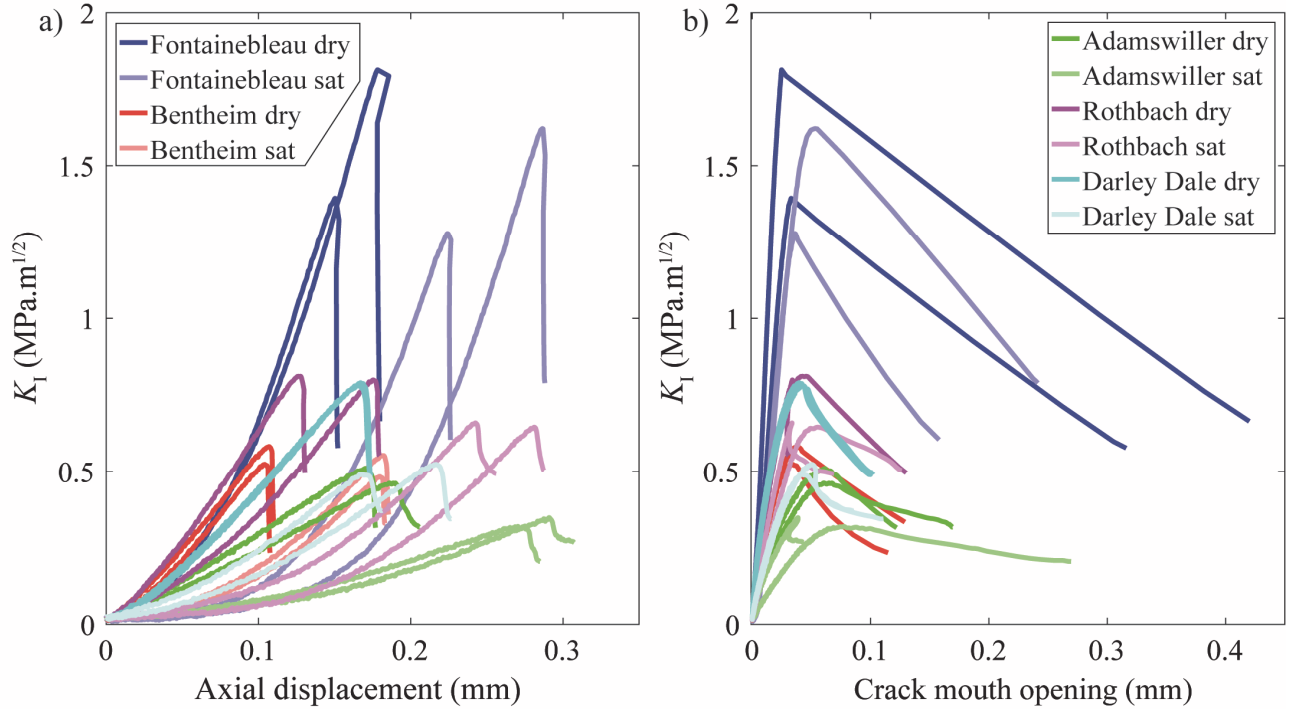


Figure 3. 6: Mechanical data of the fracture toughness experiments: mode I stress intensity factor as a function of a) the axial displacement and b) the crack mouth opening for the five tested sandstones under dry and water-saturated conditions (sat). The peak value of the recorded K_I is the critical stress intensity factor (or fracture toughness), K_{Ic} , of the sample. For the experiments performed on Bentheim sandstone under water-saturated conditions, the crack mouth opening data were not recorded due to the detachment of the “L-shape” metal plates holding the extensometer at the beginning of the experiments. Importantly, the post-peak behaviour is not to be considered as the crack length has increased (i.e., a_1 increases in equation 3.2.2, modifying the computation of K_I).

K_{Ic} is a decreasing function of the porosity (Figure 3. 7a). Additionally, water-saturated samples failed at a lower value of K_{Ic} than dry samples (Figure 3. 7a and Table 3. 3). Indeed, K_{Ic} under water-saturated condition is 10, 6, 25, 18 and 34 % lower than under dry conditions for FS, BS, AS, RS and DS, respectively (Figure 3. 7a). Similar results are found for the fracture energy, G_c , with a reduction of 44, 21, 49, 43 and 52 % for FS, BS, AS, RS and DS, respectively (Figure 3. 7b).

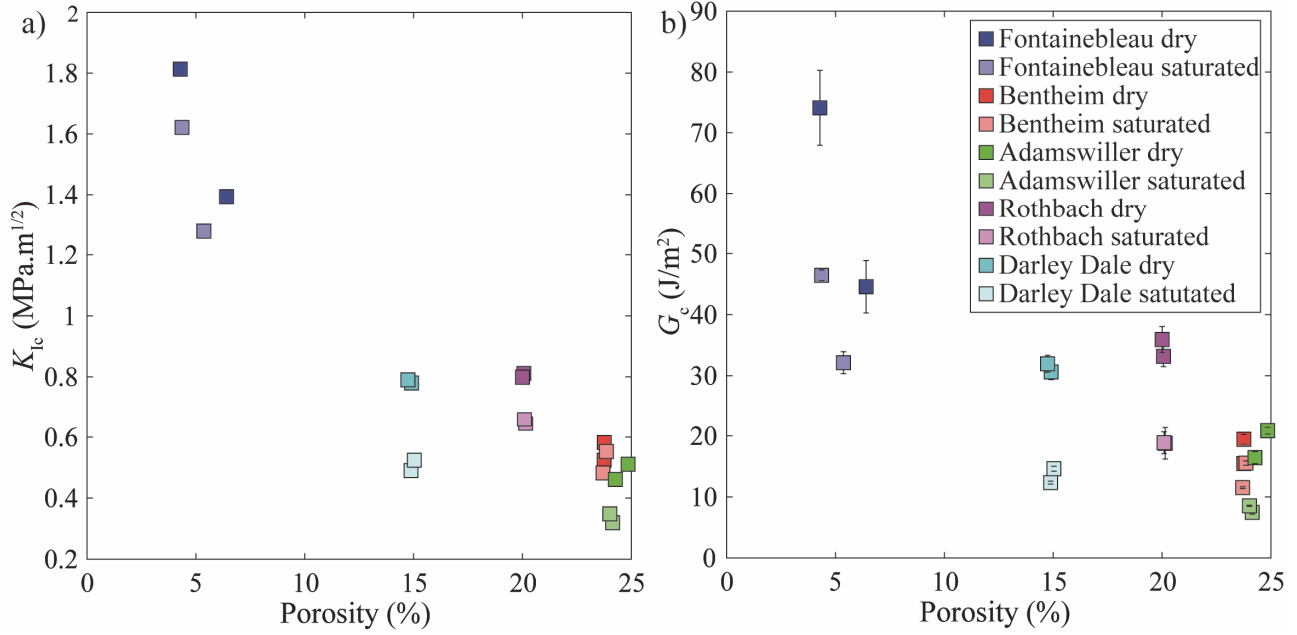


Figure 3. 7: a) Fracture toughness and b) fracture energy as a function of the sample's initial porosity for the five tested sandstones under both dry and water-saturated conditions.

3.4.3 Friction

For all the tested sandstones and under both dry and water-saturated conditions, the friction data show similar behaviour (Figure 3. 8). At all the normal stresses, first, a linear increase of the shear stress as a function of the horizontal displacement is observed (Figure 3. 8a). During this phase, the fault is stuck (i.e., not moving) and the sample deforms elastically. This phase ends when the shear stress reaches the shear strength, and fault starts to slide (red circle in Figure 3. 8a). The shear stress at the onset of sliding as a function of the normal stress form a single line, with the slope being the friction coefficient (μ_s), and the y-intercept being the fault cohesion (C) (Figure 3. 8b-f). After the onset of sliding, the sample continues to slide at an almost constant shear stress, and typically reaches a steady-state value equal to, or slightly lower than, μ_s (Figure 3. 8a). Note that for FS, and at elevated normal stresses (i.e., $\sigma_n \geq 15$ MPa), unstable slip behaviour was observed, as indicated by stick-slip sequences. Also note that, for BS, AS, RS and DS, the samples collapsed at elevated normal stresses.

The experiments demonstrate that the static frictions of the water-saturated samples are generally lower than that of the dry samples (Figure 3. 8 and Table 3. 3). Indeed, the static friction coefficients are 18, 16 and 19 % lower for FS, AS and DS under water-saturated conditions compared to dry conditions. They are, however, equivalent under both conditions for BS and RS. Note that no trend of the static friction with the porosity could be found.

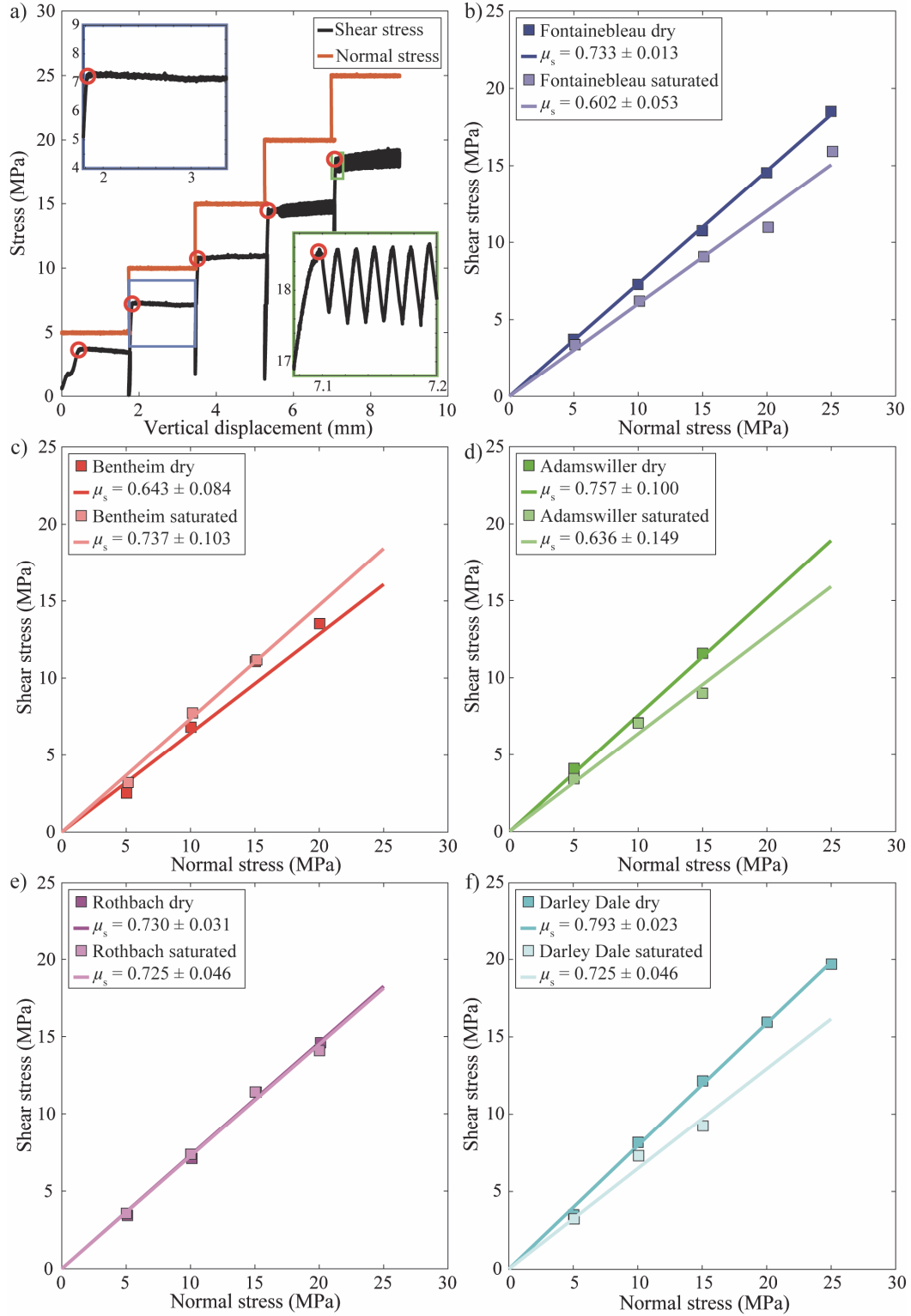


Figure 3. 8: Friction experiment data obtained for the five tested sandstones under dry and water-saturated conditions. a) shear and normal stresses as a function of the vertical displacement (i.e. shear direction) for a typical friction experiment (FS under dry conditions). For all the normal stresses, red circles show the shear stress at the onset of sliding used to compute the static friction and cohesion. Additionally, two zooms are presented to show two typical behaviours observed: The blue box presents a zoom on an example of stable sliding where the sample static friction and steady-state friction are equivalent. The green box presents a zoom on unstable sliding behaviour where the cumulative slip is accommodated through stick-slips. Picked shear stress at the onset of sliding as a function of the applied normal stress for b) FS, c) BS, d) AS, e) RS and f) DS under dry and water-saturated experiments. The best fit of the data following $\tau = \mu_s \sigma_n$ is presented for the five tested sandstones under both dry and water-saturated conditions. The value of μ_s is presented in the figures' legends. Note that for BS, AS, RS and DS the sample collapsed at elevated normal stresses.

Table 3. 3: Summary of the static Young modulus (E_s), the UCS, K_{Ic} and μ_s obtained experimentally under both dry and water-saturated conditions.

Sample	E_s^{dry} (GPa)	E_s^{sat} (GPa)	UCS ^{dry} (MPa)	UCS ^{sat} (MPa)	UCS ^{sat} / UCS ^{dry}	K_{Ic}^{dry} (MPa.m ^{1/2})	K_{Ic}^{sat} (MPa.m ^{1/2})	$K_{Ic}^{sat} /$ K_{Ic}^{dry}	μ_s^{dry}	μ_s^{sat}	$\mu_s^{sat} /$ μ_s^{dry}
FS	59.8	58.7	283.75 ± 92.6	255.05 ± 52.3	0.90	1.60 ± 0.30	1.45 ± 0.24	0.91	0.733	0.602	0.82
BS	15.3	15.4	52.86 ± 3.1	48.87 ± 3.9	0.92	0.55 ± 0.04	0.52 ± 0.05	0.95	0.643	0.737	1.15
AS	10.4	8.9	49.23	37.73	0.77	0.49 ± 0.03	0.33 ± 0.02	0.67	0.757	0.636	0.84
RS	17.1	17.3	60.01 ± 2.0	57.06 ± 0.7	0.95	0.81 ± 0.01	0.65 ± 0.01	0.80	0.730	0.725	0.99
DS	15.1	15.2	65.55 ± 7.1	45.53 ± 0.9	0.70	0.79 ± 0.01	0.51 ± 0.02	0.65	0.793	0.646	0.81

3.5 Discussion

The experimental results show that, among the five tested sandstones, water-saturated conditions (compared to dry conditions) cause a reduction in: i) the fracture toughness and fracture energy; and ii) the static friction, which can explain the reduction of the UCS, as well as the onset of dilatancy.

In the following, the effect of water weakening on sandstone strength and the possible involved mechanisms are discussed. Micro-mechanical models are described and used to interpret and discuss the mechanisms involved in the water weakening.

3.5.1 Water weakening of sandstone

The performed uniaxial compression experiments showed that the UCS is reduced by 10, 8, 23, 5 and 30 % for FS, BS, AS, RS and DS, respectively, in presence of water compared to dry conditions. Note that for FS, due to the sample strength variability under similar condition, no clear conclusion can be drawn on the water weakening. Similar water weakening values of strength can be found in the literature. For DS, Baud et al. (2000) measured a triaxial strength water weakening ranging from 12 to 17%. Other studied sandstones present similar weakening values that typically range from 8 to 50% (Baud et al., 2000, 2015; Hadizadeh & Law, 1991; Hawkins & McConnell, 1992; Zang et al., 1996). Finally, for FS, previous measurements have also shown no significant strength reduction with the presence of water (Duda & Renner, 2013; Revirion et al., 2009).

Under compressive loading, the macroscopic brittle failure of a rock occurs by damage/micro-crack nucleation, propagation and coalescence (e.g., Ashby & Sammis, 1990; Brace et al., 1966; Brace & Bombolakis, 1963). In turn, the physical parameters that define the aptitude of cracks to nucleate and propagate are the fracture toughness (or fracture energy) and the static friction. Interestingly, our experimental results demonstrate that both the mode I fracture toughness and the static friction of the tested sandstones are reduced in the presence of water (**Erreur ! Source du renvoi introuvable.** and **Erreur ! Source du renvoi introuvable.**), in agreement with Baud et al. (2000). Indeed, among the five tested sandstones, water saturation (compares to dry conditions) causes a reduction of: the fracture toughness and fracture energy ranging from 6 to 35 % and 21 to 52 %, and the static friction from 0.643 to 0.737.

respectively, and the static friction ranging from 0 to 19 %. This is in agreement with previous results on sandstones and other rocks, where water saturation was previously found to reduce K_{Ic} (e.g., Guha Roy et al., 2017; Maruvanchery & Kim, 2019; Nara et al., 2012; Wang et al., 2007; Zhou et al., 2018) and μ_s (e.g., Byerlee, 1967; Dieterich & Conrad, 1984; Jaeger, 1959; Rutter, 1972), see Table 3. 4 and Table 3. 5. However, the rock strength weakening, as well as K_{Ic} and μ_s , are variable depending on the tested rock sample, raising the question: What is controlling the efficiency of the water weakening in rocks?

Table 3. 4: Literature data for uniaxial and triaxial strength under both dry and water-saturated conditions.

Sample	$P_c - P_f$ (MPa)	Strength ^{dry} (MPa)	Strength ^{sat} (MPa)	Strength ^{sat} / Strength ^{dry}	reference
Darley Dale	10	126	110	0.87	Baud et al. (2000)
	30	190	163	0.86	
	50	263	217	0.83	
Berea	10	115	36	0.31	
	40	186	83	0.45	
Pegnant	0	253	144	0.57	Hadizadeh and Law (1991)
Flechtingen	0	82	55	0.67	Zang et al. (1996)
Ruhr	20	211	215	1.02	Duda and Renner (2013)
Wilkeson	20	181	160	0.88	
Fontainebleau	20	616	586	0.95	
Bentheim	30	184	183	0.99	Reviron et al. (2009)
Fontainebleau	0	71	77	1.08	
Applecross	0	141.3	99.3	0.7	Hawkin and McConnell (1992)
Donegal Quartzite	0	237.9	184	0.77	
Basal Quartzite	0	247	202.1	0.82	
Brownstones	0	152	107.4	0.71	
Pilton	0	173.3	152.2	0.88	
Upper Cromhall	0	161.4	143.9	0.89	
Millstone Grit	0	59.3	39.6	0.67	
Holcombe Brook Grit	0	119.1	49	0.41	
Siliceous Sandstone	0	198.4	182.2	0.92	
Elland Flags	0	59.9	31.4	0.52	
Thornhill Rock	0	89.9	38.4	0.43	
Middle Coal Measures	0	37.1	25.3	0.68	
Crackington Formation	0	298.2	232.3	0.78	
Pennant	0	114.2	50	0.44	
Annan	0	66.3	43.6	0.66	

Penrith	0	66	53.1	0.8	Heap et al. (2019)
Redcliffe	0	36.1	22.4	0.62	
Midford Sands	0	23.2	14.6	0.63	
Ardingly	0	42.2	36.9	0.87	
Ashdown	0	30.6	32.3	1.06	
Greensand	0	10.5	2.3	0.22	
Voltzia unit	0	152.4	105.1	0.69	
Intermédiaires unit	0	147	99.5	0.68	
Karlstal unit	0	101.4	76.9	0.76	
Rehberg unit	0	102.1	56.5	0.55	
Trifels unit	0	90.9	60	0.66	This study
Annweiler unit	0	244	188.8	0.77	
Anté-Annweiler unit	0	82.1	45.8	0.56	
Adamswiller	0	42.5	32.7	0.77	
Rothbach	0	57.8	43.6	0.75	
Fontainebleau	0	283.75 ± 92.6	255.05 ± 52.3	0.90	
Bentheim	0	52.86 ± 3.1	48.87 ± 3.9	0.92	
Adamswiller	0	49.23	37.73	0.77	
Rothbach	0	60.01 ± 2.0	57.06 ± 0.7	0.95	
Darley Dale	0	65.55 ± 7.1	45.53 ± 0.9	0.70	

Table 3. 5: Literature data of fracture toughness and frictional parameter under both dry and water-saturated conditions. RH = Relative Humidity.

Sample	K_{Ic}^{dry} (MPa.m ^{1/2})	K_{Ic}^{sat} (MPa.m ^{1/2})	$K_{Ic}^{sat}/K_{Ic}^{dry}$	reference	comment
Dholpur sandstone	0.37	0.25	0.68	Guha Roy et al. (2017)	
Jabalpur white sandstone	0.79	0.54	0.68		
Jabalpur red sandstone	1.05	0.74	0.7		
Jharia shale	0.31	0.15	0.48		
Kumamoto andesite	1.91 ± 0.03	1.66 ± 0.05	0.87	Nara et al. (2012)	here dry is for 20<RH<30% and saturated for 80<RH<90%
Oshima granite	2.14 ± 0.09	2.06 ± 0.06	0.96		
Berea sandstone	0.36 ± 0.01	0.30 ± 0.01	0.83		
Shirahama sandstone	0.73 ± 0.01	0.39 ± 0.02	0.53		
Kushiro sandstone	0.89 ± 0.07	0.60 ± 0.02	0.67		
Monroe County sandstone	0.44 ± 0.08	0.22 ± 0.04	0.5	Maruvanchery and Kim (2019)	
Kunming sandstone	0.51 ± 0.01	0.29 ± 0.01	0.57	Zhou et al. (2018)	here, saturated corresponds to a water content of 3.5%
Fontainebleau sandstone	1.60 ± 0.30	1.45 ± 0.24	0.91	This study	
Bentheim sandstone	0.55 ± 0.04	0.52 ± 0.05	0.95		
Adamswiller sandstone	0.49 ± 0.03	0.33 ± 0.02	0.67		
Rothbach sandstone	0.81 ± 0.01	0.65 ± 0.01	0.80		
Darley Dale sandstone	0.79 ± 0.01	0.51 ± 0.02	0.65		
Sample	μ_s^{dry}	μ_s^{sat}	μ_s^{sat}/μ_s^{dry}	reference	comment
Hawkesbury sandstone	0.52	0.47	0.90	Jaeger (1959)	
Granitic gneiss	0.71	0.61	0.86		
Westerly granite	0.60	0.60	1	Byerlee (1967)	
Westerly granite	0.85 to 1.00	0.55 to 0.65	0.65	Dieterich and Conrad (1984)	
Fontainebleau	0.733	0.602	0.82	This study	

sandstone			
Bentheim sandstone	0.643	0.737	1.15
Adamswiller sandstone	0.757	0.636	0.84
Rothbach sandstone	0.730	0.725	0.99
Darley Dale sandstone	0.793	0.646	0.81

The experiments performed show that the porosity has no influence on sandstone weakening (Figure 3. 5). This is in agreement with the study of Hawkins & McConnell (1992) performed on sandstones with initial porosities ranging from about 2 to 40%. Hawkins & McConnell (1992), however, found a correlation between the mineral content and the efficiency of the water weakening of the sandstones: The sensitivity to water increases with higher clay mineral content, and decreases for high quartz content. To investigate the effect of quartz and clay-minerals, and more generally of mineral composition, on the water weakening effect, we computed the normalised onset of dilatancy C' and the normalised UCS, that is, the ratio between the axial stress of the water-saturated experiments and of the dry ones ($\sigma_{ax}^{sat} / \sigma_{ax}^{dry}$). These were plotted as a function of the principal mineral content of the sandstones obtained from X-ray crystallography analysis (Figure 3. 9). This comparison revealed a mixed effect of the mineral composition. In general, increasing the quartz and phyllosilicate (i.e., including clay-mineral) content (Figure 3. 9a and b) reduces and increases, respectively, the tested sandstone's water-weakening in agreement with Hawkins & McConnell (1992). However, no clear conclusion can be drawn as exceptions which lie far outside the general trend remain (e.g., RS in Figure 3. 9a). Additionally, no effect of the K-feldspar and plagioclase content can be deduced (Figure 3. 9c and d).

To further investigate the effect of mineral content on the sandstone deformations, the normalised mode I fracture toughness (i.e., ratio between water-saturated K_{Ic}^{sat} and the average dry K_{Ic}^{dry}) and the normalized static friction (i.e., ratio between the water-saturated and the dry static friction, $\mu_s^{sat} / \mu_s^{dry}$) were also computed, and plotted against the principal mineral content (Figure 3. 10 and Figure 3. 11). The results do not suggest a clear effect of the mineral content on the water weakening of K_{Ic} : A non-clear trend may be drawn suggesting that water weakening efficiency is increased with decreasing the quartz content (Figure 3. 10a) and increasing phyllosilicate content (Figure 3. 10b). None of the other mineral contents show any trend. Finally, no influence of the mineral content can be seen on the water weakening effect of μ_s (Figure 3. 11). These results are in agreement with previous studies (see Table 3. 4 and Table 3. 5), where no direct correlations between lithology or mineralogy and water weakening of K_{Ic} and μ_s , were found. Then, what are the mechanisms involved in K_{Ic} and μ_s reduction in presence of water?

The reduction of μ_s under water saturated conditions may originate from either a decrease of the adhesion forces at the contact point, and/or an asperity strength reduction (James H. Dieterich & Conrad, 1984). However, the present data do not allow for the distinction of one or the other mechanism to prevail. For the reduction of K_{Ic} under water saturated conditions, it has been interpreted by previous study to originate from: stress corrosion (e.g., Kataoka et al., 2015), mineral dissolution

(e.g., Maruvanchery & Kim, 2019), capillary forces at the crack tip (e.g., Nara et al., 2012), clay weakening (e.g., Wang et al., 2007), grain contact lubrication (e.g., Guha Roy et al., 2017), or a reduction of surface energy via adsorption mechanisms (e.g., Baud et al., 2000). In the experiments performed, the reduction of the surface energy in presence of water is the most plausible. Indeed, the surface energy of quartz (main mineral in the tested sandstones composition) drop from an estimated value of about 2000 mJ.m^{-2} in vacuum, to $406\text{-}458 \text{ mJ.m}^{-2}$ at 100% room humidity, and to $335\text{-}385 \text{ mJ.m}^{-2}$ under water saturated conditions (Parks, 1984). Such reductions are in agreement with the obtained reduction of K_{Ic} under water saturated conditions compared to dry conditions (see equation 3).

Additionally, the strain at failure was found to be much lower for water saturated experiments compared to dry. Similar behaviour was measured for Buntsandstein sandstone deformation under uniaxial compression (Heap et al., 2019). However, such behaviour is inhibited, or even reversed, as soon as confining pressure, as low as 2.5 MPa, is applied during the deformation of the samples (Baud et al., 2000; Heap et al., 2019). One possible cause of lower strain at failure under water saturated and uniaxial compression conditions compare to dry, is that water presence helps at localizing the deformation. This process would be inhibited as soon as a confining pressure is applied as confining pressure also favour localized deformations (see Paterson & Wong (2005), section 3.2 and reference therein). Note however, that the macroscopic post-mortem inspection of the tested sandstone didn't reveal significant deformation localisation comparing dry and water saturated experiments (see Appendix A).

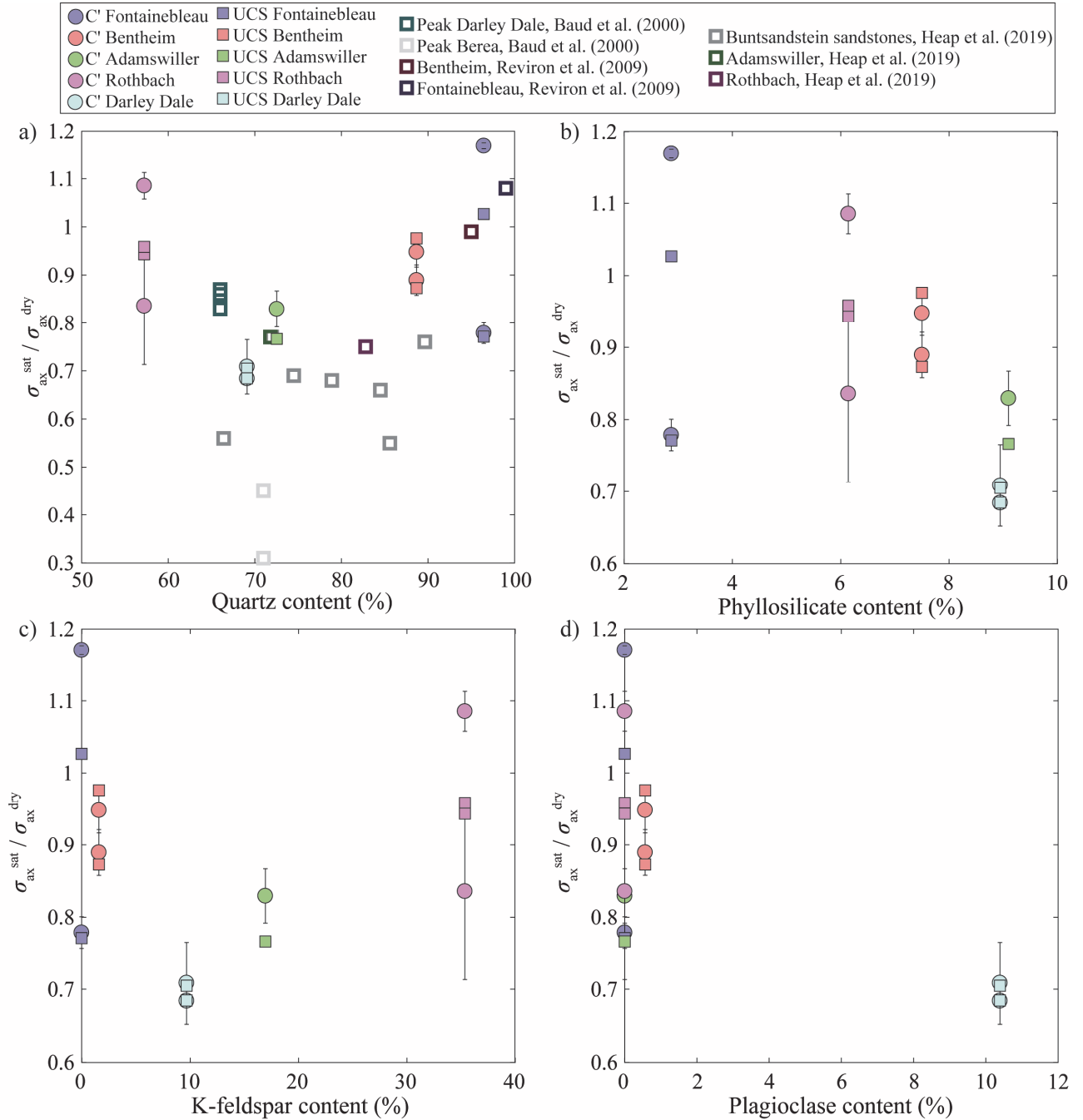


Figure 3. 9: Normalised axial stress at the onset of dilatancy C' and normalized peak stress as a function of the rock mineral content: a) quartz, b) phyllosilicates, c) K-feldspar and d) plagioclase. For C' data, the error bars correspond to the picking difference between the deviation of linearity of the axial stress – axial strain curves and the onset of AE events. For quartz content, literature data from Baud et al. (2000); Heap et al. (2019); Reviron et al. (2009) are also reported.

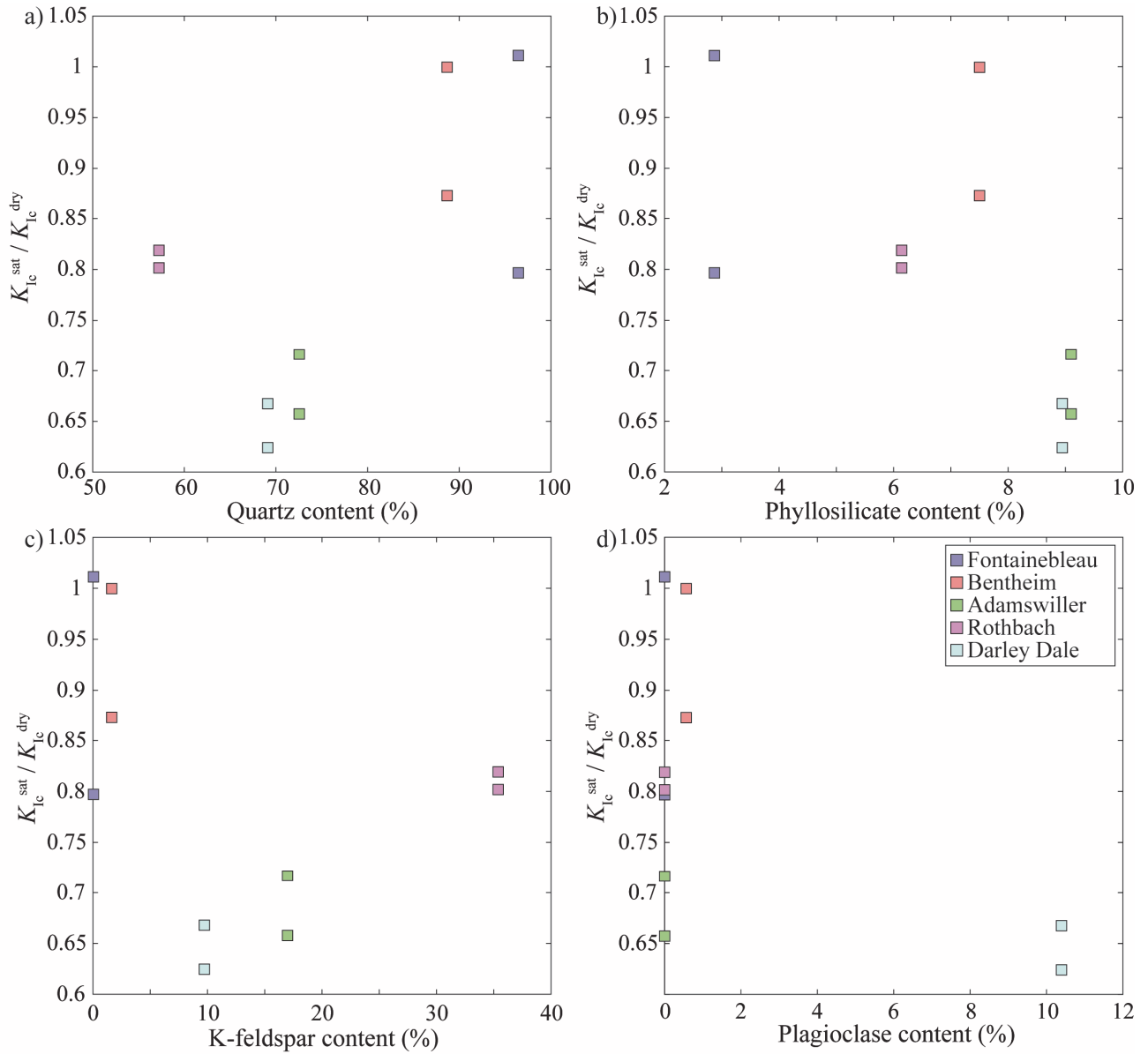


Figure 3. 10: Normalised fracture toughness (i.e., ratio between water-saturated K_{Ic} and the average dry K_{Ic}) as a function of the rock mineral content: a) quartz, b) phyllosilicates, c) K-feldspar and d) plagioclase.

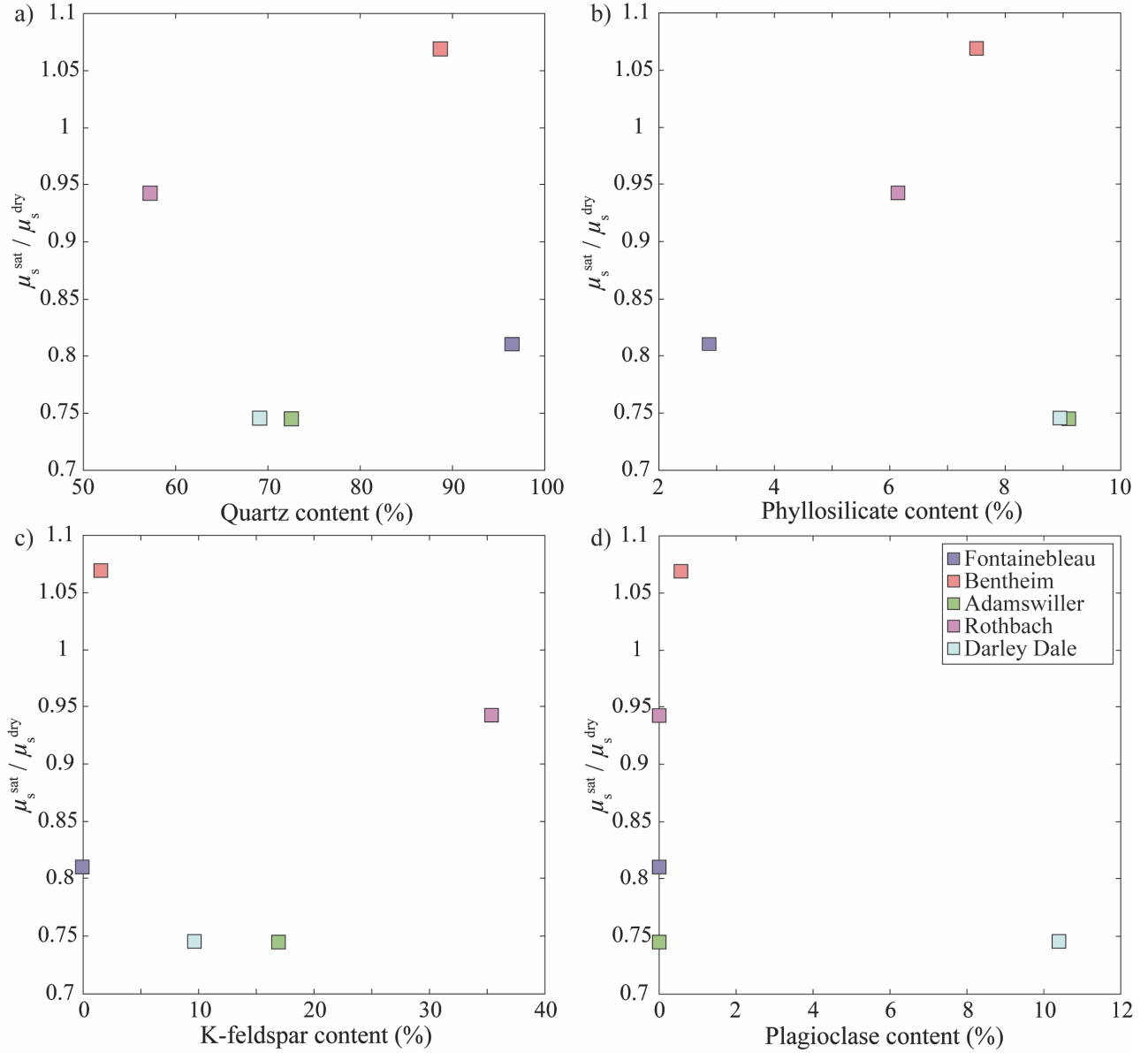


Figure 3. 11: Normalised static friction (i.e., ratio between water-saturated and dry μ_s) as a function of the rock mineral content: a) quartz, b) phyllosilicates, c) K-feldspar and d) plagioclase.

3.5.2 Micro-mechanical interpretation of water weakening under uniaxial compression

In this section, first, two micro-mechanical models are described: a pore emanating cracks model and a wing crack model. These models are then used to predict the water weakening of sandstones. Time-dependent effects (such as subcritical crack growth) are not considered in these models. Our experiments were performed at high loading rates, limiting such mechanisms.

The pore emanating cracks and a wing crack models were chosen because they are widely used in the geo-mechanical community and because they represent the two extreme cases of crack nucleation and damage growth initiated from geometrical defects (Ashby & Sammis, 1990), which we believe are relevant for sandstones.

3.5.2.1 Description of micro-mechanical models

The pore emanating cracks model was developed by Sammis & Ashby (1986). It considers an isotropic elastic medium of initial porosity ϕ made of spherical pores of radius a_{pore} , submitted to axial stress (σ_{ax}). While the axial stress is increased, stress concentrations occur at the poles of the pores with tensile stress oriented perpendicular to σ_{ax} . A pair of cracks of length l emanating from each pore is subjected to mode I stress intensity factor K_{I} . Cracks grow when the stress intensity factor reaches a critical value (i.e., the fracture toughness) K_{Ic} . With the crack length increasing, the cracks start to interact, facilitating their propagation. Under uniaxial compression, the crack's length as a function of the remote stress applied is given by (Sammis & Ashby, 1986):

$$\sigma_{\text{ax}}(l) = \frac{K_{\text{Ic}}}{\sqrt{\pi a_{\text{pore}}}} \frac{1}{\left(\frac{1.1 \sqrt{\frac{l}{a_{\text{pore}}}}}{\left(1 + \frac{l}{a_{\text{pore}}}\right)} + \frac{\sqrt{2}}{\pi} \sqrt{\phi} \sqrt{\frac{l}{a_{\text{pore}}} + 1} \right)} \quad \text{Equation (3.4.1)}$$

Equation 3.4.1 has a maximum value of σ_{ax} corresponding to the UCS of the rock sample. Note that the analytical solution of this model can be found in Baud et al. (2014). Considering that dry and water-saturated rock samples have the same initial porosity (ϕ) and pore radius (a_{pore}), the pore emanating cracks model predicts that the ratio of the UCS for saturated and dry rock samples is simply the ratio of the fracture toughnesses under saturated and dry conditions:

$$\frac{\text{UCS}^{\text{sat}}}{\text{UCS}^{\text{dry}}} = \frac{K_{\text{Ic}}^{\text{sat}}}{K_{\text{Ic}}^{\text{dry}}} \quad \text{Equation (3.4.2)}$$

Where the subscripts sat and dry stand for the water-saturated and dry parameters, respectively.

The wing crack model was developed by Ashby & Sammis (1990). It considers an isotropic elastic medium containing uniformly-spaced penny-shaped cracks of half-length a_{crack} oriented at an angle θ from σ_{ax} . When the axial stress is increased, a shear stress τ and a normal stress σ_n are transmitted to the inclined cracks. When the shear stress overcomes the frictional strength of the cracks' surfaces (i.e. when $\tau > \mu_s \sigma_n$), the cracks start to slide. This sliding generates tensile stresses at the tips of the inclined cracks. If the resolved stress intensity, K_{I} , at the inclined crack tips overcomes the fracture toughness K_{Ic} of the material, wing cracks nucleate. Under uniaxial conditions, the initiation of the wing cracks occurs on the most favourably oriented cracks at (Ashby & Hallam, 1986; Nemat-Nasser & Horii, 1982):

$$\sigma_{\text{C}'} = \frac{\sqrt{3}}{\sqrt{1 + \mu_s^2 - \mu_s}} \frac{K_{\text{Ic}}}{\sqrt{\pi a_{\text{crack}}}} \quad \text{Equation (3.5.1)}$$

Further increase of the axial stress causes the wing cracks to grow, resulting in their eventual interaction. Under uniaxial conditions, the remote uniaxial stress and the wing crack length are linked by (Ashby & Sammis, 1990):

$$\sigma_{\text{ax}}(l) = \frac{K_{\text{Ic}}}{\sqrt{\pi a_{\text{crack}} A_1 (c_1 + c_2)}} \quad \text{Equation (3.5.2)}$$

$$\text{with } A_1 = \pi \sqrt{\frac{\beta}{3}} (\sqrt{1 + \mu_s^2} - \mu_s) \quad \text{Equation (3.5.3)}$$

$$c_1 = \pi^{-2} \left(\frac{l}{a_{\text{crack}}} + \beta \right)^{-\frac{3}{2}} \quad \text{Equation (3.5.4)}$$

$$c_2 = \frac{2(\pi\alpha)^{-2} \sqrt{\frac{l}{a_{\text{crack}}}}}{D_0^{-\frac{2}{3}} - \left(1 + \frac{l}{\alpha a_{\text{crack}}}\right)^2} \quad \text{Equation (3.5.5)}$$

where $\alpha = \cos(\theta)$ is the projection of the inclined crack on the plane parallel to the axial stress, $D_0 = \frac{4}{3} \pi N_V (\alpha a)^3$ is the initial damage of the sample, $N_V = \rho_{\text{crack}} / a_{\text{crack}}^3$ is the number of cracks per unit volume (with ρ_{crack} being the initial crack density), and β is an empirical parameter to restrict K_I to finite values when l is small. Equation 3.5.1 has a maximum value of σ_{ax} , corresponding to the UCS of the rock sample. Note that an analytical solution of this model can be found in Baud et al. (2014). Considering that dry and water-saturated rock samples have the same initial crack radius (a_{crack}) and crack density (ρ_{crack}), the wing crack model predicts that the ratio between saturated and dry stresses at C' and the UCS are equivalent:

$$\frac{\text{UCS}^{\text{sat}}}{\text{UCS}^{\text{dry}}} = \frac{K_{\text{Ic}}^{\text{sat}} / A_1^{\text{sat}}}{K_{\text{Ic}}^{\text{dry}} / A_1^{\text{dry}}} = \frac{K_{\text{Ic}}^{\text{sat}} / \left(\sqrt{1 + (\mu_s^{\text{sat}})^2} - \mu_s^{\text{sat}} \right)}{K_{\text{Ic}}^{\text{dry}} / \left(\sqrt{1 + (\mu_s^{\text{dry}})^2} - \mu_s^{\text{dry}} \right)} = \frac{\sigma_{\text{C}'}^{\text{sat}}}{\sigma_{\text{C}'}^{\text{dry}}} \quad \text{Equation (3.5.6)}$$

To summarize, taking the ratio between the UCSs performed under water-saturated and dry conditions (i.e., $\text{UCS}^{\text{sat}}/\text{UCS}^{\text{dry}}$) as a proxy for water weakening effect, one can notice that while the pore emanating cracks model predicts only a fracture toughness dependency, the wing crack model predicts both that the fracture toughness and the static friction influence the water weakening of the rock strength.

3.5.2.2 Water weakening: experimental data and models prediction

Inserting the measured fracture toughness (K_{Ic}) and static friction (μ_s) under dry and water-saturated conditions, we now compare the predictions of the effect of water on sandstone's UCS and axial stress at C' from the pore emanating cracks model and the wing crack model (i.e., equations 3.4.2 and 3.5.6, respectively), and the UCS and C' obtained through experimental testing (Figure 3. 12).

As predicted by the wing crack model (equation 5.6), the experimental water weakening of the axial stress at C' and the UCS are of similar magnitude for the majority of the tested sandstones. Additionally, both models predict a water weakening effect on the UCS of the tested sandstones. The models are in good agreement with some experimental data. In particular, the pore emanating cracks model accurately predicts the water weakening at the UCS for DS, and both models accurately predict the weakening of FS and BS. However, in the majority of cases, both models overestimate (by about 10 to 20%) the water weakening of the tested sandstones.

The systematic overestimations of the water weakening effect might arise from 3 possible causes:

- 1) The use of macroscopically (centimetre scale) measured K_{Ic} and μ_s while the micro-mechanical models require micro-scale mechanical parameters. In sandstones, fractures can propagate at both the grain junction and within the minerals. In our experiments (paragraph 3.4.2), characterization of the post-mortem samples revealed that fractures mostly propagate at grain junctions, with K_{Ic} values of 1.60, 0.55, 0.49, 0.81 and 0.79 MPa.m^{1/2} under dry conditions and 1.45, 0.52, 0.33, 0.65 and 0.51 MPa.m^{1/2} under water-saturated conditions for FS, BS, AS, RS and DS, respectively. These values are lower than those of the sandstones' constituted materials. Indeed, quartz, orthoclase (i.e., K-feldspar) and albite (i.e., Na-plagioclase), have K_{Ic} values of 1.5 ± 0.3 , 1.1 ± 0.4 and 0.78 ± 0.06 MPa.m^{1/2}, respectively (Dal Bó et al., 2013; Whitney et al., 2007). Therefore, if during uniaxial compression of sandstones, cracks do not only propagate at the grain junction but also within the grains, higher values than the those obtained with CCNBD samples must be used. Additionally, μ_s was also not measured at the micro-scale. Indeed, in the preformed friction experiments we tested the resistance to motion of surfaces composed of many grains. In the wing crack model, the friction that needs to be overcome to induce a stress intensity factor at the crack tip is the friction of the inclined cracks. In the case of sandstones, the inclined cracks are grain contacts with very variable roughnesses due to the grain shapes and/or interlocking, which can lead to a higher value of the micro-scale static friction compared to the macro-scale one. Importantly, water's effect at microscale can differ from the one at macroscale. Further, the use of macroscopically measured K_{Ic} and μ_s , while the micro-mechanical models require micro-scale mechanical parameters, should strongly affect the absolute values of K_{Ic} and μ_s , albeit the ratio between dry and water-saturated measurements are probably affected much less.
- 2) The micro-mechanical models are, as all models, oversimplifying the mechanisms at hand. Even if our tests were performed under room-pressure conditions, water-saturated experiments can be affected by drainage conditions during fast crack propagation. However, considering the high porosity/permeability of the tested sandstones, undrained conditions are quite unlikely.

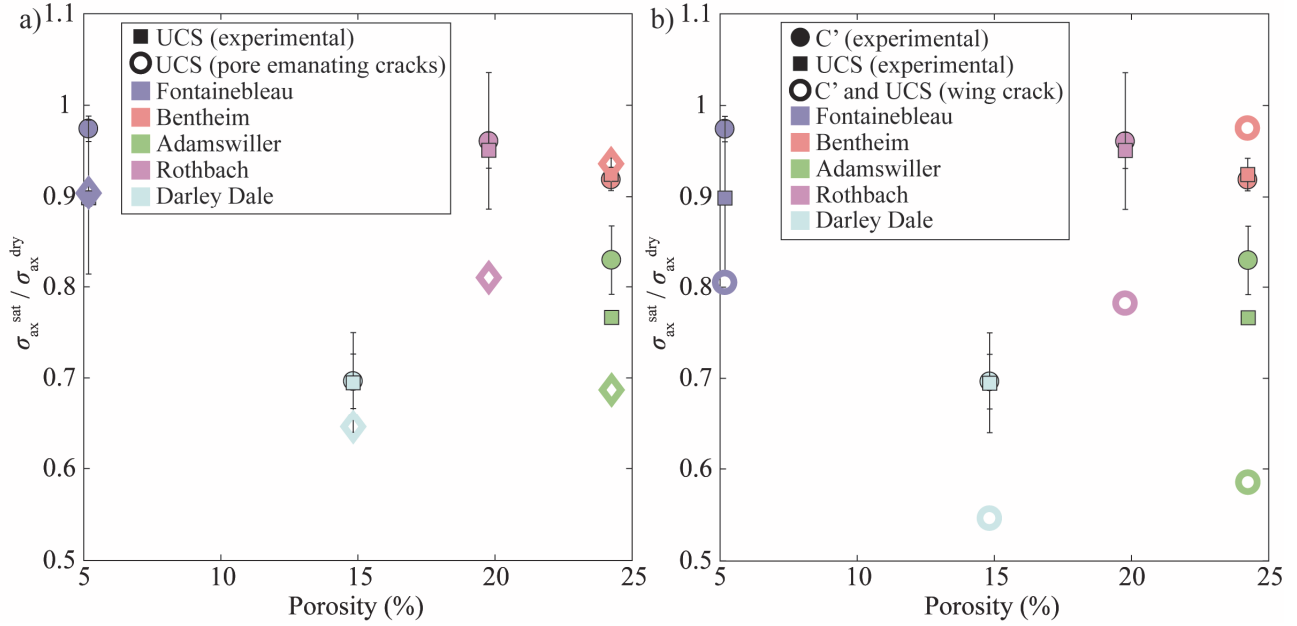


Figure 3. 12: The ratios of axial stress at C' (circles) and the uniaxial compressive strength (squares and diamonds) between water-saturated and dry experiments obtained experimentally (full symbols) and obtained via a) the pore emanating cracks model, and b) the wing crack model as a function of the sample porosity. The colour corresponds to the rock tested. Note that water weakening dependence in the pore emanating cracks model is present only in K_{Ic} (equation 3.4.2), while for the wing crack model it is present in both K_{Ic} and μ_s (equation 3.5.6).

3.5.2.3 Extrapolation to water weakening under triaxial conditions

Under triaxial conditions, no expressions of the pore emanating cracks model exist in the literature for conventional loading. Therefore, only the wing-crack model is discussed here. This model is highly used in the geo-mechanics community and in general allows for a satisfactory explanation of experimental data (see Ashby & Sammis (1990) section 4) and water weakening (see above section). The important variables to determine rock strength are: 1) the static friction of the cracks (μ_s), 2) the initial flow size (i.e., the initial half inclined crack length a_{crack}), 3) the mode I fracture toughness of the material (K_{Ic}), and 4) the initial damage (D_0). Usually, those parameters are found through a best fit of the experimental data. Trying to infer these parameters is not trivial. Even if several authors have shown that K_{Ic} is a pressure dependent parameter, with higher values at higher confining pressures (e.g., Abou-Sayed et al., 1978; Al-Shayea et al., 2000; Balme et al., 2004; Funatsu et al., 2004; Gehne et al., 2020; Minami Kataoka et al., 2017; Schmidt & Huddle, 1977; Stoeckhert et al., 2016; Thallak et al., 1993; Vásárhelyi, 1997), the experiments performed here resulted in consistent values of K_{Ic} and μ_s (see paragraph 3.5.2.2 for a discussion on the use of obtained parameters into micro-mechanical models). However, trying to infer a_{crack} and D_0 physically is challenging, particularly for sedimentary rocks, when crack length and number of cracks are hardly assessable. In order to understand how these four parameters influence the prediction of sandstone strength, a parametric study was performed. We compared the strength of Darley Dale sandstone, under dry and water-saturated conditions, predicted by the wing crack model under triaxial conditions (see Ashby & Sammis (1990) for a description of the model under triaxial stress) and obtained experimentally (UCS from this study and triaxial strength from Baud et al. (2000)) (Figure 3. 13). DS was chosen as it presents the highest water weakening of the tested samples. In each panel of Figure 3. 13, one parameter is taken as a variable while reference values are used for the 3

others, i.e., $K_{Ic} = 0.785 \text{ MPa}\cdot\text{m}^{1/2}$ (measured for dry Darley Dale), $\mu_s = 0.8036$ (measured for dry Darley Dale), $a_{\text{crack}} = 110 \text{ }\mu\text{m}$ (= half of the average grain size measured via an optical microscopic survey), and $D_0 = 0.44$ (from Baud et al. (2000) for dry Darley Dale sandstone). This parametric study demonstrates that the four parameters have a huge impact on the modeled strength. For example, for the reference parameters taken, changing D_0 from 0.1 to 0.7, a_{crack} from 100 to 1000 μm , K_{Ic} from 0.1 to 1.9 $\text{MPa}\cdot\text{m}^{1/2}$, or μ_s from 0.2 to 1, multiplies the modeled UCS by 2.5, 3.1, 19, and 2, respectively. Additionally, it shows that D_0 and μ_s are controlling the dependency on the effective confining pressure ($P_c - P_f$), i.e., the slope of the predicted strength as a function of the effective confining pressure (Figure 3. 13a and d); and a_{crack} and K_{Ic} are controlling the y-intercept, i.e., changing a_{crack} or K_{Ic} moves the curve to a parallel prediction in the strength – effective confining pressure diagram (Figure 3. 13b and c). Allowing the four parameters free to fit the data leads to many possible outcomes which explain the experimental data. Note however, that for dry conditions, using K_{Ic} and μ_s measured in this study coupled with D_0 estimated by Baud et al. (2000) (i.e., 0.44), provides an excellent strength prediction for samples where $500 < a_{\text{crack}} < 800 \text{ }\mu\text{m}$ (values close to the linear extent of the grain junction observed under an optical microscope (Figure 3. 1)). For water-saturated conditions, using K_{Ic} and μ_s measured in this study, the model provides a satisfactory strength prediction for $a_{\text{crack}} = 500 \text{ }\mu\text{m}$ and $D_0 = 0.25$. Additionally, C' and the strength predicted by the wing crack model hold for other sandstones (e.g., Baud et al., 2000, 2014).

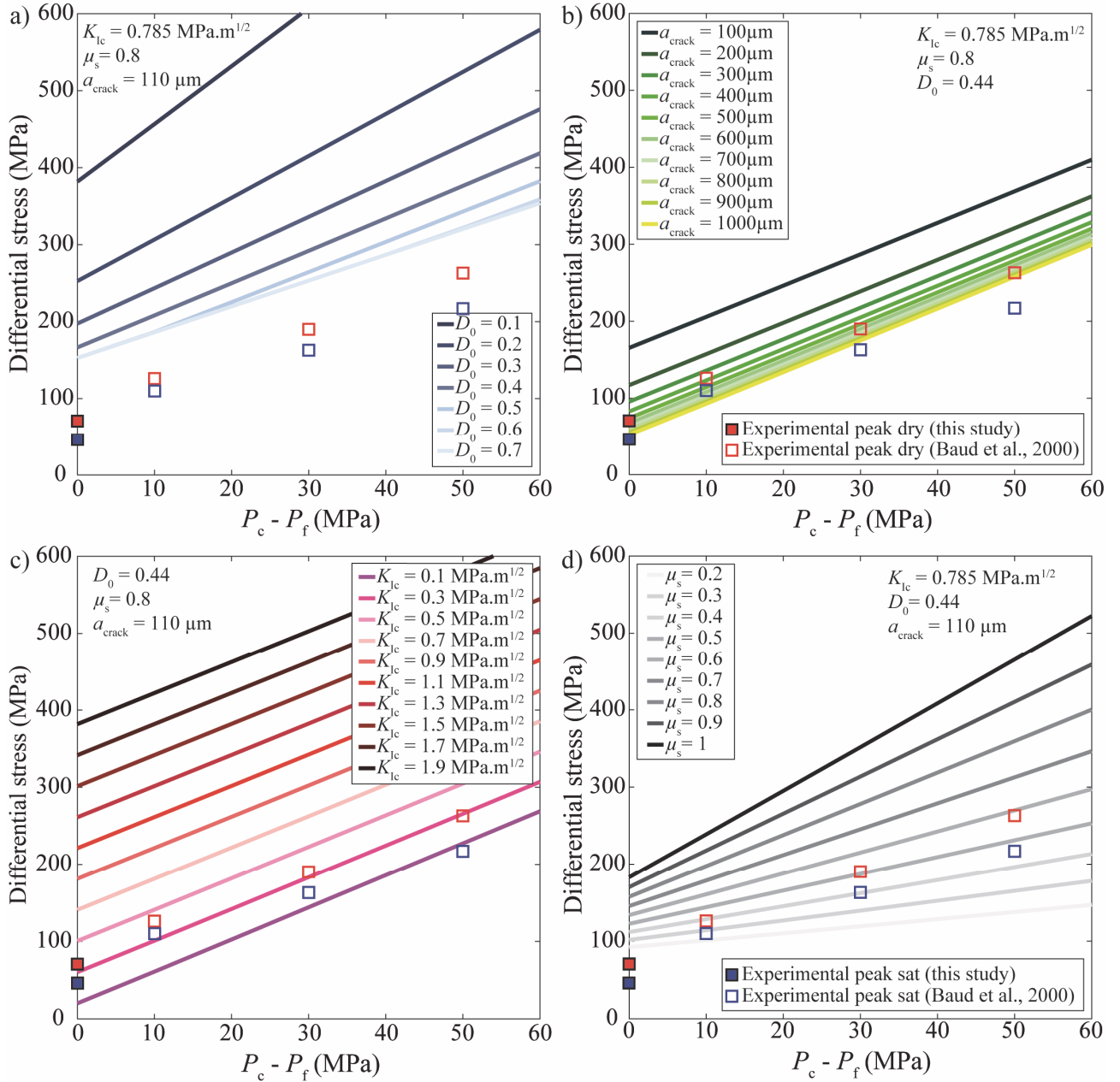


Figure 3. 13: Parametric study of the influence of a) the initial damage, b) the initial flow size, c) the mode I fracture toughness, and d) the static friction triaxial strength predicted by the wing crack model for dry and water-saturated (sat) Darley Dale sandstone. For reference, the UCS measured here and triaxial strength measured by Baud et al. (2000) are plotted. The reference parameters used (when they are fixed) are: $K_{lc} = 0.785 \text{ MPa.m}^{1/2}$ (measured for dry Darley Dale), $\mu_s = 0.8$ (measured for dry Darley Dale), $a_{crack} = 110 \text{ }\mu\text{m}$ (= half of the average grain size measured via an optical microscopic survey), and $D_0 = 0.44$ (from Baud et al. (2000) for dry Darley Dale sandstone). For all, θ (crack angle compared to the direction of compression) is taken to be 30° .

3.6 Conclusions

More than 50 destructive (uniaxial compression, fracture toughness and friction) experiments, complemented by more than 100 non-destructive (porosity and ultra-sonic) measurements have been used to better understand the effect of the presence of fluid on the short-term strength of five sandstones. The samples' UCSs and fracture toughnesses are directly linked to the measured initial porosities. Additionally, water saturation (compare to a dry sample) causes a reduction of i) the fracture toughness and fracture energy by 6 to 35 % and 21 to 52 %, respectively; ii) the static fric-

tion by 0 to 19 %, explaining the reduction of the UCS and onset of dilatancy by 0 to 30 %. The mechanisms of the water weakening on the sandstones' compressive strengths are directly linked to the reduction of the fracture toughnesses (or equivalently of the fracture energies) and to the static frictions of the materials. However, the mechanisms involved in the water weakening of the fracture toughnesses and static frictions are complex and future experimental investigations are needed to better constrain the processes at hand.

The introduction of the experimentally-measured fracture toughnesses and static frictions into micro-mechanical models (the pore emanating cracks model and wing crack model) has been used to predict the water weakening of the sandstones' uniaxial compressive strengths. It has been shown that the models predict the water weakening relatively well, with a general slight overestimation (10 to 20%). Finally, a parametric analysis was performed on the wing crack model, revealing that a sandstone's absolute strength can be estimated by means of physical and mechanical parameter measurements.

Chapter 4 Time-dependent deformations of sandstone during pore fluid pressure oscillations: Implications for natural and induced seismicity

Authors: Corentin Noël¹, Lucas X. Pimienta¹, Marie Violay¹

¹ Laboratory of Experimental Rock Mechanics, Ecole Polytechnique Fédérale de Lausanne, Lausanne, Switzerland

Status: Published in the Journal of Geophysical Research: Solid Earth. The article also appears in the special issue: Physical Properties of Rocks, Friction and Fracturing: the Walsh Volume

Reference: Noël, C., Pimienta, L., & Violay, M. (2019). Time-dependent deformations of sandstone during pore fluid pressure oscillations: Implications for natural and induced seismicity. Journal of Geophysical Research: Solid Earth, 124(1), 801-821. <https://doi.org/10.1029/2018JB016546>

Contributions: C. Noël prepared and characterized the sample. C. Noël has run the experiments. All the authors have participated to the experimental strategy. C. Noël has carried out the data treatment. All the authors have contributed to the data analysis. C. Noël has written the manuscript. All the authors have contributed to guide the discussion of the manuscript. M. Violay has acted as a supervisor.

Highlights:

- Laboratory investigation of the effect of pore fluid pressure oscillations on the creep behaviour of Fontainebleau sandstone
- At low oscillating periods, the amplitude does not affect the strength and deformation rate but these change dramatically at larger periods
- Acoustic emissions and dilation rates strongly depend on pore fluid pressure oscillations, but dilatancy at failure is constant

4.1 Abstract

In tectonically active regions, natural seismicity is often correlated with the seasonal hydrology, suggesting that cyclic loading variations might trigger seismicity. Moreover, recent field observations suggest that cyclic fluid injection strategies into geological reservoirs could produce less seismicity than monotonic injections. Here we present 10 brittle creep laboratory triaxial experiments that bring new constraints on fluid-rock interactions during cyclic pore fluid variations. The experiments were performed on Fontainebleau sandstone with various pore fluid pressure conditions: (i) with constant pore fluid pressure levels from 1 to 10 MPa, at constant Terzaghi effective pressure ($P_c - P_f = 30$ MPa); and (ii) with cyclic (sinusoidal) pore fluid pressure oscillations of varying amplitudes (from 0 to 8 MPa) and periods (from 30 to 3000 s) around a mean value of 5 MPa. During deformation, the rock's mechanical properties and the high-frequency acoustic emission signals were monitored to investigate the physics underlying the rupture processes. Under macroscopically drained conditions, rather than their amplitude, the period of the oscillations appeared to strongly affect the rock sample strength, time-to-failure, and dilatancy behaviour. Moreover, even for small variations of pore fluid amplitude, and at all pore fluid pressure period, pore fluid pressure and acoustic emissions were strongly correlated. Our experiments demonstrate that pore fluid pressure oscillations may strongly affect rocks mechanical behaviour and associated seismic activity.

Keywords: fluid-rock interaction, creep, fluid pressure oscillation, seasonal seismicity, induced seismicity, triaxial experiment

4.2 Introduction

Rock masses are porous media with internal pore networks and multiscale discontinuities often filled by pressurized fluids. The presence of fluid affects the mechanical behaviour of the rock mass through chemical and mechanical interactions (e.g., Handin et al., 1963; Robinson, 1959). Pore fluid pressure decreases the *in situ* effective stresses, lowering the rock strength and bringing the rock mass closer to failure conditions. Fluids also promote rock-fluid interactions that enhance subcritical crack growth and/or rock alteration (Anderson & Grew, 1977; Atkinson, 1984; Brantut et al., 2013). These rock-fluid interaction phenomena are strongly time-dependent and may result in rock weakening.

Over the past decade, brittle time-dependent deformation has been the subject of a number of experimental and theoretical studies (Baud & Meredith, 1997; Brantut et al., 2014; Carter & Kirby, 1978; Heap et al., 2009b; Lockner, 1993; Mallet et al., 2015; Scholz, 1968; see Brantut et al., 2013 for a review). They show that crack nucleation, growth, and coalescence can occur at stresses below the short-term peak strength, a phenomenon known as subcritical crack growth (Atkinson, 1984; Olsson, 1974). In turn, the subcritical crack growth velocity is controlled by two main mechanisms: (1) the stress intensity at the crack tip; and (2) the stress corrosion at the crack tip, which is important in silica bearing materials (Freiman, 1984; Michalske & Freiman, 1983). A method to study this phenomenon is to perform uniaxial or triaxial experiments where a constant stress (below the rock strength) is applied to a rock sample until failure. Such experiments are called static fatigue tests and are also commonly referred as brittle creep tests. While stresses are maintained constant, the sample strain rate first decreases with time down to a minimum and then increases until macro-

scopic failure (Figure 4. 1). The minimum strain rate experienced by the rock increases, that is, the time-to-failure decreases, when the (1) axial stress (σ_{ax}) increases (Baud & Meredith, 1997), (2) temperature increases (Heap 2009a), and (3) effective confining pressure decreases (Lockner, 1998; Ngwenya et al., 2001). Varying pore fluid pressure level, while keeping effective pressure constant, seems to not influence the deformation rates (Heap et al., 2009b).

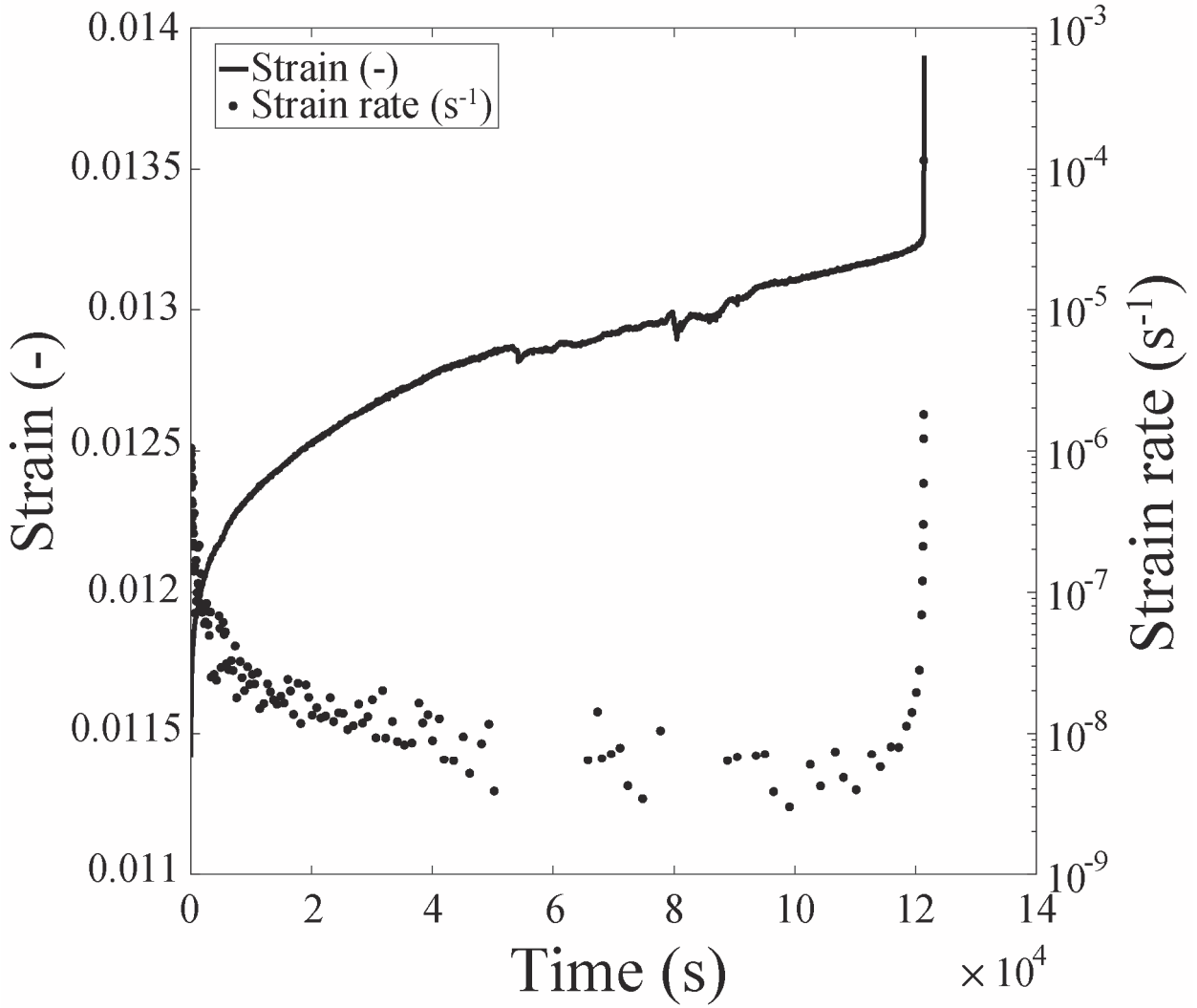


Figure 4. 1 Typical strain (solid curve) and strain rate (dots) as functions of time during a constant stress phase of a brittle creep experiment. Here the curves show a Fontainebleau sandstone deformed at 581-MPa axial stress, 35-MPa confining pressure, and 5-MPa pore fluid pressure.

However, if the rock mass is subjected to repeated pore fluid pressure variations, a dynamic fatigue induced by pore fluid pressure variations might occur (in addition to that of a rock mass subjected to constant pore fluid pressure). This phenomenon is hereafter referred to as hydraulic fatigue. Pore fluid pressure variations can be due to natural or anthropogenic causes such as oceanic tides (e.g., Wang & Davis, 1996), seasonal hydrology (e.g., Bettinelli et al., 2008), build ups in volcanic edifices (e.g., Farquharson et al., 2016), or geo-engineering purposes such as geothermal energy or carbon sequestration (e.g., Verdon et al., 2013), and might depend on the drainage conditions of the crust. In tectonically active regions, recent studies demonstrated that strain as well as part of the seismicity is modulated by natural fluid loading variations. This can originate from

changes in stress field conditions and/or loading rate variation (e.g., Bettinelli et al., 2008; Chanard et al., 2018; Craig et al., 2017; Johnson et al., 2017). Moreover, recent numerical studies on reservoir mechanical behaviour showed that, for a given *in situ* pore fluid pressure, different injection strategies result in different seismic responses of the reservoir. Indeed, cyclic fluid injection seems to trigger less induced seismicity compared to a monotonic injection strategy (Yoon et al., 2014; Zang et al., 2013). Particularly, the number of events and the maximum event magnitude are reduced (Zang et al., 2018). The present study of hydraulic fatigue phenomena on long-term rock behaviour aims to investigate the mechanisms governing the deformations under cyclic pore fluid pressure variations.

While dynamic fatigue phenomena have been subjected to many studies, little has been done on hydraulic fatigue. Indeed, most of the dynamic fatigue studies investigated the mechanical response of a dry rock sample submitted to a cyclic (often axial) loading of constant amplitude and mean stress value (Cerfontaine & Collin, 2017). The principal characteristics of mechanical fatigue tests performed under dry conditions are (1) strength reduction of the rock samples (e.g., Royer-Carfagni & Salvatore, 2000) as compared to short-term strength; (2) residual and permanent deformations accumulated cycle after cycle; and (3) variation of the residual strain accumulated after cycles during experiment, with the first and last cycles before rupture having the highest strain accumulation (e.g., Liu & He, 2012).

Only rare experimental studies investigate hydraulic fatigue processes during long-term experiments (Chanard et al., 2015; Chanard, 2015; Farquharson et al., 2016; Zhuang et al., 2016) and show contradictory results: In sandstone samples, the maximum recorded number of acoustic emissions (AEs) was shown to be inversely correlated with the pore fluid pressure oscillations (i.e., a maximum number of emissions while the pore fluid pressure is at the lowest level) (Chanard et al., 2015; Chanard, 2015). In andesites, however, the opposite behaviour was observed (Farquharson et al., 2016). In this paper, we report new results on laboratory brittle creep triaxial deformation tests performed on Fontainebleau sandstone (FS). In particular, we focus on the effect of pore fluid pressure level and pore fluid pressure cyclic variations.

4.3 Experimental methodology

4.3.1 Starting sample

FS (South of Paris, France) is an early Oligocene quartz arenite (Haddad et al., 2006). It is made of almost 100% randomly oriented quartz grains cemented by quartz cement. FS spans a large range of porosity and permeability values depending on the sample's degree of cementation (Bourbié & Zinszner, 1985; David et al., 1994; Duda & Renner, 2013; Song & Renner, 2008). The rock was chosen because it is homogeneous and isotropic at the scale of the block, so that samples from the same block have reproducible transport (e.g., Fredrich et al., 1993), poroelastic (Fabre & Gustkiewicz, 1997; Sulem & Ouffroukh, 2006), and mechanical (Bied et al., 2002; Haied & Kondo, 1997; Reviron et al., 2009; Schubnel et al., 2007) properties.

Cores of FS were diamond drilled from a unique block to a diameter of 36 mm. Cylinders were then sawed and the opposite faces grounded flat in order to prevent any parallelism defect (± 100 -

μm precision) for a final length of 72 mm. All these preparation processes were done using tap water as a cooling fluid. The sample cylinders were then used for physical characterization and triaxial tests.

Before triaxial testing, samples were characterized in terms of microscope imaging, porosity, permeability, and ultrasonic P-wave velocity to ensure sample reproducibility.

An optical microscopic survey confirmed that FS is a pure quartz sandstone (>99.9% quartz), composed of 200- to 300- μm grains cemented together by quartz cement (Figure 4. 2a). It presents large quasi-spherical pores (20 – 100 μm) at the junction between grains (Figure 4. 2a and b). Some cracks with high aspect ratios ($\approx 10^{-3}$) are also present at the grain contact or within the quartz grains.

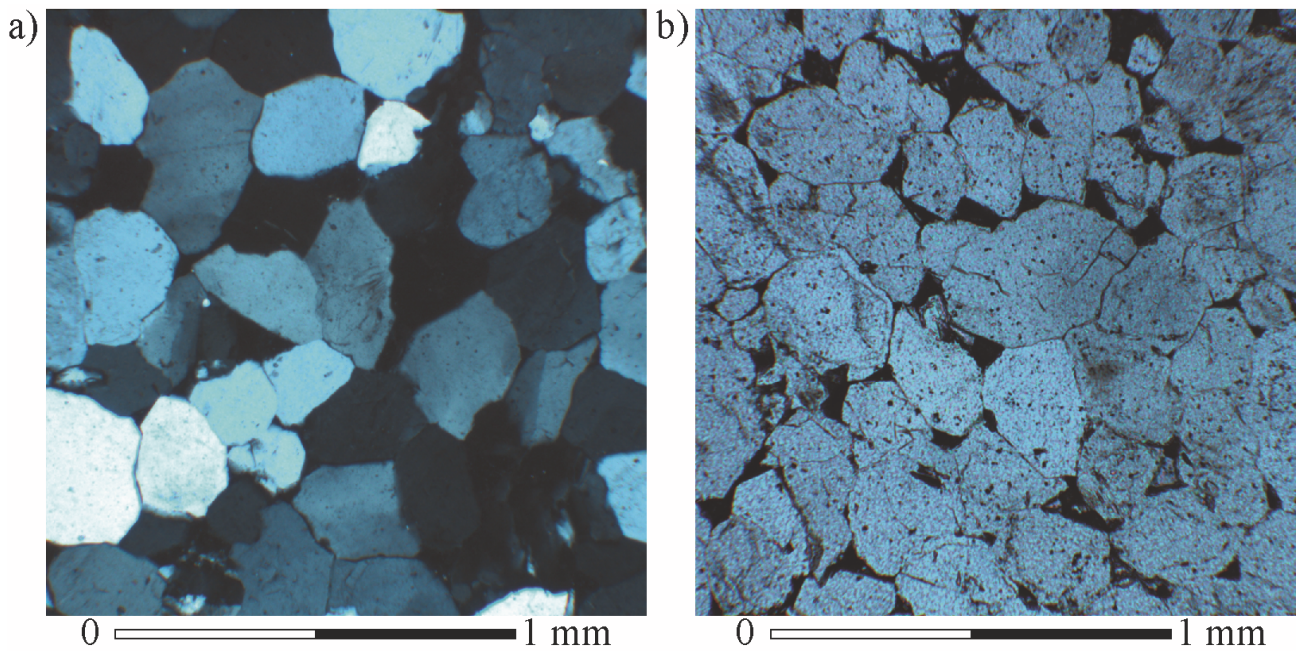


Figure 4. 2: Optical microscope images of the intact studied FS. (a) General cross-polarized light view and (b) general plan polarized light view, a physical blue filter was inserted in the microscope head such that pores appear in dark.

Porosity was measured using three different methods: (i) helium pycnometer (*Gas Pycnometer Accupyc II 1340*) using Boyle's law (Boyle, 1662); (ii) triple weight method using Archimedes' principle (see Guéguen & Palciauskas, 1994); and (iii) from the dry sample density, assuming it is composed of 100% of quartz. Samples from the chosen block of FS had a measured porosity of $6.8 \pm 0.3\%$. Very similar values using helium pycnometer, triple weight, and the density methods were found, that is, 7.0 ± 0.4 , 6.8 ± 0.3 , and $6.6 \pm 0.4\%$ respectively. The small differences may originate from the accuracy of the bulk volume measurements. Since the density method gave similar results to the two other methods, the porosity can be consistently considered as mainly connected.

Permeability was measured on an intact sample using the steady state Darcy flow method (i.e., by imposing a constant pore fluid pressure difference between sample ends) at a Terzaghi effective pressure ($P_c - P_f$) comprised between 1 and 15 MPa. It showed a decrease from $6 \times 10^{-16} \text{ m}^2$ to $3 \times 10^{-16} \text{ m}^2$ between 1 and 7 MPa Terzaghi effective pressure, respectively. Beyond 7 MPa, permeability remained quasi-constant, which is expected to correspond to the closure of the interconnected crack

network (Bernabe, 1987; Brace, 1978a; Pimienta et al., 2017; Trimmer et al., 1980). Values found are consistent with earlier studies on FS samples of similar porosity (e.g., Bourbié & Zinszner, 1985). The characteristic time for water diffusion across the sample length l was calculated, as $t_d = \frac{l^2 \eta \beta}{k}$ (Fischer & Paterson, 1989), from the measured permeability k , the known fluid viscosity $\eta = 10^{-3}$ Pa.s, and storage capacity β values found in literature (Duda & Renner, 2013; Song & Renner, 2008). This characteristic diffusion time was found to be $t_d < 3$ s. The period of pore fluid pressure oscillation was chosen larger than this time, ensuring drained conditions during triaxial experiments.

Ultrasonic compressional (P-wave) velocity has been measured at room conditions using two P-wave piezoelectric transducers (*Olympus V103-RB*) placed on opposite faces of the samples. The electrical signal was delivered by a multi-frequency generator (*Aim TTI TG1010A*) and recorded with a numerical oscilloscope. Measurements were made at 1-MHz resonance frequency, at room pressure and temperature, using the method introduced by Birch (1960), that is, by handpicking the time of the wave's first arrival and calculating the velocity of the wave across the sample length l . The average ultrasonic P-wave velocity measured under ambient conditions was $V_p = 2022 \pm 185$ m/s.

4.3.2 Triaxial deformation

4.3.2.1 Apparatus

Triaxial deformations were performed in a Hoek cell (Figure 4. 3) placed under a uniaxial press (*Walter and Bai*). The system allowed an oil confining pressure (P_c) up to 70 MPa (± 50 -kPa resolution). The lower and upper end platens (Figure 4. 3c and 3h) were specifically chosen to allow for a maximum axial stress (σ_{ax}) of 1 GPa (± 100 -kPa resolution). The end platens allow for the distribution of pore fluid pressure homogeneously (Figure 4. 3b) and for the placement of piezoelectric transducers (Figure 4. 3a) in a cavity isolated from any stresses. Pore fluid pressure (P_f) was imposed with de-aired distilled water from a step motor pump, with 200-cm³ capacity and allowing pressures up to 30 MPa. The pore fluid pressure was measured at the top and the bottom of the sample (Figure 4. 3i) using precision pressure sensors (± 10 -kPa resolution). Pump fluid volume (V_f) variation was also monitored thanks to encoders directly mounted on the pump (± 1 -mm³ resolution). In addition, wideband (200 – 950 kHz) AE sensors were placed in each end platen to monitor the high-frequency AE events radiated from the samples during the tests. The emitted signal was amplified to 40 dB through preamplifiers. The trigger was set to only record events with an amplitude higher than 0.056 V, that is, ≈ 1.75 times higher than the background noise of the experimental setup (measured at 0.032 V) to prevent noise recording. Each event that fulfilled this condition was recorded at a 1-MHz sampling rate, in a window of 400 μ s. Axial displacements were measured using Linear Variable Differential Transformers mounted outside of the cell with a precision of 10 μ m.

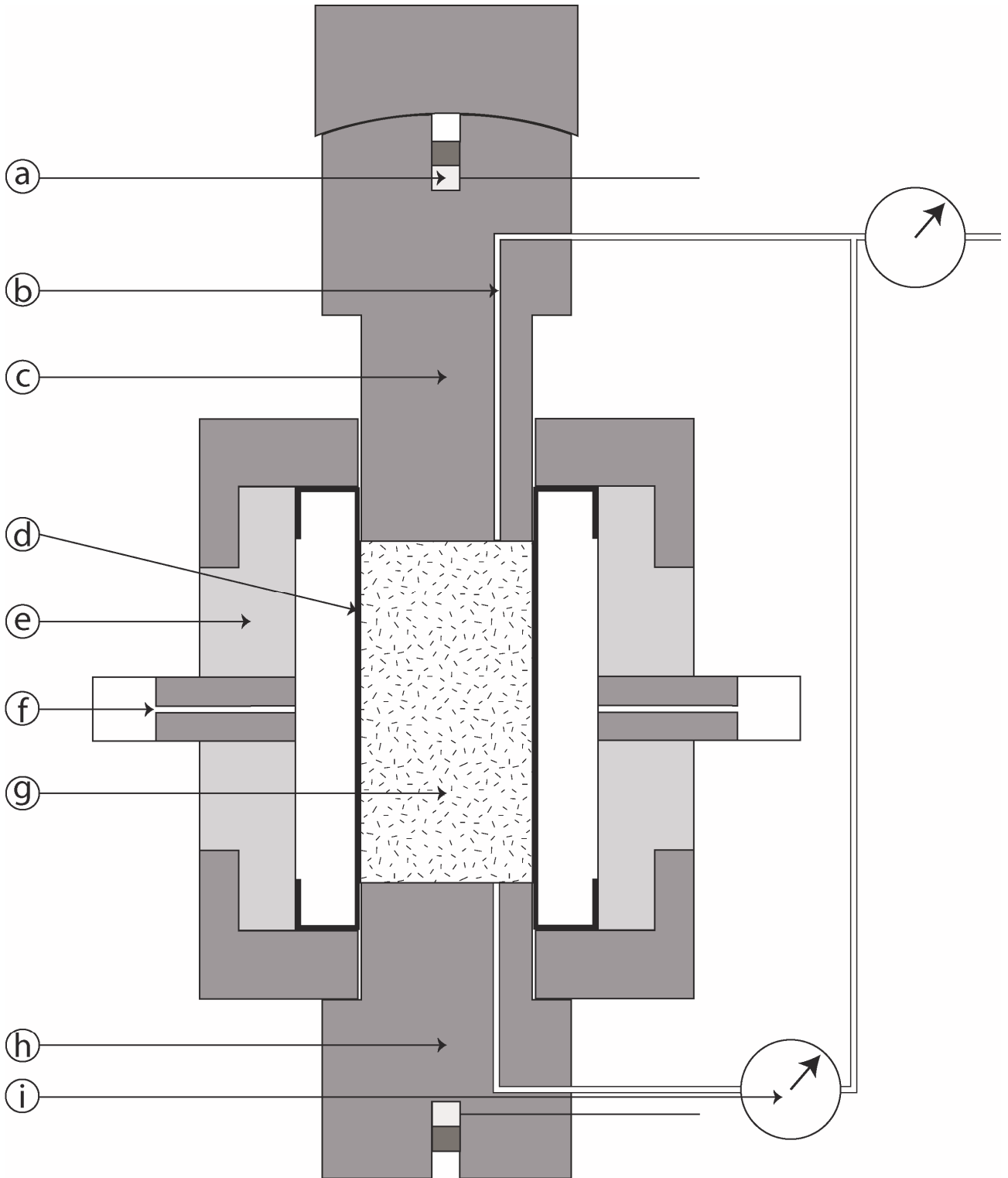


Figure 4. 3: Cross-section drawing of the Hoek cell used for triaxial experiments. (a) acoustic emission sensor, (b) pore fluid system, (c) upper end platen, (d) jacket, (e) confining cell, (f) confining oil inlet, (g) sample, (h) lower end platen, and (i) pressure sensor.

4.3.2.2 Constant displacement rate experiments

Constant displacement rate experiments, corresponding to a macroscopic axial strain rate of $\dot{\epsilon}_{ax} \approx 10^{-5} \text{s}^{-1}$, were performed to infer the short-term mechanical behaviour of the FS. Both dry and water-saturated experiments were performed. For dry experiments, samples were oven dried for 48 hr

at 106 °C. For water-saturated experiments, samples were first saturated under vacuum with de-aired distilled water at ambient pressure conditions and then placed directly into the Hoek cell. For these experiments, confining pressure (P_c) ranged between 0 and 55 MPa and pore fluid pressure from 0 (i.e., dry) to 15 MPa (Table 4. 1). First, confining pressure and axial stress were increased simultaneously (i.e., isostatic increase), and the pore fluid pressure was increased to the target value. Then, a constant axial displacement rate of 7.2×10^{-4} mm/s was imposed, and the resulting axial stress was recorded until the sample failure.

Table 4. 1: Constant Velocity Experiments ($\dot{\epsilon}_{ax} \approx 10^{-5} \text{ s}^{-1}$) Performed and Mechanical Data Obtained for the Studied Fontainebleau sandstone. For the experiments at $P_f = 0$ MPa (dry) the experiments were performed under dry condition (i.e., no water).

P_c (MPa)	P_f (MPa)	E (GPa)	Q at D' (MPa)	Q at C' (MPa)	Q_{peak} (MPa)
0	0 (dry)	51.9	-	-	155.1
15	5	52.7	132.7	51.0	366.0
25	15	54.7	143.2	55.15	357.7
25	5	55.0	232.8	104.4	474.6
35	15	61.2	228.9	125.3	504.9
35	5	55.8	346.0	108.0	566.4
45	15	62.5	250.5	138.2	627.2
45	5	56.0	403.2	156.6	700.6
40	0 (dry)	55.3	-	-	700.1
55	15	64.3	378.8	144.3	669.1

4.3.2.3 Constant stress experiments

Brittle creep behaviour was determined by performing conventional (i.e., constant stress) and stress-stepping creep tests. Samples were loaded, using the same method as for the constant displacement rate experiments, until a percentage of the short-term peak differential stress (Q_{peak}) was reached. Then, both confining pressure and axial stress were kept constant and the samples were allowed to deform over time. For the conventional experiments, the stresses (confining pressure and axial stress) were kept constant at 97% of the short-term rock strength until the sample failed. For the stress-stepping experiments, samples were first loaded to 80% of the short-term rock strength during 24 hours. Then, the axial stress was increased every 24 hours to 85, 90, 95, 97, 98% of the short-term strength until the sample failed within the time step interval. This stress step strategy (i.e., decreasing the stress step interval after 95% of the Q_{peak}) was used to increase the number of recorded data at high differential stress.

To investigate the effects of pore fluid pressure and cyclic variations on the long-term behaviour of FS, two sets of experiments were performed. The first set aimed to investigate the effect of pore fluid pressure level on brittle creep deformations of FS. To this end, we performed creep tests at constant pore fluid pressure, with various pore fluid pressure levels (from 1 to 10 MPa) but the same Terzaghi effective pressure ($P_c - P_f = 30$ MPa). The second set of experiments aimed to investigate the effect of repeated pore fluid pressure oscillations during long-term deformations of FS. To this end, we performed creep tests with cyclic (i.e., sinusoidal) pore fluid pressure oscillations. During the constant stress phases, the axial stress and the confining pressure were held constant, while

the pore fluid pressure was oscillating with a chosen peak-to-peak amplitude (A) and period (T). These cyclic pore fluid pressure experiments were all performed at the same constant confining pressure of $P_c = 35$ MPa and mean pore fluid pressure (i.e., average over one oscillation) $P_f^{\text{mean}} = 5$ MPa values. As only the pore fluid pressure was oscillating, both effective axial stress and effective confining pressure oscillations were induced. Pore fluid pressure oscillations were started only once the target axial stress was reached and the fluid was injected from both top and lower end platens. Oscillation periods from 30 to 3,000 s were chosen so that T was large enough for the sample to always be drained. Note that for stress stepping experiments, as axial stress was increased every 24 hours, each stress step had a different cumulative strain. However, they have the same number of pore fluid pressure oscillations allowing a comparison from one step to another. To investigate the amplitude effects of the fluid oscillations, experiments were performed with cyclic pore fluid pressure variations of $T = 30$ s and A ranging from 0 to 8 MPa (i.e., the effective confining pressure was varied up to $\approx 27\%$ for $A = 8$ MPa). The period of 30 s was chosen to maximize the number of pore fluid pressure oscillations during one experiment (i.e., 2880 per step). To investigate the period effects of the oscillations, experiments were performed with constant $A = 4$ MPa and T ranging from 30 to 3000 s. A listing of experiments is reported in Table 4. 2.

Table 4. 2: Summary of the experimental conditions for constant stress (creep) experiment performed on Fontainebleau sandstone.

Sample	P_c	Q	Pore fluid pressure			Minimum strain rate	Comment
			Mean	Amplitude	Period		
	(MPa)	(MPa)	(MPa)	(MPa)	(s)	(s ⁻¹)	
FFB8	35	547.70	5	-	-	4.73×10^{-9}	Failure
FFB11	35	445.80	5	-	-	1.42×10^{-9}	Failure
		475.79				1.61×10^{-9}	
		505.90				2.18×10^{-9}	
		535.93				2.83×10^{-9}	
		548.09				3.31×10^{-9}	
		553.99				5.95×10^{-9}	
FFB35	40	441.01	10	-	-	1.46×10^{-9}	Failure
		470.84				1.61×10^{-9}	
		500.85				2.38×10^{-9}	
		530.92				3.11×10^{-9}	
		542.81				8.17×10^{-9}	
		548.98				1.95×10^{-8}	
FFB14	31	449.78	1	-	-	1.13×10^{-9}	Failure
		479.47				2.07×10^{-9}	
		509.80				1.94×10^{-9}	
		540.14				3.51×10^{-9}	
		551.97				4.41×10^{-9}	
		558.09				6.37×10^{-9}	
FFH5	35	547.10	5	1	30	3.95×10^{-9}	Failure
FFB10	35	445.77	5	1	30	1.15×10^{-9}	Failure
		475.64				1.69×10^{-9}	
		505.82				1.57×10^{-9}	
		535.88				3.55×10^{-9}	
		548.04				3.91×10^{-9}	
		553.97				5.08×10^{-9}	
FFH12	35	559.89	5	4	30	1.03×10^{-8}	Failure
		445.96				1.35×10^{-9}	
		475.98				1.80×10^{-9}	
		505.88				1.91×10^{-9}	
		536.09				2.95×10^{-9}	
		547.86				3.23×10^{-9}	

		553.80				3.44×10^{-9}	
		559.86				1.53×10^{-8}	Failure
FFB13	35	445.70	5	8	30	1.89×10^{-9}	
		475.71				1.68×10^{-9}	
		505.89				2.30×10^{-9}	
		535.82				3.44×10^{-9}	
		547.02				5.33×10^{-9}	
		553.83				7.10×10^{-9}	Failure
FFB33	35	445.85	5	4	300	1.83×10^{-9}	
		475.98				1.91×10^{-9}	
		505.90				4.14×10^{-9}	
		536.06				1.75×10^{-7}	Failure
FFB32	35	445.89	5	4	3000	1.83×10^{-9}	
		475.89				2.24×10^{-9}	
		506.01				4.24×10^{-9}	
		536.06				3.49×10^{-8}	Failure

4.3.3 Data treatment and analysis

For constant displacement rate experiments, displacement measured from Linear Variable Differential Transformer sensors was corrected from elastic distortion of the apparatus column (i.e., press column and anvils), calibrated using a metal plug of known stiffness. For all triaxial tests, axial strain was then inferred from the corrected axial displacement over the sample length. Porosity change was calculated from the ratio between the injected pore fluid volume (V_f) and initial bulk volume of the sample.

For each creep experiment, and for each stress step, axial strain and AE events were recorded as a function of time. The minimum strain rate and AE rate were computed as the minimum derivative of the strain and cumulative number of AE events as a function of time, respectively. These rates reflect the sample sensitivity to the stress conditions (Brantut et al., 2013, 2014; Heap et al., 2015; Heap 2009b; Nicolas et al., 2017). Note that using a stress stepping method with time steps of 24 hours, minimum strain rates can be overestimated for low axial stresses, that is, when strains are small. However, the method deployed in this paper allows for the number of pore fluid pressure oscillations to be kept constant for each stress step, which facilitates the comparison from one step to another when aiming to understand pore fluid pressure's implication on deformation mechanisms.

When investigating the effect of pore fluid pressure oscillations, further data processing was attempted to correlate AE events and pore fluid pressure oscillations. For each stress step performed, AE events were split with time interval corresponding to the period of the pore fluid pressure oscillation as it was made by Chanard (2015). This allowed for the investigation of the distribution of

stacked AE events over a period of pore fluid pressure oscillation for each cyclic experiment and stress step.

4.4 Results

4.4.1 Constant displacement rate experiments

Mechanical data (Table 4. 1 and Figure 4. 4) from the constant displacement rate experiments were used to characterize the short-term behaviour of the rock. Samples first showed a linear increase in strain with differential stress until the onset on dilatancy, noted C' (Figure 4. 4a). This phase was accompanied by a decrease in porosity due to crack closure. After the elastic deformation, the sample deformed in a nonlinearly decreasing function with differential stress prior reaching a peak (Q_{peak}), corresponding to the sample strength (Figure 4. 4a and Figure 4. 4b). This phase was accompanied by a dilatant dominant behaviour, starting at D' (Figure 4. 4a), due to crack nucleation, growth, and coalescence. Before Q_{peak} was reached, and almost simultaneously after C', an increase in AE events was observed (Figure 4. 4c). Then, following Q_{peak} , the samples entered a strain-softening phase (i.e., stress drop). After this stress drop, a quasi-constant residual strength remained. The post-mortem analysis of the samples showed that the deformation was always localized along anastomosed shear fractures oriented at about 30° from σ_1 .

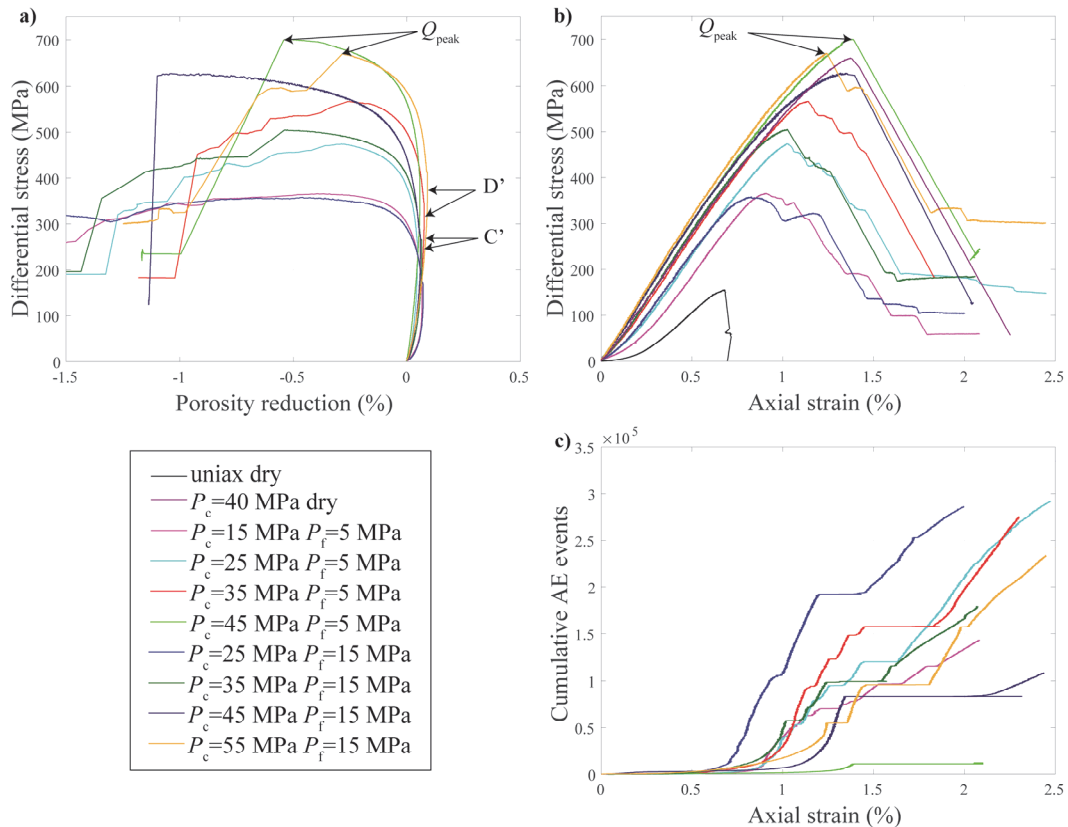


Figure 4. 4: Mechanical and AE events data of the FS tested with constant displacement rate experiments ($\dot{\epsilon}_{ax} \approx 10^{-5} \text{ s}^{-1}$). (a) Differential stress as function of the porosity reduction, (b) differential stress as function of the axial strain, (c) cumulative AE events as function of axial strain. For two experiments, Q_{peak} , D', and C' are shown. Note that the AE data were correlated with the mechanical data, having an increase in events before each stress drop. FS = Fontainebleau sandstone; AE = acoustic emission.

The final deformations and the mechanical curves were typical of the brittle regime. Therefore, the brittle failure envelope, applying Hoek and Brown criterion (Hoek & Brown, 1980), and damage envelopes, applying a linear regression, were computed from Q_{peak} and Q at D' values, respectively (Figure 4. 5). The Hoek and Brown criterion can be written as $Q = (m\sigma_{\text{UCS}}(P_c - P_f) + s\sigma_{\text{UCS}}^2)^{\frac{1}{2}}$, where m and s were found by best fit to be 72 and 0.94, respectively, and σ_{UCS} is the uniaxial compressive strength. The linear regression of the damage envelope is of type $Q = c(P_c - P_f) + d$, where $c = 7.4$ and $d = 70$ MPa. The experiments performed at similar $P_c - P_f$ but different pore fluid pressure conditions present similar strength. For example, for $P_c - P_f = 40$ MPa, $Q_{\text{peak}} = 700.1$, 700.6, and 669.1 MPa, respectively, for the dry, 5, and 15 MPa pore fluid pressure experiments. Therefore, for our experiments, we assumed that the Terzaghi effective pressure holds for FS at failure, that is, with an effective stress coefficient equal to 1.

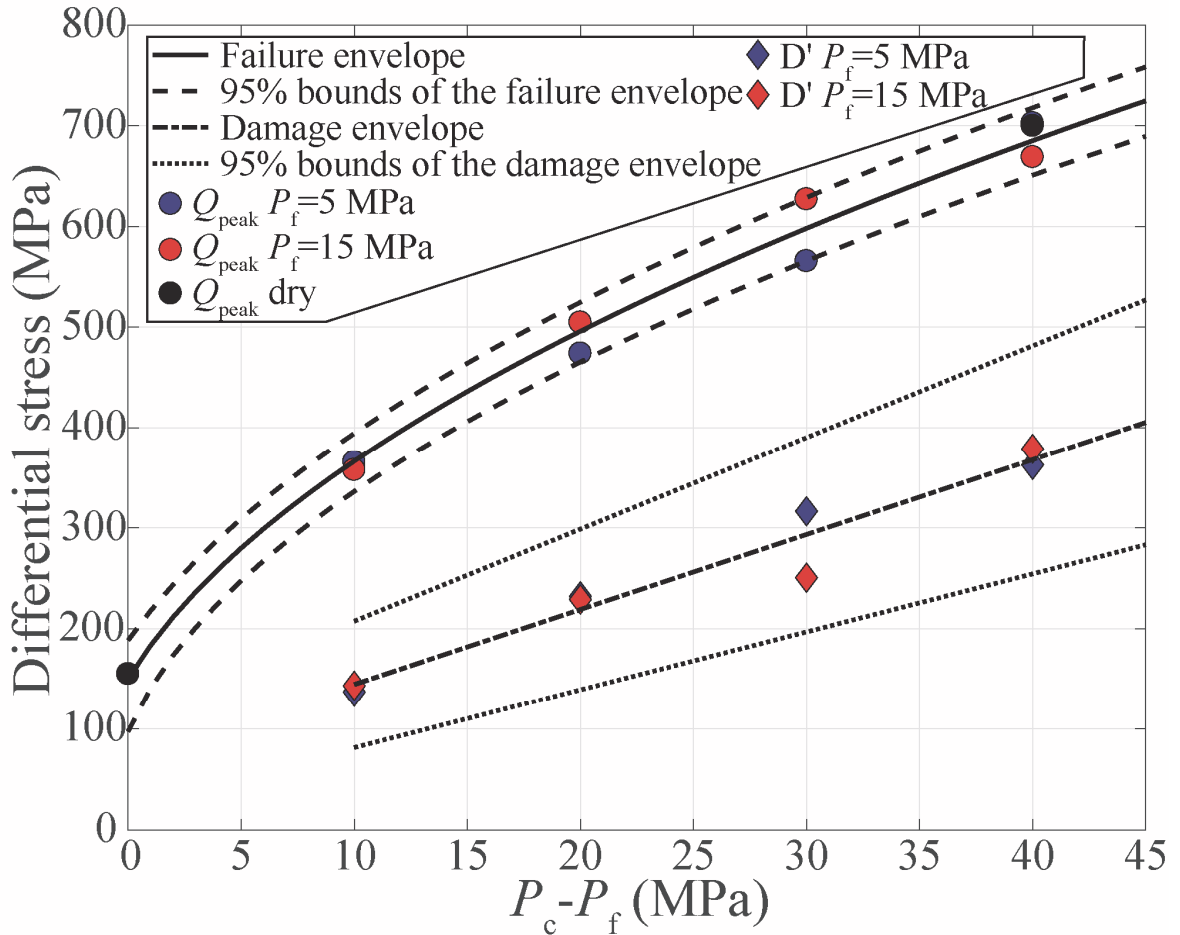


Figure 4. 5: Q_{peak} (circles) and the Q at D' (diamonds) of the tested FS at $\dot{\epsilon}_{ax} \approx 10^{-5} \text{ s}^{-1}$ plotted in a diagram of differential stress as function of Terzaghi effective pressure ($P_c - P_f$). The failure envelope (solid line) and damage envelopes (dash dotted lines) inferred from the Q_{peak} and the Q at D', respectively, are reported. Hoek and Brown parameters found are $m = 72$ and $s = 0.94$. The linear regression parameters for the damage envelope are $c = 7.4$ and $d = 70$ MPa. The dashed and dotted curves are the 95% confident bound of the envelopes. FS = Fontainebleau sandstone.

4.4.2 Creep experiments at constant pore fluid pressure

For the conventional constant stress experiments (Figure 4. 6a), strain and AE rates as function of time (Figure 4. 6b and c) present a typical deceleration phase toward a minimum value ($4.76 \times 10^{-9} \text{ s}^{-1}$ and 0.4 event/s, respectively), followed by an abrupt accelerating phase leading to rock failure.

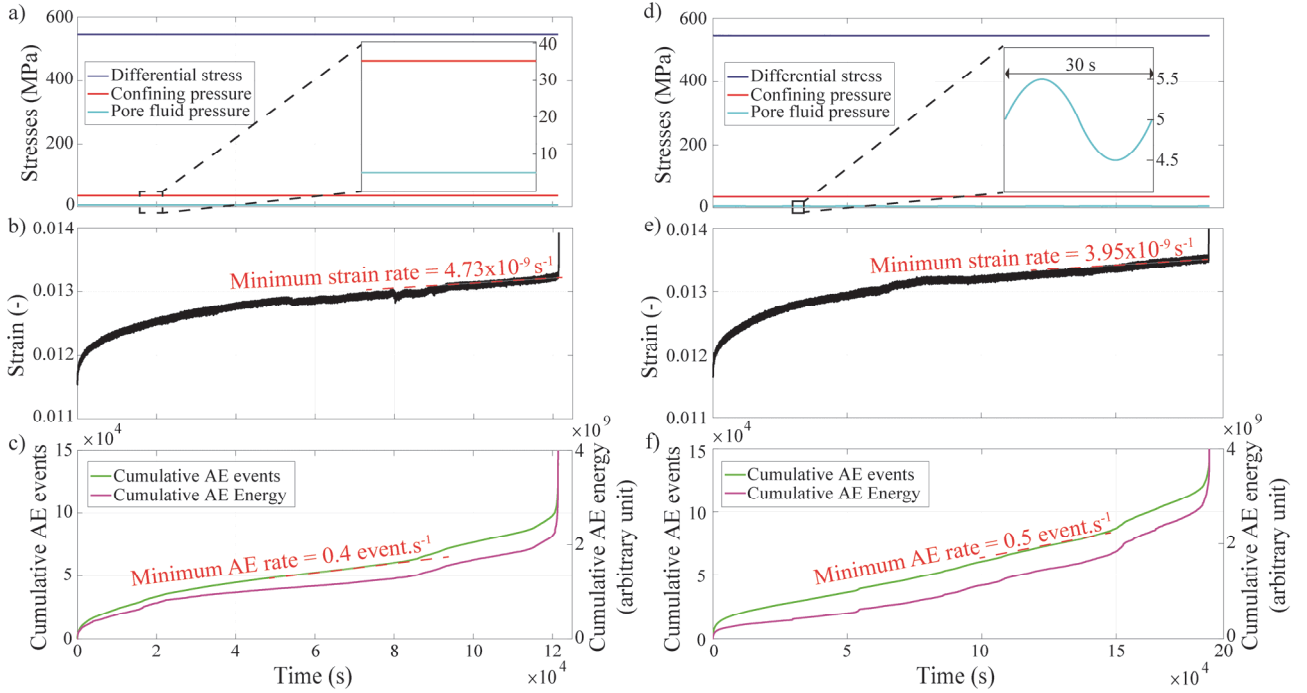


Figure 4. 6: Experimental curves obtained from the conventional creep experiment with $P_c = 35 \text{ MPa}$ and constant $P_f = 5 \text{ MPa}$ (a–c), and oscillating pore fluid pressure of $A = 1 \text{ MPa}$ and $T = 30 \text{ s}$ (d–f). (a and d) Stresses applied versus time, with a zooming window on the confining and pore fluid pressure. (b and e) Measured strain as a function of recording time, with the minimum strain rate obtained reported (dashed red curve). (c and f) Cumulative AE events (green line) and energy (pink line) as function of time, with the minimum AE rate reported (dashed red line). AE = acoustic emission.

We performed three stress stepping creep tests, at a Terzaghi effective pressure of 30 MPa with three different pore fluid pressures of 1, 5, and 10 MPa, to test the effect of pore fluid level on the creep behaviour. From all experiments, both the minimum strain and AE rates increased with the applied differential stress (Figure 4. 7a and b). Stress stepping and conventional creep experiments showed similar strain and AE rate patterns at a given applied stress. It suggests that for $Q \geq 547 \text{ MPa}$ the time of constant stress step was sufficient for samples to approach a minimum strain rate values.

At different pore fluid pressures, but similar Terzaghi effective pressures, all the samples failed at Q between 549 and 558 MPa, corresponding to 98% of the short-term strength. For all stress steps, the experiments had very similar values of minimum strain and AE rates, ranging from 10^{-9} to $7 \times 10^{-9} \text{ s}^{-1}$ and 6×10^{-3} to 4.4 event/s, respectively, when increasing Q from 440 to 560 MPa. Only the experiment at a pore fluid pressure of 10 MPa showed a deviation from the other ones, with a large increase in minimum strain rate near the rupture. These results suggest that for similar Terzaghi effective pressure conditions, static fluid pressure level does not influence brittle creep kinetics.

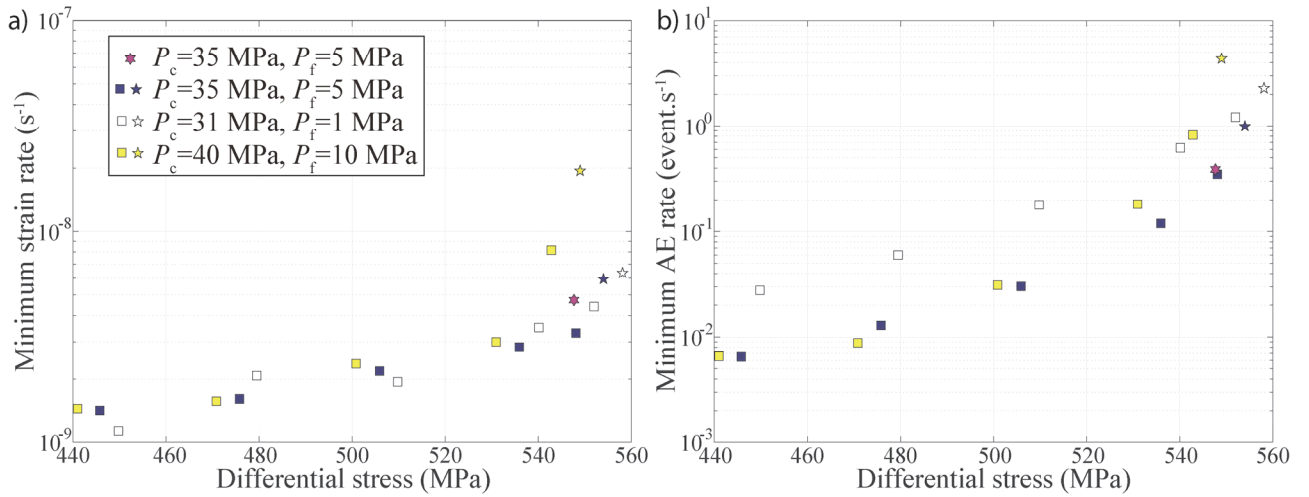


Figure 4. 7: Semi-log plot of the (a) minimum strain rates and (b) minimum AE rates found as function of differential stress applied for three stress stepping experiments and one conventional creep experiment at $P_c - P_f = 30$ MPa. Each colour represents an experiment, and the stars highlight the conditions at failure. The measurement errors are represented by the size of the data points. AE = acoustic emission.

4.4.3 Creep experiments under oscillating pore fluid pressure

4.4.3.1 Amplitude effects

The amplitude effect of oscillatory pore fluid pressure on mechanical and seismic behaviour was tested with five creep experiments (one conventional and four stress stepping), at constant $P_c = 35$ MPa and $P_f^{\text{mean}} = 5$ MPa. For all the tests, the oscillation period was kept constant, at $T = 30$ s, and the peak-to-peak amplitude A ranged from 0 to 8 MPa.

During the constant stress phase of the conventional creep experiments performed at $A = 1$ MPa (Figure 4. 6d), strain and AE rates (Figure 4. 6e and f) present a decelerating phase toward a minimum value of $3.95 \times 10^{-9} \text{ s}^{-1}$ and 0.5 event/s, respectively, followed by an accelerating phase leading to the rock failure.

For all amplitudes of pore fluid pressure, both minimum strain and AE rates increased with the applied differential stress (Figure 4. 8a and b). Again, stress stepping and conventional creep tests at $Q = 547$ MPa showed very similar results.

Surprisingly, very similar results were obtained independently of the amplitude of the oscillation. All experiments failed at Q between 553 and 560 MPa. For all the pore fluid pressure amplitudes, minimum strain and AE rates showed the same increase with Q , ranging from 10^{-9} to 10^{-8} s^{-1} and 4.0×10^{-3} to 2.4 event/s, respectively when increasing Q from 440 to 560 MPa. In summary, with a period of 30 s, the oscillating amplitude did not affect the stress to failure and the minimum strain and AE rates during each stress step. This holds even for very large pore fluid oscillations of 8 MPa, that is, variation of up to 27% of the effective confining pressure. Note that at the last stress step ($Q = 554$ MPa), when P_f reached its maximum value (9 MPa), the stress conditions corresponded to $\approx 99\%$ of the short-term sample strength (Figure 4. 5).

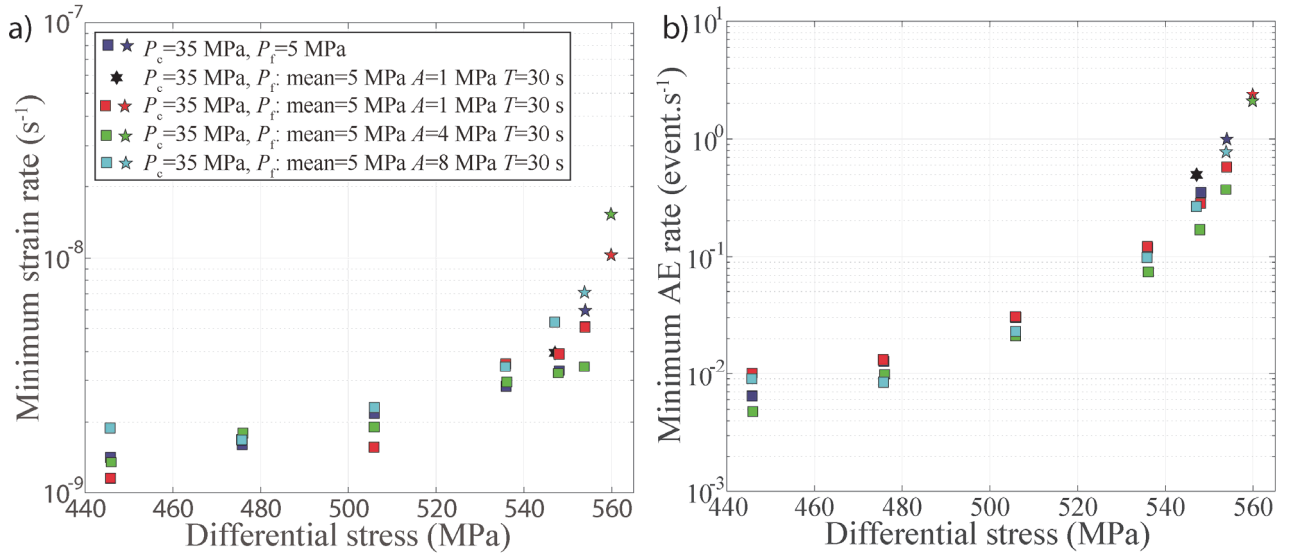


Figure 4. 8: Semi-log plot of the (a) minimum strain rates and (b) minimum AE rates found as function of differential stress applied for four stress stepping and one conventional creep experiments, with varying amplitudes of pore fluid pressure oscillation at a constant period of $T=30$ s. Each colour represents an experiment, and the stars highlight the conditions at failure. The measurement errors are represented by the size of the data points. AE = acoustic emission.

For each step and experiment, the total number of AE events N per step was computed (Figure 4. 9). We observed that (i) N increased with Q ; (ii) N did not highlight any apparent correlation with the imposed amplitude of pore fluid pressure oscillation; and (iii) the total number of AE events during each experiment (i.e., sum of N) showed no correlation with increasing the amplitude of pore fluid pressure oscillation, being 158, 181, 143, and 114 k for $A = 0, 1, 4$, and 8 MPa, respectively.

Investigating the AE stacking over one oscillation of pore fluid pressure (Figure 4. 9) showed that (i) for $A = 0$ MPa, AE events were almost constant during each stress step. (ii) During the first stress step (80% of Q_{peak}), no strong correlation between the pore fluid pressure level and the AEs was observed, independent of the amplitude of oscillations. For higher stress steps, and $A > 0$ MPa (i.e., 1, 4, and 8 MPa), an increase of AE events was concomitant with the maximum level of pore fluid pressure of the oscillation. Moreover, increasing Q close to failure promoted the occurrence of AEs at the peak of oscillations. This behaviour was enhanced by increasing the amplitude of oscillations. (iii) For $A = 8$ MPa, a correlation between the AE events and the minimum pore fluid pressure level was also observed in addition to the correlation with the maximum pore fluid level. It was dominant in the first stress steps (from $Q = 446$ to 506 MPa), and minor for higher stress steps (from $Q = 548$ MPa). In summary, AE correlations with pore fluid oscillations increased with both an increase of Q and A .

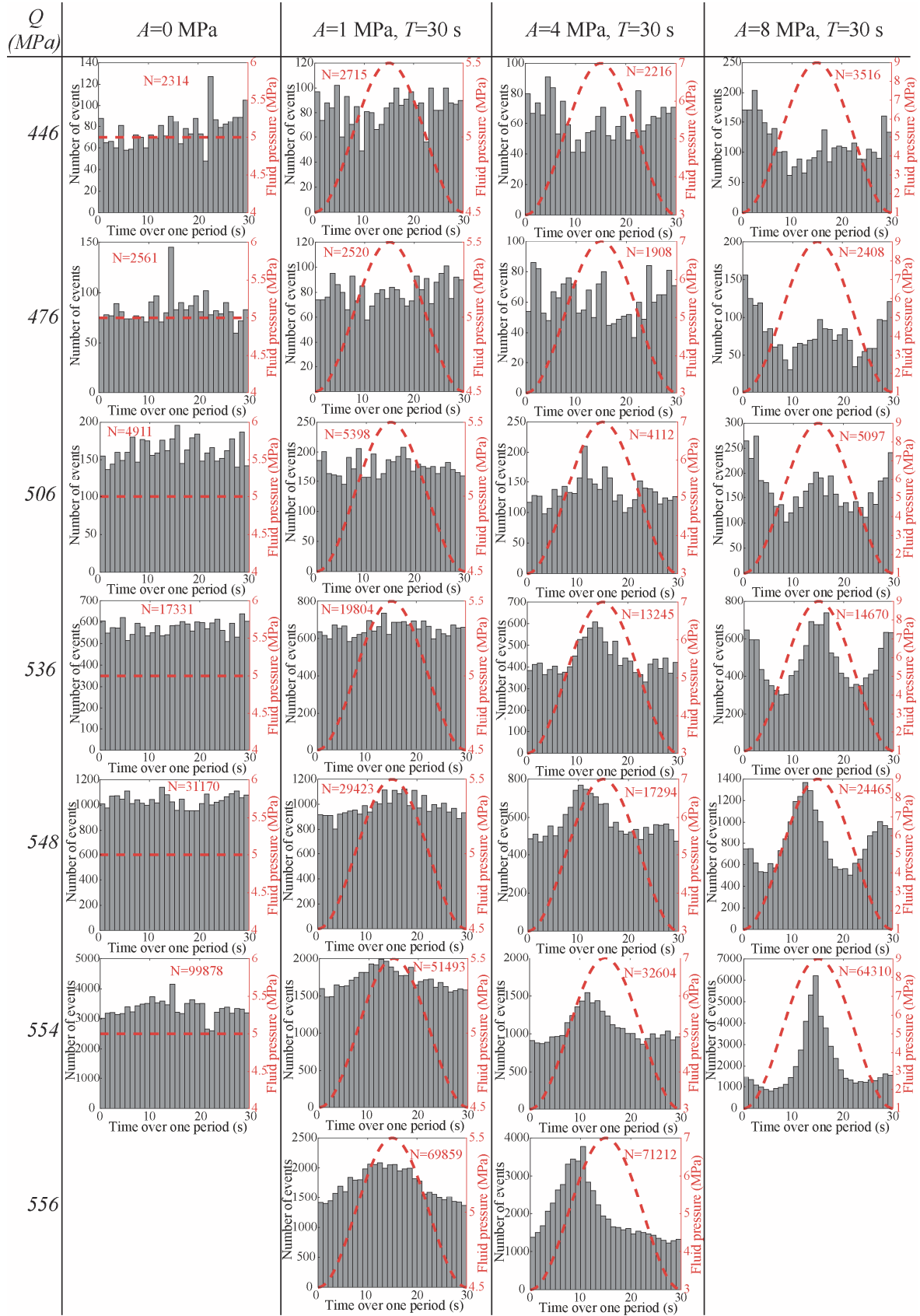


Figure 4. 9: AE events stacked over one oscillation of pore fluid for the reference experiment (i.e., $A = 0$ MPa) and the three experiments with $A = 1, 4$, and 8 MPa and $T = 30$ s. The bar charts represent the number of AE event for each step of applied Q . The red dashed lines represent the pore fluid oscillation. N is the total number of AE during the step. AE = acoustic emission.

4.4.3.2 Period effects

At constant $P_c = 35$ MPa and $P_f^{\text{mean}} = 5$ MPa, we performed three stress stepping experiments with pore fluid pressure oscillations of the same peak-to-peak amplitude of $A = 4$ MPa but different periods T of 30, 300, and 3,000 s. Those experiments were compared to the reference one, that is, $A = 0$ MPa (Figure 4. 10).

Under all conditions described above, both minimum strain and AE rates increased with the applied differential stress (Figure 4. 10).

Until $Q = 476$ MPa, the minimum strain rates reached were similar for every experiment, ranging from 1.35×10^{-9} to $2.29 \times 10^{-9} \text{ s}^{-1}$. Starting from $Q > 467$ MPa, experiments with larger T (i.e., 300 and 3000 s) showed larger minimum strain rates compared to that at lower T and reference experiments (Figure 4. 10a). For example, at $Q = 506$ MPa, the minimum strain rate was approximately twice as large for the two experiments with larger periods, that is, of about 2×10^{-9} and $4 \times 10^{-9} \text{ s}^{-1}$ for small and large T , respectively. Similarly, oscillations of large T values increased AE rates observed at each stress step, with minimum rates being twice as large (Figure 4. 10b). Finally, the effect of T is even more evident on the time-to-failure. Indeed, samples subjected to $T > 30$ s failed at $Q = 536$ MPa, corresponding to failure after 3 days, while experiment with low T failed at $Q = 560$ MPa, corresponding to failure after 6 days.

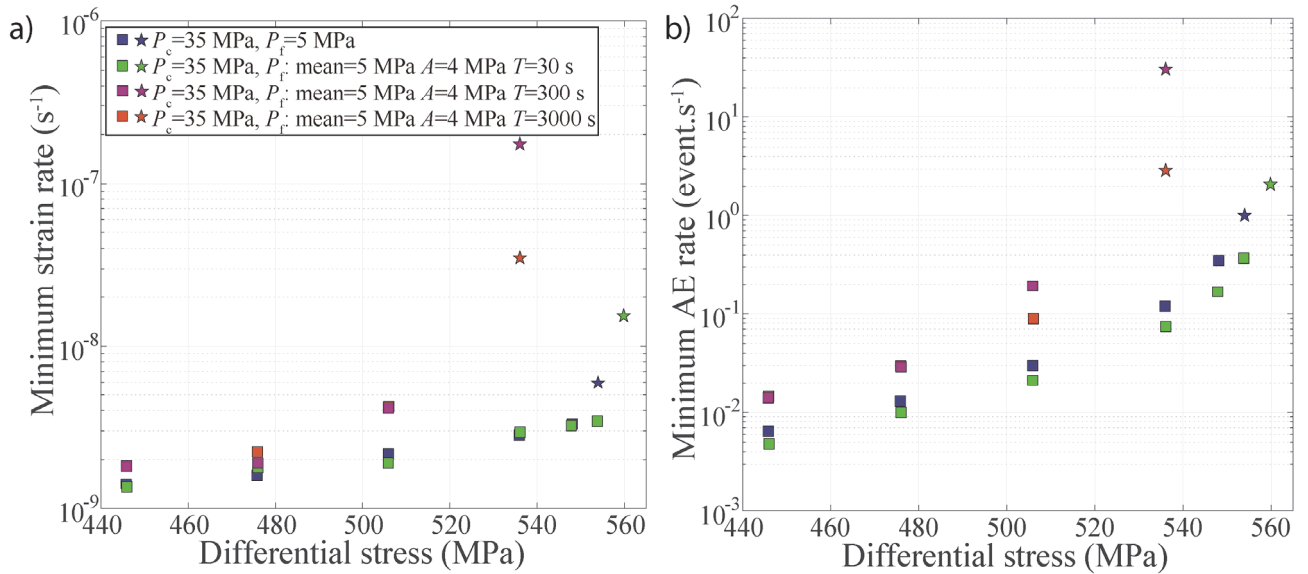


Figure 4. 10: Semi-log plot of the (a) minimum strain rates and (b) minimum AE rates found as function of differential stress applied for three stress stepping creep experiment with $A = 4$ MPa, compared to a constant pore fluid pressure experiment with the same average conditions. Each colour represents an experiment, and the stars show the conditions at failure. The measurement errors are represented by the size of the data points. AE = acoustic emission.

The total number of AE events per step N (Figure 4. 11) showed that (i) N increased with Q . (ii) N was greater for larger periods (i.e., 300 and 3000 s) compared to shorter ones (i.e., 30 s). (iii) The total number of AE events were very similar for each experiment, with an average total number of 114 k and a standard deviation of 397 events.

AE stacking over one oscillation period of pore fluid pressure (Figure 4. 11) showed (i) an increase of AE events concomitant with the maximum level of pore fluid pressure of the oscillation and (ii) a stronger correlation when increasing Q and T .

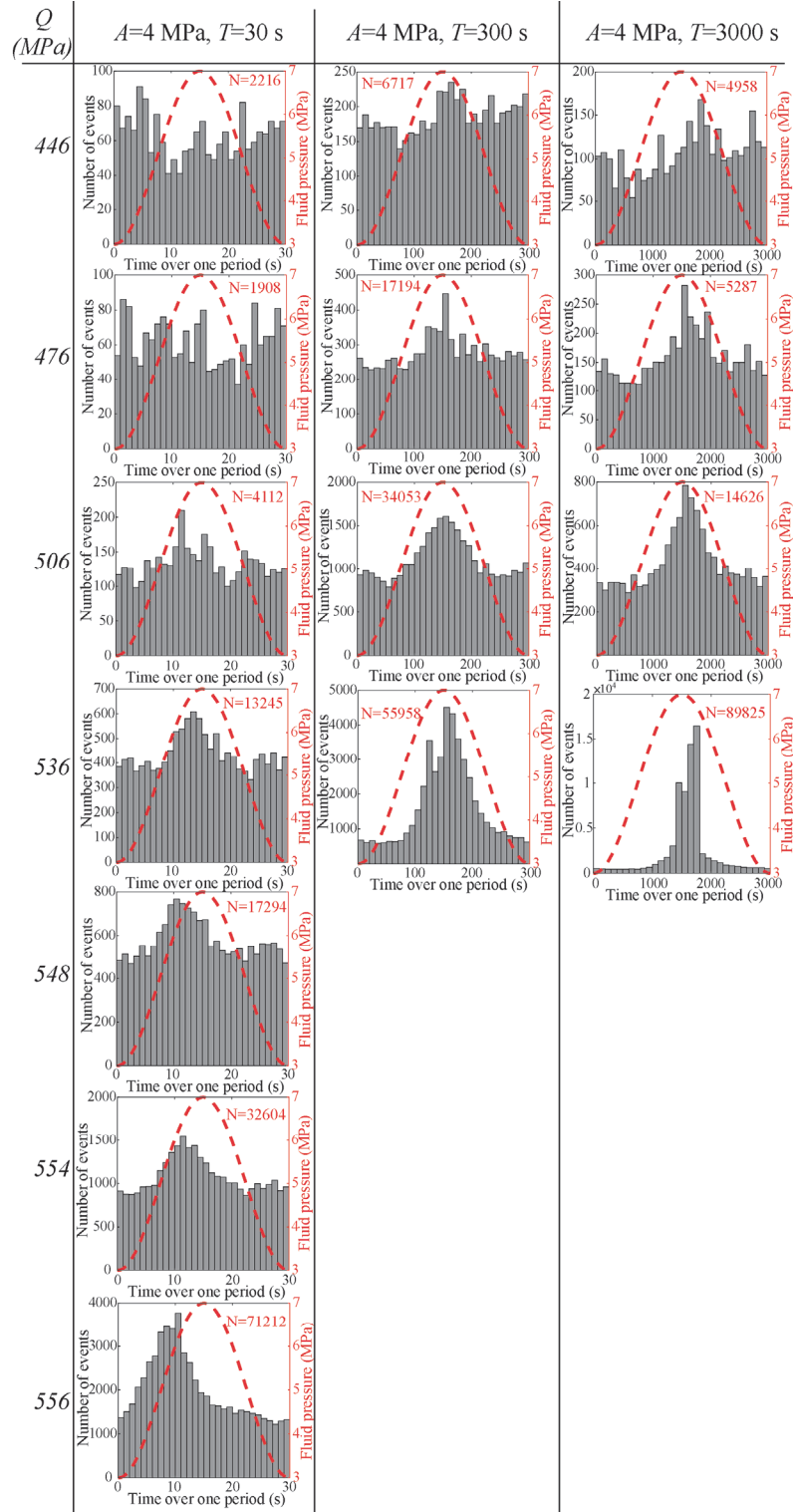


Figure 4. 11: AE events stacked over one oscillation of pore fluid for the three experiments with $T = 30, 300, \text{ and } 3000 \text{ s}$ and $A = 4 \text{ MPa}$. The bar charts represent the number of AE events for each steps of applied Q . The red dashed lines represent the pore fluid oscillations. N is the total number of AE during the step. AE = acoustic emission.

For those experiments, we computed the relative strain rates as the local gradient of the strain-time curve (i.e., $[\dot{\epsilon}_{ax}(t + dt) - \dot{\epsilon}_{ax}(t)]/dt$) for each stress step and we stacked them over one oscillation period (Figure 4. 12). For low periods of oscillations ($T= 30$ s), the relative strain rate was not affected by the pore fluid pressure oscillations. However, for higher periods ($T= 300$ and 3000 s) and high differential stress, the relative strain rates were correlated with the pore fluid pressure oscillations. Moreover, the maximum relative strain rate was in phase with the maximum of pore fluid pressure. This behaviour mimics the one of the AE events that were mostly emitted when the pore fluid pressure reached a maximum and at high differential stresses.

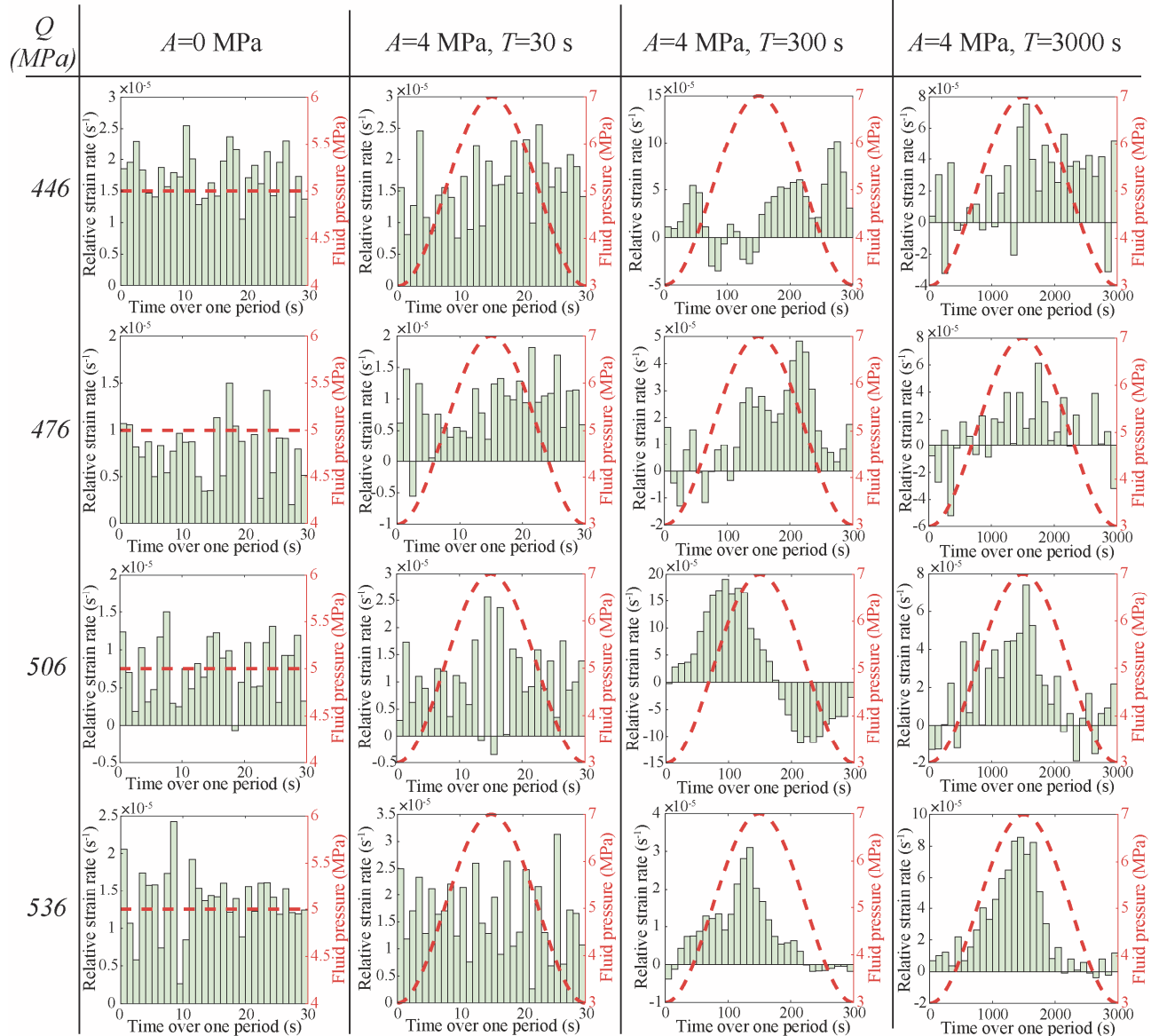


Figure 4. 12: Relative strain rate stacked over one period of pore fluid pressure oscillation for the reference experiment ($A = 0$ MPa) and three experiments with an amplitude of 4 MPa and periods from 30 to 3000 s. The four first stress steps are presented. The green bar chart represents the relative strain rate. The red dashed lines represent the pore fluid oscillation.

4.4.3.3 Dilatancy

Dilatancy (or porosity change) curves were obtained as a function of time during pore fluid cyclic experiments (Figure 4. 13). For experiments at $T = 30$ s, dilatancy behaviour similar to the reference experiment was observed. For experiments with $A = 4$ MPa and $T = 300$ and 3000 s, dilatancy was much faster at all stress steps compared to low T experiments, especially for the first phase of creep (i.e., immediately after load increase). Interestingly, for all the oscillating periods and amplitudes, most samples failed when porosity increase reached approximately 1%.

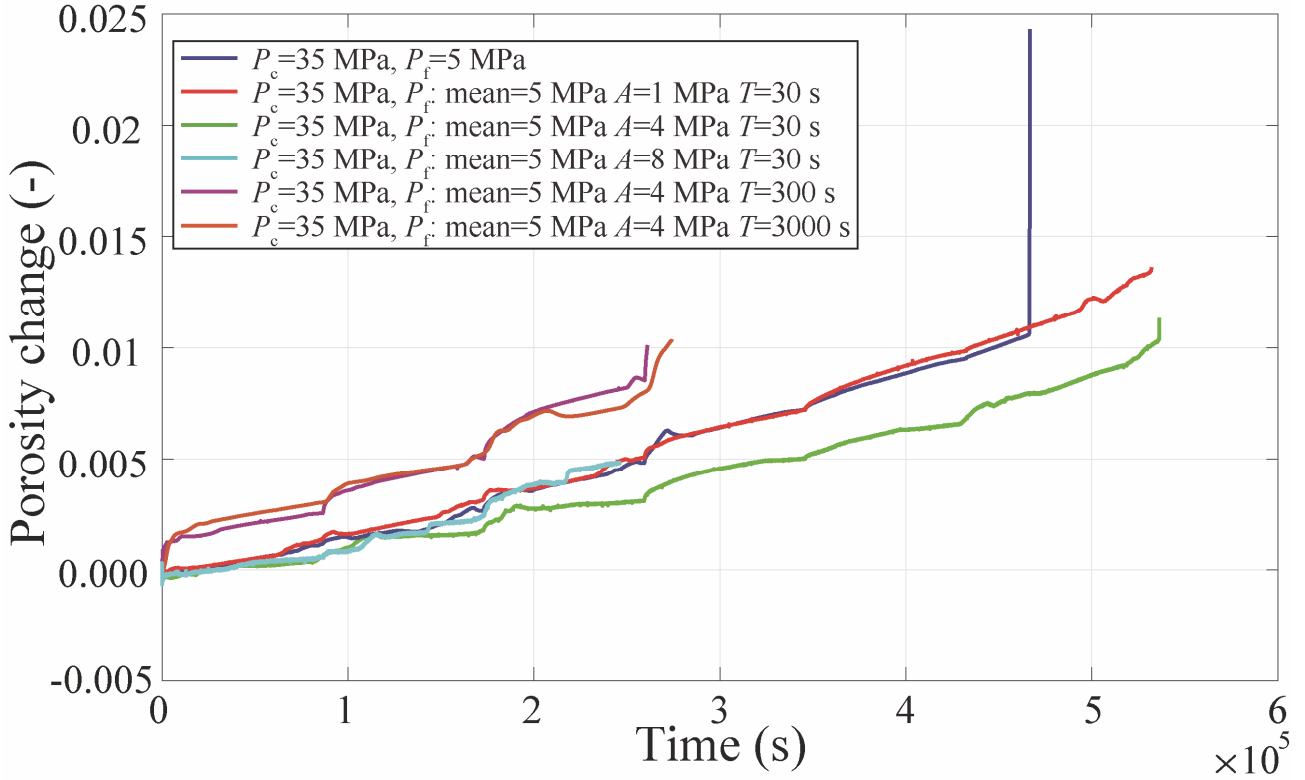


Figure 4. 13: Porosity change as function of time for the reference experiment ($A = 0$ MPa) and all pore fluid oscillation experiments performed. Due to pore pump encoder issues, the porosity changes for $A = 8$ MPa is given only for the first three steps of stress.

4.5 Interpretation and discussion

Mechanical and AE data from our brittle creep experiments showed the following:

- 1) At equivalent Terzaghi effective pressure, the pore fluid level had no influence on sample creep deformation, time-to-failure, and AE rate.
- 2) Samples exhibited dilatancy behaviour during deformation. The dilation rate depended on the pore fluid oscillation period. However, the amount of dilatancy at failure was constant and around 1% under all the tested conditions.
- 3) On the contrary to pore fluid amplitude, the oscillation period influenced the time-to-failure, failure strength, and dilatancy rate.
- 4) Pore fluid oscillations controlled the acoustic event rate, with an increase of AE rate at the maximum of pore fluid pressure. Correlation between oscillations and AE rate increased with (i) increasing the differential stress applied to the sample and getting closer

to sample rupture, and (ii) increasing the pore fluid oscillation amplitude and period. We noticed an out-of-phase increase of AE rate for high P_f amplitude ($A = 8$ MPa).

5) AE distribution mimics the relative strain rate distribution during deformation.

In the following, these five main results as well as their implications to the upper crust deformation are discussed.

4.5.1 Pore fluid pressure level

Both short- and long-term mechanical behaviours of the FS showed no apparent dependence to pore fluid level for constant Terzaghi effective confining pressure. Moreover, comparing short-term experiments under dry and water-saturated conditions, no effect of fluid was observed. It implies that the short-term behaviour of FS is not affected by water-induced weakening and that both short- and long-term behaviours are governed by a simple Terzaghi effective stress law, with an effective stress coefficient equal to 1. This result is in agreement with previous experimental work on short-term failure performed on FS and other pure quartz sandstones (e.g., Bied et al., 2002; Reviron et al., 2009; Schubnel et al., 2007). It is also in agreement with brittle creep experiment results obtained by Heap et al. (2009b) on Darley Dale sandstone.

4.5.2 Dilatancy and soft stimulations

Recently, cyclic fluid injections were proposed as an alternative to conventional monotonic fluid injections for geo-reservoir stimulations. The method is referred to as *soft stimulation* and aims to increase the reservoir performance while reducing the induced seismicity compared to conventional stimulations. During the field operations, fluid injections are performed by controlling the injection flow rate rather than the pore fluid pressure. Despite this difference with our experimental protocol, the data produced in this study can help to interpret the mechanical and seismic behaviour of reservoir during soft stimulations.

Our mechanical results showed that a cyclic pore fluid pressure can increase the dilatancy rate by up to a factor of 2 when applying long period pore fluid pressure oscillations to the sample (Figure 4. 13). This phenomenon is important in the first phase of creep and during the first pore fluid cycle. Recent numerical and field studies also demonstrated that cyclic fluid injections into a geo-reservoir increased the hydraulic performance (i.e., permeability) of the fracture network compared to monotonic injections (Zang et al., 2013, 2018). This has important applications for CO₂ sequestration or geothermal reservoir stimulations, where an increase of reservoir permeability and dilatancy would enhance, respectively, the reservoir productivity and storage capacity. However, our experiments also demonstrated that a dilatancy threshold exists after which macroscopic failure occurs. This is in agreement with previous observation of a critical dilatancy before the onset of macroscopic failure (Kranz & Scholz, 1977). For reservoir applications, getting close to this critical dilatancy could provoke fast failure of the reservoir and seismic activity. In the case of FS, the maximum dilatancy is around 1%.

Additionally, soft stimulations into geo-reservoir were shown to have the advantage of reducing the number of events and the maximum event magnitude compared to monotonic fluid injections (Yoon et al., 2014; Zang et al., 2013, 2018). On the contrary, during our experiments, the total

number of AE events (a proxy for the seismicity) was equivalent for constant and cyclic pore fluid pressure experiments. However, cyclic pore fluid pressure oscillations modify the AE event distribution.

Finally, from numerical modelling, Yoon et al. (2014) suggested the existence of a Kaiser effect during cyclic stimulations of reservoirs, that is, seismic events are seen only when the pore fluid pressure conditions overcome the previous maximum pressure. These results are not in complete agreement with our observations. Indeed, AE events were emitted continuously and at every pressure oscillation cycle during the experiments, even at low pore fluid pressure values. Therefore, no Kaiser effect could be noticed. The reason for the difference could be that, even if the axial stress was kept constant, the sample's inelastic deformation was increasing due to a creep mechanism and AE events were produced. In geo-reservoirs, creep mechanisms are also expected to occur. Therefore, no Kaiser effect should also occur in reservoir. However, stresses are released after every seismic event, which is not the case for our experimental conditions where stresses are artificially kept constant.

4.5.3 Pore fluid pressure controlling the deformation and AE event rates

To understand the underlying deformation mechanics during a creep experiment with oscillating pore fluid pressure, a creep model based on the work of Brantut et al. (2012) was tested. The model allowed for the investigation of the creep deformation from the crack to the macroscopic scale. It assumed an isotropic elastic medium containing a set of penny-shaped cracks of radius a oriented at an angle φ from the principal stress σ_1 . Both shear stress τ and normal stress σ_n are acting on the cracks during a triaxial experiment (where $\sigma_3 = \sigma_2 = P_c$). When the shear stress overcomes the frictional strength (i.e., $\tau > \mu\sigma_n$), where μ is the friction coefficient), sliding along the crack occurs. After some sliding, wing cracks (opening cracks subparallel to σ_1) can initiate at the crack tip.

The mode I stress intensity factor at the tip of wing crack of length l can be express as (Ashby & Sammis, 1990; Brantut et al., 2012):

$$K_I = [(A_1\sigma'_1 - A_3\sigma'_3)(c_1 + c_2) - \sigma'_3c_3] \times \sqrt{\pi a} \quad \text{Equation (4. 1)}$$

$$\text{with } c_1 = \pi^{-2} \left(\frac{l}{a} + \beta \right)^{-\frac{3}{2}}, \quad \text{Equation (4. 2)}$$

$$c_2 = \frac{2(\pi\alpha)^{-2} \sqrt{\frac{l}{a}}}{\rho_0^{-\frac{2}{3}} - \left(1 + \frac{l}{aa}\right)^2}, \quad \text{Equation (4. 3)}$$

$$c_3 = \frac{2}{\pi} \sqrt{\frac{l}{a}} \quad \text{Equation (4. 4)}$$

A_1 and A_3 being constants given by Ashby & Sammis (1990), $\alpha = \cos(\varphi)$ being the projection of the crack in the vertical plane, and $D_0 = \frac{4}{3}\pi N_V(\alpha a)^3$ represents the initial damage of the sample, with N_V being the number of cracks per unit of volume. β is an empirical parameter to restrict K_I to finite values when l is small; following Brantut et al. (2012) it was taken to be 1.15.

Without stress corrosion, wing crack can grow only when K_I overcomes K_{IC} . When the stress allows the wing crack to grow, its length increases such that $K_I = K_{IC}$. A relationship between the wing crack length and the remote stresses applied on the sample can be found by rewriting equation (4. 1) (Brantut et al., 2012):

$$\sigma'_1(l) = \frac{\left(\frac{K_{IC}}{\sqrt{\pi a}} + \sigma_3(c_3 + A_3(c_1 + c_2)) \right)}{A_1(c_1 + c_2)} \quad \text{Equation (4. 5)}$$

Equation (4. 5) has a maximum value of σ_1 , corresponding to the short-term strength of the rock sample. At a lower stress than the rock strength, equation (4. 5) provides a starting (equilibrium) crack length l_0 of a creep experiment.

During a brittle creep experiment, stress corrosion allows the crack to grow under a stress intensity factor $K_I < K_{IC}$. Under these conditions, the crack growth rate can be described using Charles's law (Atkinson, 1984; Charles, 1958a, 1958b):

$$\frac{dl}{dt} = \dot{l}_0 \left(\frac{K_I}{K_{IC}} \right)^n \quad \text{Equation (4. 6)}$$

Where \dot{l}_0 is the characteristic crack speed and n is the stress corrosion index. Under constant stress conditions, combining equations (4. 1) and (4. 6) provides a differential equation that describes the evolution of wing crack length over time. The irreversible strain (ϵ_1) can then be inferred as (Brantut et al., 2012):

$$\frac{d\epsilon_1}{dt} = \frac{3D_0}{(\alpha a)^3} (l + \alpha a) \frac{K_I \sqrt{\pi a}}{E} (A_1(c_1 + c_2)) \frac{dl}{dt} \quad \text{Equation (4. 7)}$$

This model was used to simulate a creep experiment on FS with oscillating pore fluid pressure. The stress conditions were set to $\sigma_1 = 580$ MPa, $P_c = \sigma_3 = 35$ MPa, $P_f^{\text{mean}} = 5$ MPa, and three different oscillating pore fluid pressure conditions: with $A = 4$ MPa and $T = 300$ s, $A = 1$ MPa and $T = 300$ s, $A = 4$ MPa and $T = 3000$ s (Figure 4. 14). The constants used to model subcritical crack growth in FS (Figure 4. 14) were obtained from the literature (Atkinson, 1979; Brantut et al., 2012; Whitney et al., 2007; see Table 4. 3).

For all the pore fluid pressure conditions tested, the model shows two main results that we classified as global and punctual deformations (Figure 4. 14).

The global deformation follows the two creep phases observed during the laboratory experiments, with K_I (Figure 4. 14a.1, Figure 4. 14b.1, and Figure 4. 14c.1) and ϵ_1 (Figure 4. 14a.2, Figure 4. 14b.2, and Figure 4. 14c.2) first decreasing toward a minimum value and then increasing toward infinity (i.e., rock failure). Oscillating the pore fluid pressure directly impacts this global behaviour, that is, increasing amplitude (Figure 4. 14a and b) and period (Figure 4. 14a and c) shortens the time-to-failure and increases the minimum strain rate. Indeed, increasing the pore fluid pressure induces inelastic strain and increase the micro-crack length. Because of the nonlinear behaviour of the creep mechanisms when stresses are close to the sample strength, longer oscillation periods also affect the mechanical properties (Figure 4. 14a and c), which is consistent with the earlier experimental observations (Figure 4. 12). However, at small oscillation periods, the model predicts

a stronger dependence on the amplitude than in our experiments, a difference which might originate either from the choice of model parameters (e.g., characteristic crack speed $[\dot{l}_0]$ or stress corrosion index $[n]$)—leading to an overestimation of the amplitude effect relative to the period effect—or from an additional physical effect specific to hydraulic fatigue, hence not accounted for in a creep model.

In addition to the global deformation, the predicted K_I and ε_1 showed oscillations in-phase with the pore fluid pressure oscillations (Figure 4. 14). Thus, both AE rate and strain rate are expected to increase as pore fluid pressure reaches its maximum, which is in agreement with our experimental observations (Figure 4. 9, Figure 4. 11 and Figure 4. 12) and with previous work performed on andesite (Farquharson et al., 2016). These results are also consistent with the observed periodic stick-slip triggering during shear stress oscillations in dry and wet granite (Bartlow et al., 2012; Beeler & Lockner, 2003; Lockner & Beeler, 1999).

To summarize, the model results are in overall agreement with mechanical and AE data obtained. The model predicts the two deformation phases of creep, as observed in our experiments, and a variation of the time-to-failure and minimum strain rate depending on the period of the pore fluid pressure oscillations. The model also predicts a maximum deformation rate in-phase with the maximum of pore fluid pressure, which is consistent with the in-phase increase of AE events and strain rate during our experiments.p

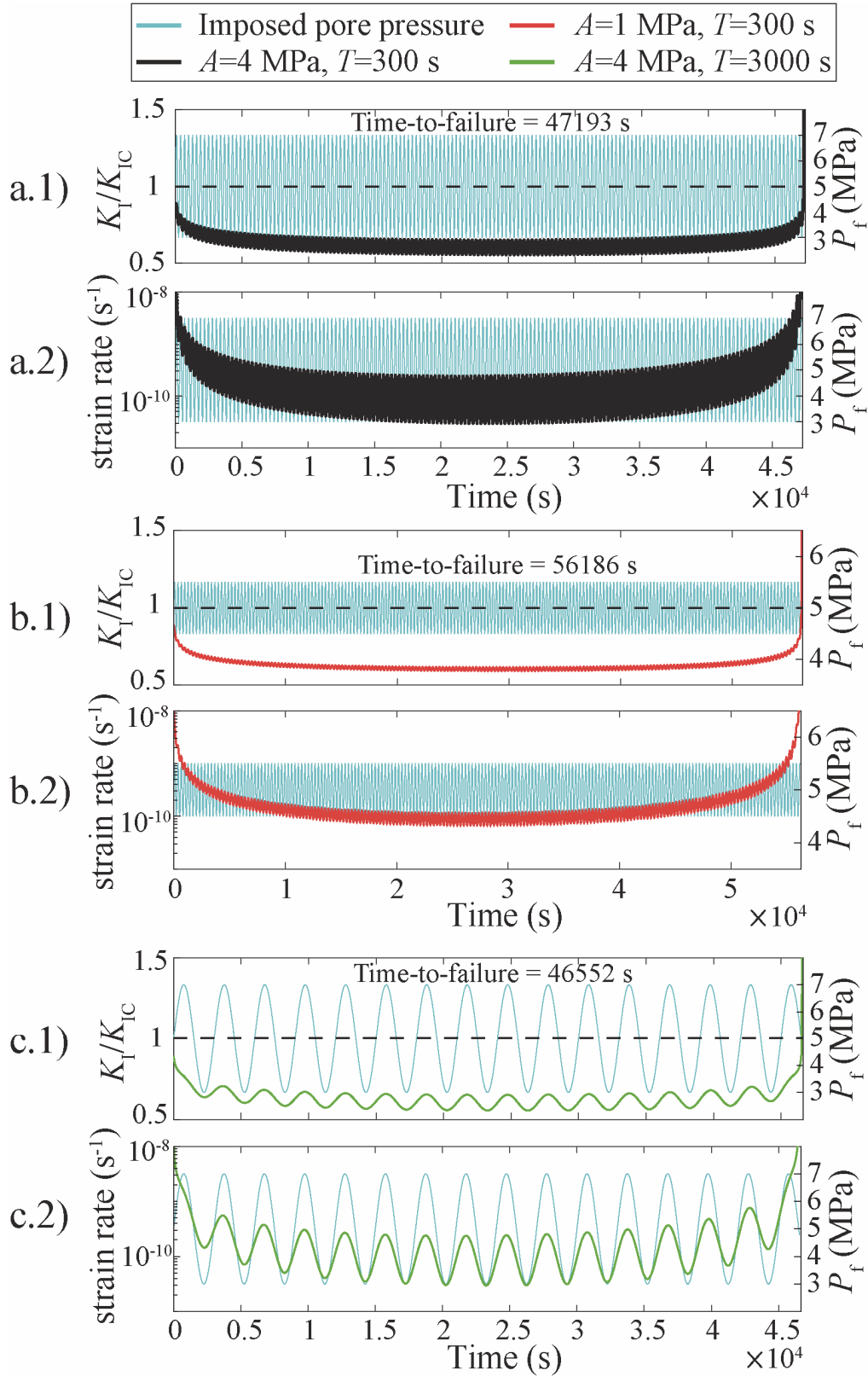


Figure 4.14: Evolution of (1) the stress intensity factor normalized by its critical value (K_I/K_{IC}) and of (2) the strain rate ($\dot{\epsilon}_I$) as function of time for the performed creep model at $P_c = \sigma_3 = 35$ MPa, $\sigma_1 = 580$ MPa, and using the parameters in Table 4.3. Three oscillating pore fluid pressures were tested: (a) $A = 4$ MPa and $T = 300$ s (dark curves), (b) $A = 1$ MPa and $T = 300$ s (red curves) and (c) $A = 4$ MPa and $T = 3000$ s (green curves). The pore fluid pressure is represented by the light blue curve. The time-to-failure is noted for each pore fluid pressure condition.

Table 4. 3: Value used to model subcritical crack growth in FS. FS = Fontainebleau sandstone. ^a Grain size of FS. ^b Estimated from fits of short-term experiments. ^c From Whitney et al. (2007), K_{IC} for quartz mineral. ^d From Brantut et al. (2012), value for Crab Orchard sandstone. ^e From Atkinson (1979), value for quartz mineral. ^f From equation (4. 5) at $\sigma_1 = 580$ MPa.

Parameter	Value
Crack orientation from σ_1 , φ	$\pi/4$
Initial flow size ^a , a (μm)	250
Friction coefficient, μ	0.7
Uncracked rock Young's modulus (GPa)	75
Initial damage ^b , D_0	2.87×10^{-3}
Mode I stress intensity factor ^c , K_{IC} (MPa.m ^{1/2})	1.5
Characteristic crack speed ^d , (\dot{l}_0) (m.s ⁻¹)	1.6×10^{-6}
Stress corrosion index ^e , n	12.0
Starting crack length ^f , l_0 (μm)	440

4.5.4 Implication for the upper crust deformation

In the upper crust, tectonic strain rates vary from 10^{-15} s⁻¹ or lower during inter-seismic phases to 10^3 s⁻¹ during co-seismic events. During the inter-seismic phase, time-dependent mechanisms are expected to govern the evolution of rock mass strength. Of these time-dependent deformation mechanisms, stress corrosion is often pointed out as the dominant one. Here we observe that rock mass subjected to pore fluid pressure variations may also suffer from hydraulic fatigue, which severely lower its strength. In our experiments, hydraulic fatigue mechanisms increased the deformation rate by up to a factor 2.

In tectonically active areas such as the Himalayas or California, seasonal hydrology tends to be correlated with natural seismicity (e.g., Bettinelli et al., 2008; Johnson et al., 2017). The mechanism involved is the changes in Coulomb stress rates on faults due to a loading, which can either stabilize or promote the fault failure. Most studies show that natural seismicity is correlated with an increase of the crust load. Taking AE data as a proxy for seismic events (see Lockner, 1993b for a discussion of the correspondence), we showed that even small amplitudes of pore fluid pressure variations would influence seismic event rates.

Even if the total number of events were relatively similar for all the performed experiments, when an oscillating pore fluid pressure was applied, different event distributions were noticed. This correlation between events and pore fluid pressure was noticed at each stress step and for each pore fluid pressure oscillation. It can be even seen for small pore fluid amplitude variations and low differential stress (Figure 4. 9 and Figure 4. 11). It implies that pore fluid pressure perturbations have a dominant and direct effect on seismic event distribution.

Our data also give new constraints on the correlation between seismicity and pore fluid pressure variation. Particularly, correlation can be favoured by (i) high stress conditions compared to rock strength, (ii) high pore fluid pressure amplitude, and (iii) high pore fluid pressure period variations.

4.6 Conclusions

Laboratory data of 10 short- and 10 long-term creep experiments on Fontainebleau sandstone were reported. The creep experiments were carried with different pore fluid pressure conditions, and the sample mechanical and acoustic behaviours were monitored giving new constraints on the rock-fluid interactions:

1. At a constant Terzaghi effective pressure, increasing the pore fluid pressure level up to a factor of 10 did not influence the rock strength in either the short-term or long-term, and the sample creep deformation and AEs rates were also not influenced.
2. Under the tested stress conditions, all samples failed after about 1% dilatancy. However, the dilatancy rate depended on pore fluid oscillation period.
3. During the experiments, the dilatancy rate is directly correlated to the AE rate. Under the tested conditions, doubling the dilatancy rate implied the doubling of the AE rate.
4. Under macroscopically drained conditions, the period of pore fluid pressure oscillations reduced the time-to-failure and strength of a rock sample and increased its dilatancy rate. This is consistent with predictions from a model accounting for subcritical crack growth and creep deformations.

Pore fluid pressure perturbations had a dominant and immediate effect on seismic event distribution. During the experiments, the pore fluid oscillations were controlling the AE event rate, with an observed increase of emissions at the maximum of pore fluid pressure. The correlations increased when the rock was getting closer to failure and increased with the pore fluid pressure amplitude and period.

Acknowledgments

This work was funded by the grant FRICTION: Fault Reactivation during CO₂ sequestration supported by Gaznat SA. M.V. Thanks to the ERC before grant 757290. L. P. thanks the EPFL/Marie Curie support grant progress number 665667. The authors want to thank Laurent Gastaldo for laboratory assistance. We also thank Chiara Cornelio for modelling help, François Pas-selègue and Alexandre Schubnel for the helpful discussions and suggestions, and Barnaby Fryer for proofreading. The authors thank the Editor, David Lockner, and an anonymous reviewer for their constructive comments. Raw data can be found at <https://zenodo.org/> or requested from the corresponding author at corentin.noel@epfl.ch.

Chapter 5 Fault reactivation during fluid pressure oscillations: transition from stable to unstable slip

Authors: Corentin Noël¹, François X. Passelègue¹, Giorgetti Carolina¹, Marie Violay¹

¹ Laboratory of Experimental Rock Mechanics, Ecole Polytechnique Fédérale de Lausanne, Lausanne, Switzerland

Status: Published in the Journal of Geophysical Research: Solid Earth.

Reference: Noël, C., Passelègue, F. X., Giorgetti, C., & Violay, M. (2019). Fault reactivation during fluid pressure oscillations: transition from stable to unstable slip. *Journal of Geophysical Research: Solid Earth*, 124(11), 10940-10953. <https://doi.org/10.1029/2019JB018517>

Contributions: C. Noël prepared and characterized the sample. C. Noël has run the experiments. All the authors have participated to the experimental strategy. C. Noël has carried out the data treatment. All the authors have contributed to the data analysis. C. Noël has written the manuscript. All the authors have contributed to guide the discussion of the manuscript. M. Violay has acted as a supervisor.

Highlights:

- Laboratory investigation of the effect of fluid pressure oscillations on the fault stability behaviour
- Fluid pressure signal controls the time distribution of the instabilities
- Fluid pressure oscillations promote seismic rather than aseismic slip; the higher the amplitude of the oscillations the more unstable the fault is

5.1 Abstract

High-pressure fluid injection in deep geo-reservoirs can induce earthquakes. Recent observations suggest that cyclic injections might trigger less seismicity than monotonic injections. Here, we report triaxial laboratory experiments conducted on faulted quartz-rich sandstone that provide new insight into the physics of fault – fluid interactions subjected to cyclic fluid pressure variations. The experiments were performed at 30 and 45 MPa confining pressure, imposing constant or sinusoidal fluid pressure oscillations of amplitudes ranging from 0 to 8 MPa in addition to a far-field constant loading rate (10^{-4} and 10^{-3} mm.s $^{-1}$). The results show that (i) in agreement with the Mohr-Coulomb theory, faults reactivate at the static friction criterion, which is generally reached at the maximum fluid pressure during oscillations. (ii) Oscillating fluid pressure perturbations promote seismic behaviour rather than aseismic slip, and (iii) increasing the oscillation’s amplitude enhances the onset of seismic activity along the fault. We demonstrate that this behaviour is caused by slip rate variations resulting from the fluid pressure oscillations. Without fluid pressure oscillations, increasing the far-field loading rate also promotes seismic activity. Our experiments demonstrate that the seismicity intensification due to cyclic fluid injections could be promoted at shallow depth, where confining pressure is relatively low, resulting in large strain rate perturbations.

Keywords: fluid-fault interaction, fluid pressure oscillation, friction, slip stability, induced seismicity, triaxial experiment.

5.2 Introduction

In the past 20 years, the growing interest in and the use of deep geo-reservoirs for purposes such as carbon storage, waste water disposal, or geothermal energy exploitation has induced massive increases in seismicity in some normally “quiet” regions (e.g., Ellsworth, 2013). Indeed, high-pressure fluid injection can reduce the effective normal stress ($\sigma_n - P_f$) acting on a fault, bringing the system closer to failure. If the effect of a linear increase in fluid pressure on fault reactivation has been widely studied (e.g., French et al., 2016; Passelègue et al., 2018; Rutqvist et al., 2016; Scuderi & Collettini, 2018), only little is known about cyclic fluid pressure perturbations (Chanard et al., 2019; Farquharson et al., 2016; Noël et al., 2019a). In addition, while the quasi-static reactivation of faults is well understood, the influence of such fluid pressure perturbations on the slip behaviour of faults remains poorly constrained. Yet, such fluid pressure perturbations are common in the upper crust. They can originate from natural causes such as oceanic tides (e.g., Wang & Davis, 1996), seasonal hydrology (e.g., Bettinelli et al., 2008; Chanard et al., 2014), gas-rich magma ascent in volcanic edifices (e.g., Michaut et al., 2013), or originate from anthropogenic causes due to fluid production from (e.g., Candela et al., 2019) or injection into geo-reservoirs (e.g., Verdon et al., 2013).

Based on anthropogenic perturbation, it has been suggested that cyclic fluid stimulation results in a different seismic response of the reservoir compared to monotonic fluid injections. Cyclic injections seem to trigger less induced seismicity than traditional monotonic injections (Yoon et al., 2014; Zang et al., 2013). Recent *in situ* and laboratory studies experimented with cyclic injection strategies and found that not only the number of seismic events but also the maximum recorded event magnitude is reduced (Zang et al., 2018). With the growing interest in the use of geo-

reservoirs, such cyclic stimulation might be of great interest for future injections. However, only a small number of experimental studies have been performed with the aim of increasing the comprehension of such phenomena, and those were mainly conducted on intact rock samples (Chanard et al., 2019; Farquharson et al., 2016; Noël et al., 2019a; Zhuang et al., 2016).

In this paper, we report triaxial deformation experiments performed on faulted Fontainebleau sandstone (FS), a quartz-rich sandstone. Particularly, we focus on the effect of oscillating fluid pressure.

5.3 Experimental methodology

5.3.1 Starting sample

FS (south of Paris, France) was used as starting material for this study. It is composed of almost 100% quartz, with randomly oriented grains cemented by quartz. The connected porosity was measured to be $6.5\% \pm 0.3\%$ at ambient conditions using the triple weight method (see Guéguen & Palciauskas, 1994). The permeability was measured using the steady-state Darcy flow method. Increasing the effective confining pressure from 20 to 50 MPa leads to a decrease of the permeability from 4 to $2 \times 10^{-15} \text{ m}^2$. Cylinders of FS were diamond drilled (36.5-mm diameter), sawed, and opposite faces ground flat to prevent any parallelism defects ($\pm 100 \text{ }\mu\text{m}$ precision). Cylinders were then sawed at $\alpha = 30^\circ$ from their axes to create an elliptical fault interface. The fault surfaces were rectified and then polished with a *Struers® MDpiano 80* abrasive disk (comparable to no. 80 SiC abrasive paper). The roughness of each fault surface was measured on a $1 \times 1\text{-cm}$ area using a 3D optical profilometer (*Contour GT-I3D-Optical Microscope, Bruker*). The initial roughness (here, defined as the mean quadratic height of the surface [Rq]) before sample deformation was mainly controlled by the porosity and was found to be characterized by $Rq = 17.4 \pm 0.5 \text{ }\mu\text{m}$. According to the permeability (k), the sample length ($l = 75 \text{ mm}$), water viscosity ($\eta = 10^{-3} \text{ Pa}\cdot\text{s}$), and typical storage capacity ($\beta = 10^{-11} \text{ Pa}^{-1}$) values for FS (Duda & Renner, 2013; Song & Renner, 2008), the characteristic time for water to diffuse across the sample was computed via $t_d = \frac{l^2 \eta \beta}{k}$ (Fischer & Paterson, 1989). We found $t_d < 1 \text{ s}$, and we planned our experiments so that the samples were always macroscopically drained, that is, $t_d \ll \text{oscillations period}$.

5.3.2 Apparatus

We used an instrumented Hoek cell (Figure 5. 1A) placed under a uniaxial press (*Walter and Bai*) as the deforming apparatus. The system allowed for an oil confining pressure ($P_c = \sigma_2 = \sigma_3$) up to 70 MPa ($\pm 50\text{-kPa}$ resolution) and a maximum axial stress ($\sigma_{ax} = \sigma_1$) of 1 GPa ($\pm 100\text{-kPa}$ resolution). Fluid pressure (de-aired distilled water, P_f) was imposed from the bottom of the sample with a step motor pump. The pore fluid pump had a 200-cm³ capacity and allowed for pressures up to 15 MPa. P_f was measured at the top and the bottom of the sample using precision pressure sensors ($\pm 10\text{-kPa}$ resolution). Pump fluid volume (V_f) variation was also monitored thanks to encoders directly mounted on the pump ($\pm 1\text{-mm}^3$ resolution). In addition, piezo-ceramic crystal (PI ceramic PRYY + 0400, 5-mm diameter and 1 mm thick) was glued to the bottom piston to monitor high-frequency acoustic emission (AE) events radiated from the samples during the tests. The emitted signal was amplified to 40 dB through a preamplifier. The trigger was set to only record events with

an amplitude higher than 0.056 V, that is, ≈ 1.75 times higher than the background noise of the experimental setup (measured at 0.032 V) to prevent noise recording. Each event that fulfilled this criterion was recorded at a 1-MHz sampling rate, within a time window of 400 μ s. Axial displacements were measured using linear optoelectronic transducers mounted outside of the cell with a precision of 1 μ m. The contribution of the jacket during the sample deformation was evaluated by shearing a faulted aluminium sample (pre-cut at 30° from its axis), having its opposite faces covered with a Teflon sheet. The jacket contribution was found to be negligible under the tested stress conditions.

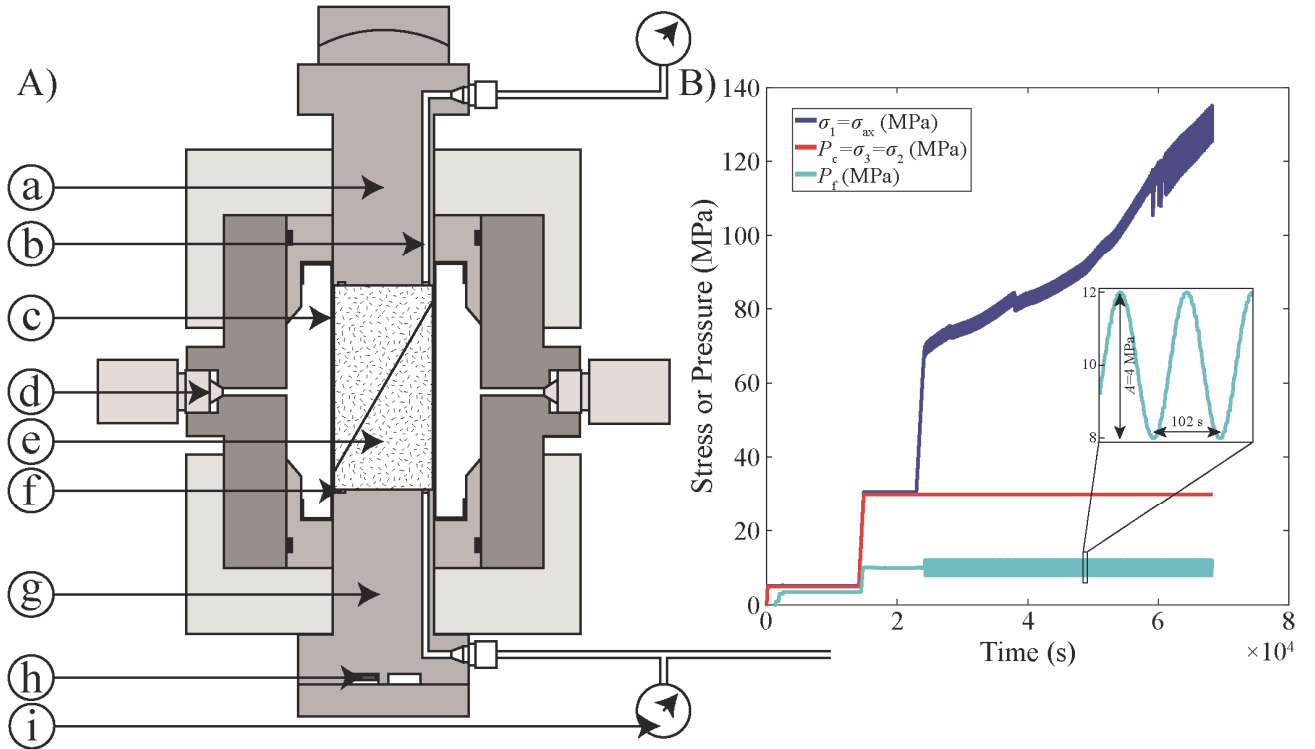


Figure 5. 1: (A) Cross-section drawing of the Hoek cell used for triaxial experiments. (a) top piston, (b) fluid pipes, (c) jacket, (d) confining oil inlet, (e) saw-cut sample, (f) drainage grooves allowing homogeneous fluid pressure distribution, (g) bottom piston, (h) acoustic emission sensor, and (i) pressure sensor. (B) Axial stress, confining, and fluid pressure applied as function of time. The inset displays the fluid pressure oscillations imposed during the experiment.

5.3.3 Experimental procedure

The procedure applied is presented in Figure 5. 1B. Faulted FS samples were placed into the Hoek cell and P_c was increased to 5 MPa. The sample was then pumped down to vacuum and pore fluid was injected at 1 MPa from the bottom piston. Once fluid pressure was equilibrated at the bottom and the top of the sample, P_f was increased to 3 MPa (i.e., $P_c - P_f = 2$ MPa) for 5 to 8 hr to ensure full sample saturation. Then, confining and fluid pressure were increased together to $P_c = 30$ or 45 MPa and $P_f = 10$ MPa. When V_f was equilibrated, the axial stress was increased by applying a constant and slow far-field loading rate (v_{ax} , between 10^{-4} and 10^{-3} mm.s $^{-1}$) on the axial pistons. Experiments were performed either with constant or cyclic (sinusoidal) fluid pressure. For cyclic fluid pressure experiments, the oscillations started only once the sample started to behave inelastically (stress – displacement curve deviating from linearity). The oscillations were imposed around a mean value of $P_f^{mean} = 10$ MPa with a peak-to-peak amplitude (A) ranging from 1 to 8 MPa and a

constant period of 102 s, systematically allowing the sample to remain under macroscopic drained conditions.

5.3.4 Data analysis

Friction along the fault interface (μ) was computed as the ratio between the shear stress (τ) and the effective normal stress ($\sigma_n - P_f$), calculated from the principal stress following

$$\mu = \frac{\tau}{\sigma_n - P_f} \quad \text{Equation (5. 1)}$$

$$\text{with } \tau = \frac{\sigma_1 - \sigma_3}{2} \sin(2\alpha) \quad \text{Equation (5. 2)}$$

$$\text{and } \sigma_n = \frac{\sigma_1 + \sigma_3 - 2P_f}{2} - \frac{\sigma_1 - \sigma_3}{2} \cos(2\alpha) \quad \text{Equation (5. 3)}$$

where σ_1 and σ_3 are the axial and the radial stresses, respectively, and α is the angle between the axial stress and the fault plane.

For the experiments where fluid pressure oscillated, we investigated the correlation between fast audible stress drops (hereafter referred to as stick-slip or unstable slip) and AE events with the fluid pressure oscillations. First, for each experiment, stick-slip and AE events were split with time intervals corresponding to the period of the fluid pressure oscillation as described in Noël et al. (2019). This allowed for the estimation of the distribution of events over the period of a fluid pressure oscillation. Second, to further investigate the correlation between the events and fluid pressure oscillations, AE events catalogue was treated following Schuster's method (Schuster, 1897). In the events catalogue, each event was attributed a phase angle and a unit length that depends on its position with respect to a forcing function (here the fluid pressure oscillations). Thus, each event was represented by a phasor of unit length. The sum of the N event phasors gave a vector of length R . The probability of a random walkout to reach a distance R from the origin can be given by $prob = \exp(-R^2/N)$ (Heaton, 1975; Rydelek & Hass, 1994; Schuster, 1897). If the walkout exceeds a given length, then the probability that the event phases are non-random is high, and the catalogue contains a significant correlation with the tested function. In our analysis, the fluid pressure maximum and minimum corresponded to a phase of 90° (i.e., upward) and 270° (i.e., downward), respectively.

5.4 Results

Stress – displacement curves (Figure 5. 2) first show a linear increase of the effective axial stress ($\sigma_1 - P_f$) as the axial displacement increases (i.e., elastic behaviour). This first elastic stage is followed by a deviation from linearity (i.e., onset of fault sliding) that occurs at $\mu \approx 0.53 \pm 0.02$, independent of the conditions tested. After this point, a stress hardening phase is observed, during which the fault slides in a stable manner. Finally, depending on the experimental conditions, the sliding behaviour may become seismic.

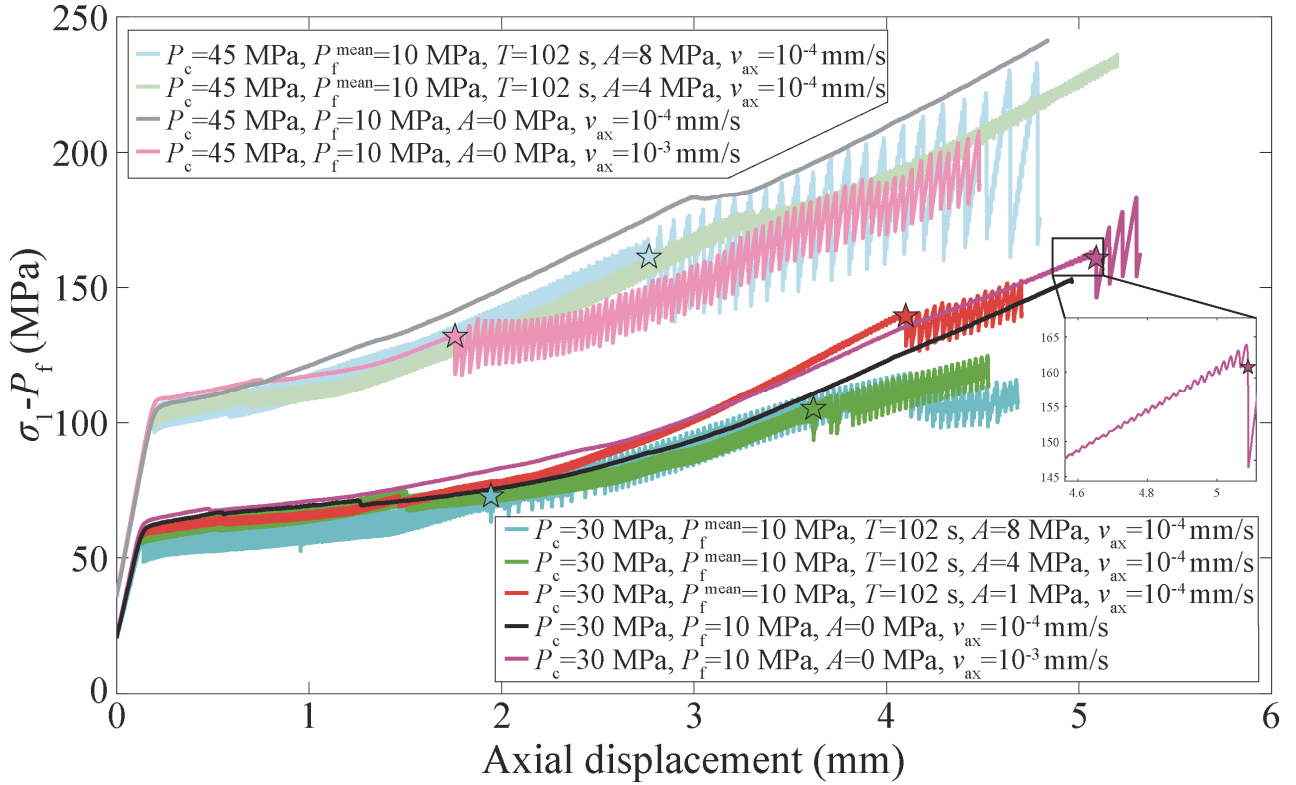


Figure 5. 2: Effective axial stress as a function of axial displacement during triaxial deformation experiments. The insert window presents the transition from stable to unstable slip behaviour during the experiment performed at $P_c = 30$ MPa and $v_{ax} = 10^{-3}$ mm.s $^{-1}$. If unstable behaviour was observed during the experiment, the star indicates the onset of stick-slip motions.

For experiments performed at a slow loading rate (i.e., $v_{ax} = 10^{-4}$ mm.s $^{-1}$), fluid pressure oscillations impact the slip behaviour of the faulted sample. Indeed, when no oscillations are imposed, the fault always slides in a stable manner (black curve in Figure 5. 2). However, when fluid pressure oscillations are imposed during the hardening stage, the fault first slides in a stable manner up to a point where a fast audible stress drop (i.e., unstable slip) occurs. Following the first unstable slip (denoted by a star in Figure 5. 2), fault slip is mostly accommodated by a stick-slip sequence (i.e., repetitive unstable slip followed by non-sliding period during which the system primarily behaves elastically). The recorded stress drops during seismic events increase with the confining pressure (from 10 MPa when $P_c = 30$ MPa to about 20 to 40 when $P_c = 45$ MPa). Importantly, we observe that the transition from stable sliding to stick-slip depends on the fluid pressure oscillation amplitude. Increasing the amplitude of P_f advances the onset of unstable slip (Figure 5. 2 and Table 5. 1). Both the axial displacement (d_{ax}) and the effective axial stress ($\sigma_1 - P_f$) at the onset of stick-slips are reduced as the amplitude of P_f increases. For example, at $P_c = 30$ MPa, increasing the amplitude of P_f from 1 to 8 MPa advances the onset of unstable slip from $d_{ax} = 4.1$ to 1.9 mm and from $\sigma_1 - P_f = 139$ to 72 MPa.

Table 5. 1: Summary of the triaxial experiments performed on Fontainebleau sandstone faulted samples.

Sample	P_c	Fluid pressure		Loading rate (v_{ax})	Onset of stick-slips		Max slip rate before stick-slip $\dot{\delta}_{max}$
		Mean	Amplitude		d_{ax}	$\sigma_1 - P_f$	
	(MPa)	(MPa)	(MPa)	(mm.s ⁻¹)	(mm)	(MPa)	(mm.s ⁻¹)
FSB24	30	10	-	10 ⁻³	5.089	160.7	1.17×10 ⁻³
FSB14	30	10	-	10 ⁻⁴	-	-	1.43×10 ⁻⁴
FSB16	30	10	1	10 ⁻⁴	4.100	139.5	2.97×10 ⁻⁴
FSB17	30	10	4	10 ⁻⁴	3.620	150.2	6.06×10 ⁻⁴
FSB12	30	10	8	10 ⁻⁴	1.944	72.82	6.49×10 ⁻⁴
FSB23	45	10	-	10 ⁻³	1.758	132.1	1.17×10 ⁻³
FSB18	45	10	-	10 ⁻⁴	-	-	1.43×10 ⁻⁴
FSB22	45	10	4	10 ⁻⁴	-	-	6.41×10 ⁻⁴
FSB19	45	10	8	10 ⁻⁴	2.766	161.2	7.72×10 ⁻⁴

Without fluid pressure oscillations, experiments show that the loading rate (v_{ax}) also has an effect on the sliding behaviour of the fault: At low v_{ax} (10⁻⁴ mm.s⁻¹), the fault slip is always stable, whereas at higher v_{ax} (10⁻³ mm.s⁻¹), a transition between stable sliding to stick-slip can be observed. At higher P_c , the transition occurs for shorter cumulative displacement than at lower P_c . This transition from stable to unstable behaviour can be abrupt and unpredictable (e.g., for the experiment at $P_c = 45$ MPa) or more gentle with periodic slow stress release presenting stronger and stronger amplitude with increasing cumulative slip before the first stick-slip occurs (e.g., for the experiment at $P_c = 30$ MPa, see zoom in Figure 5. 2).

Seismic correlations for experiments performed at $v_{ax} = 10^{-4}$ mm.s⁻¹, $P_c = 30$ and 45 MPa are presented in Figure 5. 3 and Figure 5. 4, respectively. When $A = 0$ MPa, AE events are spread, and the random walks show no significant correlation with time. However, when $A > 0$ MPa, stick-slip events are triggered when the fluid pressure is close to its maximum, and an increase of AE events is concomitant with the maximum value of P_f . Increasing A tends to promote the occurrence of stick-slip and AE events around the peak of the P_f oscillations.

The random walks of experiments with $A > 0$ MPa (Figure 5. 3 and Figure 5. 4) show that AE events are highly correlated with the pore fluid oscillations (probability $\gg 99\%$). The phase correlation (i.e., phase at the end of the random walk, ψ) occurs either just at the peak of P_f (e.g., the experiment at $P_c = 30$ MPa and $A = 1$ MPa or the experiment at $P_c = 45$ MPa and $A = 8$ MPa with $\psi = 93^\circ$ and 87° , respectively) or just before the peak of P_f (e.g., the experiment at $P_c = 30$ MPa and $A = 4$ MPa or the experiment at $P_c = 45$ MPa and $A = 4$ MPa with $\psi = 69^\circ$ and 76° , respectively). For the experiment at $P_c = 30$ MPa and $A = 8$ MPa, the random walk shows two trends. First, AE events

are mainly correlated with the maximum value of P_f ($\psi \approx 100^\circ$), then they correlate with the maximum decreasing rate of P_f ($\psi \approx 180^\circ$), and finally back with the maximum value of P_f ($\psi \approx 90^\circ$).

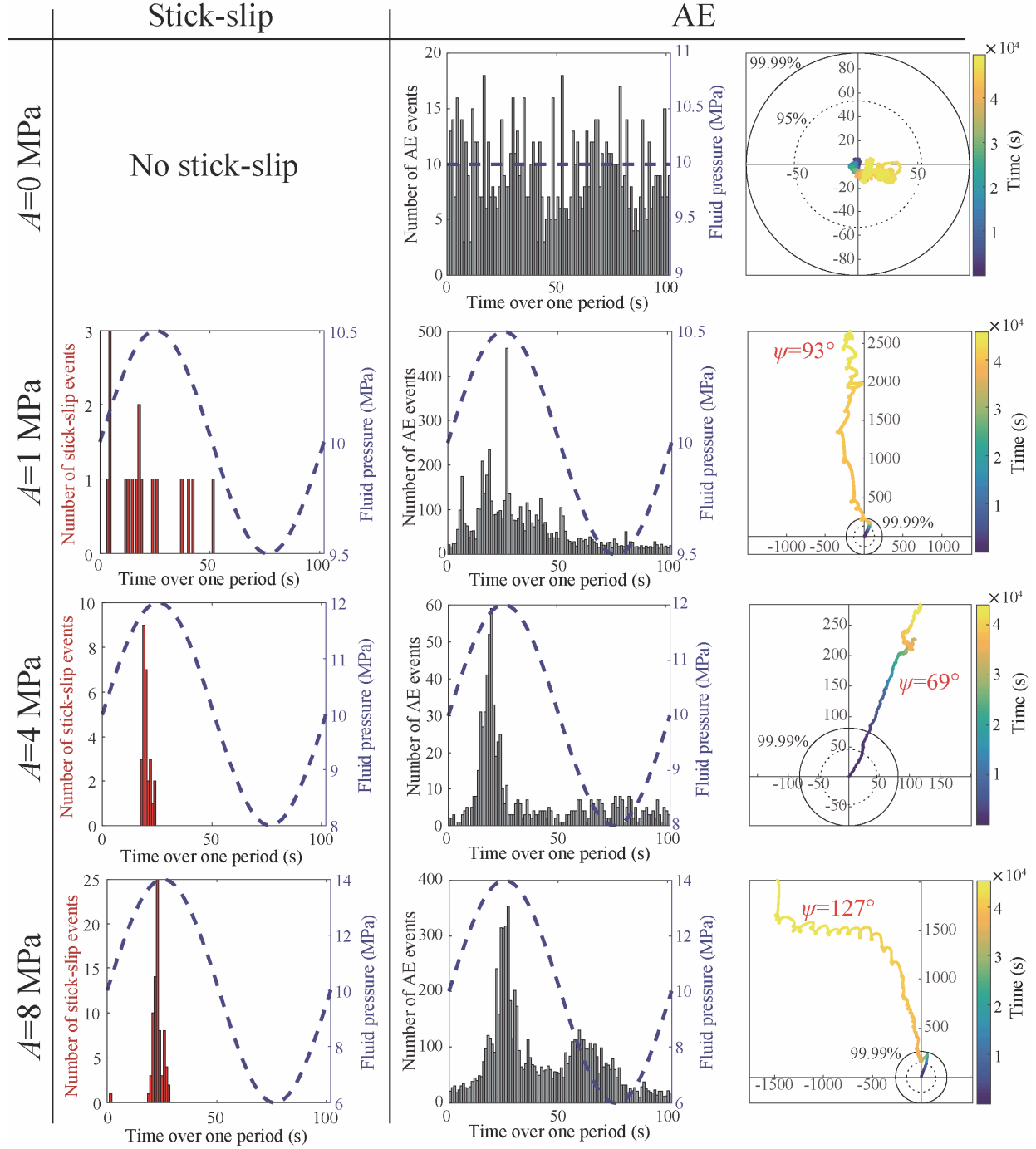


Figure 5. 3: Event analyses for experiments performed at $P_c = 30$ MPa and $v_{ax} = 10^{-4}$ mm.s $^{-1}$ with various amplitudes of fluid pressure oscillations. Stick-slip events and acoustic emission (AE) events stacked over one oscillation period are displayed by red and grey bar charts, respectively. The bar charts represent the number of events, and the blue dashed lines represent the fluid pressure oscillations. A random walk of the catalogue of AE events, with the experimental time shown by the colour bar, is also presented. If the random walk exceeds a critical distance and has a high probability ($> 95\%$) of being correlated with the P_f oscillations, the phase at the end of the random walk (ψ) is noted. The maximum and minimum of fluid pressure correspond to a phase of 90° (i.e., upward) and 270° (i.e., downward), respectively. The probability distances 95% and 99.99% are plotted (dashed and full circle, respectively).

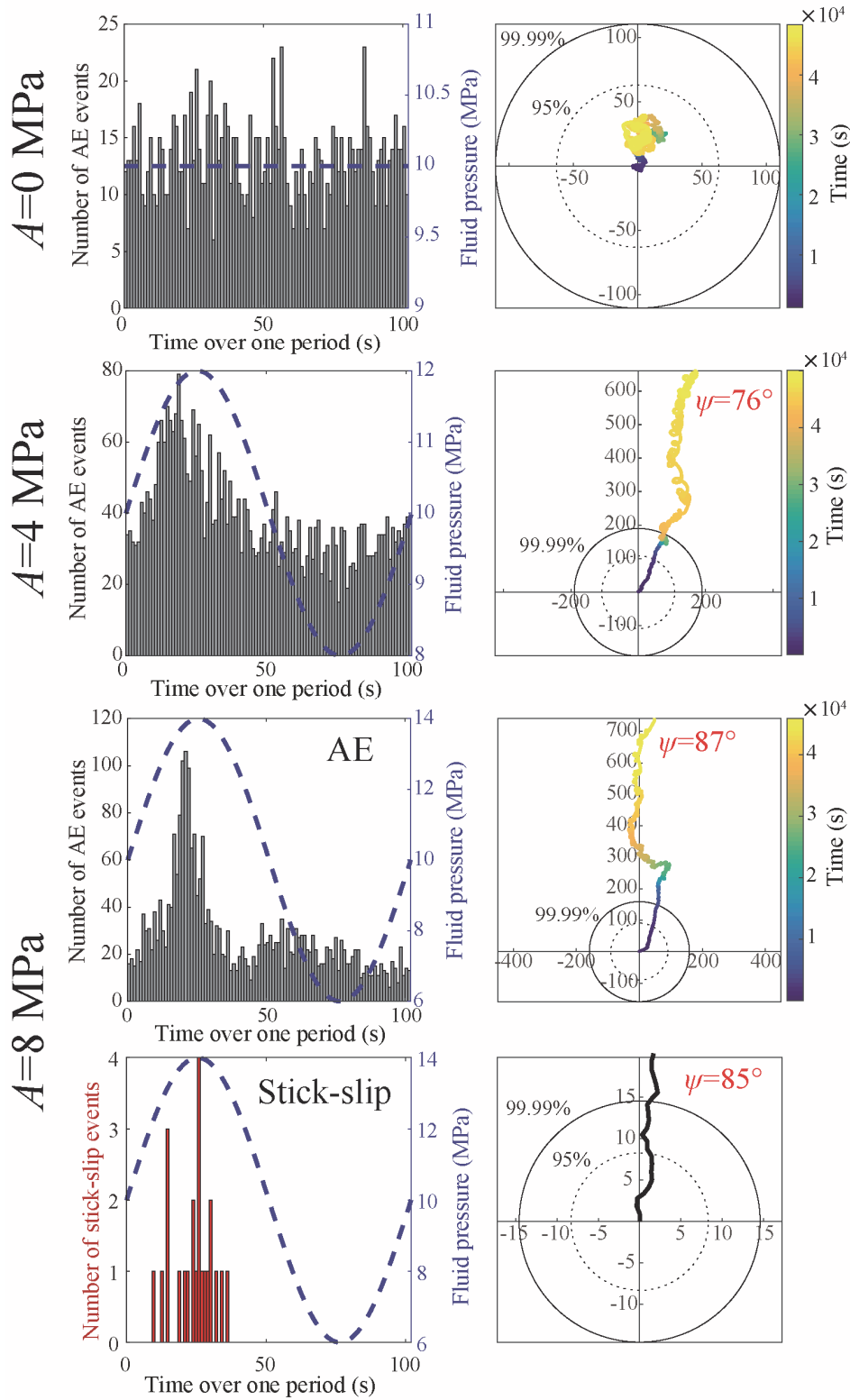


Figure 5. 4: Event analyses for experiments performed at $P_c = 45$ MPa and $v_{ax} = 10^{-4}$ mm.s $^{-1}$ with various amplitudes of fluid pressure oscillations. Stick-slip events and acoustic emission (AE) events stacked over one oscillation period are displayed by red and grey bar charts, respectively. Stick-slip events occurred only for $A = 8$ MPa. The bar charts represent the number of events, and the blue dashed lines represent the fluid pressure oscillations. A random walk of the catalogue of AE, with the experimental time shown by the colour bar, and stick-slip events is also presented. If the random walk exceeds a critical distance and has a high probability ($> 95\%$) of being correlated with the P_f oscillations, the phase at the end of the random walk (ψ) is noted. The maximum and minimum of fluid pressure correspond to a phase of 90° (i.e. upward) and 270° (i.e., downward), respectively. The probability distances 95% and 99.99% are plotted (dashed and full circle, respectively).

5.5 Interpretation and discussion

Our experimental results highlight that (i) stick-slip events are triggered after a certain amount of stable sliding that induces fault hardening. (ii) At a constant v_{ax} , fluid pressure oscillations promote unstable slip (i.e., stick-slips are triggered after a smaller displacement and at lower stresses). (iii) Increasing the amplitude of the oscillations advances the onset of unstable motion. (iv) When fluid pressure oscillations are imposed, instabilities (i.e., stick-slip and AE events) are mainly triggered close to the maximum value of fluid pressure.

In the following, we first give a brief overview of fault reactivation and frictional sliding stability conditions and then interpret and discuss our main observations.

5.5.1 Theoretical framework for fault reactivation and frictional stability

Fault reactivation and fault stability can be described with two distinct criteria. On the one hand, the Mohr-Coulomb failure criterion describes the amount of shear stress (τ) required at a given normal stress (σ_n) to induce the onset of slip. It defines the shear strength of the fault and predicts its reactivation when $\tau \geq \mu (\sigma_n - P_f)$. On the other hand, the rate-and-state friction formulation provides a comprehensive analysis of the behaviour once the fault slip has initiated. In this framework, the frictional response of a fault varies with the loading history and depends on both the instantaneous slip rate and a state variable that describes the gradual evolution of the sliding interfaces (Dieterich, 1978; Ruina, 1983). Assuming these variables, the evolution of the frictional coefficient during slip can be estimated as follows:

$$\mu = \mu_0 + a \ln\left(\frac{V}{V_0}\right) + b \ln\left(\frac{V_0 \theta}{D_c}\right) \quad \text{Equation (5. 4)}$$

where, considering the so-called slip law, the state variable θ evolution is expressed as

$$\frac{d\theta}{dt} = -\frac{V\theta}{D_c} \ln\left(\frac{V\theta}{D_c}\right) \quad \text{Equation (5. 5)}$$

with μ_0 being the reference friction at the velocity V_0 , V the slip velocity, and D_c the critical slip distance. If the friction decreases as the sliding velocity increases (i.e., velocity weakening, $(a - b) < 0$), the fault might experience dynamic instability; on the contrary, if the friction increases with an increasing sliding velocity (i.e., velocity strengthening, $(a - b) > 0$), slip is accommodated by stable sliding.

Finally, when combined with the elastic dislocation theory (elliptical crack embedded in an isotropic elastic medium), the rate-and-state formulation states that if the stiffness of the elastic medium (K) is smaller than the critical fault stiffness (K_c), frictional instability can occur (e.g., Kanamori & Brodsky, 2004). Coupling the rate-and-state friction approach with a one-dimensional spring – slider model, the transition from stable to unstable slip can be found at the critical stiffness (Dieterich, 1979; Gu et al., 1984; Rice, 1993; Ruina, 1983):

$$K_c = \frac{(b-a)(\sigma_n - P_f)}{D_c} \quad \text{Equation (5. 6)}$$

In summary, after fault reactivation (i.e., fault strength is overcome), the fault frictional behaviour can be divided into three stability domains: (1) if $(a - b) > 0$, the system is stable; (2) if $(a - b) < 0$ and $K > K_c$, the system is conditionally stable (i.e., stable under quasi-static loading); or (3) if $(a - b) < 0$ and $K < K_c$, the system is unstable.

Here we are interested in the effect of fluid pressure oscillations on the fault reactivation and stability. Using these theoretical formulations and considering drained and homogeneous conditions, a fluid pressure increase on the fault plane has two effects: First, it decreases the effective normal stress acting on the fault, promoting fault reactivation. Second, it can decrease the critical stiffness K_c , thus favouring slow and stable sliding rather than unstable events (i.e., earthquakes).

5.5.2 Fluid pressure oscillation influences the events distribution

In agreement with Byerlee's rule (Byerlee, 1978), in the performed experiments, we observe a deviation from the elastic domain at $\mu \approx 0.53 \pm 0.02$. Moreover, when fluid pressure oscillations are imposed, instabilities (i.e., stick-slip and AE events) are being triggered close to the maximum value of fluid pressure. Increasing the amplitude of P_f accentuates this behaviour (Figure 5. 3 and Figure 5. 4). Assuming a Coulomb failure criterion, a P_f increase has the effect of bringing the fault closer to failure independent of the fault slip behaviour (stable or unstable). During the oscillating fluid pressure experiments, two parameters determine the moment when the fault strength will be reached: the increase in σ_1 and the oscillations imposed in P_f . Thus, a competition between the increase in σ_1 and the increase in P_f is occurring, that is, between v_{ax} (which affects σ_1) and the period of the P_f oscillations. Let us imagine that the period of P_f oscillation is infinitely long (or that v_{ax} is infinitely fast), in this case, the strength of the fault would be reached mainly due to the increase of σ_1 and P_f would have only a minor effect. On the contrary, if the period of the P_f oscillations is small compared to the increase in σ_1 , the strength of the fault would be reached primarily due to the increase of P_f . Here, within one period of oscillation, the increase in σ_1 is low compared to the pore fluid variation such that stick-slip and AE events mainly occur around the maximum value of P_f . Increasing the amplitude from 1 to 8 MPa and keeping the same period of the oscillations amplifies this phenomenon as the strength of the fault is reached faster. In summary, the time distribution of the AE and stick-slip events is controlled by the Mohr-Coulomb failure criterion and depends on both the far-field loading and the period of the fluid pressure oscillations.

5.5.3 Fluid pressure oscillations promote early instability

In the performed experiments, stick-slips (i.e., unstable slip) are triggered after a long phase of stable sliding, sometimes preceded by smooth, slow stress release (Figure 5. 2). The experiments show also that, at low v_{ax} , imposing fluid pressure oscillations facilitates unstable behaviour (stick-slip). The higher the amplitude of the oscillations, the earlier stick-slip events are triggered. This transition can be explained by the fact that, even if the fault is velocity weakening (i.e., $(a - b) < 0$), the fault critical stiffness K_c is not reached from the beginning of the fault's sliding.

During our experiments, K_c depends on three parameters: (1) the slip hardening behaviour, (2) the fluid pressure oscillations, and (3) the cumulative slip, such that

1. Due to the experimental configuration, while slip hardening occurs and the axial stress increases, the normal stress acting on the fault plane is also increasing. Increasing the effective normal stress acting on the fault increases K_c , moving the system toward unstable behaviour (equation 5. 6). Similar observations were made on quartz gouge where increasing the applied effective normal stress moved the system toward more unstable behaviour (e.g., Leeman et al., 2016, 2018; Scuderi et al., 2017).
2. Fluid pressure oscillations also cause variation in the effective normal stress acting on the fault plane, thus provoking K_c oscillation.
3. The parameters a , b , and D_c may also change with the normal stress, slip rate, and accumulated displacement, which, in turn, may change the stability behaviour of the system (e.g., Leeman et al., 2018; Mair & Marone, 1999; Marone & Scholz, 1988; Scuderi et al., 2017). Indeed, during the fluid pressure oscillation experiments, when looking at the slip rate along the fault as a function of time, we observe that increasing the amplitude of the oscillations affects the slip rate on the fault; the slip rate is oscillating in phase with the fluid pressure oscillations, and the maximum slip rate acting on the fault ($\dot{\delta}_{\max}$) is concomitant with the maximum value of P_f . $\dot{\delta}_{\max}$ increases from 1.43×10^{-4} to 6.49×10^{-4} mm.s⁻¹ increasing A from 0 to 8 MPa (Table 5. 1). Moreover, without fluid pressure oscillations, increasing v_{ax} to 10^{-3} mm.s⁻¹ also facilitates stick-slip triggering (Figure 5. 2).

The difference in the onset of unstable slip must originate from the fluid pressure oscillations. Indeed, for all the experiments, the hardening rate is similar (Figure 5. 2) and cannot explain the enhancement of stick-slip events with increasing the amplitude of fluid pressure oscillation.

To test the other two hypotheses, we conducted complementary experiments that explored the influence of the normal stress of the fluid pressure and of the slip rate on the frictional properties of the experimental faults. These experiments consist of velocity step experiments, typically used to constrain the rate-and-state parameters (a , b , and D_c) of fault interfaces. These experiments were performed using the same apparatus and sample configuration described earlier. After saturation at low confining pressure, the samples were loaded to $P_c = 45$ MPa. Axial stress was increased by applying a constant loading rate while the normal stress was kept constant on the sample fault by regulating the confining pressure with a servo-controlled loop. The samples were first sheared at $v_{\text{ax}} = 10^{-3}$ mm.s⁻¹ for $d_{\text{ax}} = 1$ mm. Then, they were subjected to a sequence of increasing and decreasing v_{ax} between 10^{-5} and 3×10^{-3} mm.s⁻¹, that is between 1.15×10^{-5} and 3.46×10^{-3} mm.s⁻¹ along the fault plane, for $d_{\text{ax}} = 0.1$ mm (Figure 5. 5a). Two experiments were performed at $\sigma_n = 45$ MPa and at $P_f = 1$ and 10 MPa (i.e., two different effective normal stresses). This normal stress was chosen because it corresponds to the middle range of the normal stress applied during the experiments performed at $P_c = 30$ MPa. Then, we inverted the frictional parameters from experimental measurements by modelling the velocity steps, assuming the rate-and-state slip law (Ruina, 1983; equation 5. 4 and 5. 5). The inversion of the experimental data was made using the software package developed by Skarbek & Savage (2019) (Figure 5. 5b). The rate-and-state parameters found (Figure 5. 6) show (i) No significant difference between the experiment with $P_f = 1$ or 10 MPa. (ii) A transition from positive to negative ($a - b$) as the slip rate increased. The transition occurs around a velocity of 2×10^{-4} mm.s⁻¹ along the fault. (iii) D_c values do not show a significant variation with the slip rate or the effective normal stress. In summary, these results suggest that variations in the slip rate

rather than in the effective normal stress are expected to promote the transition from stable to unstable slip.

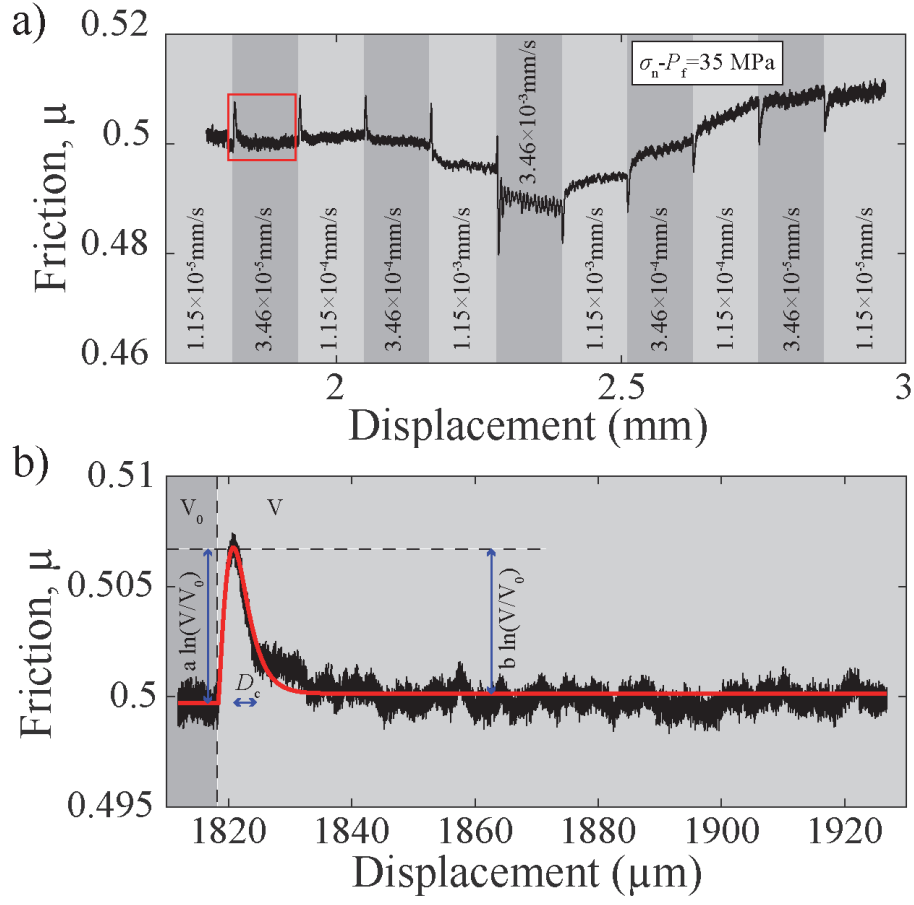


Figure 5. 5: a) Friction as a function of the displacement along the fault plane for the velocity steps experiment performed at $\sigma_n - P_f = 35$ MPa. b) Zoom on a velocity step. The experimental curve is presented in black, and the model inversion using the Skarbek & Savage (2019) software is presented in red.

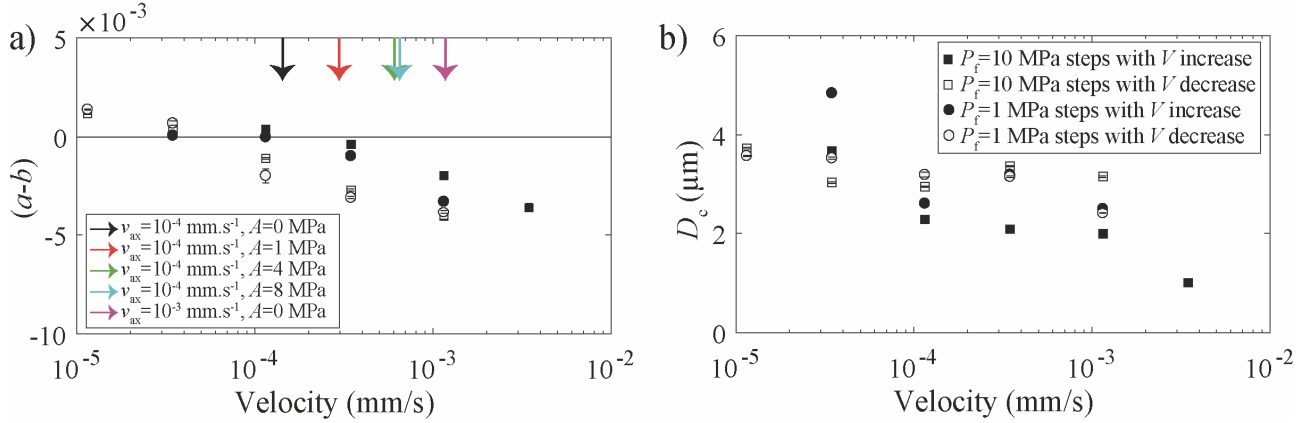


Figure 5. 6: Rate-and-state parameters obtained from the inversion of the experimental data. a) Displays $(a - b)$ and b) critical slip distance as a function of velocity. For the experiment conducted at $P_f = 1$ MPa, the inversion was not possible at the velocity of $3.46 \times 10^{-3} \text{ mm.s}^{-1}$ because stick-slip occurred (i.e., $(a - b) < 0$). The maximum displacement rate of the fault before any instability (δ_{\max}) is presented with the coloured arrows for experiments performed at $P_c = 30$ MPa.

Stability transitions with increasing loading rate have already been reported on granite (e.g., Kato et al., 1992; McLaskey & Yamashita, 2017), metagabbro (e.g., Xu et al., 2018), and polycarbonate (e.g., Guérin-Marthe et al., 2019) dry meter-scale faulted samples. The transition is often attributed to a shrinking of the measured critical nucleation length (L_c) when increasing the loading rate. L_c is defined as the critical size that a sliding patch has to expand to become unstable and is inversely proportional to the critical stiffness K_c . In our experiments, L_c could not be directly inferred from experimental measurements. However, using the rate-and-state framework, K_c can be estimated (see equation 5. 6).

Note that, even if it has been shown that the effective normal stress acting on the fault has an effect on the stability of the system (e.g., Chambon & Rudnicki, 2001; Dieterich & Linker, 1992; He et al., 1998; He & Wong, 2014; Leeman et al., 2016, 2018), here, no significant difference was found for the effective normal stress tested. Therefore, a , b , and D_c are taken to be independent of the effective normal stress. Using our experimental dataset, K_c can be estimated directly from the rate-and-state parameters found (equation 5. 6). We computed K_c normalized by the system stiffness (K) as function of the sliding velocity (Figure 5. 7). Note that K was measured by deforming an FS sample within the elastic domain while measuring the displacement of the surrounding system (the press column and FS) by the use of an external displacement sensor.

For K_c calculation, we assumed the empirical dependence of the parameters $(a - b)$ and D_c with the sliding velocity (i.e., following the trends in Figure 5. 6). Within the slip rate explored during the fluid pressure oscillating experiments (from 10^{-4} to $10^{-3} \text{ mm.s}^{-1}$), the three stability domains are crossed in our experiments (Figure 5. 7). Indeed, we observe a transition between stable and conditionally stable state at a velocity of $1.2 \times 10^{-4} \text{ mm.s}^{-1}$ and a transition between conditionally stable and unstable at velocity of about $6 \times 10^{-4} \text{ mm.s}^{-1}$. The fact that fluid pressure oscillations facilitate stick-slip triggering must originate from the slip rate oscillations in phase with P_f that in turn cause variations of K_c . In summary, the initiation of the AE and stick-slip events is controlled by the coupled rate-and-state and dislocation criterion.

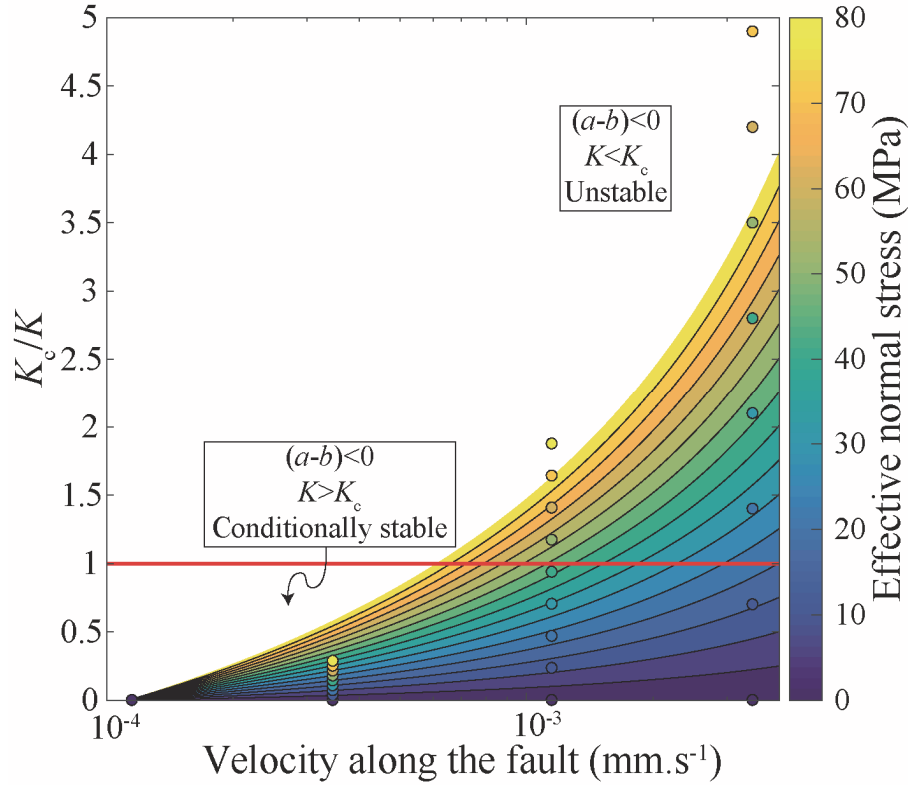


Figure 5. 7: Critical stiffness (K_c) normalized by the stiffness of the experimental surrounding system (K) as a function of the slip velocity. The colour bar shows the effective normal stress acting on the fault. The contour plot represents K_c modelled using equation (5. 6). The circles represent K_c/K using the rate-and-state parameters found experimentally. The conditionally stable and unstable domains are separated by the solid red line. The parameters used for the model were obtained from the fit of the parameters experimentally obtained in Figure 5. 6. They are: $(a - b) = -8.97 \times 10^{-4} \ln(V) - 8.2 \times 10^{-3}$, and $D_c = -4.9 \times 10^{-1} \ln(V) - 1.7$. The stiffness of the system (apparatus and Fontainebleau sandstone) was measured to be 62.9 MPa.mm^{-1} .

5.5.4 Implications for natural and induced seismicity

Our experimental results demonstrate that fluid pressure cyclic perturbations in a drained system can lead to fault reactivation and to the onset of the seismicity resulting from slip rate perturbations. The smaller the confining pressure and the larger the amplitude of the fluid pressure, the larger the seismic triggering potential of the fault in the tested material.

In natural fault systems, it is accepted that a locked velocity weakening (i.e., $(a - b) < 0$) patch on a fault can fail either in a seismic or aseismic manner. If the patch is gently loaded by a creeping surrounding area, and that $K < K_c$, the slip will accelerate to seismic velocity. On the contrary, for conditions where $K > K_c$, instability cannot nucleate. Our experimental results suggest that if this patch is subjected to fluid pressure oscillations, local variations of slip rate could change the rate-and-state parameters and increase the critical stiffness, allowing for possible seismic slip. Such acceleration of the slip rate can have many fluid-related origins such as oceanic and earth tides (e.g., Houston, 2015; Rubinstein et al., 2008; Rydelek et al., 1992; Scholz et al., 2019), seasonal hydrology (e.g., Bettinelli et al., 2008; Chanard et al., 2014), or fluid production/injection into geo-reservoir (e.g., Candela et al., 2019; Verdon et al., 2013). In the case of fluid injection, it has been recently suggested that cyclic fluid injections would trigger less seismicity compared to traditional monotonic injections (e.g., Yoon et al., 2014; Zang et al., 2013, 2018). Our experimental results suggest that, under drained conditions, cyclic fluid pressure variations within a faulted reservoir have the effect

of varying the slip rate acting on the fault, in turn increasing K_c and promoting unstable slip. However, cyclic fluid injections compared to monotonic fluid injection involve much lower strain rates increases and thus reduce the potentially induced earthquakes. During *in situ* cyclic fluid injections, fluid pressure tends to homogenize via diffusion processes into the reservoir during period of limited injection. In turn, if the injection frequency increases, this can affect both the drainage conditions and promote high deformation rates. Undrained conditions have been shown to produce local fluid overpressure and favour fault reactivation (Passelègue, Brantut, et al., 2018). Therefore, it is probable that injection frequency, in addition to injection amplitude, might affect fault stability in geo-reservoirs.

5.6 Conclusions

We conducted nine triaxial deformation experiments on faulted Fontainebleau sandstone with various fluid pressure oscillation conditions and loading rates. Two additional velocity step experiments were performed in triaxial configurations in order to constrain the rate-and-state parameters of the studied FS. The results show that:

1. Faults start to slip when $\mu = 0.52$, in agreement with Byerlee's law.
2. During pore pressure oscillations:
 - a. Fluid pressure signal controls the instability (i.e., stick-slip and AE events) distribution. In this drained case, instabilities occur mainly at the maximum value of fluid pressure.
 - b. Stick-slip events are triggered only after a certain amount of stable sliding. This amount of slip is reduced with increasing P_f oscillation amplitude. We suggest that it is not the pore fluid pressure itself that controls the onset of instability but the variation of slip rate due to the fluid oscillations.
3. From the velocity-step experiments, we find that fault stability depends on the slip rate. Increasing the slip velocity promotes unstable slip.

The stability analysis based on the rate-and-state parameters shows that the critical stiffness can be increased with increasing the fault slip rate. We thus infer that the oscillations in slip velocity induced by fluid pressure oscillations can result in critical stiffness changes, in turn promoting the transition from stable to unstable slip and controlling the instability distribution.

Acknowledgments

This work was funded by Gaznat SA (Grant FRICTION: Fault Reactivation during CO₂ sequestration). F. X. P. thanks the Swiss National Science Foundation (Grant PZENP2/173613). C. G. thanks the Swiss Federal Office of Energy (EDGAR project). M. V. thanks the ERC project befine (Grant 757290). The authors want to thank Laurent Gastaldo for laboratory assistance. We also thank Barnaby Fryer for proofreading. The authors thank the editor A. Revil, the associate editor Mike Heap, and the reviewers J. W. Rudnicki and Dave Healy for their constructive comments. Raw data can be found at <https://zenodo.org/record/3515757#.Xa6vH-gzZaQ> or requested from the corresponding author at corentin.noel@epfl.ch.

Chapter 6 Brittle faulting of ductile rock induced by pore fluid pressure build-up

Authors: Corentin Noël¹, François X. Passelègue¹, Marie Violay¹

¹ Laboratory of Experimental Rock Mechanics, Ecole Polytechnique Fédérale de Lausanne, Lausanne, Switzerland

Status: Submitted to the Journal of Geophysical Research: Solid Earth

Reference: Noël, C., Passelègue, F. X., & Violay, M. Brittle faulting of ductile rock induced by pore fluid pressure build-up. *Under Review at Journal of Geophysical Research: Solid Earth*

Contributions: C. Noël prepared and characterized the sample. C. Noël has run the experiments. All the authors have participated to the experimental strategy. C. Noël has carried out the data treatment. All the authors have contributed to the data analysis. C. Noël has written the manuscript. All the authors have contributed to guide the discussion of the manuscript. M. Violay has acted as a supervisor.

Highlights:

- Localized fracture can develop in initially ductile rocks due to pore fluid pressure increase
- Shear fracturing in the ductile rock is controlled by a brittle failure criterion and a critical dilatancy.
- Injection rate controls the final fracture distribution.

6.1 Abstract

Under upper crustal conditions, deformations are primarily brittle (i.e., localized) and accommodated by frictional mechanisms. At greater depth, deformations are ductile (i.e., distributed) and accommodated by crystal plasticity, diffusion mass transfer or cataclastic flow. The transition from the brittle to the ductile domain is not associated with a critical depth, but rather varies in time and space. One main parameter controlling the variation of this transition is the pore fluid pressure. On the one hand, a pore fluid pressure increase reduces the effective stresses and possibly increases the strain rate, bringing the system closer to brittle conditions. On the other hand, pore fluid can favour ductile mechanisms, mostly via chemical effects, by facilitating intra-crystalline plasticity, enhancing fluid-solid diffusion and fracture healing/sealing.

We report triaxial laboratory experiments that investigated the effect of pore fluid pressure increase during the ductile deformation of Tavel limestone. Three injection rates were tested: 1, 5 and 10 MPa/min. We demonstrate that: 1) Under initially ductile conditions pore fluid pressure increase immediately turns the system from compaction to dilation. 2) Dilation is due to the development of localized shear fractures. However, the macroscopic localisation of the deformation is not instantaneous when the ductile to brittle transition is surpassed; a transient creeping phase is first needed. 3) To reach macroscopic brittle failure of initially ductile samples, a critical dilatancy is required. 4) Injection rate controls the final fracture distribution. We demonstrate that pore pressure build-up in a rock undergoing ductile deformation can induce shear fracturing of the system.

Keywords: fluid-rock interactions, pore fluid pressure increase, ductile-brittle transition, micro-structure, triaxial experiment

6.2 Introduction

In the Earth's crust, irreversible deformations are usually accommodated by two distinct modes: brittle and ductile. Within the upper part of the crust, irreversible deformations are brittle and mainly localized along shear fractures (i.e. faults), limiting the rock strength to frictional and fracture motions (Paterson & Wong, 2005; Scholz, 2019). At greater depth, due to the increase of pressure and temperature, irreversible deformations are distributed, i.e. ductile (Fredrich et al., 1989; Paterson & Wong, 2005; Scholz, 2019; Wong et al., 1997), and accommodated through plastic mechanisms such as mechanical twinning, dislocation creep (B. Evans et al., 1990), grain boundary diffusion/volume diffusion creep (Goetze & Brace, 1972; Rutter, 1986) or cataclastic flow (T. Wong & Baud, 2012). In this domain, the rock strength is described by flow laws sensitive to the temperature and deformation rate (Evans & Kohlstedt, 1995; Goetze & Brace, 1972; Goetze & Evans, 1979). Because rocks are polycrystalline materials, with each crystal having its onset of plastic deformation occurring under different conditions, the transition from brittle to ductile deformation with depth is intrinsically gradual. This transitional domain is called semi-brittle and involves the coexistence of both brittle and plastic deformation mechanisms (Joanne T Fredrich et al., 1989; Meyer et al., 2019). This domain is of major importance as it marks the limit depth of seismicity (e.g. Sibson, 1977, 1982) and the limit of hydrothermal circuits in the crust (Violay et al., 2012, 2015, 2017). These two characteristics have led this domain to become of interest for deep

reservoirs (e.g. Asanuma et al., 2012; Bignall & Carey, 2011; Frioleifsson et al., 2014; Tsuchiya et al., 2015).

Experimental studies of the brittle and ductile domains have led to a few simple constitutive laws meant to describe the deformation with a single mechanism (B. Evans & Kohlstedt, 1995; D. A. Lockner, 1995). These largely empirical laws are often derived from low-temperature tests on compact rocks, (i.e. rocks with low porosity and without partial melts). In the brittle field, the empirical Coulomb failure criterion: $\tau = C + \mu' (\sigma_n - P_f)$, where τ is the shear strength, σ_n is the normal stress, P_f is the pore fluid pressure and μ' is the local slope of the failure criterion in the $\tau - \sigma_n$ space, remains the most used. However, theoretical formulations linking the remote stress applied to the rock sample to its internal damage have also been developed (e.g. Ashby & Sammis, 1990; Costin, 1983, 1985; Sammis & Ashby, 1986). The most used is the *wing-crack model* developed by Ashby and Sammis (1990). In this model, that considers the initiation of the rock damage from inclined penny shape cracks, the strength of the rock depends on the applied confining and pore fluid pressures as well as some material parameters (i.e. initial damage, fracture toughness and frictional parameters). In the ductile field, dislocation creep is often represented by a steady-state power law of Arrhenius type (B. Evans & Kohlstedt, 1995; Kohlstedt et al., 1995; Weertman, 1978): $\dot{\epsilon} = A(\sigma_1 - \sigma_3)^n \exp\left(-\frac{Q}{RT}\right)$, where A is a material constant, σ_1 and σ_3 are the maximum and minimum principal stresses, n is the stress exponent, Q is the activation energy, R the gas constant and T the temperature. Other laws exist to describe ductile deformation (see Evans & Kohlstedt, 1995); however, they are all linked to a single mechanism of deformation. Moreover, all these constitutive laws are rough generalizations that neglect the effects of important state variables such as fluid chemistry, pore geometry, rock alteration and microstructural changes. Furthermore, in the semi-brittle domain where both brittle mechanisms, such as frictional sliding or micro-cracking, and plastic mechanisms coexist, recent micromechanical models have been described (e.g., Wei & Anand, 2008); however, they are used under very specific conditions, and no simple satisfactory constitutive law exists for general cases. In summary, laboratory measurements have shown that the transition from brittle to ductile deformation is favoured by: 1) increasing the effective confining pressure, i.e. the difference between the confining and the pore fluid pressures $P_c - P_f$, (e.g. Fredrich et al., 1989; von Kármán, 1911; Paterson, 1958); 2) increasing the temperature (e.g., Heard, 1960; Tullis & Yund, 1977); 3) decreasing the strain rate (e.g. Rutter, 1972; Tullis & Yund, 1980). Therefore, depending on the in-situ conditions, the transition from brittle to ductile deformations is not related to a critical depth but varies with time and space (e.g. Handy et al., 2007).

One of the most important parameters that can move the brittle-ductile transition in time and space is the pore fluid pressure. Under ductile conditions, a pore fluid pressure increase can be related to natural causes (e.g. magma build-up in volcanic edifices, magmatic fluid pulses or fluid release during mineral phase changes) or to anthropogenic causes (e.g. for geo-energy purposes). Around the brittle-ductile transition, such pore fluid pressure variations may have a significant impact on the rock mass mode of deformation. On the one hand, pore fluid pressure variations can act as a catalyst for brittle deformation by: 1) reducing the effective confining pressure, bringing the mass rock closer to the brittle domain, particularly under drained conditions (Bernabe & Brace, 1990; Handin et al., 1963; Robinson, 1959; Rutter, 1972); and 2) increasing the strain rate if rapid variations of the pore fluid pressure are produced (e.g. Noël et al., 2019a, 2019b). On the other

hand, pore fluid can promote ductile deformations through chemically activated mechanisms by: 1) inhibiting the internal fracture of individual grains, allowing for intra-crystalline plasticity (Griggs, 1967; Heard, 1960; Rutter, 1972); 2) enhancing fluid-solid diffusion (e.g. Farver & Yund, 1991); and 3) favouring fracture healing and sealing (e.g. Renard et al., 2000; Tenthorey et al., 2003).

Despite its importance for the brittle-ductile transition, only rare experimental studies have investigated the effect of increasing pore fluid pressure from the ductile domain toward the brittle domain. For example, Schubnel et al. (2006) showed that brittle deformations are favoured in marble deforming under initially ductile conditions as a result of an effective confining pressure reduction. Additionally, Ougier-Simonin & Zhu (2013) showed that in porous sandstone, under initial conditions favouring ductile deformation of the sample (i.e. at an effective confining pressure of 70 MPa), increasing the pore fluid pressure from 10 to 18 MPa promotes strain localisation.

In this paper, we report new results from laboratory triaxial deformations performed under ductile conditions on a porous limestone. Particularly, we investigated the effect of an increase of pore fluid pressure on the transition toward the brittle domain, as well as the effect of the injection rate on ductile-brittle transitions.

6.3 Experimental methodology

6.3.1 Starting sample

Tavel limestone (North-West of Avignon, France) was used as a starting sample for the triaxial tests. It is almost 100% calcite and mainly composed of micrite particles of about 5 μm diameter cemented together (Nicolas et al., 2016, 2017; Vajdova et al., 2004a, 2010; Vincké et al., 1998). Microscope analysis (with optical and scanning electron microscopes) of the sample revealed that its porosity is composed mainly of micro-pores at the junction between micritic particles and by a small number of more or less spherical macro-pores with diameters ranging from about 5 to 50 μm , consistent with previous pore analyses by Zhu et al., (2010). A detailed microscopic description of Tavel limestone can be found in Vajdova et al. (2010) and Zhu et al. (2010). This particular limestone has been chosen because calcite is capable of deforming plastically under room temperature and relatively low confining pressure conditions, facilitating experimental work. Moreover, its measured permeability (see details below) allowed for fluid injection under drained conditions.

Cores of Tavel limestone were diamond drilled from a unique block to a diameter of 36.5 mm. From the cores, 75 mm cylinders were sawed and the opposite faces ground flat with a parallelism of $\pm 100\text{-}\mu\text{m}$ precision. Tap water was used as cooling fluid for all the preparation steps. The samples were then petro-physically characterized and used for the triaxial tests.

Porosity of the samples was measured using the triple weight method (see Guéguen & Palciauskas, 1994) and from the dry density of the samples assuming they are composed of 100% calcite. Using these two methods, similar porosity values were found: 10.6 ± 0.5 and 10.8 ± 0.5 %, respectively. Therefore, the porosity can be consistently considered as connected. The measured porosity is equivalent to the one found by Vajdova et al., (2004) and Vajdova et al., (2010), who found porosities of 10.4 and 10.6 %, respectively, and lower than the one found by Nicolas et al., (2016), who measured a porosity of 14.7 %.

Permeability of the samples was measured using the steady state Darcy flow method (i.e., by imposing a constant pore fluid pressure difference between sample ends and waiting for steady state flow to take place) under average hydrostatic conditions at effective pressures ($P_c - P_f$) between 1 and 110 MPa. The samples showed a very slight decrease of the permeability with increasing hydrostatic effective pressure from 9×10^{-18} to $2 \times 10^{-18} \text{ m}^2$ (Figure 6. 1). This low pressure dependence of the permeability suggests that the porosity contributing to the transport properties are mainly equant pores (Pimienta et al., 2017). Note that recent studies have shown that the effective stress coefficient for permeability can be higher than 1 for micritic limestone (e.g., Wang et al., 2018), possibly resulting in slightly lower permeability at elevated pore fluid pressure.

Ultrasonic P-wave velocities (V_p) were measured across the sample under hydrostatic conditions at ($P_c - P_f$) between 3 and 110 MPa (Figure 6. 1). The samples show a slight increase from 4410 ± 45 to $4580 \pm 55 \text{ m.s}^{-1}$ with effective confining pressure. These measurements are in agreement with Nicolas et al. (2016) who found that V_p increases from 4135 to 4350 m.s^{-1} with increasing P_c from 0 to 85 MPa under dry conditions. The small variation of V_p with the applied effective pressure agrees with the small variation of permeability obtained.

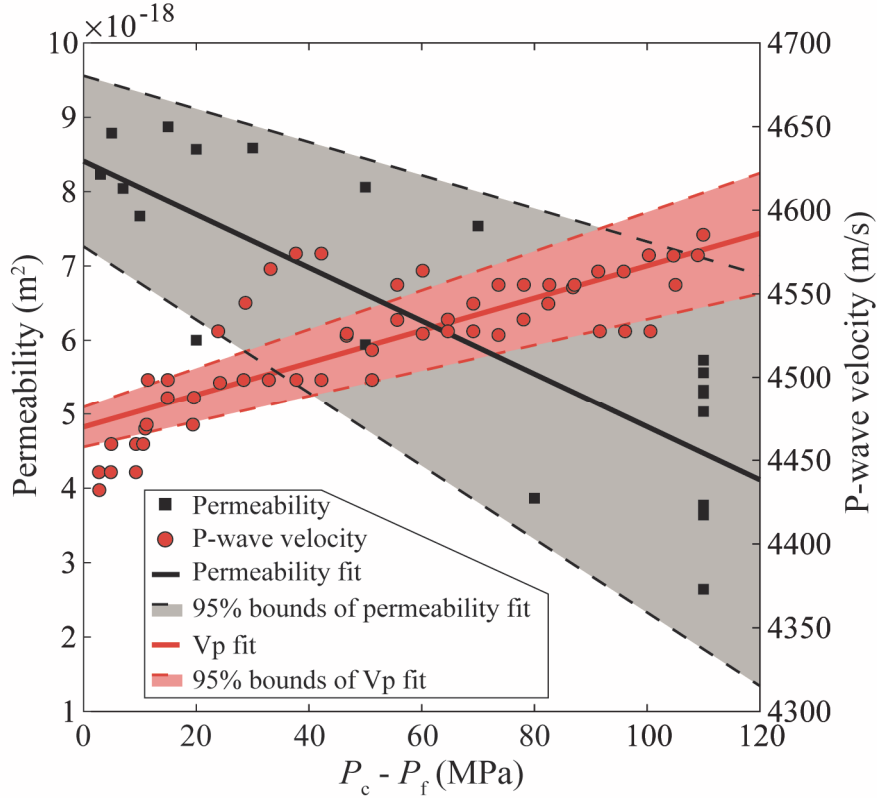


Figure 6. 1: Permeability (k) and ultrasonic P-wave velocity (V_p) as a function of the effective confining pressure ($P_c - P_f$) of the Tavel limestone. Permeability data as a function of $P_c - P_f$ were fitted by a linear regression: $k = 3.58 \times 10^{-20} (P_c - P_f) + 8.41 \times 10^{-18}$ (full black line). V_p data as a function of $P_c - P_f$ were fitted by a linear regression: $V_p = 0.968 (P_c - P_f) + 4470$ (full red line). The dotted black and red lines present the 95% interval bounds of the linear regressions of the permeability and V_p data, respectively.

6.3.2 Triaxial deformations

6.3.2.1 Apparatus

Triaxial deformation experiments were performed using a conventional triaxial cell installed at the Laboratory of Experimental Rock Mechanics at the École Polytechnique Fédérale de Lausanne (Figure 6. 2A). The system uses oil to apply a confining pressure ($P_c = \sigma_2 = \sigma_3$) up to 200 MPa (± 5 -kPa resolution). Upper and lower end platens are used to apply differential stress ($\sigma_1 - \sigma_3 = \sigma_1 - P_c = Q$) up to 1 GPa (± 100 -kPa resolution). The sample is isolated from the oil by a Viton jacket. Diffusion plates are placed at the sample ends to allow for a homogeneous pore fluid pressure distribution. Pore fluid pressure (P_f) is imposed with distilled water using step motor pumps, with a 185-cm³ capacity, up to 200 MPa (± 5 -kPa resolution). The pore fluid pressure is recorded by two precision pressure sensors (± 5 -kPa resolution) close to the sample ends. Pump fluid volume (V_f) variations are measured by encoders mounted on the pumps (± 1 -mm³ resolution). Axial displacements are measured using two internal Linear Variable Differential Transformers (LVDTs) with a precision of 1 μ m and one external LVDT at the top of the axial column with a precision of 3 μ m. In addition, two axial and two radial strain gages were glued on the sample (Figure 6. 2B), allowing for the monitoring of local strain during sample triaxial deformation, up to a maximum strain of 2%. Finally, the measurement of the evolution of elastic wave velocities during the triaxial experiments was conducted using 12 piezo-electric sensors (equipped with piezo-electric crystals: PI ceramic PRYY + 0400, 5-mm diameter and 1 mm thick) glued directly on the sample through holes drilled

in the jacket (Figure 6. 2Ah), which was resealed with ductile epoxy to prevent the intrusion of the confining oil into the sample. For these active velocity surveys, the emitted signals were pulsed at 450 V, and the received signals were amplified to 50 dB using a preamplifier and recorded at a 10-MHz sampling rate. The sensor arrangement was made so that the P-waves velocity could be measured at 30.9, 50.2 and 90° from the axis of the sample (Figure 6. 2B), allowing for P-wave velocity anisotropy analysis during sample deformation.

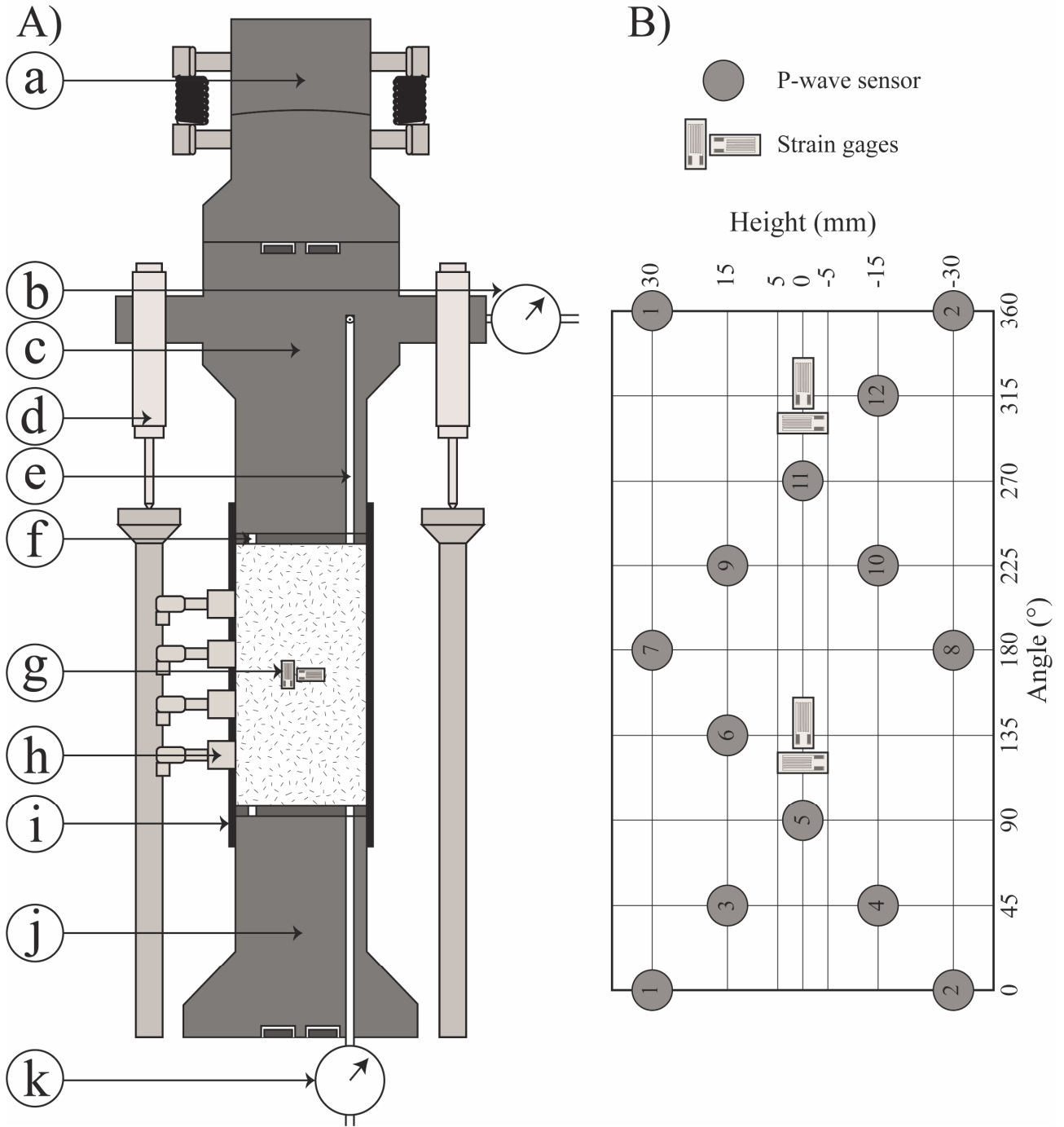


Figure 6. 2: A) Cross-section drawing of the assembly used for triaxial experiments. a) ball joint to prevent sample misalignment, b) upstream pore fluid pressure sensor, c) upper end platen, d) internal LVDT, e) pore fluid lines, f) drainage grooves to ensure homogeneous pore fluid pressure distribution, g) strain gages, h) piezo-electric sensor glued on the sample, i) Viton jacket, j) lower end platen and k) downstream pore fluid pressure sensor. B) Map of the acoustic sensors and strain gages used for injection experiments. Grey circles represent the position of the P-wave sensors and rectangles the position of the strain gages.

6.3.2.2 Constant pore fluid pressure experiments

After placing the sample into the jacket and inserting it into the high-pressure vessel, the confining pressure was raised to 5 MPa. The sample was then pumped down to vacuum and 2 MPa of pore fluid pressure was applied at the bottom of the sample. Once the pore fluid was equilibrated (i.e., once P_f measured at the top reached 2 MPa and V_f was constant), the confining pressure and

pore fluid pressure were increased simultaneously to their target values. For these experiments, the confining pressures ranged from 30 to 120 MPa and the pore fluid pressure was maintained constant at 10 MPa during the entire experiment (Table 6. 1). When V_f was equilibrated, the axial stress was increased by applying a slow constant displacement rate at the internal LVDTs of $7.5 \times 10^{-5} \text{ mm.s}^{-1}$, which corresponds to a strain rate $\dot{\epsilon}_{ax} \approx 10^{-6} \text{ s}^{-1}$. The sample was then deformed up to the brittle failure of the specimen (i.e. to a stress drop), or up to about 10% of its initial length for the experiments conducted in the ductile domain. Note that the strain rate was slow enough to maintain drained conditions in the sample during the deformation (i.e., upstream $P_f \approx$ downstream P_f , consistent with diffusion time computed by Nicolas et al., (2016)).

6.3.3 Injection experiments

For the injection experiments, the same initial procedure was applied as for the constant pore fluid pressure experiments. The initial confining pressure and pore fluid pressure were set to $P_c = 120$ and $P_f = 10$ MPa (ductile domain, see paragraph 6.4.1). After 1% of axial deformation, the pore fluid pressure was raised gradually at the bottom of the sample up to 100 MPa (i.e. $P_c - P_f = 20$ MPa). Note that at equivalent $P_c - P_f$, the axial stress and the volumetric strain are directly linked ($\epsilon_{vol} = \epsilon_{ax} + 2\epsilon_{rad}$), therefore the injections are considered to start at equivalent volumetric strain. 100 MPa pore fluid pressure limit was chosen to prevent leakage from the P_f to the confining oil. Three pore fluid pressure rates were tested: 1, 5 and 10 MPa.min⁻¹ (Table 6. 1). The mechanical deformation of the sample was stopped when the sample reached an axial strain of 2%. During sample deformation, active P-wave velocity surveys were made every 2 minutes. Note that during the full length of the injection experiments, the velocity of $7.5 \times 10^{-5} \text{ mm.s}^{-1}$ (i.e., $\dot{\epsilon}_{ax} \approx 10^{-6} \text{ s}^{-1}$) at the LVDTs continues to apply.

Table 6. 1: Summary on the experimental conditions and triaxial mechanical data performed on Tavel limestone. DCSZ stands for distributed conjugated shear zone.

Sample	P_c (MPa)	P_f (MPa)	P_f conditions	E (GPa)	$(\sigma_1 - \sigma_3)$ at D' (MPa)	$(\sigma_1 - \sigma_3)$ peak (MPa)	$(\sigma_1 - \sigma_3)$ at C* (MPa)	Failure angle (° from σ_1)	Post-mortem macro- deformation
TH5	30	10	constant	48.5	170.2	189.4	-	22	Shear failure
TB5	60	10	constant	41.5	208.0	215.8	-	33	Shear failure
TH6	90	10	constant	48.3	266.9	306.5	92.9	31	DCSZ
TH2	120	10	constant	44.4	-	-	122.4	-	Barrel shape
TB2	120	10	1 MPa.s ⁻¹	45.9	-	-	116.6	22	Shear failure + DCSZ
TB9	120	10	1 MPa.s ⁻¹	44.63	-	-	87.2	25	Shear failure + DCSZ
TB7	120	10	5 MPa.s ⁻¹	43.1	-	-	87.8	22	Shear failure + DCSZ
TB4	120	10	5 MPa.s ⁻¹	35.2	-	-	104.7	30	Shear failure + DCSZ
TH9	120	10	5 MPa.s ⁻¹	45.7	-	-	96.4	23	Shear failure + DCSZ
TB8	120	10	10 MPa.s ⁻¹	38.3	-	-	85.82	24	Shear failure + DCSZ
TH8	120	10	10 MPa.s ⁻¹	46.3	-	-	101.5	23	Shear failure + DCSZ

6.3.4 Data treatment and analysis

For each experiment, the displacement measured from the LVDTs was corrected for the elastic distortion of the apparatus column (i.e., axial column, end platens and diffusion plates for the external LVDT and end platens and diffusion plates for the internal LVDTs), calibrated using a metal plug of a known stiffness. For all the experiment, the differential stress was corrected for the friction of the axial piston in the apparatus column. For each experiment, the axial strain (ε_{ax}) was computed as the ratio between the corrected axial displacement and the initial sample length. The porosity change was computed as the ratio between the injected pore fluid volume (V_f) and initial bulk volume of the sample. Note that for the injection experiments, the porosity change was calculated by correcting the pore fluid volume linked to the pore pressure increase (i.e. due to the dilation of the pore fluid lines and water compressibility). Finally, the volumetric strain (ε_{vol}) was computed using the local measurement of the strain recorded on axial and radial strain gages assuming $\varepsilon_{vol} = \varepsilon_{ax}^{SG} + 2\varepsilon_{rad}^{SG}$, with ε_{ax}^{SG} and ε_{rad}^{SG} being the axial and radial strain measured by the strain gages, respectively. Importantly, strain gages allow for very local strain measurements such that localized deformations are often not measured by the strain gages, leading to volumetric strain underestimation in the case of large strain localization. However, overestimations are also possible if localized deformations occur at the location of the strain gages.

For each experiment, the P-wave velocities (V_p) obtained from the active surveys were corrected by the elastic effective pressure dependence (Figure 6. 1). This allowed for the removal of the poro-elastic response of the bulk due to the increase of the pore fluid pressure. We note this corrected P-wave velocity as $V_p^{\text{corrected}}$. In order to remove sample variability, the values of $V_p^{\text{corrected}}$ are then normalised by the initial values (V_{p0}) measured at $P_c - P_f = 110$ MPa before the application of the differential stress. In addition, the computed $V_p^{\text{corrected}}$ along the different pathways were used to invert the evolution of the average corrected crack densities's increase during the experiment. This inversion was performed in the framework of a transversely isotropic crack distribution, following standard procedure (see Sarout & Guéguen, 2008a, 2008b). The minimization of the difference between the theoretical and the experimental wave velocities was conducted using a least absolute method for each velocity survey. The inversion outputs the best solution for the transversely isotropic stiffness tensors from which the average crack densities (independent of their orientation form the principal stresses) are computed. Here, we computed the evolution of the crack density using $V_p^{\text{corrected}}$ instead of the absolute V_p values, to remove the poroelastic effects due to the increase of fluid pressure (like the opening of cracks inducing loss of contacts along the crack). Note that this method considers the cracks to be under dry conditions, therefore, in the case of a saturated sample, it leads to an underestimation of the crack densities. The crack densities estimated in the following correspond to the average crack densities for all possible orientations, which is computed from both vertical (α_v) and horizontal (α_h) crack densities assuming $\rho_{tot} = 2\alpha_v + \alpha_h$.

After deformation, each sample was carefully taken out of the jacket. If a macroscopic shear failure had occurred, its angle from the sample axis (i.e. equal to the orientation of σ_1) was measured. Then, samples were impregnated with epoxy under vacuum and a thin section perpendicular to the macroscopic structural deformation (if visible) was prepared and analysed under optical and scanning electron microscopes (SEM) in secondary electron mode.

6.4 Results

6.4.1 Constant pore fluid pressure experiments

Constant pore fluid experiments were performed to characterise the short-term mechanical behaviour of Tavel limestone and to constrain its brittle-ductile transition. The mechanical results (Figure 6. 3 and Table 6. 1) serve as reference for the injection experiments. For the confining pressures tested, three mechanical behaviours were observed:

- 1) For experiments performed at $P_c - P_f \leq 50$ MPa, after an initial linear increase of the differential stress ($\sigma_1 - P_c$) with the axial strain, the onset of dilatancy is reached and the curve departs from linearity. After the elastic deformation, the sample exhibits a strain hardening behaviour up to a peak value (Q_{peak} i.e., sample strength). During this phase, the deformation turns from compaction to dilation at the point denoted D' (Figure 6. 3a and c). Following this peak, the sample enters a strain softening phase after which the stress remains at a quasi-constant residual strength up to the end of the deformation.
- 2) For experiments performed at $P_c - P_f \geq 110$ MPa, after a first linear increase of the differential stress with the axial strain and the volumetric strain, the mechanical curves deviate from linearity at a point noted C* (Figure 6. 3). After this point, the sample follows a non-linear

hardening phase. Finally, a constant hardening rate is reached and the differential stress – axial strain curve again presents a linear behaviour (Figure 6. 3b). During the entire experiment, the sample deformation is accommodated by compaction (Figure 6. 3a and d).

- 3) For the experiment performed at $P_c - P_f = 80$ MPa, a mix between the two behaviours was observed. After an elastic behaviour, the deformation becomes non-linear and the sample exhibits strain hardening. Then, a quasi-linear strain hardening behaviour is observed. During this phase, the sample first compacts. After an axial strain of about 2.8 %, dilatancy become dominant at a point denoted C* (Figure 6. 3a). After an axial strain of about 7 %, the strain hardening decreases and a peak differential stress is ultimately reached at an axial strain of 9.05 % (Figure 6. 3b). Finally, the sample enters a very small strain softening phase.

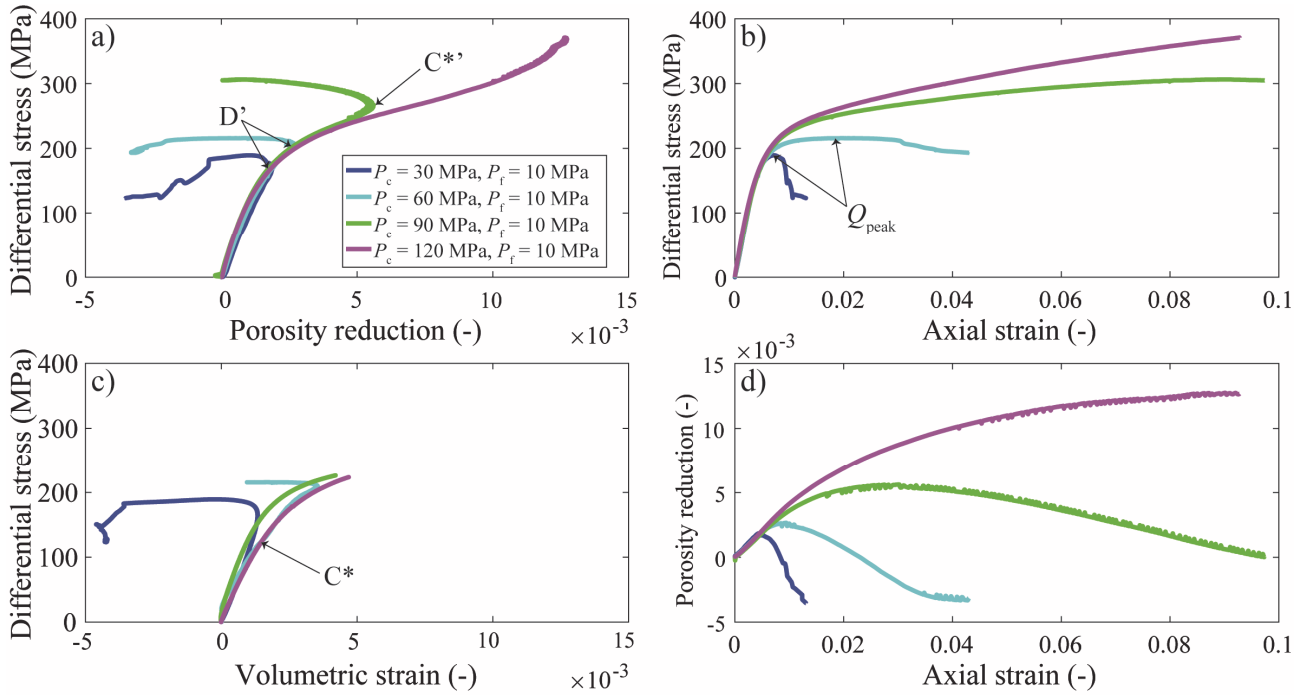


Figure 6. 3: Mechanical data obtained from Tavel limestone deformed at $P_c - P_f$ ranging from 20 to 110 MPa. a) Differential stress ($\sigma_1 - P_c$) as a function of the porosity reduction. b) Differential stress as a function of the axial strain. c) Differential stress as a function of the volumetric strain. d) Porosity reduction as a function of the axial strain. Note that the volumetric strain could not be recorded at values higher than 0.5% due to the system limitation.

The peak differential stress, the residual strength of experiments in the brittle field, as well as the differential stress at C* of the experiments in the ductile field were extracted to build the failure/damage envelope of Tavel limestone (Figure 6. 4). The values of differential stress observed at 1, 2 and 3 % of axial strain and at 0.2, 0.3 and 0.5 % of porosity reduction are reported for experiments devoid of macroscopic stress drop during the early stage. Two envelopes were defined for the brittle field using the wing crack model to fit the sample strength (Ashby & Sammis, 1990; Brantut et al., 2012, black line in Figure 6. 4), and a linear regression to fit the residual strength (black dashed line in Figure 6. 4).

More details on the mathematical formulations and parameters used for the envelopes are presented in the Appendix B.

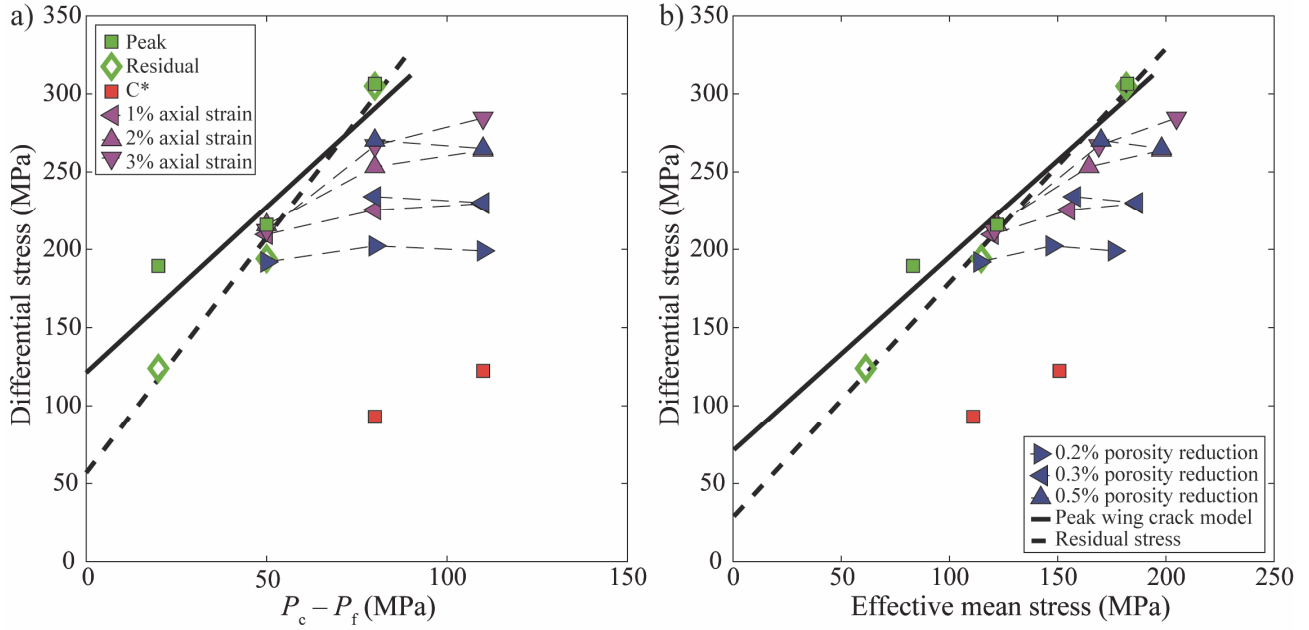


Figure 6. 4: Peak differential stress, residual strength, differential stress at C^* , differential stress at 1, 2 and 3% of axial strain and differential stress at a porosity reduction of 0.2, 0.3, 0.5% obtained from the constant pore fluid pressure experiments performed on Tavel limestone, plotted as a function of a) the effective confining stress and b) the effective mean stress. Peak differential stress data are fitted with a wing crack model (Ashby & Sammis, 1990), with an initial flow size of $0.8 \mu\text{m}$ oriented at 45° from the axial stress, a coefficient of friction of 0.6, a critical stress intensity factor of $0.2 \text{ MPa}\cdot\text{m}^{1/2}$, and an initial damage of 0.3 (similar to Vajdova et al. (2004)). Residual stress data are fitted linearly with $Q_{\text{residual}} = 3.02 \times (P_c - P_f) + 56.8$. See appendix B for more details on the parameters used in the models.

The post-mortem analyses of the samples showed that, for samples deformed at $P_c - P_f \leq 50$ MPa, the deformation was mainly localized along anastomosed shear fractures with orientations ranging between 22 and 31° from σ_1 (Table 6. 1 and Figure 6. 5b, f and i). Microscopic analysis revealed that micro-cracking is the main mechanism controlling the deformation, although twinning was also observed (Figure 6. 5f). The formation of these opened cracks is in agreement with the dilation observed during the sample deformation. The post-mortem samples deformed at $P_c - P_f \geq 110$ MPa present a barrel shape, and the deformation is distributed across the sample (Figure 6. 5d, h and k). Microscopic analysis revealed that grains endured mechanical twinning and distributed micro-cracking (Figure 6. 5h). Some macro-pores present ovoid shapes flattened perpendicularly to σ_1 (Figure 6. 5h and k). Finally, the samples deformed at $P_c - P_f = 80$ MPa showed both a deformation that occurred distributed across the sample (i.e. barrel shape) and a localised deformation along discrete shear fractures, i.e., non-continuous fractures of finite length ranging from 0.5 to 2 mm (Figure 6. 5c, g and j). Microscopic analysis revealed multiple non-continuous shear fractures with small apertures forming discrete shear zones (Figure 6. 5g and j). Additionally, distributed micro-cracking and twinning were present.

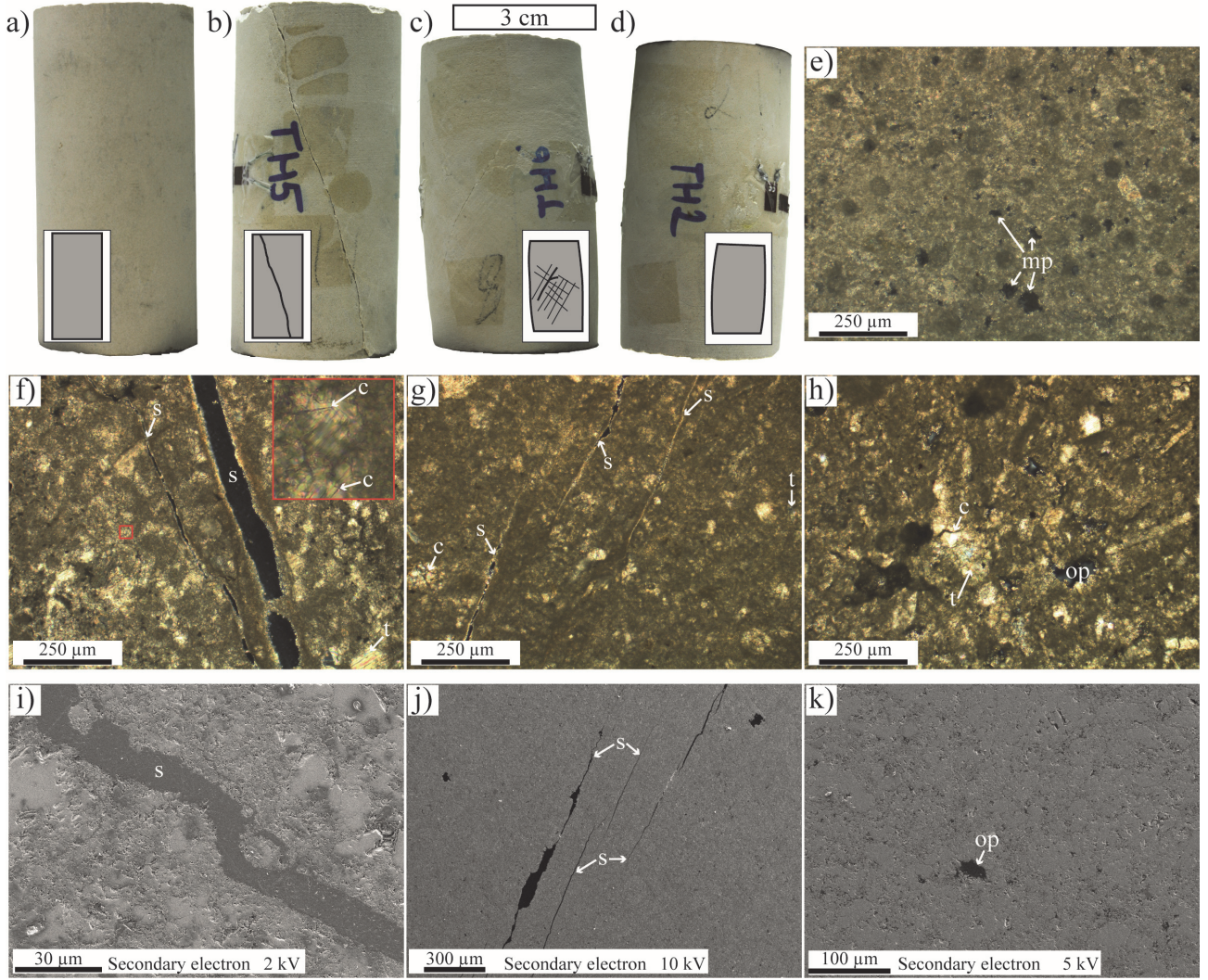


Figure 6. 5: Post-mortem analysis of the samples which were deformed under constant pore fluid pressure conditions. a-d) Macroscopic photo with schematic representation. e-h) Micrographs taken under a cross-polarized microscope. i-k) SEM image in secondary electron mode. a and e) intact sample. b, f and i) sample deformed in the brittle domain (i.e. at $P_c - P_f \leq 50$ MPa) by shear fracturing. c, g and j) sample deformed at the brittle-ductile transition (i.e. at $P_c - P_f = 80$ MPa). d, h and k) sample deformed in the ductile domain (i.e. at $P_c - P_f \geq 110$ MPa). For the micrographs (e-h), σ_1 is oriented sub-vertically. For the SEM images (i-k), σ_1 is oriented sub-vertically. A zoom on a highly cracked zone (red square) is presented in panel f. Abbreviations: mp = macro-pore, s = shear fracture, c = crack, t = twinning, op = ovoid pore.

6.4.2 Injection experiments

For the injection experiments, the evolutions of the mechanical and P-wave velocity behaviours (Figure 6. 6, Figure 6. 7 and Figure 6. 8) can be described in 5 steps. For reference, a typical mechanical behaviour of an injection experiment as well as the stress path seen by the sample is shown in Figure 6. 6. All the injection experiments presented in the following steps:

- 1) Before pore fluid injection, all the samples presented a similar mechanical behaviour, with a first linear elastic behaviour followed by a hardening phase and compaction (Figure 6. 6 and Figure 6. 7). During this phase, $V_p^{\text{corrected}}$ was constant (Figure 6. 8). This primary behaviour is similar to the experiments performed at $P_c - P_f = 110$ MPa under constant pore fluid pressure conditions (black line in Figure 6. 7), and all the experiments present relatively similar differential stresses at C* (i.e., 100.3 ± 13.8 MPa,

- Table 6. 1). At the end of this stage, and just before the injection started, the samples porosity was reduced by 0.40 to 0.45%.
- 2) When injection started (at an axial strain of about 1%), all the samples passed instantaneously from compaction to dilation (Figure 6. 6a and b and Figure 6. 7a, c and d) and the hardening rate increased (Figure 6. 6b and Figure 6. 7b). As the pore pressure rose, the hardening rate decreased and the differential stress reached a peak value after which softening was observed. These hardening and softening rate changes depended on the injection rate: the higher the injection rate, the smaller the axial strain was at the peak differential stress. Moreover, for all the experiments, the peak differential stress value was reached at $P_f \approx 50$ MPa (i.e. $P_c - P_f \approx 70$ MPa). Finally, the softening stopped when the injection reached the target value of $P_f = 100$ MPa (i.e. $P_c - P_f = 20$ MPa). During this phase, $V_p^{\text{corrected}}$ dropped quasi-linearly to between 95 and 85% of the initial value. Following the trends seen in V_p , the corrected crack density increases from about 0.05 to 0.1. Note that during the injections, the strain rate seen by the sample changes. For low injection rates (i.e., 1 MPa/min) the variations are negligible. For experiments with injection rates of 5 and 10 MPa/min, the strain rate slightly increased from 10^{-6} to 2.9×10^{-6} and $3.9 \times 10^{-6} \text{ s}^{-1}$, respectively. After the injection stopped, the strain rate quickly decreased back to 10^{-6} s^{-1} . Additionally, for high injection rates (5 and 10 MPa/min) a pore pressure gradient was produced within the sample. The delay time to reach equilibrium was 3 minutes at maximum such that the experiments can be considered undrained during moments of large pressure gradient, and drained the rest of the time. As a consequence of this drainage issue, for the injection experiments at 5 and 10 MPa.min⁻¹, a “z-shape” is visible on the differential stress as a function of the porosity reduction curve close to the peak differential stress (Figure 6. 6a and Figure 6. 7a). A ‘u-shape’ is also visible on the porosity reduction as a function of the axial strain curve at an axial strain of about 0.9% (Figure 6. 7d). These are not real porosity changes but artefacts of the correction methods (i.e. water diffusion delay).
 - 3) When the injection stopped, the softening also stopped and the differential stress remained at a quasi-constant value with increasing the axial strain (i.e. creep phase). Interestingly, this constant differential stress corresponds to the peak differential stress observed during the constant pore pressure experiment performed at $P_c - P_f = 20$ MPa (i.e. the effective pressure reached for the injection experiments). During this quasi-constant differential stress phase, the samples continued to dilate (Figure 6. 6a, b and c and Figure 6. 7a, b and c). The $V_p^{\text{corrected}}$ values continued to drop but with a shallower slope than during the previous phase (Figure 6. 8). Similarly, the corrected crack density continues to increase, albeit slower than during previous phase (Figure 6. 8).
 - 4) The creep phase ultimately led to a stress drop that marks the sample failure (Figure 6. 6 and Figure 6. 7). Note that this stress drop occurred systematically when the porosity had increased by about 1%. The stress drop didn’t significantly affect the $V_p^{\text{corrected}}$ and corrected crack density values (Figure 6. 8). Note that the stress drops were sometimes excessive due to the servo-control of the machine.
 - 5) After the stress drop, a residual stress remained. The residual differential stress had similar values to the residual stress observed during the constant pore fluid pressure experi-

ments performed at $P_c - P_f = 20$ MPa. After the stress drop, $V_p^{\text{corrected}}$ values remained constant at 92 to 82% of the initial values. The corrected crack density also remains constant, at values between 0.1 and 0.15, depending on the sample.

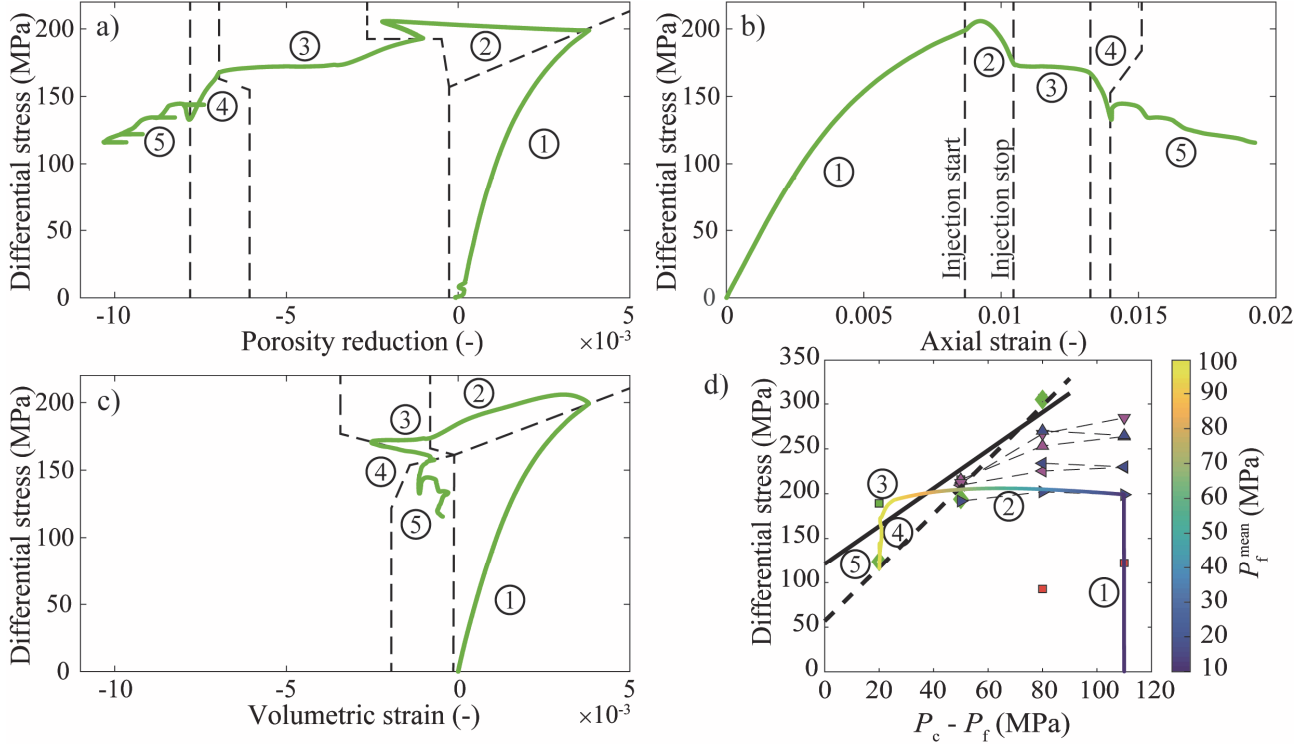


Figure 6. 6: Mechanical data obtained for the injection experiments at 5 MPa/min on Tavel limestone. a) Differential stress as a function of the porosity reduction. b) Differential stress as a function of the axial strain. c) Differential stress as a function of the volumetric strain. d) stress path seen by the sample plotted over the summary of the mechanical data obtained in the constant pore pressure experiments (i.e. Figure 6. 4). P_f^{mean} is the pore fluid pressure average between the upstream and downstream pore fluid pressure sensors. On the four panels, the numbers 1 to 5 refer to the 5 principal steps observed in injection experiments (see the main text for more details).

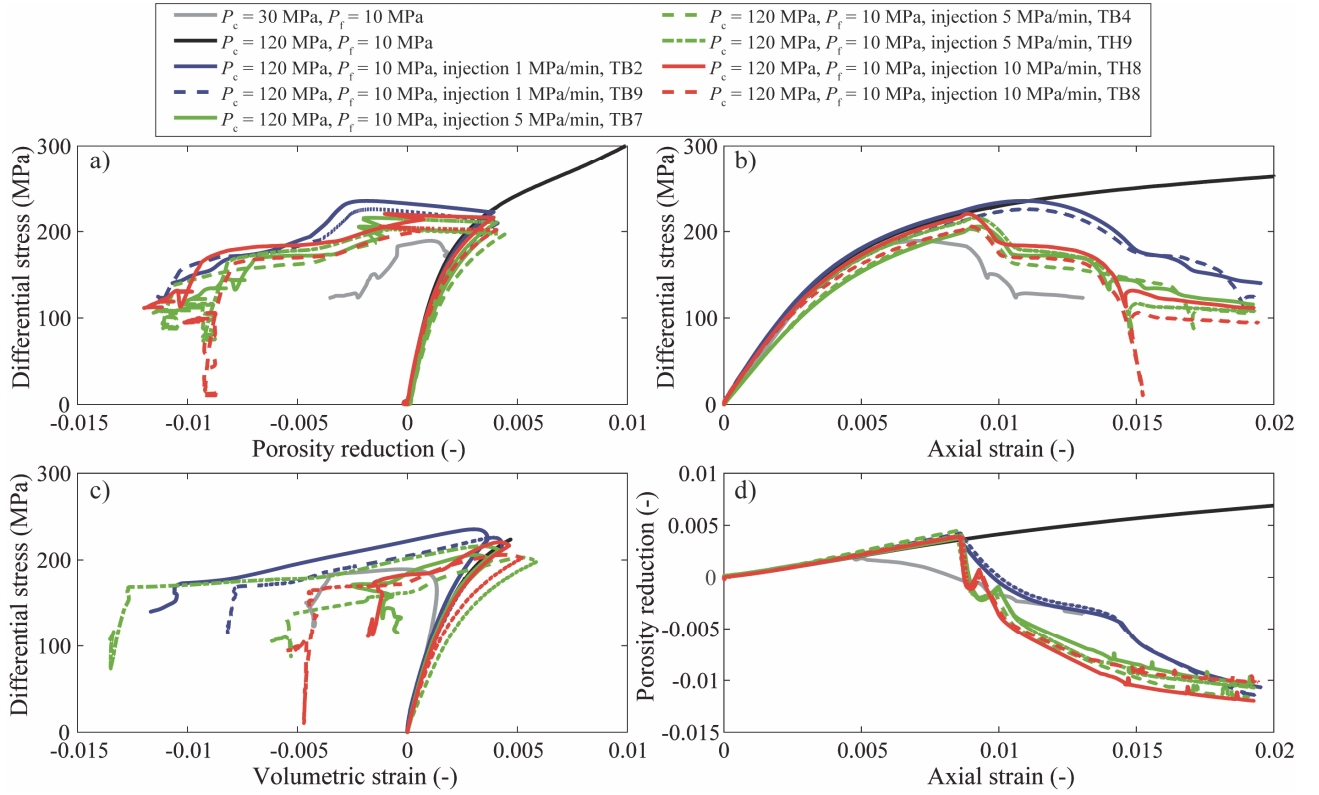


Figure 6. 7: Mechanical data obtained for the injection experiments on Tavel limestone (coloured curves). Constant pore fluid experiments at $P_c - P_f = 110$ and 20 MPa are also plotted for reference (black and grey curves, respectively). a) Differential stress as a function of the porosity reduction. b) Differential stress as a function of the axial strain. c) Differential stress as a function of the volumetric strain. d) porosity reduction as a function of the axial strain. The experiments performed with injection rates of 1, 5 and 10 MPa.min⁻¹ are represented by blue, green and red colours, respectively. Note that for the injection experiments at 5 and 10 MPa.min⁻¹, the “z-shape” and “u-shape” visible on the curves of differential stress as a function of porosity reduction (close to the peak differential stress) and porosity reduction as function of the axial strain (at about 0.9% of axial strain), respectively, are not real porosity changes but artefacts due to the correction methods (i.e. diffusion delay).

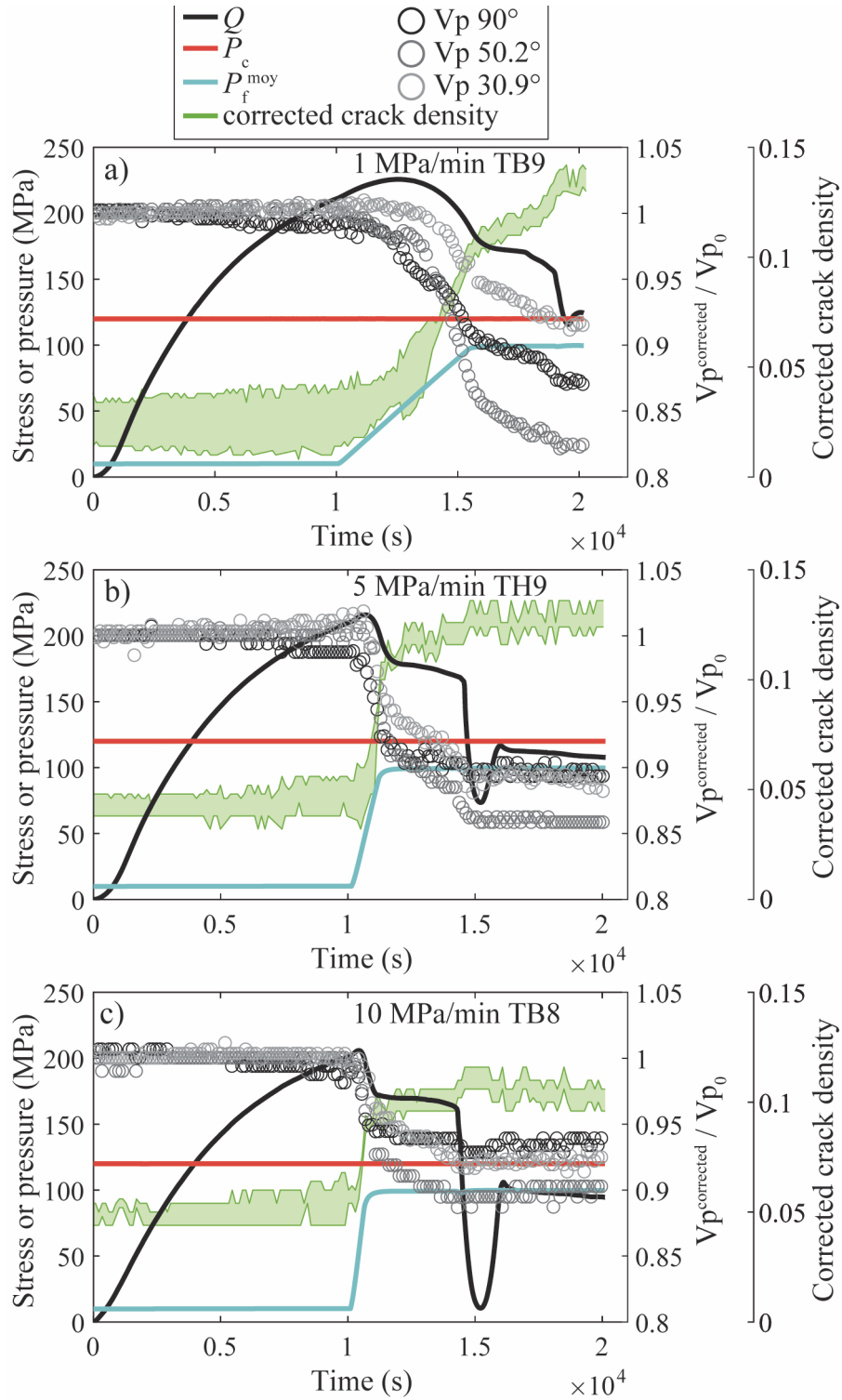


Figure 6. 8: P-wave velocities at 90, 50.2 and 30.9° from σ_1 corrected for poroelasticity and normalised by the reference velocity (see paragraph 6.3.4 for precision) as a function of time. The computed corrected crack density values are shown in green. The green zone delimitates the uncertainty of the computation. The differential stress, confining pressure and pore fluid pressure are represented by the black, red and light blue curves, respectively. a) Sample TB9 with an injection rate of 1 MPa.min⁻¹. b) Sample TH9 with an injection rate of 5 MPa.min⁻¹. c) Sample TB8 with an injection rate of 10 MPa.min⁻¹. Note that the corrected crack densities are underestimated due to the method used (see paragraph 6.3.4 for more details).

Post-mortem analyses of the samples showed that all samples presented a principal anastomosed shear fracture oriented between 22 and 30° from σ_1 (Table 6. 1 and Figure 6. 9). Most of the sam-

ples also presented distributed discrete shear fractures oriented at 20 to 35° from σ_1 . However, increasing the injection rate from 1 to 10 MPa.min⁻¹ reduced the number of these distributed shear fractures (Figure 6. 9a, b and c). Indeed, at low injection rates (i.e. 1 MPa.min⁻¹), the macroscopic shear fracture is surrounded by discrete millimetric- to centimetric-scale fractures forming a wide deformation zone around the principal fault (Figure 6. 9d, g and j). For a medium injection rate (i.e. 5 MPa.min⁻¹), the macroscopic fracture is wider and surrounded by a small amount of fractures of finite length (Figure 6. 9e, h and k). Finally, for high injection rates (i.e. 10 MPa.min⁻¹), the macroscopic shear fracture is marked by 3 to 4 parallel fractures, and only few scattered cracks of finite length are present (Figure 6. 9f, i and l). In summary, the lower the injection rate, the more the macroscopic shear fracture is bounded by distributed fractures of finite length.

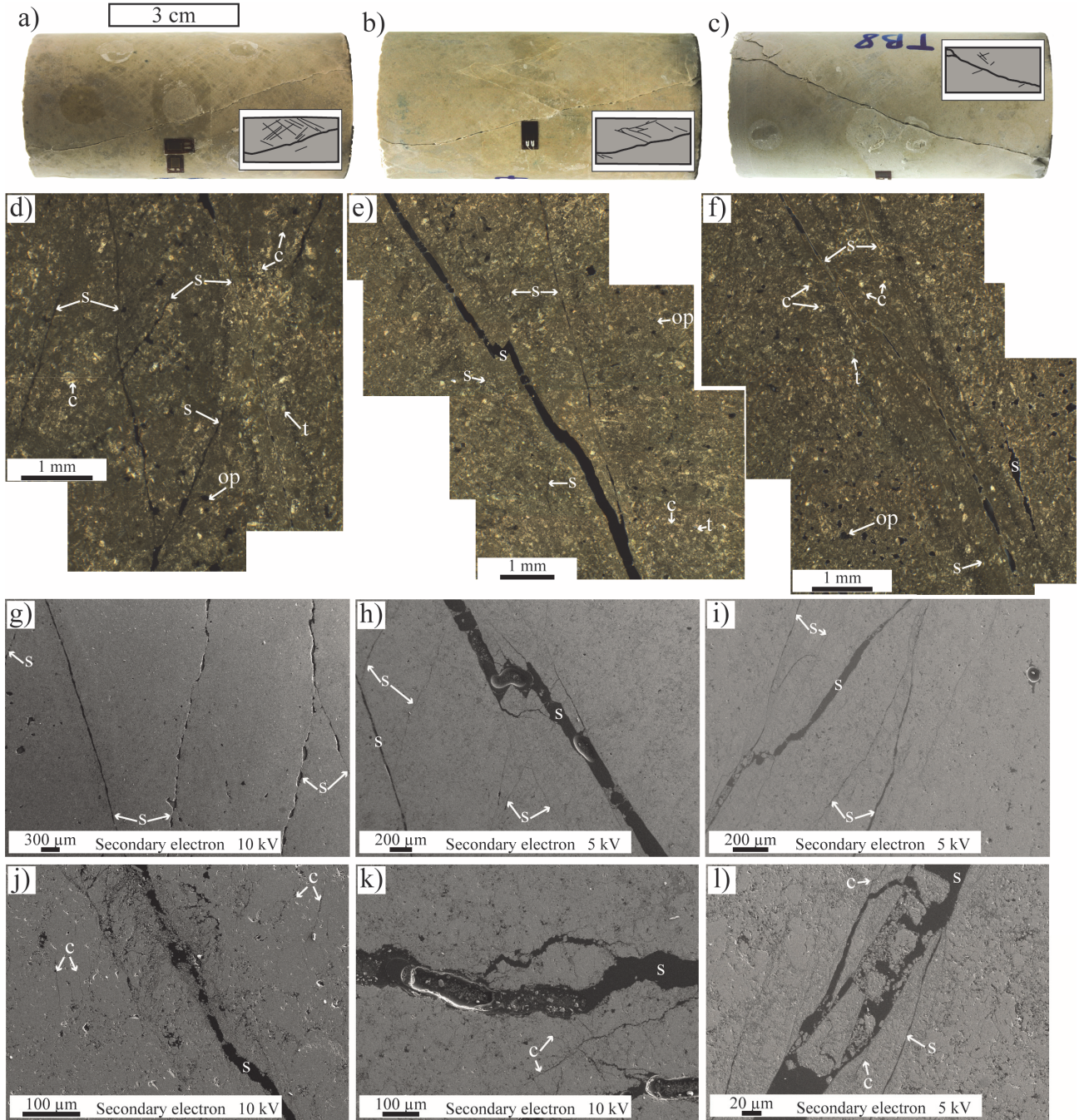


Figure 6. 9: Injection experiment post-mortem analysis of the samples. a-c) Macroscopic photo with schematic representation. d-f) Mosaic of micrographs taken under cross-polarized microscope. g-l) SEM images in secondary electron mode. a, d, g and j) sample deformed with an injection rate of 1 MPa.min⁻¹. b, e, h and k) sample deformed with an injection rate of 5 MPa.min⁻¹. c, f, i and l) sample deformed with an injection rate of 10 MPa.min⁻¹. For these micrographs, σ_1 is oriented vertically. Note that the panels magnifications are different. Abbreviations: s = shear fracture, c = crack, t = twinning, op = ovoid pore.

6.5 Interpretation and discussion

The experiments performed in this study highlight that:

- 1) Tavel limestone exhibits a brittle-ductile transition at room temperature and an effective confining pressure around 80 MPa.
- 2) An increase of pore fluid pressure in a rock sample submitted to ductile conditions turns the system instantaneously to dilation.
- 3) The combination of the P-wave velocity decrease and sample dilation constrain the moment when localized shear deformation take place. The micro-cracking of the sample starts when the ductile-brittle transition is overcome. However, macroscopic failure is not instantaneous when the ductile-brittle deformation is passed. A transient creeping phase is necessary to achieve the macroscopic shear failure of the specimen.
- 4) To obtain a macroscopic brittle failure of initially ductile samples (marked by the stress drop), a critical dilatancy is required. Under our experimental conditions and strain rates, a dilatancy of about 1% was systematically needed to obtain shear fracturing.

In the following, we first discuss the brittle-ductile transition of Tavel limestone with increasing effective confining pressure. Then, we discuss and interpret the brittle deformations obtained during the ductile-to-brittle transition induced by an increase in the fluid pressure and compare them to the ones observed during constant fluid pressure experiments conducted through the transition. Finally, we discuss the implications of our experimental results for natural and induced deep seismicity.

6.5.1 Brittle-ductile transition with increasing effective confining pressure

To facilitate the discussion of the injection experiments, we summarize here the principal characteristics of the brittle to ductile transition in Tavel limestone and compare it with previous studies. The microstructural analysis (Figure 6. 5) of the constant pore fluid pressure experiments show that Tavel limestone deformed by localised shear fractures at $P_c - P_f \leq 50$ MPa, by discrete shear zones at $P_c - P_f = 80$ MPa, and by distributed micro-cracking, mechanical twinning and macro-pore deformations at $P_c - P_f \geq 110$ MPa. These observations agree with the mechanical data obtained (Figure 6. 3). Indeed, at low effective pressure, dilatant deformations are directly linked to micro-crack formation, whereas at high effective confining pressure compaction is related to mechanical twinning and pore deformation (i.e. with pore volume reduction by cataclastic pore collapse) (Zhu et al., 2010). The mechanical data (Figure 6. 3) and microstructural analysis (Figure 6. 5) demonstrate that Tavel limestone has a brittle-ductile transition around an effective confining pressure of 80 MPa at room temperature. This is in agreement with previously published data by Nicolas et al. (2016) and Vajdova et al. (2004) who observed a transition at 70 MPa and between 50 and 100 MPa effective pressure, respectively.

Interestingly, the brittle-ductile transition occurs at the point where the strength (i.e. Q_{peak}) and the residual friction envelopes cross (full and dotted black lines in Figure 6. 4). This characteristic has been observed previously (e.g. Barton, 1976; Byerlee, 1968; Maurer, 1965; Mogi, 1974; Murrell, 1967). Experimental data showed that the fracture strength of the material is less pressure dependent than frictional strength (e.g. Paterson & Wong, 2005) (Figure 6. 4). Therefore, under high effective pressure, it is assumed that non-frictional deformation mechanisms are more efficient

than frictional ones, leading to distributed deformation. Indeed, considering the ideal case of a rock deforming in the brittle field by wing cracks emanating from sharp sliding inclined cracks (i.e. wing crack model), if crack sliding is avoided by the pressure effect, coalescence of micro-cracks will be prevented, and other mechanisms of deformation will be favoured (i.e. cracks nucleating from other discontinuities, mechanical twinning, pore collapse, etc.). This allows for the brittle-ductile transition to be overcome through an increase in the effective confining pressure.

6.5.2 Ductile to brittle deformation induced by pore pressure increase

The injection experiments performed showed that an initially ductile rock mass can undergo localised shear fracturing (i.e. brittle deformations) due to pore fluid pressure increase. Previous experiments on Carrara marble by Schubnel et al. (2006), led to an equivalent result. Indeed, lowering the effective confining pressure from 120 to 5 MPa by means of pore fluid pressure increase, caused the brittle failure of the sample that was initially deforming in the ductile domain. Similar results were obtained by Ougier-Simonin & Zhu (2013) when increasing the pore fluid pressure from 10 to 18 MPa during the deformation of Berea sandstone at $P_c = 80$ MPa. Under the initial conditions they tested (i.e. $P_c - P_f = 70$ MPa), Berea sandstone is in a transitional regime between brittle faulting and cataclastic flow. Increasing the P_f by 8 MPa was enough to cause localized shear failure of the sample. Together, these results demonstrate the importance of pore fluid pressure variation on the ductile to brittle transition.

The obtained results add new constraints on the role and the mechanical effect of pore fluid pressure increase in a system that deforms in an initially ductile manner:

- 1) While deformation was primarily compactant in the ductile regime, samples underwent immediate dilation when the pore fluid pressure was raised (Figure 6. 7). V_p data can be used to better understand what happened in this primary phase. Indeed, using V_p data and the inferred corrected crack density, one can approximate the microstructural deformations at hand. By correcting V_p data for the initial poroelastic response (see paragraph 6.3.4), we were able to discriminate between the elastic opening of the existing crack (i.e. constant $V_p^{\text{corrected}}$) and new micro-cracks formation/elongation (i.e. drop of the $V_p^{\text{corrected}}$). In general, $V_p^{\text{corrected}}$ data were dropping immediately after the pore fluid pressure was increased. Consistent with the velocity data, the computed corrected crack density immediately increased when the pore fluid pressure was raised. This led us to infer that immediate dilation of the sample was due to micro-crack formation.
- 2) We also demonstrated that the macroscopic failure of the sample is not instantaneous when the ductile-brittle transition is passed. First, a softening phase occurred up to the moment we reached the target P_f of 100 MPa. Then, a transient creep phase, corresponding to the sample strength at equivalent effective confining pressure, was needed before failure. During this creep phase dilation increased up to about 1% prior to failure. Again, using V_p and corrected crack density data, we can differentiate two distinct phases of $V_p^{\text{corrected}}$ decrease and corrected crack density increase during the injection experiments: a first fast $V_p^{\text{corrected}}$ decreasing phase during the pore fluid pressure increase and a second slower decreasing phase during the creep phase (Figure 6. 8). These two phases can also be distinguished on the corrected crack density with 2 different increasing slopes.

We can thus infer that while the pore fluid pressure was increased (i.e. the first, fast phase of $V_p^{\text{corrected}}$ decrease and corrected crack density increase) micro-cracking was intense. However, once the target pore fluid pressure of 100 MPa was reached, the micro-cracking state of the sample was not enough to result in coalescence. Therefore, a creeping phase occurred, during which micro-cracks continued their nucleation and propagation (i.e. the second, slower phase of $V_p^{\text{corrected}}$ decrease and corrected crack density increase). Once the micro-crack density was high enough (i.e. in the case of Tavel limestone at 1% dilation), coalescence occurred and the sample macroscopically failed under shearing. The inferred two phases of fast then slower micro-crack density increase agree with the two phases of faster and then slower porosity increase (Figure 6. 7a and d). This result is in agreement with previous observations in the brittle field where a critical dilatancy is needed before the onset of macroscopic shear failure (Kranz & Scholz, 1977). Previous experimental and field studies that measured P-wave velocity during rock or fault macroscopic shear failure (i.e., stress drop) have shown that V_p slightly decreases prior to and during shear failure (e.g., Kaproth & Marone, 2013; Niu et al., 2008; Scuderi et al., 2016; Shreedharan et al., 2021; Taira et al., 2015). Here, such variation could not be measured during the sample macroscopic shear failure due to the large interval between two V_p measurements (i.e., every 2 minutes, while stress drop is quasi-instantaneous). Note that the crack densities estimated at the failure of the specimens are smaller than the percolation threshold (i.e., critical crack density) for failure observed in previous studies (i.e., ≈ 0.13 rather than 0.3) (e.g., Passelègue et al., 2018; Wang et al., 2013). This is probably related to an underestimate of the crack density in fluid saturated media, as observed in previous studies (e.g., Sarout & Guéguen, 2008a, 2008b).

In summary, in a ductile system, pore fluid pressure increase can switch the system to brittle deformation. However, the pore fluid pressure needs to remain high for a certain period of time/strain so that the micro-mechanical state of the rock evolves to a critical dilatancy state after which failure under macroscopic shearing can be induced. The importance of the rate at which the pore fluid pressure is raised can influence the final microstructural state of the rock mass (Figure 6. 10a). Indeed, for low injection rates, the system remains at the pressure of the ductile-brittle transition for a longer period of time (Figure 6. 10a), allowing for the development of transition deformations features (i.e. distributed shear zones) (stage 3 in Figure 6. 10a) contributing to the damaging of the sample, lowering the creep phase required before sample macroscopic shear failure (stage 4 in Figure 6. 10). However, high injection rates induce the transition from ductile to brittle mode of deformation without causing abundant damage (stage 3 in Figure 6. 10a), forcing its creation during a creep phase at elevated pore fluid pressure (stage 4 in Figure 6. 10a) to reach the macroscopic shear failure of the specimen.

Following recent data analysis methods (see Aubry et al., 2020; Meyer et al., 2019), strain partitioning between brittle and ductile deformations can be obtained by comparing the strain measured with the LVDTs and with the strain gages. This method helps in the differentiation between bulk deformation and sliding on a fault plane. Indeed, while the LVDTs are measuring the total axial strain, the strain gages (if not placed on the final macroscopic fault, otherwise they were not taken into account) are measuring the bulk strain but not the fault sliding that releases energy without

storing strain in the surrounding bulk. By correcting the strain from the elastic deformations (i.e. using the sample's Young's modulus), the inelastic axial strain (i.e. involving only microscopic damage) at the LVDTs and strain gages can be obtained. The slope of the inelastic axial strain measured at the strain gages as a function of the inelastic axial strain measured at the LVDTs allows for the differentiation between bulk deformations and macroscopic fault sliding (Figure 6. 10b and c). A slope of unity indicates deformation occurring in the bulk of the sample, whereas a slope of zero indicates that deformations are localized and very probably accommodated by fault sliding. At low injection rates ($1 \text{ MPa} \cdot \text{min}^{-1}$) the onset of macroscopic fault sliding occurred before P_f attained 100 MPa (Figure 6. 10b), while at high injection rates ($10 \text{ MPa} \cdot \text{min}^{-1}$) a bulk axial strain of about 0.3 % was needed after P_f attained 100 MPa to reach the onset of fault sliding. These data highlight the importance of the damage history of rock masses regarding possible strain localisation, fault formations and possible earthquake nucleation.

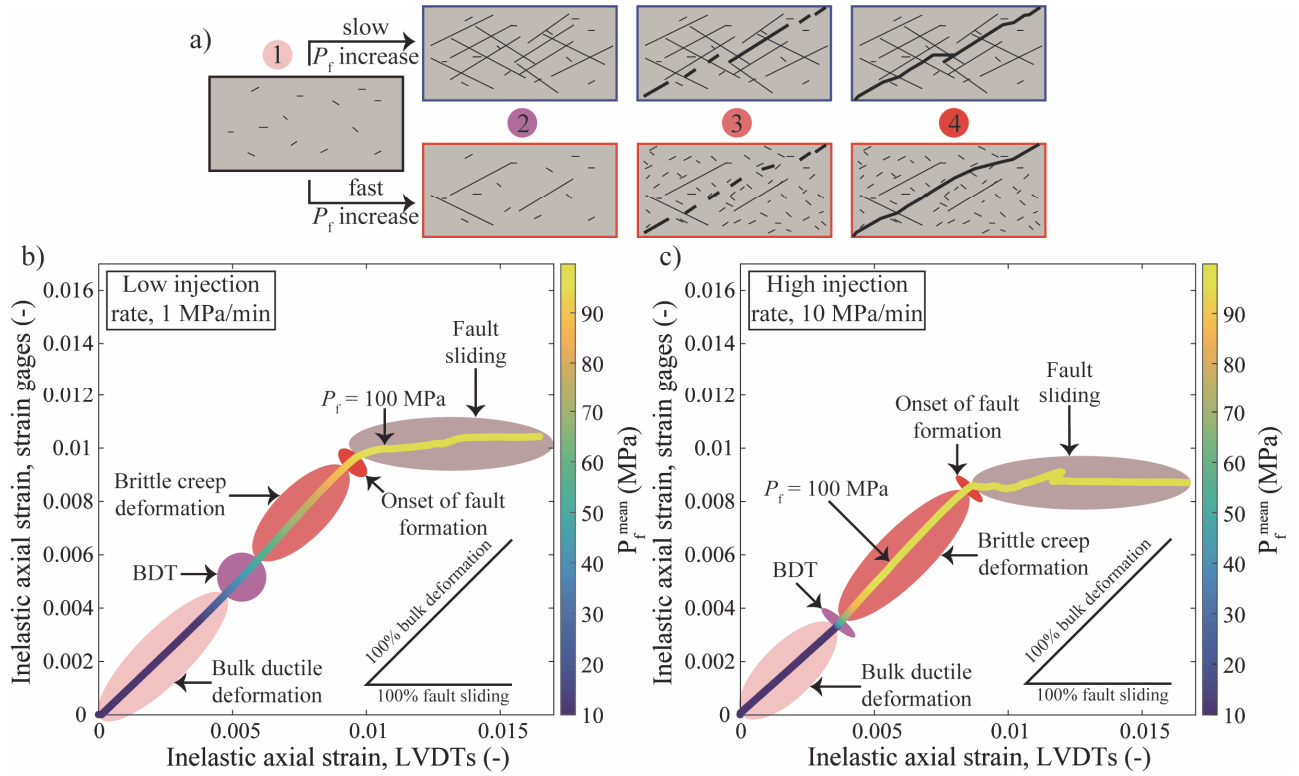


Figure 6. 10: a) Conceptual microscopic model of the deformations occurring during fluid injection into a ductile rock mass. Step 1 represents the bulk ductile deformations. Step 2 represents the ductile-brittle transition. Step 3 represents the brittle creep deformations. Step 4 show the onset of macro-fault formation. b and c) Inelastic axial strain measured at the strain gages as a function of the inelastic axial strain measured at the LVDTs for low (b) and high (c) injection rates. The colour bar shows the pore fluid pressure. In such a plot, a slope of one means that both LVDTs and strain gages record the same deformation and that strain is accumulated in the bulk. However, a slope of zero indicates that the strain gages do not see the deformation seen by the LVDTs, which reveal that strain is localized (i.e. very probably accommodated through fault sliding). The different domains of deformation are segregated into the following categories: at $P_c - P_f \geq 80 \text{ MPa}$ deformation is ductile; at $80 \geq P_c - P_f \geq 60 \text{ MPa}$ deformation is typical of the brittle-ductile transition (BDT); at $P_c - P_f \leq 60 \text{ MPa}$ deformation is brittle; if the slope is unity, creep is occurring; if the slope is less than unity sliding on macroscopic fault is occurring. The steps 1 to 4 in panel a) are represented in the panel b and c by the same colours.

6.5.3 Implication for deep deformations and earthquakes

Under crustal environments where ductile deformations are favoured, pore fluid pressure variations are not rare. They can result from magma build-up in volcanic edifices, dyking, magmatic

fluid pulses (e.g. Caricchi et al., 2011; Farquharson et al., 2016; Nishi et al., 1996) or fluid release during mineral phase changes (e.g. Moore & Vrolijk, 1992). We demonstrate that such pore fluid pressure increases would cause the brittle-ductile transition to migrate to greater depth, possibly leading to shear failure and seismicity at unexpected depths. This result is in agreement with field data suggesting that periods of elevated pore fluid pressures are responsible for ductile shear zones to be overprinted by brittle deformation (e.g. Marchesini et al., 2019; Prando et al., 2020; Wehrens et al., 2016).

In the context of ductile deep reservoir stimulation for geo-energy purposes (e.g. Asanuma et al., 2012; Bignall & Carey, 2011; Frioleifsson et al., 2014; Tsuchiya et al., 2015) our study suggests that injection would primarily produce dilation of the mass rock, possibly increasing its permeability and facilitating fluid circulation. However, the data presented here and previous studies on limestone suggest that porosity changes are relatively small in carbonates (e.g., Nicolas et al., 2016, 2017; Vajdova et al., 2004), inducing relatively small permeability variations (Meng et al., 2019). Additionally, operators should keep in mind that seismicity would never be suppressed in an initially ductile reservoir under fluid stimulation. Indeed, at such depth, rock permeability is low (Violay et al., 2015, 2017), requiring large permeability increases for viable exploitation. This would involve elevated pore fluid pressures for extensive periods of time which would certainly lead to shear failure of the reservoir and possibly to large-magnitude induced seismicity.

Additional experimental and numerical data are needed to better constrain the mechanics of such deep reservoirs. For example, the effect of temperature on the reservoir rock's mechanics could not be tested in our experiments. However, temperature has been shown to be a primordial parameter in brittle-ductile transition mechanics (e.g., Heard, 1960; Tullis & Yund, 1977). On the one hand, high temperature favours plastic mechanisms and ductile deformations. On the other hand, as long term injection may lower the in situ reservoir temperature, it may induce thermal cracking (e.g., Fredrich & Wong, 1986), or stress field variations (e.g., Fryer et al., 2020). A combination of the pore fluid pressure and temperature variations of deep crustal rocks must be studied for safe injections.

6.6 Conclusions

We conducted four constant pore fluid pressure experiments to constrain the brittle-ductile transition of Tavel limestone. Seven additional experiments with pore fluid pressure increase during the ductile deformation of Tavel limestone were performed. These new data provide new constraints on the role of pore fluid pressure variations at conditions close to and below the brittle-ductile transition:

- 1) In an initially ductile rock mass where deformations are controlled by compaction mechanisms, a pore fluid pressure build-up causes the system to instantaneously dilate due to micro-cracking of the rock.
- 2) Localized shear fracturing can develop in an initially ductile rock mass by mean of an increase of the pore fluid pressure. However, the localisation is not instantaneous when the ductile to brittle transition is passed but is linked to the damage history of the rock sample. In the performed experiments, a transient creeping phase is necessary before macroscopic shear failure occurs.

- 3) A critical dilatancy (of about 1% for Tavel limestone) has to be reached in order to obtain shear failure of an initially ductile rock subjected to a pore fluid pressure increase.

Acknowledgments

This work was funded by Gaznat SA (Grant FRICTION: Fault Reactivation during CO₂ sequestration). M. V. thanks the ERC project BEFINE (Grant 757290). The authors thank Baroz Gregoire from CIME laboratory (EPFL) for SEM technical assistance. We also thank Barnaby Fryer and Gabriel Meyer for proofreading. We thank the Carrières Lugan and Sébastien Violay for providing the rock samples. The authors thank the editor Y. Bernabe, associated editor A. Schubnel, along with M. Scuderi and one anonymous reviewer for their constructive comments. Raw data can be found at <https://zenodo.org/record/4268408#.X6wcs2hKiUk> (doi: 10.5281/zenodo.4268408).

Chapter 7 General conclusion and perspectives

7.1 Main findings

The experimental work performed during this thesis has allowed for the better constraint of porous rock (i.e., sandstone and limestone) deformations during fluid injection stimulations in geo-reservoirs. Particularly, fluid-rock matrix and fluid-fault interactions have been investigated at conditions relevant of deep geo-reservoirs targeted for CO₂ sequestration. The results obtained could be extended to natural conditions or to any other geo-reservoirs presenting similar characteristics such as for geothermal energy or waste water storage reservoirs, under certain conditions. This work focused on four main questions:

- 1) How does the presence of fluid affect the short-term rock strength? What are the involved mechanisms?
- 2) How does cyclic stimulation affect the mechanics of intact reservoir rock over time? Does it reduce induced seismicity compared to traditional monotonic injections?
- 3) How does cyclic stimulation affect fault mechanics? Does it favour stable or unstable sliding?

How does a ductile deformation influence the response of rock matrix to hydraulic stimulations? Does the injection rate control the dilatancy and shear localisation?

7.1.1 Short-term water weakening

More than 40 destructive (uniaxial compression, fracture toughness and friction) experiments, complemented by more than 100 non-destructive (porosity and ultra-sonic) measurements have been performed to understand the effect of the presence of fluids on the short-term strength of five sandstones (Chapter 3). Water presence drastically weakens sandstone's strength. Mechanical data shows a reduction of the uniaxial compressive strength, and of the onset of dilatancy, ranging from 0 to 35 %. This reduction is due to the reductions of both the mode I fracture toughness (ranging from 6 to 35%) and the static friction (ranging from 0 to 26 %). By introducing the measured fracture toughness and static friction, the pore-emanating cracks and wing crack models predict the water weakening relatively well with a general slight overestimation (10 to 20%). Finally, a parametric analysis was performed which revealed that a sandstone's absolute strength may be estimated with the wing crack model by means of physical and mechanical parameter measurements.

7.1.2 Pore fluid pressure oscillations on intact rock

Laboratory data from 10 short- and 10 long-term creep experiments performed on Fontainebleau sandstone were performed to better constrain the influence of cyclic pore fluid pressure on intact reservoir mechanical behaviour (Chapter 4). The investigation includes strain (minimum and relative strain rate) and AE events (total number and AE rate) analysis, as well as micro-mechanical model predictions. It has been found that under drained conditions, pore fluid pressure oscillations affect the mechanical behaviour of porous intact rocks. More than the amplitude of the oscillations, the period controls the time-to-failure, failure strength and dilatancy rate of the sample. Because of the non-linearity of long-term (i.e., creep) mechanisms of deformation, large periods of oscillation induce more damage than faster oscillations. Additionally, it has been demonstrated that the pore fluid pressure oscillation controls the AE events (a proxy for the seismicity): the AE events rate oscillates in-phase with the pore fluid pressure variations. Increasing the differential stress, the amplitude and the period of the oscillations accentuate this behaviour.

7.1.3 Pore fluid oscillations on faulted rock

Laboratory data from 11 triaxial experiments performed on Fontainebleau sandstone were performed to better constrain the influence of cyclic pore fluid pressure on fault mechanical behaviour (Chapter 5). The investigation includes strain, stick-slip and AE events analyses, as well as stability analyses using the rate-and-state friction formulation. The study shows that under drained conditions, pore fluid pressure oscillations strongly affect the mechanical behaviour of faults. Indeed, the pore fluid pressure signal directly controls the instabilities' (i.e., stick-slip and AE events) distribution, with an increase of events at moments of elevated pore fluid pressure. For initially stable slipping faults, pore fluid pressure oscillations cause in-phase slip rate perturbations, which in turns cause a reduction of the rate-and-state parameters ($a - b$) of the fault, leading to seismic event nucleation. The higher the pore fluid pressure oscillations amplitude, the lower the stress and the displacement at the onset of seismic event are.

7.1.4 Pore fluid pressure increase in ductile rock

Four constant pore fluid pressure experiments, coupled with 7 fluid injection experiments in initially ductile Tavel limestone were performed to understand how ductile reservoirs react to fluid injections (Chapter 6). The study shows that, under quasi-drained conditions, a pore fluid pressure increase within a rock undergoing ductile deformation causes instantaneous dilation of the system due to micro-cracking of the rock. Further increasing the pore fluid pressure leads to the development of localized deformations (i.e., brittle) and shear fracturing of the rock. The macroscopic localization of the deformation is not instantaneous when the ductile to brittle transition is passed but is linked to the damage history of the rock. Indeed, a creeping phase, where micro-cracking of the rock sample occurs at quasi-constant stress, is necessary prior to macroscopic shear failure of the rock samples. The time and strain length of this creeping phase is controlled by the rate of increase of pore fluid pressure: the faster the injection, the longer the creeping phase. Additionally, a critical dilatancy threshold (i.e., percolation threshold) is needed to obtain shear failure of the rock.

7.2 Implications for reservoir deformations

As mentioned in chapter 1, recent studies on reservoir mechanical behaviour have shown that, for a given *in-situ* pore fluid pressure, different injection strategies result in different seismic responses of the reservoir. Cyclic injections (i.e., soft stimulation) are proposed as an alternative to conventional monotonic fluid injections for geo-reservoir stimulations. This technique aims to increase the reservoir performance while reducing the induced earthquakes compare to conventional monotonic injections (see e.g., Yoon et al., 2014; Zang et al., 2013, 2018).

In this thesis, the experiments are performed under controlled laboratory scale (i.e., centimetre scale) and even if extrapolation to reservoir scale is not trivial, the obtained results constitute a primary base that constrains the mechanisms involved in reservoir rock deformation during different injection strategies. It has been shown that cyclic pore fluid pressure perturbations control the distribution of seismic events under the long-term deformation of brittle reservoir rocks and faults, with higher seismic rates at moments of elevated pore fluid pressure. At greater depth, where brittle processes are inhibited, an increase in the pore fluid pressure may activate brittle process ultimately leading to reservoir shear fracturing and potential seismicity. Interestingly, both for brittle and initially ductile intact reservoirs, the macroscopic shear failure of the reservoir can be expected when a critical dilatancy (i.e., percolation threshold) is reached, in agreement with previous observations (Kranz & Scholz, 1977). In the case of Fontainebleau sandstone and Tavel limestone, the maximum dilatancy prior macroscopic failure is around 1%. Additionally, fluid injection can activate slip on faults that are present within the reservoir. Even if the reactivation is initially stable, fluid pressure variation on the fault plane might change the fault velocity, and in turn, change the sliding behaviour from stable to unstable (i.e., nucleating earthquake).

Note that in the performed experiments, the pore fluid pressure is homogeneously or quasi-homogeneously distributed within the samples. For geo-engineering purpose, and particularly for the case of CO₂ geological sequestration, the injected volumes expected are so high that undrained conditions and pore fluid pressure gradients within the reservoir are to be expected. Local overpressure might favour local higher deformation rates or fault reactivation (Passelègue, Brantut, et al., 2018) that could favour shear failure and induced seismicity at lower bore hole injection pressures than expected.

In the end, can a cyclic injection strategy reduce the potential of induced seismicity? This experimental study demonstrates that reservoir rock deformations are very much controlled by the effective stress conditions. It has also been demonstrated that earthquakes can nucleate on initially creeping faults (i.e., fault with slip accommodated through stable motion) due to small pore fluid pressure variations. Therefore, at the reservoir scale, a cyclic injection strategy might trigger less seismicity only because they leave more time for pore fluid pressure to homogenise within the reservoir, and so lower pore fluid pressures are reached compare to monotonic injections. However, it should be kept in mind that reservoir faulting or fault reactivation will never be suppressed for the fluid volumes that are targeted to be injected for geo-energy purpose.

7.3 Future work

This work has answered preliminary questions on the effect of fluid weakening and oscillating pore fluid pressure on rocks and faults, as well as on the effect of pore fluid pressure build-up in ductile rocks. It has also led to new questions that need to be addressed in the future.

Fracture toughness and frictional parameters water weakening

As detailed in Chapter 3, water-saturated sandstones, present a reduction of the uniaxial compressive strength, as well as an onset of dilatancy, compared to dry conditions. It was demonstrated that strength reduction is primarily linked to the reduction in both the mode I fracture toughness and the static friction. However, this study did not investigate the mechanism(s) involved in water weakening of the fracture toughness and static friction.

Previous experimental work also demonstrates that the fracture toughness of rock can be reduced in the presence of water. For example, full water saturation of sandstones typically reduces their mode I fracture toughness by 30 to 50% compared to dry conditions (e.g., Guha Roy et al., 2017; Maruvanchery & Kim, 2019; Nara et al., 2012). An abundance of mechanisms can explain this water weakening: stress corrosion (e.g., Kataoka et al., 2015), mineral dissolution (e.g., Maruvanchery & Kim, 2019), capillary forces at the crack tip (e.g., Nara et al., 2012), clay weakening (e.g., Wang et al., 2007), grain contact lubrication (e.g., Guha Roy et al., 2017), or reduction of surface energy via adsorption mechanisms (e.g., Baud et al., 2000). Here, the performed experiments didn't allow for discrimination between the mechanisms involved in the five tested sandstones water weakening. Additional experiments, including strain rate variation, other rock types or simpler materials (e.g., PMMA or synthetic monomineralic rocks) are needed to constrain the mechanisms involved in fracture toughness water weakening.

Previous experimental studies also found that the frictional parameters decrease in presence of water for granite (e.g., Byerlee, 1967), quartzite (e.g., Dieterich & Conrad, 1984), limestone (e.g., Rutter, 1972), granitic gneiss (e.g., Jaeger, 1959) or sandstones (e.g., Jaeger, 1959). Two main possibilities can explain such a reduction: 1) water decreases the adhesion forces at contact points, and 2) water reduces the strength of the asperities supporting the shear stress. Here, no mechanisms could be determined for the static friction water weakening. As frictional parameters are a function of the mechanical behaviour of the asperities (i.e., contact points of the surface), future laboratory experiments are needed to better constrain the influence of water at the asperity scale.

Influence of corrosive fluids

In this thesis, the experiments were all performed using distilled water as pore fluid. For the purposes of geo-reservoir injections, and particularly for CO₂ sequestration, the relation between rock and acidic fluids might be different than that with water. Experimental studies demonstrate that calcite can be dissolved under a continuous flow of CO₂ (e.g., Grgic, 2011; Luquot & Gouze, 2009; Sterpenich et al., 2009). For sandstones cemented by calcite, such dissolution may lead to massive strength reduction of the rock matrix and potentially to reservoir fracturing. For safe CO₂ sequestration, additional long-term experiments on calcite or calcite-cemented rocks are needed to characterise the impact of corrosive fluids on the long-term strength of the reservoir rock.

Distributed deformation in sandstones

Under relatively low confining pressure (i.e., low depth), highly porous rocks might deform in the ductile regime by cataclastic flow. The deformations involve cataclastic pore collapse and pore volume reduction (Wong & Baud, 2012). If such deformations occur within a geo-reservoir, the permeability and porosity of the reservoir will be reduced drastically (e.g., Vajdova et al., 2004). Moreover, Heap et al. (2015) demonstrated that compaction bands can develop under low differential stress conditions during long-term deformations of sandstones. Together, these mechanisms can lead to massive porosity reduction of the reservoir and unwanted surface deformation such as large-scale subsidence. Additional studies coupling hydraulic properties and bulk volume strain reduction linked with cataclastic pore collapse deformation are needed to understand and prevent such undesired deformations.

Temperature effects

In this thesis, all the experiments were performed at room temperature. However, at a typical geo-reservoir depth of 1 to 2 km, the temperature may reach 60 to 90°C. It has been demonstrated that increasing temperature: reduces the short-term (e.g., Friedman et al., 1979; Wong, 1982) and long-term (e.g., Heap et al., 2009b) strength of the rocks in the brittle domain, change the frictional stability of faults (e.g., Blanpied et al., 1991; Scholz, 1998; Stesky et al., 1974) and favours ductile deformations (Heard, 1960). For CO₂ sequestration and other geo-engineering purposes, the injected fluid may be at lower temperatures than the reservoir rock, possibly changing the *in-situ* temperature conditions. Additionally, injecting cold fluid into geo-reservoir may cause thermal cracking (e.g., Fredrich & Wong, 1986), or stress field variations (e.g., Fryer et al., 2020; Vilarrasa & Rutqvist, 2017). A combination of pore fluid pressure variations coupled with temperature changes may lead to complex non-linear stress changes. Future experimental work is planned to better constrain the influence of temperature reductions on fault reactivation and reservoir deformations.

Caprock mechanics and hydraulic properties

Safe CO₂ sequestration into geo-reservoirs implies long-term sequestration. The upward migration of CO₂ is prevented by an impermeable caprock. In this thesis, only the porous and permeable reservoir rock mechanics have been studied. However, the base of the caprock might be subjected to similar pore fluid pressures as the reservoir rock (even if slightly delayed due to diffusion time). Therefore, experimental work is needed to better constrain caprock mechanics while it is subjected to pore fluid pressure variations.

Additionally, faults can extend or propagate from the reservoir rock to the caprock. Faults generally have higher permeabilities than intact rock (e.g., Evans et al., 1997), and they might become a preferential path for CO₂ upward migration. Even if studies demonstrate relatively small permeability variations with fault slip for clay rocks (e.g., Orellana et al., 2019), the hydraulic properties of caprock and caprock faults are important parameters that must be studied for safe CO₂ sequestration.

Bibliography

- Abou-Sayed, A. S., Brechtel, C. E., & Clifton, R. J. (1978). In situ stress determination by hydrofracturing: A fracture mechanics approach. *Journal of Geophysical Research*, 83(B6), 2851–2862. <https://doi.org/10.1029/JB083iB06p02851>
- Al-Shayea, N. A., Khan, K., & Abduljawwad, S. N. (2000). Effects of confining pressure and temperature on mixed-mode (I-II) fracture toughness of a limestone rock. *International Journal of Rock Mechanics and Mining Sciences*, 37(4), 629–643. [https://doi.org/10.1016/S1365-1609\(00\)00003-4](https://doi.org/10.1016/S1365-1609(00)00003-4)
- Anderson, O. L., & Grew, P. C. (1977). Stress corrosion theory of crack propagation with applications to geophysics. *Reviews of Geophysics*, 15(1), 77–104. <https://doi.org/10.1029/RG015i001p00077>
- Asanuma, H., Muraoka, H., Tsuchiya, N., & Ito, H. (2012). The concept of the Japan Beyond-Brittle Project (JBBP) to develop EGS reservoirs in ductile zones. *Transactions - Geothermal Resources Council*, 36, 359–364.
- Ashby, M. F., & Hallam, S. D. (1986). The failure of brittle solids containing small cracks under compressive stress states. *Acta Metallurgica*, 34(3), 497–510. [https://doi.org/10.1016/0001-6160\(86\)90086-6](https://doi.org/10.1016/0001-6160(86)90086-6)
- Ashby, M. F., & Sammis, C. G. (1990). The damage mechanics of brittle solids in compression. *Pure and Applied Geophysics*, 133(3), 489–521. <https://doi.org/10.1007/BF00878002>
- Ashby, M. F., & Verrall, R. A. (1973). Diffusion-accommodated flow and superplasticity. *Acta Metallurgica*, 21(2), 149–163. [https://doi.org/10.1016/0001-6160\(73\)90057-6](https://doi.org/10.1016/0001-6160(73)90057-6)
- Atkinson, B. K., & Avdis, V. (1980). Fracture mechanics parameters of some rock-forming minerals determined using an indentation technique. *International Journal of Rock Mechanics and Mining Sciences & Geomechanics Abstracts*, 17(6), 383–386. [https://doi.org/10.1016/0148-9062\(80\)90523-9](https://doi.org/10.1016/0148-9062(80)90523-9)
- Atkinson, B. K., & Meredith, P. G. (1981). Stress corrosion cracking of quartz: a note on the influence of chemical environment. *Tectonophysics*, 77(1–2), T1–T11. [https://doi.org/10.1016/0040-1951\(81\)90157-8](https://doi.org/10.1016/0040-1951(81)90157-8)
- Atkinson, Barry Kean. (1979). A fracture mechanics study of subcritical tensile cracking of quartz in wet environments. *Pure and Applied Geophysics*, 117(5), 1011–1024. <https://doi.org/10.1007/BF00876082>
- Atkinson, Barry Kean. (1980). Stress corrosion and the rate-dependent tensile failure of a fine-grained quartz rock. *Tectonophysics*, 65(3–4), 281–290. [https://doi.org/10.1016/0040-1951\(80\)90078-5](https://doi.org/10.1016/0040-1951(80)90078-5)

- Atkinson, Barry Kean. (1984). Subcritical Crack Growth in Geological Materials. *Journal of Geophysical Research*, 89(B6), 4077–4114. <https://doi.org/10.1029/JB089iB06p04077>
- Aubry, J., Passelègue, F. X., Escartín, J., Gasc, J., Deldicque, D., & Schubnel, A. (2020). Fault Stability Across the Seismogenic Zone. *Journal of Geophysical Research: Solid Earth*, 125(8), e2020JB019670. <https://doi.org/10.1029/2020JB019670>
- Balme, M. R., Rocchi, V., Jones, C., Sammonds, P. R., Meredith, P. G., & Boon, S. (2004). Fracture toughness measurements on igneous rocks using a high-pressure, high-temperature rock fracture mechanics cell. *Journal of Volcanology and Geothermal Research*, 132(2–3), 159–172. [https://doi.org/10.1016/S0377-0273\(03\)00343-3](https://doi.org/10.1016/S0377-0273(03)00343-3)
- Bartlow, N. M., Lockner, D. A., & Beeler, N. M. (2012). Laboratory triggering of stick-slip events by oscillatory loading in the presence of pore fluid with implications for physics of tectonic tremor. *Journal of Geophysical Research B: Solid Earth*, 117(B11411). <https://doi.org/10.1029/2012JB009452>
- Barton, N. (1976). The shear strength of rock and rock joints. *International Journal of Rock Mechanics and Mining Sciences and Geomechanics Abstracts*, 13(9), 255–279. [https://doi.org/10.1016/0148-9062\(76\)90003-6](https://doi.org/10.1016/0148-9062(76)90003-6)
- Baud, P., & Meredith, P. G. (1997). Damage accumulation during triaxial creep of Darley Dale sandstone from pore volumetry and acoustic emission. *International Journal of Rock Mechanics and Mining Sciences & Geomechanics Abstracts*, 34(3–4), Paper No. 024. [https://doi.org/10.1016/S1365-1609\(97\)00060-9](https://doi.org/10.1016/S1365-1609(97)00060-9)
- Baud, Patrick, Zhu, W., & Wong, T. (2000). Failure mode and weakening effect of water on sandstone. *Journal of Geophysical Research: Solid Earth*, 105(B7), 16371–16389. <https://doi.org/doi.org/10.1029/2000JB900087>
- Baud, Patrick, Klein, E., & Wong, T. (2004). Compaction localization in porous sandstones: Spatial evolution of damage and acoustic emission activity. *Journal of Structural Geology*, 26(4), 603–624. <https://doi.org/10.1016/j.jsg.2003.09.002>
- Baud, Patrick, Vajdova, V., & Wong, T. (2006). Shear-enhanced compaction and strain localization: Inelastic deformation and constitutive modeling of four porous sandstones. *Journal of Geophysical Research: Solid Earth*, 111(B12). <https://doi.org/10.1029/2005JB004101>
- Baud, Patrick, Wong, T., & Zhu, W. (2014). Effects of porosity and crack density on the compressive strength of rocks. *International Journal of Rock Mechanics and Mining Sciences*, 67, 202–211. <https://doi.org/10.1016/j.ijrmms.2013.08.031>
- Baud, Patrick, Reuschlé, T., Ji, Y., Cheung, C. S. N., & Wong, T. (2015). Mechanical compaction and strain localization in Bleurswiller sandstone. *Journal of Geophysical Research: Solid Earth*, 120(9), 6501–6522. <https://doi.org/10.1002/2015JB012192>
- Beeler, N. M., & Lockner, D. A. (2003). Why earthquakes correlate weakly with the solid Earth tides: Effects of periodic stress on the rate and probability of earthquake occurrence. *Journal of Geophysical Research*, 108(B8). <https://doi.org/10.1029/2001JB001518>
- Benson, S. M., & Cole, D. R. (2008). CO₂ sequestration in deep sedimentary formations. *Elements*, 4(5), 325–331. <https://doi.org/10.2113/gselements.4.5.325>

- Bernabe, Y. (1987). The effective pressure law for permeability during pore pressure and confining pressure cycling of several crystalline rocks. *Journal of Geophysical Research*, 92(B1), 649–657. <https://doi.org/10.1029/JB092iB01p00649>
- Bernabe, Y., & Brace, W. F. (1990). Deformation and Fracture of Berea Sandstone. In A. Duba, W. Durham, J. Handin, & H. Wang (Eds.), *The Brittle-Ductile Transition in Rocks, Volume 56, Geophysical Monograph Series* (pp. 91–101). Washington, D.C.: American Geophysical Union.
- Bésuelle, P., Baud, P., & Wong, T. (2003). Failure mode and spatial distribution of damage in Rothbach sandstone in the brittle-ductile transition. *Pure and Applied Geophysics*, 160(5–6), 851–868. <https://doi.org/10.1007/PL00012569>
- Bettinelli, P., Avouac, J. P., Flouzat, M., Bollinger, L., Ramillien, G., Rajaure, S., & Sapkota, S. (2008). Seasonal variations of seismicity and geodetic strain in the Himalaya induced by surface hydrology. *Earth and Planetary Science Letters*, 266(3–4), 332–344. <https://doi.org/10.1016/j.epsl.2007.11.021>
- Bied, A. El, Sulem, J., & Martineau, F. (2002). Microstructure of shear zones in Fontainebleau sandstone. *International Journal of Rock Mechanics & Mining Sciences*, 39, 917–932.
- Bignall, G., & Carey, B. (2011). A deep (5 km?) geothermal science drilling project for the Taupo Volcanic Zone—Who wants in? In *33rd New Zealand Geothermal Workshop*. Auckland, New Zealand.
- Biot, M. A., & Willis, D. G. (1957). The elastic coefficients of the theory of consolidation. *Journal of Applied Mechanics*, 24, 594–601.
- Birch, F. (1960). The velocity of compressional waves in rocks to 10 kilobars, Part 1. *Journal of Geophysical Research*, 65(4), 1083–1102. <https://doi.org/10.1029/JZ065i004p01083>
- Blanpied, M. L., Lockner, D. A., & Byerlee, J. D. (1991). Fault stability inferred from granite sliding experiments at hydrothermal conditions. *Geophysical Research Letters*, 18(4), 609–612. <https://doi.org/10.1029/91GL00469>
- Bourbié, T., & Zinszner, B. (1985). Hydraulic and acoustic properties as a function of porosity in Fontainebleau Sandstone. *Journal of Geophysical Research*, 90(B13), 11524. <https://doi.org/10.1029/JB090iB13p11524>
- Boyle, R. (1662). *A defence of the doctrine touching the spring and weight of the air*. London: Printed by F.G. for Thomas Robinson Bookseller in Oxon.
- Brace, W. F. (1978a). A note on permeability changes in geologic material due to stress. *Pure and Applied Geophysics*, 116(4–5), 627–633. <https://doi.org/10.1007/BF00876529>
- Brace, W. F. (1978b). Volume changes during fracture and frictional sliding: A review. *Pure and Applied Geophysics*, 116(4–5), 603–614. <https://doi.org/10.1007/BF00876527>
- Brace, W. F., & Bombolakis, E. G. (1963). A note on brittle crack growth in compression. *Journal of Geophysical Research*, 68(12), 3709–3713.
- Brace, W. F., Paulding, B. W., & Scholz, C. (1966). Dilatancy in the fracture of crystalline rocks. *Journal of Geophysical Research*, 71(16), 3939–3953. <https://doi.org/10.1029/JZ071i016p03939>

- Brantut, N., Baud, P., Heap, M. J., & Meredith, P. G. (2012). Micromechanics of brittle creep in rocks. *Journal of Geophysical Research: Solid Earth*, 117(B8). <https://doi.org/10.1029/2012JB009299>
- Brantut, N., Heap, M. J., Meredith, P. G., & Baud, P. (2013). Time-dependent cracking and brittle creep in crustal rocks: A review. *Journal of Structural Geology*, 52(1), 17–43. <https://doi.org/10.1016/j.jsg.2013.03.007>
- Brantut, N., Heap, M. J., Baud, P., & Meredith, P. G. (2014). Rate- and strain-dependent brittle deformation of rocks. *Journal of Geophysical Research: Solid Earth*, 116, 1818–1836. <https://doi.org/10.1002/2013JB010448>.
- Burlini, L., Di Toro, G., & Meredith, P. (2009). Seismic tremor in subduction zones: Rock physics evidence. *Geophysical Research Letters*, 36(8). <https://doi.org/10.1029/2009GL037735>
- Byerlee, J. (1967). High Confining Pressure Some experiments made. *Journal of Geophysical Research*, 72(14), 3639–3648. <https://doi.org/10.1029/JZ072i014p03639>
- Byerlee, J. (1978). Friction of Rocks. In *Rock friction and earthquake prediction* (Birkhäuser, pp. 615–626). Basel. Retrieved from https://doi.org/10.1007/BF00876528%0Afile:///C:/artikkelit/Lehdet/Pure_and_applied_GeoPhy/Byerlee-1978--Friction_of_rocks.pdf
- Byerlee, J. D. (1968). Brittle-ductile transition in rocks. *Journal of Geophysical Research*, 73(14), 4741–4750. <https://doi.org/10.1029/jb073i014p04741>
- Candela, T., Osinga, S., Ampuero, J.-P., Wassing, B., Pluymaekers, M., Fokker, P. A., et al. (2019). Depletion-induced seismicity at the Groningen gas field: Coulomb rate-and-state models including differential compaction effect. *Journal of Geophysical Research: Solid Earth*. <https://doi.org/10.1029/2018JB016670>
- Caricchi, L., Pommier, A., Pistone, M., Castro, J., Burgisser, A., & Perugini, D. (2011). Strain-induced magma degassing: Insights from simple-shear experiments on bubble bearing melts. *Bulletin of Volcanology*, 73(9), 1245–1257. <https://doi.org/10.1007/s00445-011-0471-2>
- Carroll, M. M. (1980). Compaction of Dry or Fluid-Filled Porous Materials. *Journal of the Engineering Mechanics Division*, 106(5), 969–990.
- Carter, N. L., & Kirby, S. H. (1978). Transient creep and semibrittle behavior of crystalline rocks. *Pure and Applied Geophysics*, 116(4), 807–839. <https://doi.org/10.1007/BF00876540>
- Celia, M. A., Bachu, S., Nordbotten, J. M., Gasda, S. E., & Dahle, H. K. (2004). Quantitative estimation of CO₂ leakage from geological storage: Analytical models, numerical models, and data needs. In *Proceedings of 7th International Conference on Greenhouse Gas Control Technologies.(GHGT-7)* (pp. 663–672). <https://doi.org/10.1016/B978-008044704-9/50067-7>
- Cerfontaine, B., & Collin, F. (2017). Cyclic and Fatigue Behaviour of Rock Materials: Review, Interpretation and Research Perspectives. *Rock Mechanics and Rock Engineering*. <https://doi.org/10.1007/s00603-017-1337-5>
- Chambon, G., & Rudnicki, J. W. (2001). Effects of normal stress variations on frictional stability of a fluid-infiltrated fault. *Journal of Geophysical Research: Solid Earth*, 106(B6), 11353–11372. <https://doi.org/10.1029/2001JB900002>

- Chanard, K., Nicolas, A., Hatano, T., Petrelis, F., Latour, S., Vinciguerra, S., & Schubnel, A. (2019). Sensitivity of acoustic emission triggering to small pore pressure cycling perturbations during brittle creep. *Geophysical Research Letters*, 46(13), 7414–7423. <https://doi.org/10.1029/2019GL082093>
- Chanard, K., Avouac, J. P., Ramillien, G., & Genrich, J. (2014). Modeling deformation induced by seasonal variations of continental water in the Himalaya region: Sensitivity to Earth elastic structure. *Journal of Geophysical Research: Solid Earth*, 119, 5097–5113. <https://doi.org/10.1002/2013JB010451>
- Chanard, K., Latour, S., & Schubnel, A. (2015). Dynamic acoustic emission triggering by small periodic pore pressure variations during brittle creep experiments. In *AGU Fall Meeting Abstracts*.
- Chanard, Kristel. (2015). *Rôle des hétérogénéités géométriques et rhéologiques sur les ruptures sismiques*. Ecole Normale Supérieure.
- Chanard, Kristel, Fleitout, L., Calais, E., Barbot, S., & Avouac, J. P. (2018). Constraints on Transient Viscoelastic Rheology of the Asthenosphere From Seasonal Deformation. *Geophysical Research Letters*, 45(5), 2328–2338. <https://doi.org/10.1002/2017GL076451>
- Chang, C., Zoback, M. D., & Khaksar, A. (2006). Empirical relations between rock strength and physical properties in sedimentary rocks. *Journal of Petroleum Science and Engineering*, 51(3–4), 223–237. <https://doi.org/10.1016/j.petrol.2006.01.003>
- Charles, R. J. (1958a). Static Fatigue of Glass. I. *Journal of Applied Physics*, 29(11), 1549–1553. <https://doi.org/10.1063/1.1722991>
- Charles, R. J. (1958b). Static fatigue of glass. II. *Journal of Applied Physics*, 29(11), 1554–1560. <https://doi.org/10.1063/1.1722992>
- Chevalier, G., Diamond, L. W., & Leu, W. (2010). Potential for deep geological sequestration of CO₂ in Switzerland: A first appraisal. *Swiss Journal of Geosciences*, 103(3), 427–455. <https://doi.org/10.1007/s00015-010-0030-4>
- Costin, L. S. (1983). A microcrack model for the deformation and failure of brittle rock. *Journal of Geophysical Research: Solid Earth*, 88(B11), 9485–9492. <https://doi.org/10.1029/JB088iB11p09485>
- Costin, L. S. (1985). Damage mechanics in the post-failure regime. *Mechanics of Materials*, 4(2), 149–160. [https://doi.org/10.1016/0167-6636\(85\)90013-4](https://doi.org/10.1016/0167-6636(85)90013-4)
- Craig, T. J., Chanard, K., & Calais, E. (2017). Hydrologically-driven crustal stresses and seismicity in the New Madrid seismic zone. *Nature Communications*, 8(1), 2143. <https://doi.org/10.1038/s41467-017-01696-w>
- Dal Bó, M., Cantavella, V., Sánchez, E., Hotza, D., & Gilabert, F. A. (2013). Fracture toughness and temperature dependence of Young's modulus of a sintered albite glass. *Journal of Non-Crystalline Solids*, 363(1), 70–76. <https://doi.org/10.1016/j.jnoncrysol.2012.12.001>
- David, C., Menéndez, B., & Bernabé, Y. (1998). The mechanical behaviour of synthetic sandstone with varying brittle cement content. *International Journal of Rock Mechanics and Mining Sciences*, 35(6), 759–770. [https://doi.org/10.1016/S0148-9062\(98\)00003-5](https://doi.org/10.1016/S0148-9062(98)00003-5)

- David, Christian, Wong, T.-F., Zhu, W., & Zhang, J. (1994). Laboratory measurement of compaction-induced permeability change in porous rocks: Implications for the generation and maintenance of pore pressure excess in the crust. *Pure and Applied Geophysics*, 143(1–3), 425–456. <https://doi.org/10.1007/BF00874337>
- Dieterich, J. H. (1978). Time-dependent friction and the mechanics of stick-slip. *Pure and Applied Geophysics*, 116(4–5), 790–806. <https://doi.org/10.1007/BF00876539>
- Dieterich, J. H. (1979). Modeling of rock friction: 1. Experimental results and constitutive equations. *Journal of Geophysical Research*, 84(9), 2161–2168. <https://doi.org/10.1007/BF00876539>
- Dieterich, J. H., & Linker, M. F. (1992). Fault stability under conditions of variable normal stress. *Geophysical Research Letters*, 19(16), 1691–1694. <https://doi.org/10.1029/92GL01821>
- Dieterich, James H., & Conrad, G. (1984). Effect of Humidity on Time- and Velocity-Dependent Friction in Rocks. *Journal of Geophysical Research*, 89(B6), 4196–4202. <https://doi.org/10.1029/jb089ib06p04196>
- Duda, M., & Renner, J. (2013). The weakening effect of water on the brittle failure strength of sandstone. *Geophysical Journal International*, 192(3), 1091–1108. <https://doi.org/10.1093/gji/ggs090>
- Dunn, D. E., LaFountain, L. J., & Jackson, R. E. (1973). Porosity dependence and mechanism of brittle fracture in sandstones. *Journal of Geophysical Research*, 78(14), 2403–2417. <https://doi.org/10.1029/JB078i014p02403>
- Durney, D. W. (1972). Solution-transfer, an Important Geological Deformation Mechanism. *Nature*, 235, 315–317. <https://doi.org/10.1038/235315a0>
- Edmond, J. M., & Paterson, M. S. (1972). Volume changes during the deformation of rocks at high pressures. *International Journal of Rock Mechanics and Mining Sciences & Geomechanics Abstracts*, 9(2), 161–182. [https://doi.org/10.1016/0148-9062\(72\)90019-8](https://doi.org/10.1016/0148-9062(72)90019-8)
- Ellsworth, W. L. (2013). Injection-Induced Earthquakes. *Science*, 341(July), 1225942. <https://doi.org/10.1785/gssrl.83.2.250>
- Evans, B., & Kohlstedt, D. L. (1995). Rheology of rocks. In *Rock physics & phase relations: A handbook of Physical Constants* (Vol. 3, pp. 148–165). <https://doi.org/10.1029/RF003p0148>
- Evans, B., Fredrich, J. T., & Wong, T.-F. (1990). The Brittle-Ductile Transition in Rocks' Recent Experimental and Theoretical Progress. In A. G. Duba, W. B. Durham, J. W. Handin, & H. F. Wang (Eds.), *The Brittle-Ductile Transition in Rocks* (Vol. 56). Washington, DC: AGU. <https://doi.org/10.1029/GM056p0001>
- Evans, J. P., Forster, C. B., & Goddard, J. V. (1997). Permeability of fault-related rocks, and implications for hydraulic structure of fault zones. *Journal of Structural Geology*, 19(11), 1393–1404. [https://doi.org/10.1016/S0191-8141\(97\)00057-6](https://doi.org/10.1016/S0191-8141(97)00057-6)
- Fabre, D., & Gustkiewicz, J. (1997). Poroelastic properties of limestones and sandstones under hydrostatic conditions. *International Journal of Rock Mechanics and Mining Sciences*, 34(1), 127–134. [https://doi.org/10.1016/S0148-9062\(96\)00037-X](https://doi.org/10.1016/S0148-9062(96)00037-X)
- Farquharson, J., Heap, M. J., Baud, P., Reuschlé, T., & Varley, N. R. (2016). Pore pressure embrittlement in a volcanic edifice. *Bulletin of Volcanology*, 78(1).

<https://doi.org/10.1007/s00445-015-0997-9>

- Farver, J. R., & Yund, R. A. (1991). Oxygen diffusion in quartz: Dependence on temperature and water fugacity. *Chemical Geology*, 90(1–2), 55–70. [https://doi.org/10.1016/0009-2541\(91\)90033-N](https://doi.org/10.1016/0009-2541(91)90033-N)
- Fischer, G. J., & Paterson, M. S. (1989). Dilatancy During Rock Deformation at High Temperatures and Pressures. *Journal of Geophysical Research*, 94(B12), 17607–17617. <https://doi.org/10.1029/JB094iB12p17607>
- Fowell, R. J., & Xu, C. (1993). The cracked chevron notched Brazilian disc test- geometrical considerations for practical rock fracture toughness measurement. *International Journal of Rock Mechanics and Mining Sciences & Geomechanics Abstracts*, 30(7), 821–824. [https://doi.org/10.1016/0148-9062\(93\)90029-D](https://doi.org/10.1016/0148-9062(93)90029-D)
- Fowell, R. J., & Xu, C. (1994). The use of the cracked Brazilian disc geometry for rock fracture investigations. *International Journal of Rock Mechanics and Mining Sciences and Geomechanics Abstracts*, 31(6), 571–579. [https://doi.org/10.1016/0148-9062\(94\)90001-9](https://doi.org/10.1016/0148-9062(94)90001-9)
- Fowell, R. J., Hudson, J. A., Xu, C., Chen, J. F., & Zhao, X. (1995). Suggested method for determining mode I fracture toughness using Cracked Chevron Notched Brazilian Disc (CCNBD) specimens. *International Journal of Rock Mechanics and Mining Sciences and Geomechanics Abstracts*, 32(1), 57–64. [https://doi.org/10.1016/0148-9062\(94\)00015-U](https://doi.org/10.1016/0148-9062(94)00015-U)
- Fowell, R. J., Xu, C., & Dowd, P. A. (2006). An update on the fracture toughness testing methods related to the cracked Chevron-notched Brazilian disk (CCNBD) specimen. *Pure and Applied Geophysics*, 163(5–6), 1047–1057. <https://doi.org/10.1007/s00024-006-0057-7>
- Fredrich, J. T., Greaves, K. H., & Martin, J. W. (1993). Pore geometry and transport properties of Fontainebleau sandstone. *International Journal of Rock Mechanics and Mining Sciences And*, 30(7), 691–697. [https://doi.org/10.1016/0148-9062\(93\)90007-Z](https://doi.org/10.1016/0148-9062(93)90007-Z)
- Fredrich, Joanne T., & Wong, T. F. (1986). Micromechanics of thermally induced cracking in three crustal rocks. *Journal of Geophysical Research*, 91(B12), 12743–12764. <https://doi.org/10.1029/JB091iB12p12743>
- Fredrich, Joanne T., Evans, B., & Wong, T. (1989). Brittle to plastic transition in Carrara Marble. *Journal of Geophysical Research*, 94(B4), 4129–4145. <https://doi.org/10.1029/JB094iB04p04129>
- Freiman, S. W. (1984). Effect of chemical environments on slow crack growth in glasses and ceramics. *Journal of Geophysical Research*, 89(B6), 4072–4076. <https://doi.org/10.1029/JB089iB06p04072>
- French, M. E., Zhu, W., & Banker, J. (2016). Fault slip controlled by stress path and fluid pressurization rate. *Geophysical Research Letters*, 43(9), 4330–4339. <https://doi.org/10.1002/2016GL068893>
- Friedman, M., Handin, J., Higgs, N. G., & Lantz, J. R. (1979). Strength and ductility of four dry igneous rocks at low pressures and temperatures to partial melting. In *20th U.S. Symposium on Rock Mechanics* (pp. 35–50). Austin, Texas.
- Frioleifsson, G. O., Elders, W. A., & Albertsson, A. (2014). The concept of the Iceland deep

- drilling project. *Geothermics*, 49, 2–8. <https://doi.org/10.1016/j.geothermics.2013.03.004>
- Fryer, B., Siddiqi, G., & Laloui, L. (2020). Injection-induced seismicity: Strategies for reducing risk using high stress path reservoirs and temperature-induced stress preconditioning. *Geophysical Journal International*, 220(2), 1436–1446. <https://doi.org/10.1093/gji/ggz490>
- Funatsu, T., Seto, M., Shimada, H., Matsui, K., & Kuruppu, M. (2004). Combined effects of increasing temperature and confining pressure on the fracture toughness of clay bearing rocks. *International Journal of Rock Mechanics and Mining Sciences*, 41(6), 927–938. <https://doi.org/10.1016/j.ijrmms.2004.02.008>
- Gehne, S., Forbes Inskip, N. D., Benson, P. M., Meredith, P. G., & Koor, N. (2020). Fluid-Driven Tensile Fracture and Fracture Toughness in Nash Point Shale at Elevated Pressure. *Journal of Geophysical Research: Solid Earth*, 125(2), e2019JB018971. <https://doi.org/10.1029/2019JB018971>
- Goetze, C., & Brace, W. F. (1972). Laboratory observations of high-temperature rheology of rocks. In *Developments in Geotectonics: The Upper Mantle* (Vol. 4, pp. 583–600). ELSEVIER PUBLISHING COMPANY, AMSTERDAM. <https://doi.org/10.1016/B978-0-444-41015-3.50036-7>
- Goetze, Christopher, & Evans, B. (1979). Stress and temperature in the bending lithosphere as constrained by experimental rock mechanics. *Geophysical Journal of the Royal Astronomical Society*, 59(3), 463–478. <https://doi.org/10.1111/j.1365-246X.1979.tb02567.x>
- Grgic, D. (2011). Influence of CO₂ on the long-term chemomechanical behavior of an oolitic limestone. *Journal of Geophysical Research: Solid Earth*, 116(7), 1–22. <https://doi.org/10.1029/2010JB008176>
- Griffith, A. A. (1920). The Phenomena of Rupture and Flow in Solids. *Philosophical Transactions of the Royal Society of London. Series A, Containing Papers of a Mathematical or Physical Character*, 221(582–593), 163–198. <https://doi.org/10.1098/rsta.1921.0006>
- Griggs, D. (1967). Hydrolytic Weakening of Quartz and Other Silicates. *Geophysical Journal of the Royal Astronomical Society*, 14(1–4), 19–31. <https://doi.org/10.1111/j.1365-246X.1967.tb06218.x>
- Gu, J.-C., Rice, J. R., Ruina, A. L., & Tse, S. T. (1984). Stability of quasi-static slip in a single degree of freedom elastic system with rate and state dependent friction. *Journal of the Mechanics and Physics of Solids*, 32(3), 167–196. [https://doi.org/10.1016/s0022-5096\(98\)00113-6](https://doi.org/10.1016/s0022-5096(98)00113-6)
- Guéguen, Y., & Palciauskas, V. (1994). *Introduction to the physics of rocks*. Princeton, New Jersey: Princeton University Press.
- Guérin-Marthe, S., Nielsen, S., Bird, R., Giani, S., & Di Toro, G. (2019). Earthquake Nucleation Size: Evidence of Loading Rate Dependence in Laboratory Faults. *Journal of Geophysical Research: Solid Earth*, 124(1), 689–708. <https://doi.org/10.1029/2018JB016803>
- Guha Roy, D., Singh, T. N., Kodikara, J., & Das, R. (2017). Effect of Water Saturation on the Fracture and Mechanical Properties of Sedimentary Rocks. *Rock Mechanics and Rock Engineering*, 50(10), 2585–2600. <https://doi.org/10.1007/s00603-017-1253-8>

- Haddad, S. C., Worden, R. H., Prior, D. J., & Smalley, P. C. (2006). Quartz Cement in the Fontainebleau Sandstone, Paris Basin, France: Crystallography and Implications for Mechanisms of Cement Growth. *Journal of Sedimentary Research*, 76(2), 244–256. <https://doi.org/10.2110/jsr.2006.024>
- Hadizadeh, J., & Law, R. D. (1991). Water-weakening of sandstone and quartzite deformed at various stress and strain rates. *International Journal of Rock Mechanics and Mining Sciences and Geomechanics Abstracts*, 28(5), 431–439. [https://doi.org/10.1016/0148-9062\(91\)90081-V](https://doi.org/10.1016/0148-9062(91)90081-V)
- Haied, A., & Kondo, D. (1997). Strain localisation in Fontainebleau sandstone: macroscopic and microscopic investigations. *International Journal of Rock Mechanics & Mining Sciences*, 34(3–4). [https://doi.org/10.1016/S1365-1609\(97\)00216-5](https://doi.org/10.1016/S1365-1609(97)00216-5)
- Handin, J., Hager, R. V. J., Friedman, M., & Feather, J. N. (1963). Experimental deformation of sedimentary rocks under confining pressure: pore pressure tests. *American Association of Petroleum Geologists*, 47(5), 717–755.
- Handy, M. R., Hirth, G., & Bürgmann, R. (2007). Continental Fault Structure and Rheology from the Frictional-to-Viscous Transition Downward. In N. Handy, M.R., Hirth, G., Hovius (Ed.), *Tectonic Faults: Agents of Change on a Dynamic Earth* (pp. 139–182). MIT Press. <https://doi.org/10.7551/mitpress/6703.003.0008>
- Hawkins, A. B., & McConnell, B. J. (1992). Sensitivity of sandstone strength and deformability to changes in moisture content Sandstones studied. *Quarterly Journal of Engineering Geology and Hydrogeology*, 25, 115–130. <https://doi.org/10.1144/GSL.QJEG.1992.025.02.05>
- He, C., & Wong, T. (2014). Effect of varying normal stress on stability and dynamic motion of a spring-slider system with rate- and state-dependent friction. *Earthquake Science*, 27(6), 577–587. <https://doi.org/10.1007/s11589-014-0098-4>
- He, C., Ma, S., & Huang, J. (1998). Transition between stable sliding and stick-slip due to variation in slip rate under variable normal stress condition. *Geophysical Research Letters*, 25(17), 3235–3238. <https://doi.org/10.1029/98GL02518>
- Heap, M. J., Baud, P., & Meredith, P. G. (2009). Influence of temperature on brittle creep in sandstones. *Geophysical Research Letters*, 36(19). <https://doi.org/10.1029/2009GL039373>
- Heap, M. J., Baud, P., Meredith, P. G., Bell, A. F., & Main, I. G. (2009). Time-dependent brittle creep in darley dale sandstone. *Journal of Geophysical Research: Solid Earth*, 114(7). <https://doi.org/10.1029/2008JB006212>
- Heap, M. J., Brantut, N., Baud, P., & Meredith, P. G. (2015). Time-dependent compaction band formation in sandstone. *Journal of Geophysical Research: Solid Earth*, 120(7), 4808–4830. <https://doi.org/10.1002/2015JB012022>
- Heap, Michael J., Villeneuve, M., Kushnir, A. R. L., Farquharson, J. I., Baud, P., & Reuschlé, T. (2019). Rock mass strength and elastic modulus of the Buntsandstein: An important lithostratigraphic unit for geothermal exploitation in the Upper Rhine Graben. *Geothermics*, 77, 236–256. <https://doi.org/10.1016/j.geothermics.2018.10.003>
- Heard, H. C. (1960). Transition from brittle fracture to ductile flow in Solenhofen limestone as a function of temperature, confining pressure, and interstitial fluid pressure. In D. Griggs & J. Handin (Eds.), *Rock deformation* (pp. 193–226). Geological Society of America Memoirs, 79.

- Heaton, T. H. (1975). Tidal triggering of earthquakes in Iwo-jima island. *Geophysical Journal International*, 43(2), 307–326. <https://doi.org/10.1111/j.1365-246X.1975.tb00637.x>
- Herring, C. (1950). Diffusional viscosity of a polycrystalline solid. *Journal of Applied Physics*, 21(5), 437–445. <https://doi.org/10.1063/1.1699681>
- Hoek, E., & Brown, E. T. (1980). *Underground Excavations in Rock*. London, Inst. of Mining and Metallurgy.
- Hofmann, H., Zimmermann, G., Farkas, M., Huenges, E., Zang, A., Leonhardt, M., et al. (2019). First field application of cyclic soft stimulation at the Pohang Enhanced Geothermal System site in Korea. *Geophysical Journal International*, 217(2), 926–949. <https://doi.org/10.1093/gji/ggz058>
- Horii, H., & Nemat-Nasser, S. (1985). Compression-induced microcrack growth in brittle solids: Axial splitting and shear failure. *Journal of Geophysical Research: Solid Earth*, 90(B4), 3105–3125. <https://doi.org/10.1029/JB090iB04p03105>
- Houston, H. (2015). Low friction and fault weakening revealed by rising sensitivity of tremor to tidal stress. *Nature Geoscience*, 8(5), 409–415. <https://doi.org/10.1038/ngeo2419>
- Inglis. (1913). Stresses in a plate due to the presence of cracks and sharp corners. *Trans Inst Naval Archit*, 55, 219–241.
- Jaeger, J. C. (1959). The frictional properties of joints in rock. *Geofisica Pura e Applicata*, 43(1), 148–158. <https://doi.org/10.1007/BF01993552>
- Jaeger, J. C. (1969). *Elasticity, Fracture and Flow with Engineering and Geological Applications*. Springer, Dordrecht. <https://doi.org/10.1007/978-94-011-6024-7>
- Johnson, C. W., Fu, Y., & Bürgmann, R. (2017). Seasonal water storage, stress modulation, and California seismicity. *Science*, 356(6343), 1161–1164. <https://doi.org/10.1126/science.aak9547>
- Kanamori, H., & Brodsky, E. E. (2004). The physics of earthquakes. *Reports on Progress in Physics*, 67(8), 1429–1496. <https://doi.org/10.1088/0034-4885/67/8/R03>
- Kaproth, B. M., & Marone, C. (2013). Slow earthquakes, preseismic velocity changes, and the origin of slow frictional stick-slip. *Science*, 341(6151), 1229–1232. <https://doi.org/10.1126/science.1239577>
- von Kármán, T. (1911). Festigkeitsversuche unter allseitigem Druck. *Verein Deutsch Ing*, 55, 1749–1757.
- Kataoka, M., Obara, Y., & Kuruppu, M. (2015). Estimation of Fracture Toughness of Anisotropic Rocks by Semi-Circular Bend (SCB) Tests Under Water Vapor Pressure. *Rock Mechanics and Rock Engineering*, 48(4), 1353–1367. <https://doi.org/10.1007/s00603-014-0665-y>
- Kataoka, Minami, Mahdavi, E., Funatsu, T., Takehara, T., Obara, Y., Fukui, K., & Hashiba, K. (2017). Estimation of Mode I Fracture Toughness of Rock by Semi-Circular Bend Test under Confining Pressure Condition. *Procedia Engineering*, 191, 886–893. <https://doi.org/10.1016/j.proeng.2017.05.258>
- Kato, N., Yamamoto, K., Yamamoto, H., & Hirasawa, T. (1992). Strain-rate effect on frictional strength and the slip nucleation process. *Tectonophysics*, 211(1–4), 269–282.

[https://doi.org/10.1016/0040-1951\(92\)90064-D](https://doi.org/10.1016/0040-1951(92)90064-D)

- Kohlstedt, D. L., Evans, B., & Mackwell, S. J. (1995). Strength of the lithosphere: Constraints imposed by laboratory experiments. *Journal of Geophysical Research: Solid Earth*, 100(B9), 17587–17602. <https://doi.org/10.1029/95JB01460>
- Kranz, R. L., & Scholz, C. H. (1977). Critical Dilatant Volume of Rocks at the Onset of Tertiary Creep. *Journal of Geophysical Research*, 82(30), 4893–4898. <https://doi.org/10.1029/JB082i030p04893>
- Leeman, J. R., Saffer, D. M., Scuderi, M. M., & Marone, C. (2016). Laboratory observations of slow earthquakes and the spectrum of tectonic fault slip modes. *Nature Communications*, 7. <https://doi.org/10.1038/ncomms11104>
- Leeman, J. R., Marone, C., & Saffer, D. M. (2018). Frictional Mechanics of Slow Earthquakes. *Journal of Geophysical Research: Solid Earth*, 123(9), 7931–7949. <https://doi.org/10.1029/2018JB015768>
- Lisabeth, H. P., & Zhu, W. (2015). Effect of temperature and pore fluid on the strength of porous limestone. *Journal of Geophysical Research: Solid Earth*, 120(9), 6191–6208. <https://doi.org/10.1002/2015JB012152>
- Liu, E., & He, S. (2012). Effects of cyclic dynamic loading on the mechanical properties of intact rock samples under confining pressure conditions. *Engineering Geology*, 125, 81–91. <https://doi.org/10.1016/j.enggeo.2011.11.007>
- Lockner, A. (1998). A generalized law for brittle deformation of Westerly granite. *Journal of Geophysical Research*, 103(B3), 5107–5123.
- Lockner, D. (1993a). Room temperature creep in saturated granite. *Journal of Geophysical Research*, 98(B1), 475–487. <https://doi.org/10.1029/92JB01828>
- Lockner, D. (1993b). The role of acoustic emission in the study of rock fracture. *International Journal of Rock Mechanics and Mining Sciences & Geomechanics Abstracts*, 30(7), 883–899. [https://doi.org/10.1016/0148-9062\(93\)90041-B](https://doi.org/10.1016/0148-9062(93)90041-B)
- Lockner, D. a., & Beeler, N. M. (1999). Premonitory slip and tidal triggering of earthquakes. *Journal of Geophysical Research*, 104(B9), 20133–20151. <https://doi.org/10.1029/1999JB900205>
- Lockner, D. A. (1995). Rock Failure. In *Rock Physics & Phase Relations: A handbook of physical constants* (Vol. 3, pp. 127–147). <https://doi.org/10.1029/RF003p0127>
- Louis, L., Baud, P., & Wong, T. (2009). Microstructural inhomogeneity and mechanical anisotropy associated with bedding in rothbach sandstone. *Pure and Applied Geophysics*, 166(5–7), 1063–1087. <https://doi.org/10.1007/s00024-009-0486-1>
- Luquot, L., & Gouze, P. (2009). Experimental determination of porosity and permeability changes induced by injection of CO₂ into carbonate rocks. *Chemical Geology*, 265(1–2), 148–159. <https://doi.org/10.1016/j.chemgeo.2009.03.028>
- Lyall, K. D. (1965). *Plastic deformation of galena: an experimental study of the plastic deformation and recrystallisation of single crystals and polycrystalline aggregates of galena*. Australian National University. <https://doi.org/10.25911/5d6f9c360841c>

- Mair, K., & Marone, C. (1999). Friction of simulated fault gouge for a wide range of velocities and normal stresses. *Journal of Geophysical Research*, 104(B12), 22899–28914. <https://doi.org/10.1029/1999JB900279>
- Mallet, C., Fortin, J., Guéguen, Y., & Bouyer, F. (2015). Brittle creep and subcritical crack propagation in glass submitted to triaxial conditions. *Journal of Geophysical Research: Solid Earth*, 120(2), 879–893. <https://doi.org/10.1002/2014JB011231>
- Marchesini, B., Garofalo, P. S., Menegon, L., Mattila, J., & Viola, G. (2019). Fluid-mediated, brittle-ductile deformation at seismogenic depth - Part 1: Fluid record and deformation history of fault veins in a nuclear waste repository (Olkiluoto Island, Finland). *Solid Earth*, 10(3), 809–838. <https://doi.org/10.5194/se-10-809-2019>
- Marone, C., & Scholz, C. H. (1988). The depth of seismic faulting and the upper transition from stable to unstable slip regimes. *Geophysical Research Letters*, 15(6), 621–624. <https://doi.org/10.1029/GL015i006p00621>
- Maruvanchery, V., & Kim, E. (2019). Effects of water on rock fracture properties: Studies of mode I fracture toughness, crack propagation velocity, and consumed energy in calcite-cemented sandstone. *Geomechanics and Engineering*, 17(1), 57–67. <https://doi.org/10.12989/gae.2019.17.1.057>
- Maurer, W. C. (1965). Shear Failure of Rock Under Compression. *Society of Petroleum Engineers Journal*, 5(02), 167–176. <https://doi.org/10.2118/1054-pa>
- Mclaskey, G. C., & Yamashita, F. (2017). Slow and fast ruptures on a laboratory fault controlled by loading characteristics. *Journal of Geophysical Research: Solid Earth*, 122(5), 3719–3738. <https://doi.org/10.1002/2016JB013681>
- Meng, F., Baud, P., Ge, H., & Wong, T. fong. (2019). The Effect of Stress on Limestone Permeability and Effective Stress Behavior of Damaged Samples. *Journal of Geophysical Research: Solid Earth*, 124(1), 376–399. <https://doi.org/10.1029/2018JB016526>
- Meredith, P. G., & Atkinson, B. K. (1983). Stress corrosion and acoustic emission during tensile crack propagation in Whin Sill dolerite and other basic rocks. *Geophysical Journal of the Royal Astronomical Society*, 75(1), 1–21. <https://doi.org/10.1111/j.1365-246X.1983.tb01911.x>
- Meredith, P. G., & Atkinson, B. K. (1985). Fracture toughness and subcritical crack growth during high-temperature tensile deformation of Westerly granite and Black gabbro. *Physics of the Earth and Planetary Interiors*, 39(1), 33–51. [https://doi.org/10.1016/0031-9201\(85\)90113-X](https://doi.org/10.1016/0031-9201(85)90113-X)
- Meredith, Philip G. (1983). *A fracture mechanics study of experimentally deformed crustal rocks*. Imperial College London.
- Metz, B., Davidson, O., De Coninck, H., Loos, M., & Meyer, L. (2005). *IPCC special report on carbon dioxide capture and storage*. Intergovernmental Panel on Climate Change. Geneva (Switzerland).
- Meyer, G. G., Brantut, N., Mitchell, T. M., & Meredith, P. G. (2019). Fault reactivation and strain partitioning across the brittle-ductile transition. *Geology*. <https://doi.org/10.1130/G46516.1>
- Michalske, T. A., & Freiman, S. W. (1983). Stress corrosion of Ceramic Materials. *Journal of the American Ceramic Society*, 66(4).

- Michaut, C., Ricard, Y., Bercovici, D., & Sparks, R. S. J. (2013). Eruption cyclicity at silicic volcanoes potentially caused by magmatic gas waves. *Nature Geoscience*, 6(10), 856–860. <https://doi.org/10.1038/ngeo1928>
- Mogi, K. (1974). On the pressure dependence of strength of rocks and the coulomb fracture criterion. *Tectonophysics*, 21(3), 273–285. [https://doi.org/10.1016/0040-1951\(74\)90055-9](https://doi.org/10.1016/0040-1951(74)90055-9)
- Moore, J. C., & Vrolijk, P. (1992). Fluids in accretionary prisms. *Reviews of Geophysics*, 30(2), 112–135. <https://doi.org/10.1029/92RG00201>
- Murrell, S. A. F. (1967). The Effects of Triaxial Stress Systems on the Fracture of Rocks, and on the Nature of Faulting and Earthquakes. *Geophysical Journal International*, 14(1–4), 81–87. <https://doi.org/10.1111/j.1365-246X.1967.tb06226.x>
- Nara, Y., Morimoto, K., Hiroyoshi, N., Yoneda, T., Kaneko, K., & Benson, P. M. (2012). Influence of relative humidity on fracture toughness of rock: Implications for subcritical crack growth. *International Journal of Solids and Structures*, 49(18), 2471–2481. <https://doi.org/10.1016/j.ijsolstr.2012.05.009>
- Nemat-Nasser, S., & Horii, H. (1982). Compression-induced nonplanar crack extension with application to splitting, exfoliation, and rockburst. *Journal of Geophysical Research: Solid Earth*, 87(B8), 6805–6821. <https://doi.org/10.1029/JB087iB08p06805>
- Ngwenya, B. T., Main, I. G., Elphick, S. C., Crawford, R., & Smart, G. D. (2001). A constitutive law for low-temperature creep of water-saturated sandstones. *Journal of Geophysical Research*, 106(B10), 21811–21826. <https://doi.org/10.1029/2001JB000403>
- Nicolas, A., Fortin, J., Regnet, J. B., Dimanov, A., & Gúeguen, Y. (2016). Brittle and semi-brittle behaviours of a carbonate rock: Influence of water and temperature. *Geophysical Journal International*, 206(1), 438–456. <https://doi.org/10.1093/gji/ggw154>
- Nicolas, A., Fortin, J., Regnet, J. B., Verberne, B. A., Plümper, O., Dimanov, A., et al. (2017). Brittle and semibrittle creep of Tavel limestone deformed at room temperature. *Journal of Geophysical Research: Solid Earth*, 122, 1–24. <https://doi.org/10.1002/2016JB013557>
- Nielsen, S., Spagnuolo, E., Smith, S. A. F., Violay, M., Di Toro, G., & Bistacchi, A. (2016). Scaling in natural and laboratory earthquakes. *Geophysical Research Letters*, 43(4), 1504–1510. <https://doi.org/10.1002/2015GL067490>
- Nishi, Y., Sherburn, S., Scott, B. J., & Sugihara, M. (1996). High-frequency earthquakes at White Island volcano, New Zealand: Insights into the shallow structure of a volcano-hydrothermal system. *Journal of Volcanology and Geothermal Research*, 72(3–4), 183–197. [https://doi.org/10.1016/0377-0273\(96\)00005-4](https://doi.org/10.1016/0377-0273(96)00005-4)
- Niu, F., Silver, P. G., Daley, T. M., Cheng, X., & Majer, E. L. (2008). Preseismic velocity changes observed from active source monitoring at the Parkfield SAFOD drill site. *Nature*, 454(7201), 204–208. <https://doi.org/10.1038/nature07111>
- Noël, C., Pimienta, L., & Violay, M. (2019). Time-Dependent Deformations of Sandstone During Pore Fluid Pressure Oscillations: Implications for Natural and Induced Seismicity. *Journal of Geophysical Research: Solid Earth*, 124(1), 801–821. <https://doi.org/10.1029/2018JB016546>
- Noël, Corentin, Passelègue, F. X., Giorgetti, C., & Violay, M. (2019). Fault reactivation during

- fluid pressure oscillations: transition from stable to unstable slip. *Journal of Geophysical Research: Solid Earth*, 124(11), 10940–10953. <https://doi.org/10.1029/2019JB018517>
- Olsson, W. A. (1974). Microfracturing and faulting in a limestone. *Tectonophysics*, 24(3), 277–285. [https://doi.org/10.1016/0040-1951\(74\)90012-2](https://doi.org/10.1016/0040-1951(74)90012-2)
- Orellana, L. F., Giorgetti, C., & Violay, M. (2019). Contrasting Mechanical and Hydraulic Properties of Wet and Dry Fault Zones in a Proposed Shale-Hosted Nuclear Waste Repository. *Geophysical Research Letters*, 46(3), 1357–1366. <https://doi.org/10.1029/2018GL080384>
- Ougier-Simonin, A., & Zhu, W. (2013). Effects of pore fluid pressure on slip behaviors: An experimental study. *Geophysical Research Letters*, 40(11), 2619–2624. <https://doi.org/10.1002/grl.50543>
- Palchik, V. (1999). Influence of Porosity and Elastic Modulus on Uniaxial Compressive Strength in Soft Brittle Porous Sandstones. *Rock Mechanics and Rock Engineering*, 32(4), 303–309. <https://doi.org/10.1007/s006030050050>
- De Paola, N., Faulkner, D. R., & Collettini, C. (2009). Brittle versus ductile deformation as the main control on the transport properties of low-porosity anhydrite rocks. *Journal of Geophysical Research: Solid Earth*, 114(B6). <https://doi.org/10.1029/2008JB005967>
- Parks, G. A. (1984). Surface and Interfacial Free Energies of Quartz. *Journal of Geophysical Research*, 89(B6), 3997–4008. <https://doi.org/10.1029/JB089iB06p03997>
- Passelègue, F. X., Schubnel, A., Nielsen, S., Bhat, H. S., & Madariaga, R. (2013). From sub-Rayleigh to supershear ruptures during stick-slip experiments on crustal rocks. *Science*, 340(6137), 1208–1211. <https://doi.org/10.1126/science.1235637>
- Passelègue, F. X., Pimienta, L., Faulkner, D., Schubnel, A., Fortin, J., & Guéguen, Y. (2018). Development and Recovery of Stress-Induced Elastic Anisotropy During Cyclic Loading Experiment on Westerly Granite. *Geophysical Research Letters*, 45(16), 8156–8166. <https://doi.org/10.1029/2018GL078434>
- Passelègue, F. X., Brantut, N., & Mitchell, T. M. (2018). Fault reactivation by fluid injection: Controls from stress state and injection rate. *Geophysical Research Letters*, 45(23), 12,837–12,846. <https://doi.org/10.1029/2018GL080470>
- Patel, S. M., Sondergeld, C. H., & Rai, C. S. (2017). Laboratory studies of hydraulic fracturing by cyclic injection. *International Journal of Rock Mechanics and Mining Sciences*, 95, 8–15. <https://doi.org/10.1016/j.ijrmms.2017.03.008>
- Paterson, M., & Wong, T. (2005). *Experimental Rock Deformation - The Brittle Field* (Springer S). <https://doi.org/10.1007/b137431>
- Paterson, M. S. (1958). Experimental deformation and faulting in Wombeyan marble. *Geological Society of America Bulletin*, 69(4), 465–476. [https://doi.org/10.1130/0016-7606\(1958\)69\[465:EDAFIW\]2.0.CO;2](https://doi.org/10.1130/0016-7606(1958)69[465:EDAFIW]2.0.CO;2)
- Paterson, M. S. (1967). Effect of Pressure on Stress-Strain Properties of Materials. *Geophysical Journal International*, 14(1–4), 13–17. <https://doi.org/10.1111/j.1365-246X.1967.tb06217.x>
- Paterson, Mervyn S. (2013). *Materials Science for Structural Geology*. Dordrecht: Springer Geochemistry/Mineralogy. <https://doi.org/10.1007/978-94-007-5545-1>

- Pimienta, L., Sarout, J., Esteban, L., David, C., & Clennell, M. B. (2017). Pressure-Dependent Elastic and Transport Properties of Porous and Permeable Rocks: Microstructural Control. *Journal of Geophysical Research: Solid Earth*, 122(11), 8952–8968. <https://doi.org/10.1002/2017JB014464>
- Poirier, J.-P. (1985). *Creep of crystals: High-temperature deformation processes in metals, ceramics and minerals*. (A. H. Cook, W. B. Harland, N. F. Hughes, A. Putnis, J. G. Sclater, & M. R. A. Thomson, Eds.). Cambridge: Cambridge University Press.
- Prando, F., Menegon, L., Anderson, M., Marchesini, B., Mattila, J., & Viola, G. (2020). Fluid-mediated, brittle–ductile deformation at seismogenic depth – Part 2: Stress history and fluid pressure variations in a shear zone in a nuclear waste repository (Olkiluoto Island, Finland). *Solid Earth*, 11, 489–511. <https://doi.org/10.5194/se-11-489-2020>
- Renard, F., Gratier, J. P., & Jamtveit, B. (2000). Kinetics of crack-sealing, intergranular pressure solution, and compaction around active faults. *Journal of Structural Geology*, 22(10), 1395–1407. [https://doi.org/10.1016/S0191-8141\(00\)00064-X](https://doi.org/10.1016/S0191-8141(00)00064-X)
- Reviron, N., Reuschlé, T., & Bernard, J. D. (2009). The brittle deformation regime of water-saturated siliceous sandstones. *Geophysical Journal International*, 178(3), 1766–1778. <https://doi.org/10.1111/j.1365-246X.2009.04236.x>
- Rice, J. R. (1993). Spatio-temporal complexity of slip on a fault. *Journal of Geophysical Research: Solid Earth*, 98(B6), 9885–9907. <https://doi.org/10.1029/93JB00191>
- Rice, J. R., & Ruina, A. L. (1983). Stability of Steady Frictional Slipping. *Journal of Applied Mechanics*, 50(2), 343–349. <https://doi.org/10.1115/1.3167042>
- Robinson, L. H. J. (1959). Effect of pore and confining pressures on failure characteristics of sedimentary rocks. *Society of Petroleum Engineers*, 216, 26–32.
- Royer-Carfagni, G., & Salvatore, W. (2000). Characterization of marble by cyclic compression loading: experimental results. *Mechanics of Cohesive-Frictional Materials*, 5(7), 535–563. [https://doi.org/10.1002/1099-1484\(200010\)5:7<535::AID-CFM102>3.0.CO;2-D](https://doi.org/10.1002/1099-1484(200010)5:7<535::AID-CFM102>3.0.CO;2-D)
- Rubinstein, J. L., La Rocca, M., Vidale, J. E., Creager, K. C., & Wech, A. G. (2008). Tidal Modulation of Nonvolcanic Tremor. *Science*, 319(5860), 186–189. <https://doi.org/10.1126/science.1150558>
- Ruina, A. (1983). Slip instability and state variable friction law. *Journal of Geophysical Research*, 88, 10359–10370. <https://doi.org/10.1029/JB088iB12p10359>
- Rutqvist, J., Vasco, D. W., & Myer, L. (2010). Coupled reservoir-geomechanical analysis of CO₂ injection and ground deformations at In Salah, Algeria. *International Journal of Greenhouse Gas Control*, 4(2), 225–230. <https://doi.org/10.1016/j.ijggc.2009.10.017>
- Rutqvist, J., Rinaldi, A. P., Cappa, F., Jeanne, P., Mazzoldi, A., Urpi, L., et al. (2016). Fault activation and induced seismicity in geological carbon storage – Lessons learned from recent modeling studies. *Journal of Rock Mechanics and Geotechnical Engineering*, 8(6), 789–804. <https://doi.org/10.1016/j.jrmge.2016.09.001>
- Rutter, E. H. (1972). The effects of strain-rate changes on the strength and ductility of Solenhofen limestone at low temperatures and confining pressures. *International Journal of Rock*

- Mechanics and Mining Sciences And*, 9(2), 183–189. [https://doi.org/10.1016/0148-9062\(72\)90020-4](https://doi.org/10.1016/0148-9062(72)90020-4)
- Rutter, E. H. (1983). Pressure solution in nature, theory and experiment. *Journal of the Geological Society*, 140(5), 725–740. <https://doi.org/10.1144/gsjgs.140.5.0725>
- Rutter, E. H. (1986). On the nomenclature of mode of failure transitions in rocks. *Tectonophysics*, 122(3–4), 381–387. [https://doi.org/10.1016/0040-1951\(86\)90153-8](https://doi.org/10.1016/0040-1951(86)90153-8)
- Rutter, Ernest H. (1972). The influence of interstitial water on the rheological behaviour of calcite rocks. *Tectonophysics*, 14(1), 13–33. [https://doi.org/10.1016/0040-1951\(72\)90003-0](https://doi.org/10.1016/0040-1951(72)90003-0)
- Rydelek, P., & Hass, L. (1994). On estimating the amount of blasts in seismic catalogs with Schuster's method. *Bulletin of the Seismological Society of America*, 84(4), 1256–1259.
- Rydelek, P. A., Sacks, I. S., & Scarpa, R. (1992). On tidal triggering of earthquakes at Campi Flegrei, Italy. *Geophysical Journal International*, 109(1), 125–135. <https://doi.org/10.1111/j.1365-246X.1992.tb00083.x>
- Sammis, C. G., & Ashby, M. F. (1986). The failure of brittle porous solids under compressive stress states. *Acta Metallurgica*, 34(3), 511–526. [https://doi.org/10.1016/0001-6160\(86\)90087-8](https://doi.org/10.1016/0001-6160(86)90087-8)
- Sarout, J., & Guéguen, Y. (2008a). Anisotropy of elastic wave velocities in deformed shales: Part 1 — Experimental results. *Geophysics*, 73(5). <https://doi.org/10.1190/1.2952744>
- Sarout, J., & Guéguen, Y. (2008b). Anisotropy of elastic wave velocities in deformed shales: Part 2 — Modeling results. *Geophysics*, 73(5). <https://doi.org/10.1190/1.2952745>
- Schmidt, R. A., & Huddle, C. W. (1977). Effect of confining pressure on fracture toughness of Indiana limestone. *International Journal of Rock Mechanics and Mining Sciences And*, 14(5–6), 289–293. [https://doi.org/10.1016/0148-9062\(77\)90740-9](https://doi.org/10.1016/0148-9062(77)90740-9)
- Scholz, C. H. (1968a). Mechanism of creep in brittle rock. *Journal of Geophysical Research*, 73(10), 3295–3302. <https://doi.org/10.1029/JB073i010p03295>
- Scholz, C. H. (1968b). The frequency-magnitude relation of microfracturing in rock and its relation to earthquakes. *Bulletin of the Seismological Society of America*, 58(1), 399–415. Retrieved from <http://www.bssaonline.org/cgi/content/abstract/58/1/399>
- Scholz, C. H. (1998). Earthquakes and friction laws. *Nature*, 391(6662), 37–42. <https://doi.org/10.1038/34097>
- Scholz, Christopher H., Tan, Y. J., & Albino, F. (2019). The mechanism of tidal triggering of earthquakes at mid-ocean ridges. *Nature Communications*, 10(1), 2526. <https://doi.org/10.1038/s41467-019-10605-2>
- Scholz, Christopher H. (2019). *The Mechanics of Earthquakes and Faulting* (3rd edition). Cambridge University Press. <https://doi.org/10.1017/9781316681473>
- Schubnel, A., Walker, E., Thompson, B. D., Fortin, J., Guéguen, Y., & Young, R. P. (2006). Transient creep, aseismic damage and slow failure in Carrara marble deformed across the brittle-ductile transition. *Geophysical Research Letters*, 33(17). <https://doi.org/10.1029/2006GL026619>

- Schubnel, A., Thompson, B. D., Fortin, J., Guéguen, Y., & Young, R. P. (2007). Fluid-induced rupture experiment on Fontainebleau sandstone: Premonitory activity, rupture propagation, and aftershocks. *Geophysical Research Letters*, 34, L19307. <https://doi.org/10.1029/2007GL031076>
- Schuster, A. (1897). On Lunar and Solar Periodicities of Earthquakes. *Proceedings of the Royal Society of London*, 61, 455–465. <https://doi.org/10.1098/rspl.1897.0060>
- Scuderi, M. M., Marone, C., Tinti, E., Di Stefano, G., & Collettini, C. (2016). Precursory changes in seismic velocity for the spectrum of earthquake failure modes. *Nature Geoscience*, 9, 695–700. <https://doi.org/10.1038/ngeo2775>
- Scuderi, M. M., Collettini, C., Viti, C., Tinti, E., & Marone, C. (2017). Evolution of shear fabric in granular fault gouge from stable sliding to stick slip and implications for fault slip mode. *Geology*, 45(8), 731–734. <https://doi.org/10.1130/G39033.1>
- Scuderi, Marco M., & Collettini, C. (2018). Fluid Injection and the Mechanics of Frictional Stability of Shale-Bearing Faults. *Journal of Geophysical Research: Solid Earth*. <https://doi.org/10.1029/2018JB016084>
- Shreedharan, S., Bolton, D. C., Rivière, J., & Marone, C. (2021). Competition between preslip and deviatoric stress modulates precursors for laboratory earthquakes. *Earth and Planetary Science Letters*, 553, 116623. <https://doi.org/10.1016/j.epsl.2020.116623>
- Shuqing Zhang, Cox, S. F., & Paterson, M. S. (1994). The influence of room temperature deformation on porosity and permeability in calcite aggregates. *Journal of Geophysical Research: Solid Earth*, 99(B8), 15761–15775. <https://doi.org/10.1029/94JB00647>
- Sibson, R. H. (1982). Fault zone models, heat flow, and the depth distribution of earthquakes in the continental crust of the United States. *Bulletin of the Seismological Society of America*, 72, 151–163.
- Sibson, Richard H. (1977). Fault rocks and fault mechanisms. *Journal of the Geological Society*, 133(3), 191–213. <https://doi.org/10.1144/gsjgs.133.3.0191>
- Siddiqi, G., Evans, B., Dresen, G., & Freund, D. (1997). Effect of semibrittle deformation on transport properties of calcite rocks. *Journal of Geophysical Research: Solid Earth*, 102(B7), 14765–14778. <https://doi.org/10.1029/97JB01038>
- Simmons, C. J., & Freiman, S. W. (1981). Effect of Corrosion Processes on Subcritical Crack Growth in Glass. *Journal of the American Ceramic Society*, 64(11), 683–686. <https://doi.org/10.1111/j.1151-2916.1981.tb15870.x>
- Skarbek, R. M., & Savage, H. M. (2019). RSFit3000: A MATLAB GUI-based program for determining rate and state frictional parameters from experimental data. *Geosphere*, 15(5), 1665–1676. <https://doi.org/10.1130/GES02122.1>
- Skempton, A. W. (1961). Effective stress in soils, concrete and rocks. In *Pore Pressure and suction in soils* (pp. 4–16). Butterworths, London.
- Song, I., & Renner, J. (2008). Hydromechanical properties of Fontainebleau sandstone: Experimental determination and micromechanical modeling. *Journal of Geophysical Research: Solid Earth*, 113(B09211). <https://doi.org/10.1029/2007JB005055>

- Sterpenich, J., Sausse, J., Pironon, J., Géhin, A., Hubert, G., Perfetti, E., & Grgic, D. (2009). Experimental ageing of oolitic limestones under CO₂ storage conditions. Petrographical and chemical evidence. *Chemical Geology*, 265(1–2), 99–112. <https://doi.org/10.1016/j.chemgeo.2009.04.011>
- Stesky, R. M., Brace, W. F., Riley, D. K., & Robin, P. Y. F. (1974). Friction in faulted rock at high temperature and pressure. *Tectonophysics*, 23(1–2), 177–203. [https://doi.org/10.1016/0040-1951\(74\)90119-X](https://doi.org/10.1016/0040-1951(74)90119-X)
- Stoeckhert, F., Brenne, S., Molenda, M., & Alber, M. (2016). Mode I fracture toughness of rock under confining pressure. In *Rock Mechanics and Rock Engineering: From the Past to the Future* (pp. 313–318). London. <https://doi.org/10.1201/9781315388502-52>
- Sulem, J., & Ouffroukh, H. (2006). Hydromechanical behaviour of Fontainebleau sandstone. *Rock Mechanics and Rock Engineering*, 39(3), 185–213. <https://doi.org/10.1007/s00603-005-0065-4>
- Taira, T., Brenguier, F., & Kong, Q. (2015). Ambient noise-based monitoring of seismic velocity changes associated with the 2014 Mw 6.0 South Napa earthquake. *Geophysical Research Letters*, 42(17), 6997–7004. <https://doi.org/10.1002/2015GL065308>
- Tenthorey, E., Cox, S. F., & Todd, H. F. (2003). Evolution of strength recovery and permeability during fluid-rock reaction in experimental fault zones. *Earth and Planetary Science Letters*, 206(1–2), 161–172. [https://doi.org/10.1016/S0012-821X\(02\)01082-8](https://doi.org/10.1016/S0012-821X(02)01082-8)
- Terzaghi, K., Peck, R. B., & Mesri, G. (1996). *Soil mechanics in engineering practice* (3rd editio). John Wiley & Sons.
- Thallak, S., Holder, J., & Gray, K. E. (1993). The pressure dependence of apparent hydrofracture toughness. *International Journal of Rock Mechanics and Mining Sciences and Geomechanics Abstracts*, 30(7), 831–835. [https://doi.org/10.1016/0148-9062\(93\)90031-8](https://doi.org/10.1016/0148-9062(93)90031-8)
- Trimmer, D., Bonner, B., Heard, H. C., & Duba, A. (1980). Effect of Pressure and Stress on Water Transport in Intact and Fractured Gabbro and Granite. *Journal of Geophysical Research*, 85(B12), 7059–7071. <https://doi.org/10.1029/JB085iB12p07059>
- Tsuchiya, N., Asanuma, H., Okamoto, A., Sakaguchi, K., Hirano, N., Kizaki, A., & Watanabe, N. (2015). Fundamental Study for Beyond Brittle Geothermal Reservoirs. In *Proceedings World Geothermal Congress* (pp. 19–25). Melbourne, Australia.
- Tullis, J., & Yund, R. A. (1980). Hydrolytic weakening of experimentally deformed Westerly granite and Hale albite rock. *Journal of Structural Geology*, 2(4), 439–451. [https://doi.org/10.1016/0191-8141\(80\)90005-X](https://doi.org/10.1016/0191-8141(80)90005-X)
- Tullis, Jan, & Yund, R. A. (1977). Experimental deformation of dry westerly granite. *Journal of Geophysical Research*, 82(36), 5705–5718. <https://doi.org/10.1029/JB082i036p05705>
- Vajdova, V., Baud, P., & Wong, T. (2004a). Compaction, dilatancy, and failure in porous carbonate rocks. *Journal of Geophysical Research: Solid Earth*, 109(B5). <https://doi.org/10.1029/2003JB002508>
- Vajdova, V., Baud, P., & Wong, T. F. (2004b). Permeability evolution during localized deformation in Bentheim sandstone. *Journal of Geophysical Research: Solid Earth*, 109(B10). <https://doi.org/10.1029/2003JB002942>

- Vajdova, V., Zhu, W., Natalie Chen, T. M., & Wong, T. (2010). Micromechanics of brittle faulting and cataclastic flow in Tavel limestone. *Journal of Structural Geology*, 32(8), 1158–1169. <https://doi.org/10.1016/j.jsg.2010.07.007>
- Vásárhelyi, B. (1997). Influence of pressure on the crack propagation under mode I loading in anisotropic gneiss. *Rock Mechanics and Rock Engineering*, 30(1), 59–64. <https://doi.org/10.1007/BF01020113>
- Verdon, J. P., Kendall, J.-M., Stork, A. L., Chadwick, R. A., White, D. J., & Bissell, R. C. (2013). Comparison of geomechanical deformation induced by megatonne-scale CO₂ storage at Sleipner, Weyburn, and In Salah. *Proceedings of the National Academy of Sciences*, 110(30), E2762–E2771. <https://doi.org/10.1073/pnas.1302156110>
- Vilarrasa, V., & Rutqvist, J. (2017). Thermal effects on geologic carbon storage. *Earth-Science Reviews*, 165, 245–256. <https://doi.org/10.1016/j.earscirev.2016.12.011>
- Vincké, O., Boutéca, M. J., Piau, J. M., & Fourmaintraux, D. (1998). Study of the effective stress at failure. In J.-F. Thimus, Y. Abousleiman, A. H.-D. Cheng, O. Coussy, & E. Detournay (Eds.), *Poromechanics, A Tribute to Maurice A. Biot* (pp. 635–639). Rotterdam.
- Violay, M., Gibert, B., Mainprice, D., & Burg, J. P. (2015). Brittle versus ductile deformation as the main control of the deep fluid circulation in oceanic crust. *Geophysical Research Letters*, 42(8), 2767–2773. <https://doi.org/10.1002/2015GL063437>
- Violay, M., Heap, M. J., Acosta, M., & Madonna, C. (2017). Porosity evolution at the brittle-ductile transition in the continental crust: Implications for deep hydro-geothermal circulation. *Scientific Reports*, 7(1). <https://doi.org/10.1038/s41598-017-08108-5>
- Violay, Marie, Gibert, B., Mainprice, D., Evans, B., Dautria, J. M., Azais, P., & Pezard, P. (2012). An experimental study of the brittle-ductile transition of basalt at oceanic crust pressure and temperature conditions. *Journal of Geophysical Research: Solid Earth*, 117(B3). <https://doi.org/10.1029/2011JB008884>
- Wang, J. J., Zhu, J. G., Chiu, C. F., & Zhang, H. (2007). Experimental study on fracture toughness and tensile strength of a clay. *Engineering Geology*, 94(1–2), 65–75. <https://doi.org/10.1016/j.enggeo.2007.06.005>
- Wang, K., & Davis, E. E. (1996). Theory for the propagation of tidally induced pore pressure variations in layered subseafloor formations. *Journal of Geophysical Research: Solid Earth*, 101(B5), 11483–11495. <https://doi.org/10.1029/96JB00641>
- Wang, X. Q., Schubnel, A., Fortin, J., Guéguen, Y., & Ge, H. K. (2013). Physical properties and brittle strength of thermally cracked granite under confinement. *Journal of Geophysical Research: Solid Earth*, 118(12), 6099–6112. <https://doi.org/10.1002/2013JB010340>
- Wang, Y., Meng, F., Wang, X., Baud, P., & Wong, T. fong. (2018). Effective Stress Law for the Permeability and Deformation of Four Porous Limestones. *Journal of Geophysical Research: Solid Earth*, 123(6), 4707–4729. <https://doi.org/10.1029/2018JB015539>
- Weertman, J. (1978). Creep laws for the mantle of the Earth. *Philosophical Transactions of the Royal Society of London. Series A, Mathematical and Physical Sciences*, 288(1350), 9–26. <https://doi.org/10.1098/rsta.1978.0003>

- Wehrens, P., Berger, A., Peters, M., Spillmann, T., & Herwegh, M. (2016). Deformation at the frictional-viscous transition: Evidence for cycles of fluid-assisted embrittlement and ductile deformation in the granitoid crust. *Tectonophysics*, 693, 66–84. <https://doi.org/10.1016/j.tecto.2016.10.022>
- Wei, Y., & Anand, L. (2008). On micro-cracking, inelastic dilatancy, and the brittle-ductile transition in compact rocks: A micro-mechanical study. *International Journal of Solids and Structures*, 45(10), 2785–2798. <https://doi.org/10.1016/j.ijsolstr.2007.11.028>
- Whitney, D. L., Broz, M., & Cook, R. F. (2007). Hardness, toughness, and modulus of some common metamorphic minerals. *American Mineralogist*, 92(2–3), 281–288. <https://doi.org/10.2138/am.2007.2212>
- Wong, T., & Baud, P. (2012). The brittle-ductile transition in porous rock: A review. *Journal of Structural Geology*, 44, 25–53. <https://doi.org/10.1016/j.jsg.2012.07.010>
- Wong, T., David, C., & Zhu, W. (1997). The transition from brittle faulting to cataclastic flow in porous sandstones: Mechanical deformation. *Journal of Geophysical Research*, 102(B2), 3009–3025. <https://doi.org/10.1029/96JB03282>
- Wong, T. F. (1982). Micromechanics of faulting in westerly granite. *International Journal of Rock Mechanics and Mining Sciences And*, 19(2), 49–64. [https://doi.org/10.1016/0148-9062\(82\)91631-X](https://doi.org/10.1016/0148-9062(82)91631-X)
- Xu, C., & Fowell, R. J. (1994). Stress intensity factor evaluation for cracked chevron notched brazilian disc specimens. *International Journal of Rock Mechanics and Mining Sciences & Geomechanics Abstracts*, 31(2), 157–162. [https://doi.org/10.1016/0148-9062\(94\)92806-1](https://doi.org/10.1016/0148-9062(94)92806-1)
- Xu, S., Fukuyama, E., Yamashita, F., Mizoguchi, K., Takizawa, S., & Kawakata, H. (2018). Strain rate effect on fault slip and rupture evolution: Insight from meter-scale rock friction experiments. *Tectonophysics*, 733, 209–231. <https://doi.org/10.1016/j.tecto.2017.11.039>
- Yoon, J. S., Zang, A., & Stephansson, O. (2014). Numerical investigation on optimized stimulation of intact and naturally fractured deep geothermal reservoirs using hydro-mechanical coupled discrete particles joints model. *Geothermics*, 52, 165–184. <https://doi.org/10.1016/j.geothermics.2014.01.009>
- Zang, A., Wagner, C. F., & Dresen, G. (1996). Acoustic emission, microstructure, and damage model of dry and wet sandstone stressed to failure. *Journal of Geophysical Research: Solid Earth*, 101(B8), 17507–17521. <https://doi.org/10.1029/96JB01189>
- Zang, A., Yoon, J. S., Stephansson, O., & Heidbach, O. (2013). Fatigue hydraulic fracturing by cyclic reservoir treatment enhances permeability and reduces induced seismicity. *Geophysical Journal International*, 195(2), 1282–1287. <https://doi.org/10.1093/gji/ggt301>
- Zang, A., Zimmermann, G., Hofmann, H., Stephansson, O., Min, K.-B., & Kim, K. Y. (2018). How to Reduce Fluid-Injection-Induced Seismicity. *Rock Mechanics and Rock Engineering*. <https://doi.org/10.1007/s00603-018-1467-4>
- Zhou, Z., Cai, X., Ma, D., Cao, W., Chen, L., & Zhou, J. (2018). Effects of water content on fracture and mechanical behavior of sandstone with a low clay mineral content. *Engineering Fracture Mechanics*, 193, 47–65. <https://doi.org/10.1016/j.engfracmech.2018.02.028>

- Zhu, W., Baud, P., & Wong, T. (2010). Micromechanics of cataclastic pore collapse in limestone. *Journal of Geophysical Research: Solid Earth*, 115(B4). <https://doi.org/10.1029/2009JB006610>
- Zhu, W., Baud, P., Vinciguerra, S., & Wong, T. (2011). Micromechanics of brittle faulting and cataclastic flow in Alban Hills tuff. *Journal of Geophysical Research: Solid Earth*, 116(B6). <https://doi.org/10.1029/2010JB008046>
- Zhu, W., Baud, P., Vinciguerra, S., & Wong, T. (2016). Micromechanics of brittle faulting and cataclastic flow in Mount Etna basalt. *Journal of Geophysical Research: Solid Earth*, 121(6), 4268–4289. <https://doi.org/10.1002/2016JB012826>
- Zhuang, L., Kim, K. Y., Jung, S. G., Diaz, M. B., Min, K.-B., Park, S., et al. (2016). Laboratory Study on Cyclic Hydraulic Fracturing of Pocheon Granite in Korea. In *50th US Rock Mechanics/Geomechanics Symposium. American Rock Mechanics Association*. Houston, Texas, USA: ARMA 16-163.
- Zhuang, Li, Kim, K. Y., Jung, S. G., Diaz, M., Min, K.-B., Zang, A., et al. (2019). Cyclic hydraulic fracturing of pocheon granite cores and its impact on breakdown pressure, acoustic emission amplitudes and injectivity. *International Journal of Rock Mechanics and Mining Sciences*, 122, 104065. <https://doi.org/10.1016/j.ijrmms.2019.104065>
- Zoback, M. D., & Byerlee, J. D. (1975). Permeability and Effective Stress. *AAPG Bulletin*, 59, 154–158. <https://doi.org/10.1306/83D91C40-16C7-11D7-8645000102C1865D>

Appendix A

This appendix presents the post-mortem analysis of the samples uniaxial compression deformations presented in Chapter 3. The strain at failure under water saturated condition was observed to be much lower compared to dry conditions. One of the possible cause of such strain reduction at failure is that water helps at localizing the deformations (see discussion in Chapter 3 for more details). However, the analysis of the macroscopic post-mortem deformation of the sample (Figure A.1) do not reveal significant difference between the dry and the water saturated experiments. If localisation seems slightly higher for Bentheim and Rothbach sandstones under water saturated condition compared to dry (Figure A.1b and d), the other tested sandstones don't present such difference.

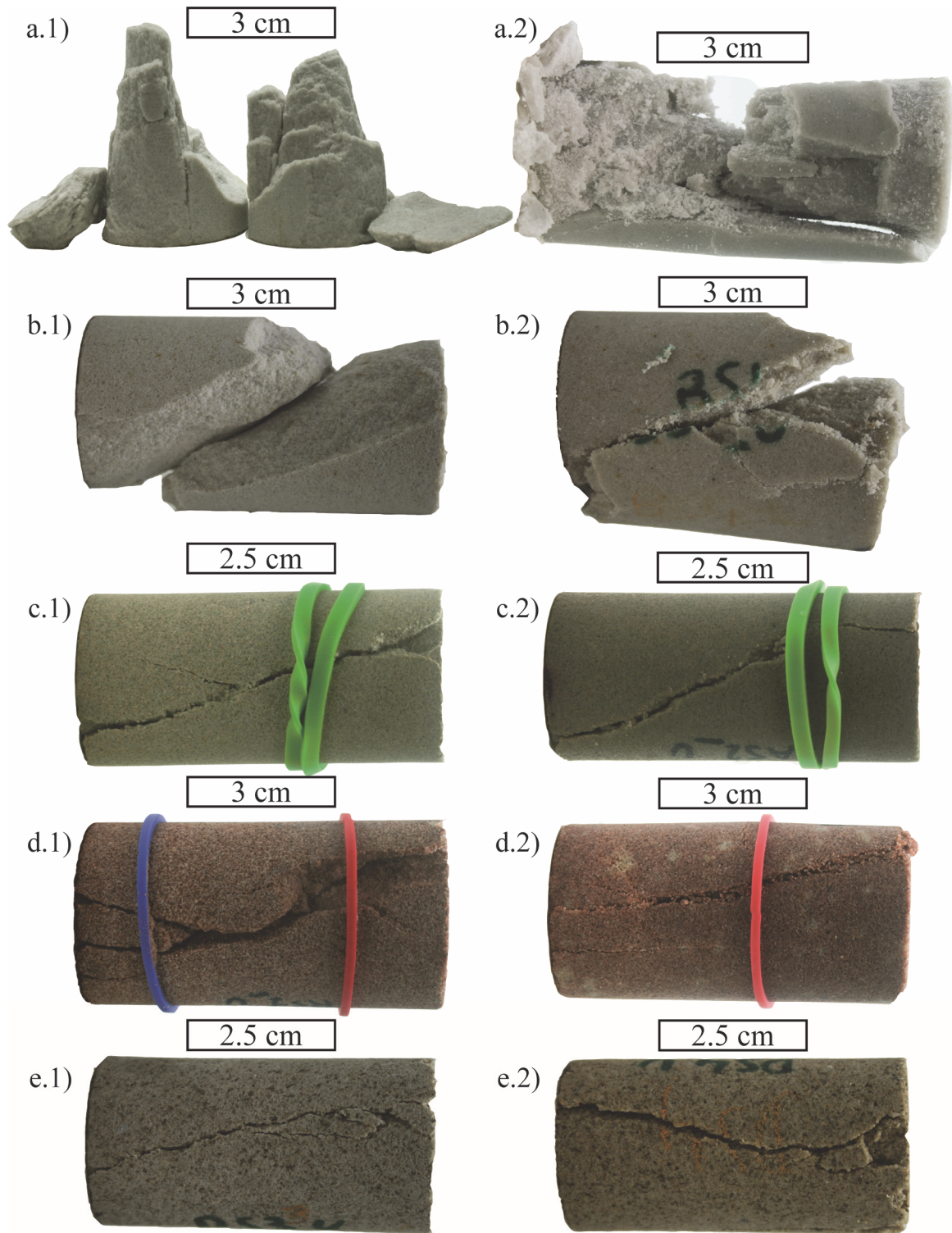


Figure A. 1: Photographies of the uniaxial post-mortem deformations of the five tested sandstones under dry (1) and water saturated (2) conditions. a) Fontainebleau sandstone, b) Bentheim sandstone, c) Adamswiller sandstone, d) Rothbach sandstone and e) Darley Dale sandstone.

Appendix B

This appendix developed the method use to obtain the mechanical envelope of the constant pore fluid pressure experiment. In Figure 6. 4, two envelopes were defined for the brittle field:

- 1) Q_{peak} (i.e., sample strength) as a function of the effective confining pressure ($\sigma_1 - P_f$) data were fitted assuming a wing crack model (Ashby & Sammis, 1990). Under compressional stress, assuming that cracks grow only when the stress intensity factor (K_I) reach a critical value (K_{Ic}), the wing crack length (l) as a function of the stress applied can be written (Brantut et al., 2012):

$$Q(l) = \frac{\left(\frac{K_{Ic}}{\pi a} + (P_c - P_f) \times (c_3 + A_3(c_1 + c_2))\right)}{A_1(c_1 + c_2)} - P_c \quad \text{Equation (B.1)}$$

$$\text{Where } c_1 = \pi^{-2} \left(\frac{l}{a} + \beta_{wc}\right)^{-\frac{3}{2}} \quad \text{Equation (B.2)}$$

$$c_2 = \frac{2(\pi\alpha)^{-2} \sqrt{\frac{l}{a}}}{\rho_0^{-\frac{2}{3}} - \left(1 + \frac{l}{\cos(\theta)a}\right)^2} \quad \text{Equation (B.3)}$$

$$c_3 = \frac{2}{\pi} \sqrt{\frac{l}{a}} \quad \text{Equation (B.4)}$$

With $A_1 = \frac{\pi\sqrt{\beta_{wc}}}{\sqrt{3}} \left(\sqrt{(1 + \mu^2)} - \mu\right)$ and $A_3 = A_1 \left(\frac{\sqrt{(1 + \mu^2)} + \mu}{\sqrt{(1 + \mu^2)} - \mu}\right)$, a the initial flow size, θ being the crack orientation from σ_1 , D_0 represents the initial damage in the sample and β_{wc} being an empirical parameter to restrict K_I to finite value for small wing crack length. The parameter used are presented in Table S1. Equation (A.1) has a maximum value, corresponding to the sample strength, which depend on the effective confining pressure ($P_c - P_f$) and was used for the envelope (black line in Figure 4).

- 2) Residual strength (Q_{residual}), corresponding to the differential stress needed to slide on the formed shear fracture, are fitted by a linear regression: $Q_{\text{residual}} = 3.02 \times (P_c - P_f) + 56.8$ (black dashed line in Figure 6. 4).

Table B. 1: Parameter used for the wing crack model (Ashby & Sammis, 1990). ¹Average radius of micropores (Zhu et al., 2010). ² K_{Ic} for calcite (Atkinson & Avdis, 1980). ³From Ashby & Sammis (1990). ⁴Modified to fit the experimental data.

Parameter	Value
Initial flow size ¹ , a (μm)	0.8
Crack orientation from σ_1 , θ	$\pi/4$
Friction coefficient, μ	0.6
Mode I stress intensity factor ² , K_{Ic} ($\text{MPa}\cdot\text{m}^{1/2}$)	0.2
β_{wc} to restrict K_I to finite values when wing length is small ³	0.1
Initial damage ⁴ , D_0	0.3

References for appendix

- Ashby, M. F., & Sammis, C. G. (1990). The damage mechanics of brittle solids in compression. *Pure and Applied Geophysics*, 133(3), 489–521. <https://doi.org/10.1007/BF00878002>
- Atkinson, B. K., & Avdis, V. (1980). Fracture mechanics parameters of some rock-forming minerals determined using an indentation technique. *International Journal of Rock Mechanics and Mining Sciences & Geomechanics Abstracts*, 17(6), 383–386. [https://doi.org/10.1016/0148-9062\(80\)90523-9](https://doi.org/10.1016/0148-9062(80)90523-9)
- Brantut, N., Baud, P., Heap, M. J., & Meredith, P. G. (2012). Micromechanics of brittle creep in rocks. *Journal of Geophysical Research: Solid Earth*, 117(B8). <https://doi.org/10.1029/2012JB009299>
- Zhu, W., Baud, P., & Wong, T. F. (2010). Micromechanics of cataclastic pore collapse in limestone. *Journal of Geophysical Research: Solid Earth*, 115(B4). <https://doi.org/10.1029/2009JB006610>

Curriculum Vitae

Corentin NOËL

Route de Vallaire, 112

1024, Ecublens

27 years old

+336 30 84 11 35

corentin.noel07@orange.fr



Research interest

I am interested in understanding the mechanisms taking place during crustal deformations. Especially, how fluid pressures can affect deformations such as faulting, fault reactivation or rock mode of deformations (brittle to ductile).

My research focuses on laboratory experiments combined with microstructure analysis and physical modelling of rock properties. I use triaxial apparatus to deform rocks under different crustal conditions. The experimental setups are equipped with sensors such as piezoelectric ceramics or strain gages to understand the physics involved in the rock deformation processes. I then extrapolate these results to give constraints on natural crust deformations.

Education

2017 – 2021

Ph.D. Mechanics (Geomechanics)

Title: Laboratory study of rock and fault deformation during fluid injection.
Laboratory of Experimental Rock Mechanics, Swiss Federal Institute of Technology Lausanne (EPFL).

Supervisor: Marie Violay

2014 – 2016

Master degree in Earth Dynamics and Natural Hazards

University of Montpellier

2011 – 2014

Bachelor degree in Earth and Environment

University of Science and Technology Lille 1

Research experience

2017 – 2021

Ph.D. student

Laboratory of Experimental Rock Mechanics, Swiss Federal Institute of Technology Lausanne (EPFL).

Supervisor: Marie Violay

Jan 2016 – Jul 2016 **Master thesis: Influence of erosion processes on rock gravitational slope deformation: analogue modelling and field study**
Géoazur laboratory
Supervisor: Stéphane Bouissou and Yann Rolland

Publications

- Noël, C., Passelègue, C., & Violay, M. (Under review). Brittle faulting of ductile rock induced by pore fluid pressure build-up. *Journal of Geophysical Research: Solid Earth*.
- Noël, C., Passelègue, F. X., Giorgetti, C., & Violay, M. (2019). Fault reactivation during fluid pressure oscillations: transition from stable to unstable slip. *Journal of Geophysical Research: Solid Earth*. <https://doi.org/10.1029/2019JB018517>
- Noël, C., Pimienta, L., & Violay, M. (2019). Time-Dependent Deformations of Sandstone During Pore Fluid Pressure Oscillations: Implications for Natural and Induced Seismicity. *Journal of Geophysical Research: Solid Earth*, 124(1), 801-821. <https://doi.org/10.1029/2018JB016546>

Conferences talk (T) and poster (P)

1. Noël, C., Passelègue, F. X. & Violay, M. (2020, December). Brittle faulting induced by pore fluid pressure increase in ductile rock mass. (P). In *AGU Fall Meeting 2020*. AGU.
2. Noël, C., Passelègue, F. X., Giorgetti, C., & Violay, M. (2019, December). From aseismic to seismic slip during fluid pressure oscillations on laboratory fault. (P) In *AGU Fall Meeting 2019*. AGU.
3. Noël, C., Passelègue, F. X. T., Pimienta, L. X., & Violay, M. (2019, April). Fault reactivation during pore pressure oscillations. (P) In *EGU General Assembly Conference*. Abstracts (Vol. 21, p. 13143).
4. Noël, C., Passelègue, F. X. T., Pimienta, L. X., & Violay, M. (2019, April). Fault reactivation during pore pressure oscillations. (P) In *Third Schatzalp Workshop on Induced Seismicity*.
5. Noël, C., Pimienta, L., & Violay, M. (2018, September). Experimental study of reservoir seismicity using different injection strategies. (T) In *International Symposium on Energy Geotechnics*.
6. Noël, C., Pimienta, L., & Violay, M. (2018, November). Time-dependent deformations of sandstone during fluid pressure oscillations: implications for natural and induced seismicity. (P) In *16th Swiss Geoscience Meeting*.
7. Noël, C., Pimienta, L., Violay, M. (2018, July). Time-dependent deformations of porous sandstone: pore fluid pressure levels and cyclic oscillations. (P) *International School of Physics "Enrico Fermi", Course 202: Mechanics of Earthquake Faulting, Varenna, Italy, 2018*.
8. Noël, C., Pimienta, L., & Violay, M. (2018, April). Time-dependent deformation of a low porosity sandstone subjected to pore pressure oscillations. (T) In *EGU General Assembly Conference*. Abstracts (Vol. 20, p. 4631).

Supervision and Teaching

Student co-supervision

- Master thesis:
 - Ali Nejjar and Jonas Kasmi, Master Thesis (2019): How do earthquakes impact landslides? Analysis of the effect of cyclic oscillations on fault reactivation. *Swiss Federal Institute of Technology Lausanne*
- Master and Bachelor projects:
 - Filali-Ansary Antoine, Laboratory project (2020): Microstructural analysis of samples undergone laboratory earthquakes. *Swiss Federal Institute of Technology Lausanne*
 - Alexandre Mudry, Laboratory project (2019): Thermal effects on exposed rock slopes: Compilation of case histories and analysis of main problems related to the influence of changing temperature (daily and seasonal) on rock slope stability. *Swiss Federal Institute of Technology Lausanne*
 - Katinka Meier and Jan Osterwalder, Laboratory project (2018): Influence of porosity on sandstone strength. *Swiss Federal Institute of Technology Lausanne*
 - Arabelle de Saussure and Julie Gros, Laboratory project (2017): Influence of porosity on sandstone strength. *Swiss Federal Institute of Technology Lausanne*

Teaching Assistant

- Master courses:
 - Geophysics (2018 & 2019), Master Course, *Swiss Federal Institute of Technology Lausanne*, French/English
- Bachelor courses:
 - Geology for engineers (2019), Bachelor course, *Swiss Federal Institute of Technology Lausanne*, French
 - Rock Mechanics and Tunnelling (2017 & 2018), Bachelor course, *Swiss Federal Institute of Technology Lausanne*, French

Personal skills

Scientific skills

Laboratory geophysics: rock triaxial deformation, rock frictional interface deformation, passive and active ultrasonic wave measurement, porosity, permeability.

Microscopy: Optical microscope, Optical profilometer

Field geophysics: seismic refraction, electrical tomography, 3D scanner, static and cinematic GPS.

Optical imaging: displacement and deformation fields measurement using digital image correlation.

Cartography: tectonics and gravitational deformation characterisation, geomorphology.

Software skills Matlab, QGIS, 7D, Illustrator

Languages French: Mother tongue
English: Full professional proficiency
Italian: Basic

Outreach activities

2018 – 2020 **Ph.D. student representative**, Doctoral school of Mechanics (EDME),
Swiss Federal Institute of Technology Lausanne.